The Lithium Plateau in Super Metal-Rich Stars

By

Donald B. Lee-Brown

Submitted to the graduate degree program in the Department of Physics and Astronomy and the Graduate Faculty of the University of Kansas in partial fulfillment of the requirements for the degree of Doctor of Philosophy.

Committee members

Bruce Twarog, Ph.D., Chairperson

Barbara Anthony-Twarog, Ph.D.

David Mechem, Ph.D.

Gregory Rudnick, Ph.D.

Stephen Sanders, Ph.D.

Date defended: May 9, 2018

The Thesis Committee for Donald B. Lee-Brown certifies
that this is the approved version of the following thesis :

The Lithium Plateau in Super Metal-Rich Stars

Bruce Twarog, Ph.D., Chairperson

Date approved: May 17, 2018

Abstract

I present a study of the lithium abundances for a sample of super metal-rich (SMR, [Fe/H] > + 0.20) main sequence dwarfs in the solar neighborhood. The SMR stars were selected to have surface temperatures in the region of the lithium plateau, a narrow region in temperature space where stars are predicted by models to preserve their initial surface Li abundances while on the main sequence. Despite these predictions, observations of lower-metallicity stars indicate that significant depletion occurs during the first few Gyr of stellar evolution. SMR stars, which represent the extreme end of Galactic chemical evolution, present an opportunity to constrain proposed mechanisms to explain this depletion. 100 SMR candidates were selected from existing surveys and followed up with spectroscopic observations using the Hydra spectrograph on the WIYN 3.5m telescope at Kitt Peak National Observatory, as well as photometric observations using the 0.9m WIYN and 40" telescopes at Kitt Peak and Mount Laguna Observatory, respectively. Using the results from ANNA, a new tool that uses a neural network to parameterize stellar spectra, as well as a more traditional equivalent width based analysis, 44 single stars with [Fe/H] > + 0.20 were identified and Li was measured for each star. Consistent with previous studies, the SMR stars can be divided into a sample of stars with measurable Li and a sample with upper limits only. Examining the low-Li stars' evolutionary states reveals that they are consistent with being evolved Li dip stars and therefore depleted their surface Li while on the main sequence before evolving to the cooler temperatures of the Li plateau. Considering only the high-Li sample, the stars are all consistent with having ages in the range 3 – 4.5 Gyr, indicating that they have already significantly depleted their Li. We find

no young (age < 1 Gyr) SMR stars in the sample, which may explain an observed turnover in the positive correlation between [Fe/H] and initial Li abundance at super-solar metallicities – the only SMR stars in the solar neighborhood are already too old to measure initial Li as they have depleted down to the 2-3 Gyr plateau value. The Li plateau for the SMR sample was measured to be A(Li) = 2.55 dex, which agrees with observations of the similarly-aged super metal-rich cluster NGC 6253 as well as more metal-poor clusters, confirming that the Li plateau abundance in stars older than 2-3 Gyr is apparently insensitive to stellar metallicity. Examining the kinematics and available elemental abundances of the SMR stars, they are shown to be indistinguishable from lower-metallicity thin disk stars aside from their high [Fe/H], consistent with an origin in the inner thin disk.

Acknowledgements

Graduate school is a bit like visiting a haunted house. You go in with what can charitably be called ignorance, quickly find yourself terrified by surprises leaping out at you from the dark, and by the halfway mark all you can think about is how badly you want to get out. This is followed by resignation to the fact that you will probably die before you see the light of day again. Eventually, you miraculously find yourself on the other side but realize that while you were gone the rest of the world kept on going about its business and your friends are now married and bought houses. Despite all this, upon further reflection you decide that it really wasn't that bad and tell everyone who will listen how awesome the whole experience was.

As one might guess, I hate haunted houses, but if I were transported back in time I'd do my Ph.D. all over again and there are a lot of people who deserve a tremendous amount of credit for that sentiment. First off, I could not have asked for better mentorship from my advisors, Bruce Twarog and Barbara Anthony-Twarog. Their guidance, support, flexibility, kindness, and especially patience carried me through graduate school and I think the best indicator of the impact they've had is that I tend think of them as family. Really, really smart family who are an inexhaustible resource for all things astronomy. And just for good measure so the record shows it, I'm going to reiterate the boundless patience they had with their errant graduate student, who was always working on some "short side project" or another and putting off his thesis work.

I was fortunate to have the opportunity to spend a few years working on a different project with Gregory Rudnick, who generously spent a considerable amount of his own time and resources helping me learn about extragalactic evolution and in general

just being a really good person to talk to about my career goals. I don't think I realized how generous that was on his part (and that of my advisors - see discussion of patience above) until well after the fact, so thank you.

Many thanks go to Constantine Deliyannis at Indiana University, who donated significant time to this project and was extremely flexible about trading observing time in order for me to get observations of my desired targets. The staff at WIYN and KPNO were also extremely generous and helpful - in particular thanks go to Di Harmer, who was an invaluable resource when working with Hydra and gave a lot of help with best observing practices, as well as Heidi Schweiker, who generously arranged for me to use part of a testing and engineering night after a string of bad weather.

My committee members certainly deserve thanks for agreeing to be locked in a room with me for hours at a time until I managed to fumble my way through everything I needed to.

There are a lot of other people who contributed to this project unofficially in some way or another over the years, and here are some who deserve special credit:

Teresa Symons and Grayson Petter both contributed in material ways to this project. Teresa's clever *photPARTY* code proved invaluable in greatly accelerating the process of analyzing my photometry, and she was always ready to patiently explain how to use it. Grayson served as the primary "beta tester" of ANNA one summer, and his bug-hunting abilities helped ANNA reach a stable form much faster than it would have otherwise.

Whenever I meet with prospective students, I make sure to highlight the pleasant and open atmosphere in our department and especially the astronomy wing. Sinan Deger, Nesar Ramachandra, John Martens, Mindy Townsend, Justin Mann, Jenn Cooper, and all the other graduate students in the department work hard to make this true. So does our department office staff and administration - I've gotten so many good restaurant

recommendations from Joel Sauerwein in the office that I really think he should make an app for them.

Michael Reeks, who is barely beating me to the Ph.D. at UVA, has been my friend-of-all-trades: best man, confidant, foodie friend, responsibilibuddy, math resource, hiking partner. His friendship is all the more surprising, given that I got both of us suspended in high school for sneaking out late at night.

Jeff Wilkerson at my alma mater, Luther College, was the first person to get me interested in astronomy - before I worked with him, the extent of my astronomy experience was sitting in my backyard as a kid thinking that it was all really boring while my dad tried to get me to look through a telescope.

My parents have always been supportive of the winding path I've taken in life to get where I am, and graduate school was no different. They've good-naturedly asked to read my papers (sorry about that, Mom and Dad) and have always welcomed me back home on short notice. Also they didn't kick me out of the house after they found out I'd been hiding uneaten sandwiches in the heat vents for years throughout elementary school, so that's something.

Finally, my wife Hannah deserves many more thanks than can be written here. Not only did she support me throughout this adventure after moving to Kansas with me, she did so while winning pharmacy school. She also puts up with my steadily growing pile of homebrewing equipment sitting in the corner of our apartment, and my general Grinch-like demeanor most evenings. Thank you, and I love you.

Contents

List of Figures

List of Tables

Chapter 1

Introduction

1.1 Background: Stellar Evolution

[1]Stars spend the vast majority of their lives maintaining hydrostatic equilibrium; that is, the outward radial pressure inside balances the inward force of gravity. Nearly 90% of a star's life is spent maintaining this pressure gradient through fusion of hydrogen into helium in the stellar core, during which time it populates the stellar *main sequence* (MS), a narrow strip in temperature - luminosity (brightness) space (Figure 1.1). While on the MS, the temperature of a star defines its *spectral class*. In order of decreasing surface temperature (and therefore mass), the stellar spectral classes are O ($\geq 30,000$ K), B, A, F, G (the Sun is a G-type star with surface temperature of 5770 K), K, and M (the seemingly random letter assignments are a historical artifact - the classifications in their original incarnation ran alphabetically).

The amount of time a star spends on the MS strongly depends on its mass. This is primarily due to the greater amount of energy required to counterbalance greater stellar mass, though stellar opacity also plays a role (see below). Thus, the more massive a star is, the faster it exhausts its supply of hydrogen, and the shorter its MS lifetime. A typical O type star with mass $20\times$ that of the sun spends approximately 5 million years on the MS, while the sun has a MS lifetime of approximately 10 billion years. Lower mass stars have MS lifetimes exceeding the age of the Universe.

Aside from the very large variance in mass, luminosity, and lifetime, stars in various regions

[1]Information in this section is generally from Carroll, B.W. & Ostlie, D.A. *An Introduction to Modern Astrophysics*, 2nd Ed. Pearson Addison-Wesley, 2007.

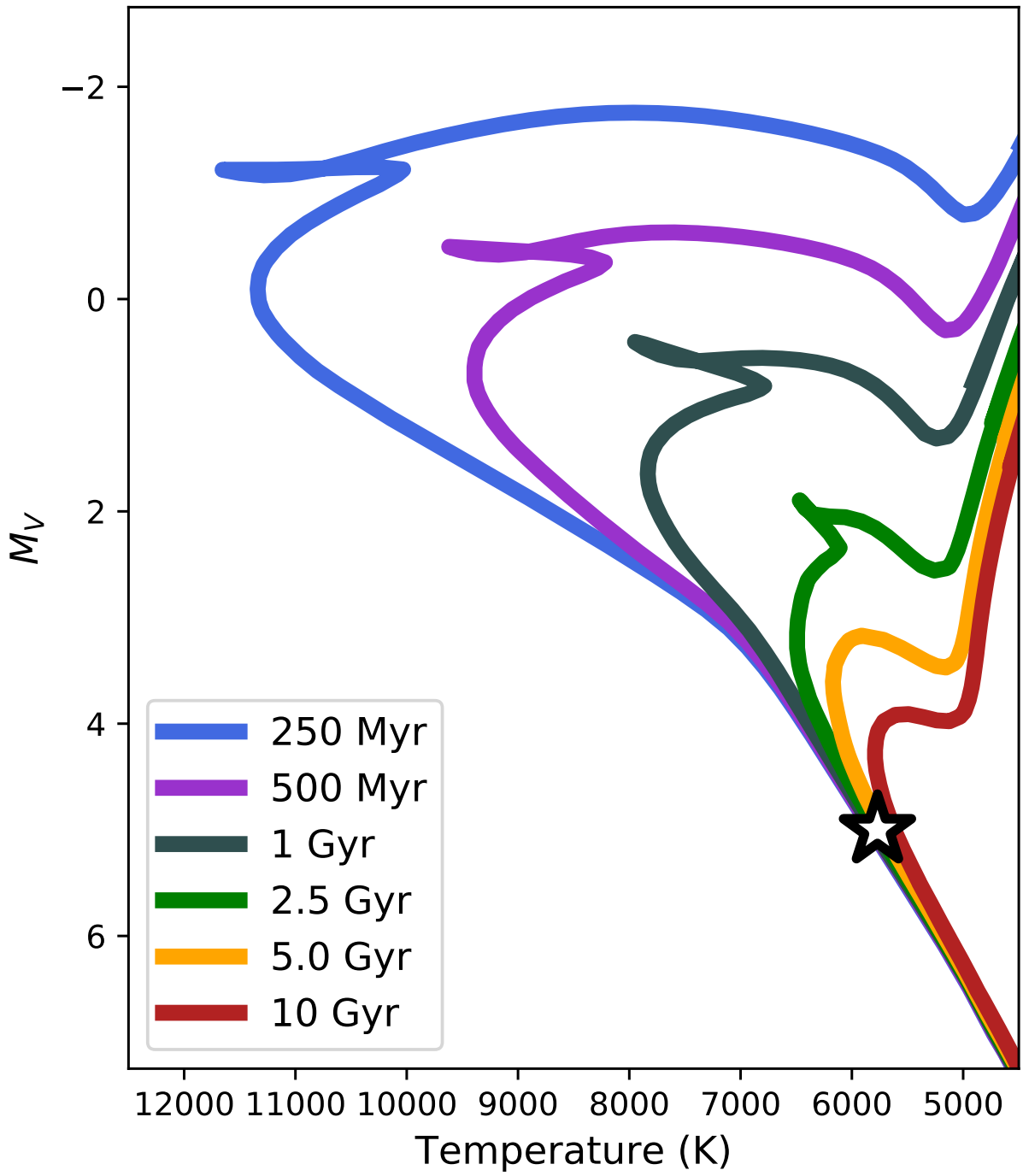

Figure 1.1: The stellar main sequence (MS) and post-MS evolutionary tracks (isochrones) for populations of various ages in temperature-absolute magnitude (in V) space. The MS is the diagonal line extending from M_V and temperatures in the upper left of the plot to M_V and temperatures in the lower right. Stars spend approximately 90% of their lives on the MS, before exhausting the supply of hydrogen in their cores and evolving off the MS. The position of the Sun is indicated by the star. PARSEC isochrones were used to make this figure (Bressan et al., 2012).

of the MS have very different structural properties. In stars more massive (hotter) than the sun, the high temperature in the stellar core is sufficient to make the dominant fusion process the carbon-nitrogen-oxygen (CNO) cycle, a strongly temperature-dependent cycle catalyzed by ^{12}C, with various isotopes of C, N, and O as intermediaries. In solar-like stars or cooler, energy production through the CNO cycle is negligible; these stars instead fuse hydrogen through the proton-proton chain (pp-chain).

The dominant fusion process has a profound impact on the structure of the stellar interior. In stars where energy production is primarily through the highly-temperature sensitive CNO cycle, the temperature gradient in the stellar core is so steep that outward radiative transport of energy is insufficient and convection is triggered. In lower mass stars, the milder temperature-dependence of the pp-chain means that radiative transport alone is sufficient to transport energy out of the core region.

Opacity plays a key role in the interior structure of stars as well. Stellar opacity, generally represented by a radially-dependent coefficient, κ, refers to the capability of stellar material to absorb and/or scatter energy; it is inversely proportional to the photon mean free path and mass density. In solar-like stars, neutral hydrogen can exist near the stellar surface; this greatly increases the opacity in the region, and radiative transport becomes inefficient. The resultant convective area forms the *surface convection zone* (SCZ), which will be of critical importance later in this work. In hotter stars, hydrogen can remain ionized throughout the stellar envelope, and the SCZ is very shallow to nonexistent; in cooler stars, the SCZ can extend more deeply into the stellar atmosphere, reaching all the way to the core for the lowest mass stars, i.e. they can be entirely convective.

A second, very important driver of opacity is the composition of the stellar interior. Stars are overwhelmingly hydrogen and helium - the sun is composed (by mass) of $\sim$71% H, $\sim$27% He, and $\leq$ 2% everything else ("metals" in astronomy). Metals can remain only partially ionized at temperatures up to several million K (compared to 10,000 K for H), and thus they have outsized impact on the opacity in the stellar envelope, greatly influencing the depth of the SCZ. [2]

[2]The abundance of an element in a star is reported as A(X)=12+$log(N_X/N_H)$, where N_X and N_H are the column densities of element X and hydrogen, respectively. Often the metallicity is reported in relation to the solar value as

1.1.1 Standard Stellar Evolution Theory

The mathematical description of the processes described above is one of the great feats of modern astronomy. In the most basic form of the theory, stars are assumed to be spherically symmetric, and the equations of state for a stellar atmosphere reduce to four partial differential equations - one each for hydrostatic equilibrium, conservation of mass, luminosity gradient, and radiative/-convective transport. These fundamental stellar equations, when combined with nuclear reaction pathways and cross sections, opacity relations, and parameters to control the extent of convection, form the *standard stellar evolution theory*, or SSET (Deliyannis et al., 1990; Pinsonneault, 1997). Throughout this paper, I will compare observational results against the predictions of SSET.

Note that in the preceding description, physical phenomena such as magnetic fields, turbulence, meridional circulation, stellar rotation, mass loss, etc. have been omitted. These proccesses are known to occur in stars, but are not included in SSET, which is fundamentally one-dimensional. Despite these omissions and its relative simplicity, SSET is remarkably successful at predicting general stellar evolutionary patterns. However, as will be shown, there is ample evidence that non-standard effects can no longer be ignored and must be incorporated into stellar models if we hope to advance our understanding of stellar structure and evolution.

1.2 Lithium: A Tracer of our Ignorance

Astronomers cannot directly observe the interiors of stars in order to assess the accuracy of SSET, but they can infer internal nuclear and hydrodynamic properties from various elemental tracers at the stellar surface. One such tracer is lithium-7 (hereafter referred to as Li), which is destroyed at temperatures exceeding 2.5 million K through proton capture: $^{7}\mathrm{Li}+p \rightarrow {}^{8}\mathrm{Be} \rightarrow 2\times{}^{4}\mathrm{He}$. The ease with which Li is destroyed (hydrogen fusion is sustained in the Sun at $\sim$14 million K) means that it can only stably exist in the outer atmospheres of stars. Li's fragility, however, and the fact that it is not produced in MS stars, mean that it is exceptionally useful in the study of stellar structure, as

[X/H], where [X/H]=A(X)-A(X)$_{solar}$. As a final note, the abundance of iron in relation to the solar value, [Fe/H], is often used as a very good approximation of the overall stellar metallicity.

its measurement offers insight into the history of internal mixing processes in a star.

According to SSET, in cool stars (temperatures lower than the cooler G stars) with deep enough convection zones that material at the stellar surface is cycled into contact with hot interior layers, atmospheric lithium is destroyed over time. On the other hand, in hotter stars (temperatures greater than the hotter G stars) with shallower SCZs, the lithium abundance should remain basically unchanged from its initial value during the MS phase. In all stars, SSET predicts an abrupt depletion of any remaining Li once a star evolves off the MS and develops deep convection zones on the giant branch (Deliyannis et al., 1990; Pinsonneault, 1997).

Unfortunately, SSET at best only qualitatively matches Li observations. Nearly every measurement of Li contradicts the quantitative predictions of SSET, and despite great effort, there exists no comprehensive model that can reproduce observed patterns. In the next sections, I will summarize the main challenges posed by Li and the current state of efforts to solve them.

1.2.1 The Cosmological Lithium Problem

Lithium was first recognized as an element that may have been nucleosynthesized in measurable quantity during the Big Bang by Wagoner et al. (1967). A string of observational efforts to measure the primordial abundance of lithium ensued (see, e.g., Boesgaard, 1976, and references therein), but the foundation of the modern "cosmological lithium problem" was provided by Spite & Spite (1982) who, in an analysis of metal-poor halo dwarfs, identified a near-constant lithium abundance of A(Li)$\sim$2.2 in stars with surface temperatures hotter than $T_{\rm eff} = 5600$ K and iron abundances $-2.2 \leq$ [Fe/H] ≤ -1.1. As the sample of stars was very metal-poor and thus likely to have formed before the Galaxy had undergone significant chemical enrichment (e.g., McWilliam, 1997), and as the surface temperatures of the sample indicated they had convection zones insufficiently deep to deplete Li, the authors concluded the plateau Li abundance represented the original, cosmological value. Steadily improving instrumentation has allowed studies to confirm the existence of the Spite plateau with increasing precision - a review of the subject by Spite et al. (2012) compiled a number of recent measurements to arrive at a plateau value of A(Li)=2.2$\pm$0.06.

Unfortunately, the exquisitely precise plateau abundance determination is entirely at odds with the results from experimental cosmology. The cosmological abundance of lithium can be predicted using the baryon-to-photon ratio η under the standard Big Bang Nucleosynthesis (BBN) model (e.g., Walker et al., 1991; Thomas et al., 1993; Iocco et al., 2007; Coc et al., 2012, 2014). The BBN calculations made possible by the WMAP cosmic microwave background (CMB) satellite (seven year results: Komatsu et al., 2011; Larson et al., 2011), while in very good agreement with observations of the other primordial elements, resulted in a ^{7}Li abundance of A(Li)=2.72, a factor of over 3 higher than the Spite plateau value (Coc et al., 2012). Recent results from *Planck* (Planck Collaboration et al., 2014) have reduced the magnitude of the difference somewhat to a factor of ~ 3, A(Li)=2.65, but precision improvements have strengthened the significance of the discrepancy to $\sim 8\sigma$ (Coc et al., 2014).

Studies have suggested modifications to BBN that may account for the discrepancy (e.g., Bailly, 2011; Kang et al., 2012), but it has proven difficult to construct a model that resolves the Li issue while preserving the remarkable agreement between CMB-derived predictions and the observed abundances of the other primoridial elements, principally deuterium and helium-4 (Coc et al., 2014). Modifications to the canonical stellar structure models, on the other hand, have led to some limited yet still unsatisfactory success. Proposed non-SSET effects that may cause the enhanced transport required to deplete surface Li from its original value in the Spite plateau stars include atomic diffusion (Richer & Michaud, 1993) and various mixing/turbulence-related effects - differential rotation (Pinsonneault et al., 1990), gravity wave excitation (Garcia Lopez & Spruit, 1991), etc. (see, e.g., Richard et al., 2005). Diffusion has conclusively been shown by a number of studies to have a non-negligible effect on surface Li over a stellar lifetime, but it cannot reproduce the Spite plateau when adopted as the sole source of Li destruction (Pinsonneault, 1997). Evidence indicates that rotation likely plays a role as well (see Section 1.2.3), but it is not clear what its relative importance is for the old, metal-poor stars defining the Spite plateau.

The resolution to the cosmological lithium problem is not likely to come about through observations of more Spite plateau stars; the issue is not one of precision but of ignorance. Assuming

that the disagreement between cosmology and Li observations is due to deficiencies in SSET, it may be that a better understanding of Li depletion in younger dwarfs (see Section 1.2.3) will help reconcile the Spite plateau with BBN. However, as halo stars represent the old, metal-poor extreme of stellar parameter space, Spite plateau stars are an important test of any proposed modifications to SSET.

1.2.2 Galactic Lithium Enrichment

As discussed in the previous section, standard BBN models indicate a primordial Li abundance of A(Li)=2.65 (Coc et al., 2014). However, measurements of the meteoric Li abundance, indicative of the initial Li abundance in the solar system when it formed $\sim$4.6 billion years ago, show a much higher abundance of A(Li)$\sim$3.3 dex (Lodders et al., 2009). Similar, super-primordial Li abundances are also seen in open clusters (e.g., Pasquini et al., 1997; Randich et al., 1997; Burkhart & Coupry, 2000). Thus, it appears clear that the Galaxy has enriched the interstellar medium (ISM) in Li by a factor of at least $\sim$ 4 since the Big Bang.

Galactic chemical evolution models generally incorporate three mechanisms for generating Li. The first is spallation of particles in the ISM by high energy galactic cosmic rays (GCRs) from e.g., Type II supernovae or shock fronts (e.g., Reeves, 1970; Knauth et al., 2000). A second source is cataclysmic stellar events - novae and supernovae are both predicted to produce Li in measurable quantities (Arnould & Norgaard, 1975; Dearborn et al., 1989; Hartmann et al., 1999; Tajitsu et al., 2015). Finally, evolved intermediate and low mass stars can undergo interior production and transport of ^{7}Be - which then decays to Li - to the stellar surface (the Cameron-Fowler mechanism; Cameron & Fowler, 1971; Sackmann & Boothroyd, 1992), followed by mass loss and ISM enrichment (Wallerstein & Sneden, 1982; Sackmann & Boothroyd, 1999; Ventura & D'Antona, 2010; García-Hernández et al., 2013). Destruction of Li is primarily through mixing in stellar atmospheres before gas is returned to the ISM (Ryan et al., 2001).

Unfortunately (though perhaps unsurprisingly to the reader given the general theme being set in this chapter), models have generally failed to reproduce the observed trends in Li (Ryan et al.,

2001). For example, the model of Fields & Olive (1999), in which Type II supernovae dominate the production of Li with a minor contribution from GCRs, matches the metal-poor galactic halo but fails to reproduce disk Li observations, in particular failing to produce enough Li to match the solar meteoric abundance. The model of Romano et al. (1999), which includes increasing contributions from novae, GCRs, and evolved stars at late galactic times, manages to produce more Li but still fails to reach the solar system Li abundance. This issue is widespread (Ryan et al., 2001) - models tend to reasonably reproduce the low metallicity evolution of Li, but underpredict the magnitude of enrichment by the time the ISM attains $\sim$solar metallicity.

The source of the "extra" Li has remained unresolved. Production through spallation is relatively well-constrained, as it also creates ^{7}Be and B, so observations of these elements must be matched (Romano et al., 1999; Suzuki et al., 1999; Ryan et al., 2001). Recent work may help constrain yields from novae (Tajitsu et al., 2015), but Li synthesis in evolved stars in particular remains poorly understood. Much of the uncertainty is due to lack of accurate Li *and* age measurements in stars over a range in metallicity; these are the principle source of experimental constraint for stellar Li production theories (see, e.g., Romano et al., 1999; Travaglio et al., 2001; Ryan et al., 2001; Lambert & Reddy, 2004), so obtaining additional measurements may help resolve the model deficiencies.

However, tracing the evolution of Galactic Li through studies of stellar populations of different ages has proven observationally difficult. An unavoidable issue is one of stellar lifetime - stars with $\sim$solar or super solar metallicities that are hot enough (i.e., massive enough) to preserve their surface lithium under SSET have already evolved well off the MS by $\sim 5-6$ Gyr (see, e.g, Hobbs & Pilachowski, 1988; Meibom et al., 2009). However, even considering younger stars, the particulars of Li enrichment are somewhat murky. Traditionally, clusters have been favored for investigating Galactic Li patterns; as they are composed of a coeval population of stars, they can provide a statistically significant sample of stars with no depletion (provided they are young enough), and precise ages can be estimated through isochrone fitting. What studies have found is that clusters spanning a wide range in age - M67 (4-5 Gyr old; Deliyannis et al., 1994), NGC

2243 (3-4 Gyr; François et al., 2013), NGC 6253 (3 Gyr; Cummings et al., 2012), NGC 3680 (1.7 Gyr; Anthony-Twarog et al., 2009), NGC 752 (1.4 Gyr; Sestito et al., 2004; Anthony-Twarog et al., 2009), Praesepe (650 Myr; Soderblom et al., 1993), and the Pleiades (100 Myr; Boesgaard et al., 1988) - all show roughly the same upper lithium abundance, A(Li)$\sim$ 2.9-3.3.

Taken at face value, these results indicate very little galactic Li enrichment over the past 5 Gyr (see, e.g., Rebolo, 1989). However, this straightforward interpretation should be taken with caution due to several issues. First, these clusters span a range in metallicity, which is predicted under SSET to impact the rate of Li depletion (e.g., Pinsonneault, 1997). Thus, even though NGC 6253 (Cummings et al., 2012) and M67 (Deliyannis et al., 1994) have the similar peak lithium abundances, A(Li)$\sim$2.8-3.0, the significantly different metallicities - M67 is essentially solar, [Fe/H]$\sim$0, while NGC 6253 is one of the most metal-rich clusters known, [Fe/H]$\sim$+0.40-0.46 - are consistent with a scenario in which higher metallicity results in higher initial Li but more aggressive depletion. Second, and perhaps more importantly, there is strong evidence for non-standard MS depletion in virtually all stars below $\sim$ 6800 K (see Section 1.2.3).

A number of studies have demonstrated that initial Li is positively correlated with [Fe/H], at least until the metallicity of the Hyades ([Fe/H]=+0.15). In particular, studies of field stars have shown that the upper envelope of A(Li) is tightly correlated with [Fe/H] - as the field stars should span a range in age at a given metallicity, this upper envelope should be representative of the initial A(Li) regardless of any non-standard MS depletion, provided that enough young stars are sampled (Ramírez et al., 2012; Delgado Mena et al., 2015; Guiglion et al., 2016; Fu et al., 2018). These observations at least qualitatively agree with the predictions of galactic chemical evolution models that take into account Li production (Ryan et al., 2001; Travaglio et al., 2001).

Above the metallicity of the Hyades, there is some tension between observations and models. In the field star studies of Delgado Mena et al. (2015), Guiglion et al. (2016) and Fu et al. (2018), there is a turnover in the A(Li) defined by the upper envelope of Li measurements above [Fe/H]$\sim$+0.20. Especially in Fu et al. (2018), this was interpreted as a signature of decreasing initial Li at supersolar metallicities, in opposition to the predictions of most chemical evolution

models (e.g., Travaglio et al. (2001) or Prantzos (2012), though see Romano et al. (2001)).

In an ideal Universe, the relation between metallicity, galactic age, and initial Li content could be disentangled by observations of clusters that vary in one of age or metallicity and not in the other, resulting in a grid of observations smoothly covering metallicities from those of NGC 2243 ([Fe/H]=-0.54; François et al. (2013)) to NGC 6253 and ages from $\sim$5 Gyr to present. Unfortunately, the general chemical evolution of the Galaxy renders this impossible; there are no known very metal-rich or very metal-poor young clusters. Observing field stars can allow for better sampling across the [Fe/H]-age plane, but field star ages are difficult to determine, and so observations of many stars are needed to "counteract" the large scatter in determined age. Progress has been made on this front (e.g., Ramírez et al., 2012; Guiglion et al., 2016), but further observations are needed to better constrain proposed chemical evolution models.

1.2.3 Lithium Depletion on the Main Sequence

While observations of Li in massive stars agree quite well with the predictions of SSET, at temperatures below $\sim$ 7000 K, a number of phenomena can be seen across a range of MS and evolved stars that defy standard models. Even considering the cooler G and K dwarfs, where SSET predicts depletion on the MS, Li abundances are typically consistently overpredicted by theory across a range in stellar age. An even more dramatic illustration of the shortcomings of SSET can be found in the Li dip that emerges in stars after a few hundred Myr. Observations and theoretical progress on these fronts are described below.

1.2.3.1 The Li Dip

The so-called *lithium dip*, as shown in Figure 1.2, occurs in a narrow region of MS stellar surface temperature - $T_{eff} \sim 6600 \pm 200$ K - and manifests itself as a dramatic decrease in surface Li abundance relative to stars outside the temperature range. The dip was first observed in the Hyades by Boesgaard & Tripicco (1986), who found stars within the dip to have depleted their Li by a factor of $\sim$ 100 relative to hotter or cooler stars. However, the much younger Pleiades showed no

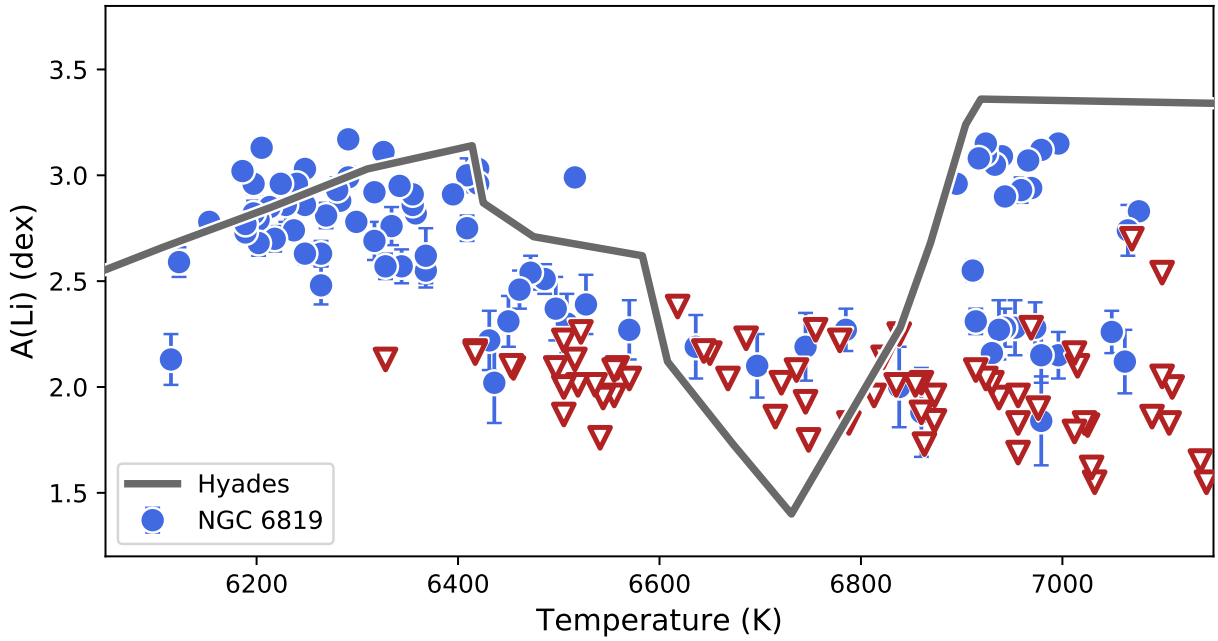

Figure 1.2: Li measurements in the dip region for NGC 6819 (blue and red points, Deliyannis et al. 2018, in prep) and the Hyades (gray line, Anthony-Twarog et al. (2009)). For the NGC 6819 data, the blue points correspond to Li detections while the red triangles indicate upper limits. The lithium dip is the dramatic decrease in A(Li) in the temperature range 6400-6800 K in both clusters. The Li plateau begins at the cool edge of the dip. The temperature data for the Hyades were shifted 150 K to account for the changes in surface temperature due to the more evolved nature of the NGC 6819 sample.

evidence for a dip (Boesgaard et al., 1988). Thus, the Li dip appears to be a MS phenomenon.

It is now known that the Li dip is correlated with Be (Boesgaard & King, 2002) and B (Boesgaard et al., 2016) depletion; these two elements are destroyed at higher temperatures than Li but still susceptible to mixing-driven depletion. It has also been shown that the surface temperature of the dip is constant with respect to [Fe/H]; this in turn implies that the mass of stars in the dip is correlated with [Fe/H] (Chen et al., 2001; Anthony-Twarog et al., 2009; Cummings et al., 2012). However, from the theoretical side, no satisfactory solution describing the formation and evolution of the Li dip yet exists.

Modifications to SSET to try and explain the presence of the dip have invoked a variety of mechanisms that enhance mixing, such as gravity waves (Montalbán & Schatzman, 2000), mass loss (Swenson & Faulkner, 1992), diffusion (Richer & Michaud, 1993), and rotation (Chaboyer et al., 1995) (for a comprehensive summary of proposed mechanisms responsible for the dip, see Stephens et al. (1997)). In particular, there seems to be widespread consensus that rotationally-driven mixing plays a key role in the formation of the Li dip (Deliyannis & Pinsonneault, 1997; Talon & Charbonnel, 2003; Boesgaard et al., 2004; Somers & Pinsonneault, 2014). Certainly observations support this; it is known that stars with Li-dip surface temperatures undergo severe rotational spindown upon arrival on the MS (Skumanich, 1972; Jeffries et al., 2002; Lanzafame & Spada, 2015).

Rotation and/or rotational spindown appear to play the strongest role in the formation of the Li-dip, but it is not yet clear what role, if any, other proposed mechanisms, e.g., mass loss (Schramm et al., 1990), play. Observations of Li and Be in clusters spanning a range in age should resolve these unanswered questions, as different models predict quite different relative abundances for stars as they age (Sills & Deliyannis, 2000). Additionally, if the Li-dip is connected with enhanced mixing due to spindown of a star's MS rotation, then patterns similar to the Li-dip should be observable in stars hotter than the dip as they evolve off the MS, their SCZs deepen, and their high MS rotation rates decline. Some observations targeting this behavior have already been reported and favor the spindown theory (Anthony-Twarog et al., 2018), but additional observations are

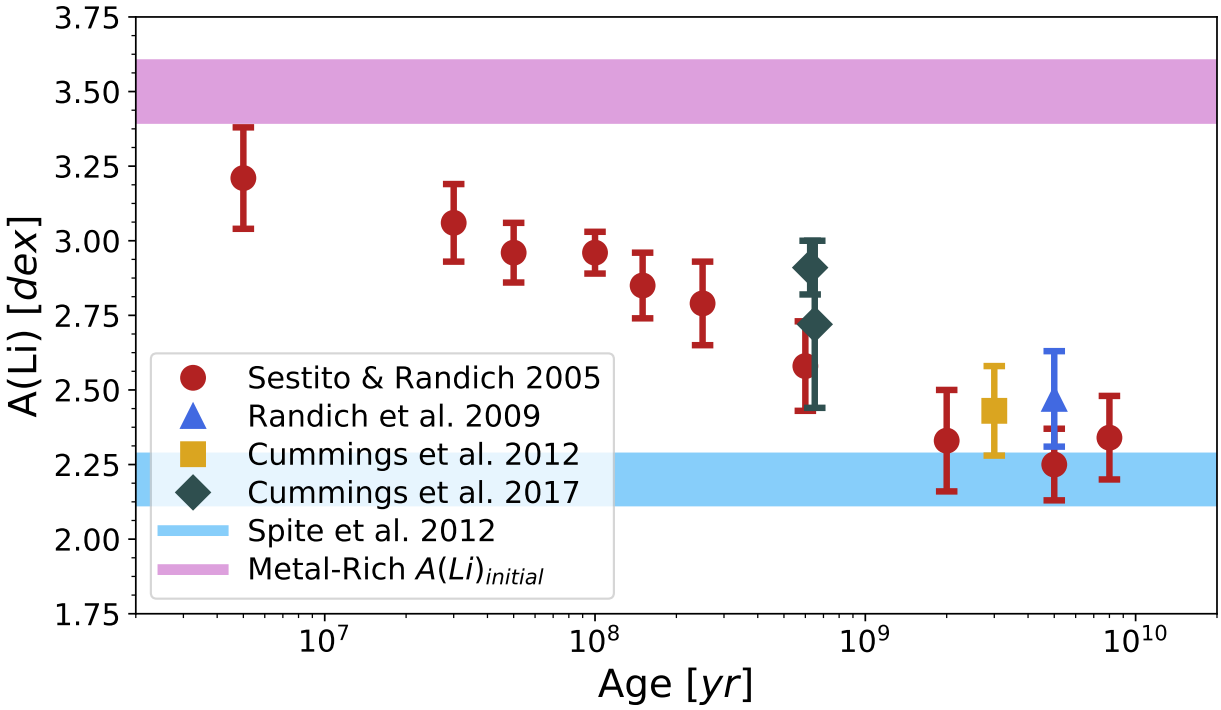

Figure 1.3: Open cluster Li plateau depletion as a function of age. Studies referenced are Sestito & Randich (2005), Randich et al. (2009), Cummings et al. (2012), and Cummings et al. (2017). The Spite abundance (lower solid band) shown is from Spite et al. (2012). The SMR initial Li abundance (upper solid band) is inferred from the results of Ramírez et al. (2012).

needed and should provide a very powerful test of the spindown-Li-dip hypothesis.

1.2.3.2 The Li Plateau

Cooler than the dip, in the temperature range $\sim 5900 - 6300$ K in solar metallicity stars (see Figure 1.2), SSET predicts that Li should be preserved, as the late F and early G stars which populate this region do not have SCZs which extend deeply enough into the stellar interior to burn Li (Deliyannis et al., 1990; Pinsonneault, 1997). As noted in Section 1.2.1, the SSET predictions of no MS depletion in this temperature regime forms the basis for the cosmological interpretation of the Spite plateau (Spite & Spite, 1982). The observations of MS Li depletion in this temperature range in more metal-rich stars cast significant doubt on the notion of a "pristine" Spite plateau abundance.

A number of open cluster studies - in particular that of Sestito & Randich (2005) - have shown

strong evidence for MS depletion in the plateau region. Assuming that initial Li is correlated with [Fe/H], stars in a typical solar-metallicity cluster should have an initial Li abundance of 3.1-3.3 dex (see Section 1.2.2). However, as shown in Figure 1.3, by the age of the Hyades (600 Myr), the average Li abundance in the plateau region in local open clusters is only 2.4-3.1 dex (Sestito & Randich, 2005; Cummings et al., 2017). This lower-than-predicted abundance is despite the fact that the typical 600 Myr open cluster examples - the Hyades and Praesepe - are actually metal-rich with [Fe/H]$\sim$+0.15, and should therefore have even higher initial A(Li).

The apparent MS Li plateau depletion continues, but then appears to dramatically slow or cease altogether by 2-3 Gyr (Sestito & Randich, 2005; Randich et al., 2009; Cummings et al., 2012; Somers & Pinsonneault, 2014). A(Li) is then approximately constant in open clusters up to 7-8 Gyr old, with a plateau value of 2.1-2.6 dex. That the lower bound of this plateau value is suspiciously coincident with the Spite value has not gone unnoticed (e.g., Sestito & Randich, 2005).

Another perplexing issue is raised by these observations as well. SSET predicts that the rate of Li depletion has a strong metallicity dependence, such that higher [Fe/H] stars at a given temperature should more rapidly deplete Li (Swenson et al., 1994; Pinsonneault, 1997). However, the uniform Li plateau value in older open clusters exists across a wide range in metallicity, from the metal-poor NGC 2243 (François et al., 2013) to the super metal-rich NGC 6253 (Cummings et al., 2012). Furthermore, given that initial A(Li) correlates with [Fe/H], why is it that clusters over this presumed wide range in initial A(Li) all depleted to essentially the same plateau value? Why does the plateau exist at all - what aspect of the internal structure of plateau stars changed by 3 Gyr in order to shut off the rapid depletion seen at younger ages?

Satisfactory answers to these questions have proven elusive. Mechanisms invoked to try and address them have generally been similar to those used to explain the presence of the Li dip. In Sestito & Randich (2005), it was determined that models incorporating diffusion and rotation as mixing processes (Chaboyer et al., 1995) were able to replicate the depletion pattern seen in clusters younger than the Hyades. However, these same models then increasingly overpredicted the

plateau abundance for stars older than the Hyades. As with the dip, rotation seems a likely culprit as plateau stars are predicted to spin down by 2 Gyr (Somers & Pinsonneault, 2014; Lanzafame & Spada, 2015), coincident with the apparent timescale of MS depletion.

1.2.3.3 Low Mass Stars

Cool stars (G dwarfs and later) spend significant time in the pre-MS phase (before hydrogen fusion commences), during which their atmospheres are deeply convective and will significantly deplete Li, with the extent of depletion increasing with decreasing surface temperature (due to a longer pre-MS phase). Once the MS phase begins, SSET predicts that the SCZs in hotter G dwarfs ($T_{eff} \geq 5000K$) will retreat to a shallow enough level to stop Li destruction (e.g., Pinsonneault, 1997). Very cool dwarfs will remain sufficiently convective to deplete Li on the MS.

Once again, observations inform us of deficiencies in SSET. For very young clusters, such as the Pleiades (100 Myr), standard models incorporating pre-MS depletion match observations very well (Jeffries, 2000). However, by the age of the Hyades (650 Myr), SSET underpredicts the amount of Li depletion in G dwarfs by a factor of 2-4 (e.g., Cummings et al., 2017). Towards even cooler temperatures, the discrepancy worsens - solar-metallicity models predict ~ 0.3 dex depletion during the pre-MS phase for stars with $T_{eff} \sim 5600$ K (Pinsonneault, 1997), yet in the Hyades this depletion is ≥ 1 dex (a factor of at least 10!). Even accounting for the greater pre-MS depletion due to the higher [Fe/H] of the Hyades (Swenson et al., 1990), it is clear that extra, "non-standard" depletion mechanisms are at work.

Indeed, one has to look no further than the Sun to see the extent of the problems in depletion models. The Sun has a present-day Li abundance of A(Li)=1.05 (Asplund et al., 2009), while as discussed previously, its initial abundance - as determined from meteorites - was A(Li)=3.28 (Lodders et al., 2009). Models predict very little pre-MS depletion, around 0.06 dex (Meléndez et al., 2010), *so the Sun is overdepleted in Li by a factor of 100* relative to its initial abundance. For a time there was some debate over whether the solar Li abundance was anomalous, given that less extreme depletion was observed in other, solar-like stars (e.g., Lambert & Reddy, 2004), but in a

review of recent results, Meléndez et al. (2010) found that in the sun and stars with similar [Fe/H] and surface temperatures as the sun, reported Li abundances ranged from A(Li)$\sim$0.6 to A(Li)$\sim$2.4 dex. Crucially, the authors found that these abundances were smoothly correlated with stellar age. This result is consistent with the trends observed in clusters, and adds to the need for models to incorporate a mechanism (or mechanisms) for MS Li depletion in dwarfs.

Fortunately, good progress on this front has been made. As with proposed solutions to the other anomalous MS Li patterns, studies have focused on the inclusion of rotation, diffusion, gravity waves, or some combination thereof to produce MS depletion. In dwarfs, the model of Talon & Charbonnel (2005), incorporating rotation, diffusion, and especially gravity waves successfully reproduces the G-dwarf depletion seen in the Hyades. The depletion in F-stars seems to be driven more by diffusion and rotation effects than gravity waves (Charbonnel & Talon, 2005; Xiong & Deng, 2009). The age-dependent depletion observed in solar-like stars is fit very well with models incorporating rotational spindown (Talon & Charbonnel, 2005; Meléndez et al., 2010).

While current models certainly show promise, there remain several unanswered questions. In particular, the unresolved issue of Galactic Li production (§1.2.2) injects considerable uncertainty into the matter - for instance, since it is not known with certainty how initial Li depends on [Fe/H] (e.g., Ryan et al., 2001), robust tests of depletion models are limited to areas of stellar parameter space where the initial Li *is* known, e.g., $\sim$solar-like stars. Additionally, in open clusters, dwarfs of a uniform age appear to deplete their Li non-uniformly (see Cummings et al., 2012). The specific rotation and spindown history of a star may be the cause of such an effect (Takeda et al., 2010; Do Nascimento et al., 2010; Pinsonneault, 2010), perhaps driven by a dispersion in radius during the pre-MS phase (Somers & Pinsonneault, 2014). There has also been spirited debate over whether or not the presence of planets may noticeably impact a star's Li abundance through, e.g., angular momentum transport during the pre-MS phase or turbulence induced by planet migration (Israelian et al., 2009; Eggenberger et al., 2010; Sousa et al., 2010; Baumann et al., 2010; Ghezzi et al., 2010; Delgado Mena et al., 2015; Mishenina et al., 2016). Hopefully observations of the sort called for in Section 1.2.2, combined with astroseismology of planet-hosts in a variety of evolutionary states

can resolve these lingering questions.

1.2.4 Evolved Stars

SSET predicts that when a low or intermediate-mass star leaves the MS, the SCZ in the star extends more deeply into the stellar atmosphere (i.e. "first dredge-up"), reaching areas of the star formerly hot enough to destroy Li. The subsequent mixing of the surface material - which still contains Li - with the Li-poor interior material results in severe dilution of the surface abundance (Deliyannis et al., 1990). When the hydrogen-fusing shell in an RGB star reaches the boundary formed by the SCZ during the first dredge-up (the RGB bump), the remaining atmospheric Li is quickly destroyed, likely through some process such as thermohaline mixing (e.g., Charbonnel & Zahn, 2007; Lattanzio et al., 2015).

Thus, once a low-mass star leaves the main sequence, it should very quickly deplete its Li through dilution and, later, destruction. However, a growing number of studies have found Li-rich RGB stars with enhancements of 10-1000 relative to the typical RGB value, A(Li)$\leq$ 0.5 (Kraft et al., 1999; Smith et al., 1999; Kumar & Reddy, 2009; Ruchti et al., 2011; Anthony-Twarog et al., 2013). These stars have either preserved their surface Li from some already-anomalously high value or, more likely, have managed to create it through some unknown physical process.

The question of how RGB stars can create Li remains unresolved. It is known that intermediate-mass giants on the asymptotic giant branch (AGB) can create Li through the Cameron-Fowler mechanism (Cameron & Fowler, 1971; Sackmann & Boothroyd, 1992), but the convective zones in low-mass RGB stars do not extend deeply enough for the Cameron-Fowler mechanism to operate (Sackmann & Boothroyd, 1999). The study by Smith et al. (1999) suggested planet engulfment as a possible mechanism; this was ruled out as a general mechanism in subsequent work by Kumar et al. (2011). The Li-rich giants studied by Ruchti et al. (2011) were generally located at the RGB bump, leading them to suggest that the Li rich phase may be a common, yet fleeting phase driven by extra mixing at the bump. The single Li-rich giant studied by Anthony-Twarog et al. (2013) led the authors to favor turbulent mixing driven by fast internal rotation as an explanation, at least

for that star. A recent study of globular cluster giants by Kirby et al. (2016) included yet another explanation for the origin of Li-rich RGB stars - standard Cameron-Fowler Li-production during the He flash phase in an intermediate-mass star followed by mass transfer of Li-rich material to an RGB companion.

Clearly, as demonstrated by the significant number of competing theories on the matter, the issue of Li-rich RGB stars remains unresolved. Much of the uncertainty is driven by the very small number of examples, as only $\sim$dozen such stars have been identified. Hopefully, with the addition of more known Li-rich RGB stars, the question of how they created their Li can be resolved.

1.3 Summary: What is Lithium Telling Us?

To summarize, the four principle issues associated with lithium are:

1. There is longstanding tension between the lithium abundances of very old stars and the predictions of cosmological models, with observations lower than predictions by a factor of $\sim$3.

2. Our galaxy has become enriched in lithium by a factor of at least 4 relative to its primordial value. Models attempting to describe this enrichment are poorly constrained, particularly with respect to stellar production of lithium.

3. Main sequence and subgiant dwarf stars cooler than $\sim$ 6000 K tend to show lower surface lithium abundances relative to model predictions (e.g., the sun is overdepleted by a factor of 50), and apparently similar stars can have lithium abundances spanning an order of magnitude or more.

4. Observed phenomena like the lithium dip in main sequence F dwarfs (factors of 100+ overdepletion) and massive lithium enhancements (order of 10-1000) in small numbers of evolved stars defy the predictions of standard evolution models.

Despite being presented as separate topics, the issues described above are clearly intertwined - this can be seen in the widespread success the inclusion of rotation has had across the range of MS temperatures. Thus, any modification to SSET that resolves one issue will likely also make progress on the others. Or to put it another way, any modifications to SSET with the aim of resolving one of the above issues must operate within the constraints imposed by the others. It is also worth noting again that the various challenges detailed above have implications that extend far beyond the study of Li. In fact, one could argue that Li is merely the "messenger", informing us of the imperfections in our models of stellar structure, galactic chemical evolution, and possibly cosmology.

1.4 Study Design: Lithium in Super Metal-Rich Stars

The previous discussions in this chapter illustrate the dramatic mismatches between our observations of Li in stellar atmospheres and theoretical expectations. This tension indicates that our understanding of stellar evolution and the internal structure of stars is still incomplete. Resolving this requires a more comprehensive set of observations than is currently available and it is this demand for more observations that serves as the primary motivation for this study.

In particular, there is a clear need for additional observations of the Li plateau region in stars spanning a range in age and metallicity. To briefly review, the plateau region consists of main sequence G stars at a given age and metallicity with surface temperatures near 6000 K (for solar metallicities) that have similar (with respect to temperature) Li abundances (see, e.g. Sestito & Randich, 2005). In metal poor halo dwarfs, the plateau occurs above 5600 K and has long been argued to be a measure of the cosmological Li abundance (Spite et al., 2012). However, despite support from standard stellar evolution models, nearly all observational evidence suggests that this interpretation may be incorrect. The main observations can be summarized as follows:

1. Open cluster studies show that over the first 1-2 Gyr of main sequence evolution, plateau-temperature stars deplete their Li from a higher initial value to A(Li)$\sim 2.4-2.6$ dex - see

Figure 1.3 (Sestito & Randich, 2005; Randich et al., 2009; Cummings et al., 2012, 2017)

2. Over the next $\sim$7 Gyr of evolution this depletion appears to slow or cease, with the plateau remaining at A(Li)$\sim 2.4-2.6$ dex, as seen in Figure 1.3 (Sestito & Randich, 2005; Randich et al., 2009; Cummings et al., 2012, 2017). Individual cluster plateau levels are statistically consistent with the Spite et al. (2012) halo star plateau level, but taken together, appear to be $0.1-0.2$ dex higher than the halo dwarf level.

3. The observed depletion pattern in open clusters occurs over a wide range in metallicity, from the [Fe/H]=-0.5 of Berkeley 32 (Randich et al., 2009) to the extremely supersolar [Fe/H]=+0.4 of NGC 6253 (Cummings et al., 2012).

4. Observations of field stars spanning a wide range in [Fe/H] and age indicate that initial Li is correlated with [Fe/H], such that the highest [Fe/H] field stars have the highest initial Li, as determined by the upper limits of the distribution of A(Li) at fixed metallicity (Ramírez et al., 2012; Guiglion et al., 2016; Fu et al., 2018). This relation holds for at least -0.5 < [Fe/H] < 0.0; at the low end of the range the upper limit of A(Li) is 2.6 dex, while at solar metallicities it is $\sim$ 3.3 dex. There is potentially a leveling off or turnover in the relationship at high [Fe/H], such that stars with [Fe/H]>+0.2 show a decrease in maximum Li abundance (Guiglion et al., 2016; Fu et al., 2018).

5. The observations of plateau-temperature field stars are consistent with the trends observed in open clusters - thin-disk stars (a younger, more metal-rich population of stars) with a spread in metallicity have A(Li) spanning a large range, while thick-disk stars (an older population of stars that are on average metal-poor) have an *upper limit* abundance of A(Li)$\sim 2.2-2.3$ (Ramírez et al., 2012).

Thus, observational evidence points to strong Li depletion for the first few Gyr of stellar evolution, after which depletion slows or ceases. The level of the plateau after this initial depletion is relatively insensitive to metallicity, which in turn implies that the more metal-rich stars (which

likely have higher initial A(Li)) more aggressively deplete their Li. The depleted plateau level is very close to the halo dwarf Spite plateau abundance. Again, it is stressed that **standard stellar evolution and structure models do not predict any of these observations!**

1.4.1 Open Questions

It is tempting to simply draw from these observations the conclusion that the Spite plateau abundance is depleted from some initial, higher A(Li) consistent with cosmological simulations and measurements. However, the patterns outlined above raise several other perplexing questions:

1. Why do stars of significantly different metallicities, and therefore different initial Li, appear to deplete to the same plateau level on approximately the same timescale? What is the mechanism driving this? Metallicity is known to impact the extent of depletion (Pasquini et al., 1997; Cummings et al., 2012; Boesgaard et al., 2015) - is the higher initial Li in metal-rich stars balanced by more aggresive depletion during the first few Gyr of evolution?

2. Do younger plateau stars stop depleting Li after ~ 2 Gyr, or do they continue to deplete more slowly, such that by the age of the Spite halo dwarfs ($\sim 10-12$ Gyr) they reach the Spite plateau abundance? What internal processes cause the apparent rapid decrease in depletion rate by 2 Gyr?

3. Does initial Li turn over at high metallicities, as indicated in Guiglion et al. (2016) and Fu et al. (2018)? This is not predicted by Galactic chemical evolution models (e.g. Prantzos, 2012).

1.4.2 Super Metal-Rich Stars

Clearly, these questions can all be addressed, either directly or indirectly, by measurement of Li in super metal-rich stars (SMR stars, i.e. [Fe/H]>+0.20) spanning a range in age. The most expedient way to do this is via observation of field stars. However, as yet there is no study specifically

targeting such stars - while the field star studies of Ramírez et al. (2012), Guiglion et al. (2016), and Fu et al. (2018) all contain metal-rich stars, there are very few of them and many of them may not be plateau stars due to the sample selection strategies employed by these studies (see, e.g., Guiglion et al., 2016).

That few stars with [Fe/H]>+0.20 were analyzed by the aforementioned studies is unsurprising; such stars are quite rare in the solar neighborhood. The existence of a small number of local, super metal-rich stars has been unequivocally shown for some time (see, e.g., Malagnini et al., 2000; Feltzing & Gonzalez, 2001). Prior to this there was some debate in the literature as to whether or not such stars even existed (see the review by McWilliam, 1997), and there were difficulties confirming or denying SMR status due to model limitations in this metal-rich regime (Taylor, 1996).

Despite the well-established existence of SMR stars, it is unclear where in the galaxy they formed. Studies to-date have been limited by small sample sizes, but have typically found nothing unusual about these stars other than their high metallicity (Feltzing & Gustafsson, 1998). Explanations for their origins have ranged from being ejected bulge stars (Barbuy & Grenon, 1990), thin-disk members (Feltzing & Gonzalez, 2001), or a population that does not conform to any typical galactic stellar sub-population (Castro et al., 1997). Ultimately, none of these potential explanations are completely satisfactory - the bulge origin runs counter to the kinematics and abundance ratios in many of the SMR stars (Feltzing & Gonzalez, 2001), and the thin-disk origin is challenged by the fact that nearby star forming regions only extend up to [Fe/H]$\sim$+0.15 (the Hyades and Praesepe, see Cummings et al., 2017).

More recently, there has been some renewed interest in SMR stars due to their increased frequency of hosting Jupiter-mass planets (Gonzalez & Laws, 2000; Robinson et al., 2007; López-Valdivia et al., 2017), but there has been little progress in determining why they exist. Cluster studies indicate that the galaxy was capable of producing highly-enriched stars relatively early in its history, as evidenced by the two known super metal-rich galactic open clusters: NGC 6791 ($\sim$ 8 Gyr, Boesgaard et al., 2015) and NGC 6253 ($\sim$3.5 Gyr, Cummings et al., 2012). The possible

connection between these clusters and the SMR field stars is as-yet unknown, and it is also not known if there are very young SMR stars (age < 1 Gyr) in the solar neighborhood.

If a reasonable sample of SMR stars can be assembled for this study, then, not only can the Li depletion patterns in these stars be investigated, but additional analysis may also help shed light on the origin of local SMR stars. In the years since the initial debates regarding the origins of these stars, many new observations have become available, including many wide-field surveys of the solar neighborhood that provide atmospheric parameter estimates (see Section 2.2). Additionally, extremely precise kinematics and parallaxes are beginning to become available thanks to ESA's Gaia mission. These data, taken together, should facilitate the identification of many additional SMR stars and provide the necessary information to answer questions regarding their origin.

1.4.3 Study Goals

In light of the above discussion, three primary goals were set for this study. These goals were set knowing that while ideally, precise ages would allow for a detailed mapping of the Li depletion in super metal-rich stars as a function of time, in practice, precise age estimates are very difficult to determine for isolated field stars. Therefore, the objectives listed below do not require age determinations.

1. What is the upper envelope of A(Li) in the observed super metal-rich stars? Assuming this is a measure of the initial A(Li) in stars of this metallicity, does it confirm the turnover observed in Delgado Mena et al. (2015), Guiglion et al. (2016), and Fu et al. (2018))?

2. What is the lower limit of A(Li) in the observed super metal-rich stars? Assuming that the ages of the sample extend beyond 2 Gyr, is the lower limit consistent with the plateau level observed in metal-poor or solar-metallicity samples?

3. What is the origin of super-metal rich stars? Do they have kinematic or chemical properties (other than [Fe/H]) that distinguish them from typical stars in the solar neighborhood?

Chapter 2

Experimental Design and Observations

2.1 Observational Strategy

The ideal targets to answer the questions outlined in Chapter 1 are main sequence and turnoff stars with temperatures in the narrow range $5800 < T_{\rm eff} < 6500$ K and high metallicities, [Fe/H] > +0.20. As stars with this temperature and metallicity are relatively rare, targets were selected from survey catalogs that provide temperature and metallicity estimates in order to maximize the probability that a star selected for followup is indeed a *bona fide* metal-rich star with Li-plateau surface temperature. It was determined that statistical considerations necessitated approximately 100 Li observations. This figure was calculated by setting as the overall goal the ability to constrain any detected Li plateau to within 0.1 dex, while assuming a 50% success rate in confirming the super metal-rich status of any candidate targets.

In addition to these basic requirements, a number of practical considerations were taken into account when selecting targets. First and foremost, it was clear from the inception of the project that the spectroscopic requirements would be challenging. As the study targeted isolated field stars, the 100-star requirement effectively meant 100 separate fields would need to be observed spectroscopically. On top of this, spectra with signal-to-noise ratios (SN) of SN$\sim$100-200 are needed to be able to resolve the small $\sim$ 10 mÅ 6708 Å feature. In order to reduce the time needed to observe each of the 100 fields while achieving the required SN, an apparent magnitude limit of V=10 was imposed, and targets were generally selected to be significantly brighter, usually $V < 9$. This meant that for observations with the 3.5m WIYN/Hydra[1] instrument (see Section 2.5),

[1]The WIYN Observatory is a joint facility of the University of Wisconsin-Madison, Indiana University, the Na-

exposure times would be < 600 seconds and many stars could be observed each night or even observed during twilight hours.

The spectroscopic instrument desired for this study, being located at a northern observatory, necessitated a declination limit of -10 degrees. In order to be as flexible as possible, targets spanning the full range in right ascension were desired so as to be able to observe at any point during the year. These two requirements, in addition to those discussed in previous paragraphs, guided the selection of catalogs used to identify metal-rich candidate stars.

2.2 Survey Mining

Ultimately, the targets for this study were selected from the catalogs produced by two surveys of stars in the solar neighborhood - the Geneva-Copenhagen survey and the N2K survey - as well as one compilation of smaller-sample, high resolution spectroscopic studies - the Hypatia catalog. These three sources proved the most fruitful for identifying metal-rich candidates, as they provided relatively well-constrained parameterizations for bright, northern-hemisphere, main sequence dwarfs. Other survey datasets were also considered, but for various reasons were not used for this study.

2.2.1 The Geneva-Copenhagen Survey

The Geneva-Copenhagen survey (Nordström et al., 2004) was an effort to build on previous Strömgren *uvby*Hβ observations of brighter F and G dwarfs in the solar neighborhood (Olsen, 1983, 1993, 1994) and provide precise atmospheric parameters and kinematics for a large sample of nearby dwarf stars. The survey can be seen as a complement to the spectroscopic survey of Edvardsson et al. (1993); the Geneva-Copenhagen survey traded the precision and detail afforded by high-dispersion spectroscopy in favor of a much larger and less biased sample (Nordström et al., 2004). The most current version of the Geneva-Copenhagen catalog provides Strömgren-derived

tional Optical Astronomy Observatory and the University of Missouri.

$T_{\rm eff}$, [Fe/H], $log(g)$, radial velocity measurements, Hipparcos and Tycho proper motion/parallax measurements where available for nearly $\sim 14,000$ nearby, predominantly main sequence stars.

For this study, the most recent $T_{\rm eff}$, [Fe/H], and $log(g)$ determinations of Casagrande et al. (2011) were used to select metal-rich candidates. The Casagrande et al. (2011) parameterizations benefit from a more precise, infrared flux-based temperature scale (Casagrande et al., 2010), which in turn provides better metallicity estimates. From the full catalog of 14,000 stars, 329 stars with magnitude $V < 10$ and parameter estimates within the ranges provided in the previous section were selected. Of these stars, 36 are cross-listed with the other catalogs listed below, while 293 are unique targets. Ultimately, 14 of the cross-listed targets and 77 unique targets were observed for this study.

2.2.2 The Hypatia Catalog

The Hypatia catalog (Hinkel et al., 2014, 2017) is a compilation of ~ 150 high-resolution spectroscopic studies of FGKM main sequence stars in the solar neighborhood (within 150 pc). Because varying spectroscopic analysis methods result in substantial systematic differences in stellar parameters when comparing different spectroscopic studies (Hinkel et al., 2016), great care was taken during the construction of the Hypatia catalog to reduce these effects. Efforts included renormalization of [Fe/H] measurements to an internally consistent solar scale, requiring multiple [Fe/H] measurements for each star, and quantifying the scatter in abundance determinations by comparing different studies. The version of the Hypatia catalog used for this study contains abundance determinations for nearly 6000 stars. A wealth of ancillary data is also available for each catalog member, including thin/thick disk status, Gaia parallaxes, individual elemental abundances, and parameterizations from other catalogs such as PASTEL (Soubiran et al., 2016).

A total of 289 metal-rich candidates were selected from the Hypatia catalog. Of these, 53 are cross-listed with other catalogs, and 236 are unique to Hypatia. 27 cross-listed and 5 unique stars were spectroscopically observed as part of this study.

2.2.3 The N2K Low-Resolution Spectroscopic Survey

The N2K ("Next 2000") project (Sato et al., 2005) was a low-resolution spectroscopic survey of Hipparcos-selected FGK dwarfs conducted using the Keck, Magellan, and Subaru telescopes. The goal of the survey was to search for hot Jupiter planets via the radial-velocity technique (e.g. Butler et al., 2001) by leveraging the well-established metallicity-massive planet correlation (e.g. Gonzalez & Laws, 2000; Fischer & Valenti, 2005). The project's moniker refers to the target selection strategy - the goal was to spectroscopically survey the next 2000 previously unobserved, brightest, metal-rich Hipparcos targets. The final N2K catalog consists of 1907 metal-rich stars with spectroscopically determined $T_{\rm eff}$, [Fe/H], and $log(g)$ (via Lick index measurement Robinson et al., 2007). Because the N2K targets are bright (7 < V < 10), of FGK spectral type, are metal-rich, and have precisely determined atmospheric parameters, the catalog is an ideal source for targets for this study.

From the N2K catalog of stellar parameters, a total of 100 stars were selected that fall within this study's sample selection bounds. 69 of these stars are unique to the N2K catalog; the other 31 are cross-listed. Of these stars, 20 of the cross-listed targets and 13 of the unique targets were eventually spectroscopically observed.

2.2.4 Other Sources

Two other large surveys were also mined for metal-rich candidates. The Sloan Extension for Galactic Understanding and Exploration (SEGUE) (Yanny et al., 2009) was a spectroscopic add-on to the ubiquitous Sloan Digital Sky Survey (SDSS) (York et al., 2000). The SEGUE catalog provides spectroscopically-derived fundamental stellar parameters for nearly 250,000 stars spanning a range in evolutionary state. However, the range in magnitude spanned by SEGUE, $14 < g < 20.3$ (SDSS g), makes single-star spectroscopy quite expensive, and while several dozen SEGUE targets were flagged for observation as part of this study, none were ultimately observed.

The RAdial Velocity Experiment (RAVE) (Steinmetz et al., 2006) was a multifiber spectroscopic survey of nearly 500,000 stars visible from southern latitudes. The principle goal of RAVE

was to measure precise radial velocities and atmospheric parameters for the selected targets; the sample was deliberately selected to significantly overlap with the kinematic solutions provided by Tycho and Gaia. Unlike SEGUE, RAVE targeted significantly brighter stars, $8 < I < 12$. However, being a survey of the southern sky, only a small subsample of RAVE targets are observable as part of this study. Three brighter, northerly RAVE stars with $I < 10$ were flagged as metal-rich candidates, but none were ultimately observed.

Finally, individual spectroscopic studies of smaller numbers of field stars were also considered as a potential source for metal-rich stars. However, as detailed in Hinkel et al. (2016), it is non-trivial to correct for the systematic differences when comparing results from different spectroscopic studies, making it difficult to assess the relative value of different studies in terms of identifying metal-rich stars. Ultimately, since the Hypatia catalog is relatively comprehensive, of good quality, and internally consistent, it was used as the only source of results from small-sample studies.

2.3 Photometric Observations

2.4 The WIYN 0.9m and MLO 40" Telescopes

The photometric observations for this study were carried out using two instruments: the 0.9m WIYN telescope at Kitt Peak National Observatory (KPNO) near Tucson, AZ[2], and the 40" telescope at Mt. Laguna Observatory near San Diego, CA. The 0.9m was equipped with the *Half Degree Imager*, a 4K $\times$ 4K chip with a 29' $\times$ 29' field of view with 0.43" pixels. The MLO 40" was equipped with a 2K $\times$ 2K chip originally from the ULTRA 1.25m technology demonstrator project (NSF grant: AST-0320784) with a $\sim 12' \times 12'$ FOV and $\sim 0.4''$ pixels. On both instruments, the full extended Strömgren system of narrow-band filters (*uvbyCaH*β) was used to image each target observed as part of this study.

[2]Kitt Peak National Observatory is part of the National Optical Astronomy Observatory, which is operated by the Association of Universities for Research in Astronomy (AURA) under cooperative agreement with the National Science Foundation

2.4.1 Reduction and Calibration of Photometry

For the 0.9m and 40" telescopes, the image calibration process was the same, and used standard Image Reduction and Analysis Facility (IRAF, www.iraf.noao.edu) software routines. First, the images were bias and overscan corrected; these steps remove the non-zero mean contribution to the recorded flux level due to the electronics and readout. Approximately 11 bias frames were collected at the start of each night of observation; these were then median-combined to create a master bias frame used for the correction to all frames. Overscan correction was done via a narrow, unexposed region of the chip and the correction is unique to each frame. Once these two steps were carried out, the images were then sorted into groups based on the filter used to collect each frame.

Once sorted, each image in a group was flat-fielded using a master flat corresponding to the correct filter. Flat-fielding removes variations in pixel response across the chip, i.e., it ensures a "flat" response, and is typically done by exposing the chip to a uniform illumination source, then deriving the relative correction that would be required to cause the resultant image to be uniform. This correction is then applied to all images. For the 0.9m WIYN data, initial flattening was accomplished via well-exposed dome flats (10 per filter). Because it is very difficult to create a perfectly uniformly illuminated screen, in that small gradients often occur across frames when flat-fielded in this way, the images were then illumination-corrected using sky flats. These flats, collected by exposing the telescope to the sky during the sky background-dominated portion of twilight, are much more uniformly illuminated, and can be used to correct for the gradients induced by using dome flats. For the MLO 40", the dome flat-field lamp was too dim to achieve adequate throughput when using the narrow-band Strömgren filters, so only sky flats were used to flat-field. For both instruments, typically 3-5 sky flat frames for each filter were collected each night, weather permitting.

Once the images were bias/overscan corrected and flat-fielded, fluxes could be measured. Because the targets for this study are bright and generally isolated, simple aperture photometry is sufficient to obtain instrumental magnitudes. This process consists of summing the pixel counts within a fixed aperture centered on the target, minus the average per-pixel background multiplied

by the total number of pixels within the aperture. The per-pixel background, which in general varies across the image, is usually derived from a selection of pixels encompassing the original aperture centered on the target. For the aperture photometry used for this study, the *photparty* (Python Automated Square-Aperture Photometry) (Symons, 2017) code was used to extract flux measurements automatically from each frame. As its name suggests, *photparty* uses simple-to-compute square apertures to rapidly derive brightness measurements. Background levels are computed locally using the median level in a series of four square apertures located around the aperture containing the target. Once fluxes were extracted using *photparty*, they were converted to instrumental magnitudes using the standard formula $m = -2.5 \times log(F) + 20$, where m is the instrumental magnitude, F is the recorded flux, and the zeropoint is set to 20. These instrumental magnitudes were then corrected for the effects of atmospheric extinction using a calibration unique to each night of observation.

After this procedure, the instrumental magnitudes were then used to calculate the various Stromgren indices. These included the temperature-sensitive $H\beta$ index, defined as $H\beta = H\beta_n - H\beta_w$, the gravity-sensitive c_1 index, defined as $c_1 = (u-v) - (v-b)$, the original, metallicity-sensitive m_1, defined as $m_1 = (v-b) - (b-y)$, and the metal-sensitive *hk* index of the extended Stromgren system defined as $hk = (Ca-b) - (b-y)$. The principle advantage of *hk* over m_1 is that since *hk* samples the strong calcium H and K lines, it is more sensitive to changes in metallicity, especially for weak-lined metal-poor stars (Twarog & Anthony-Twarog, 1995). Additionally, the $b-y$ color was calculated for each star; this color is analogous to $B-V$ in the widely used Johnson broadband filter system and can be similarly used as a temperature indicator.

After the color indices were computed, they were converted to a standard system via the standard star observations (see observing procedure below). For the *uvbyH*β indices, the Olsen (1994) catalog of observations was used for calibration (with additional $H\beta$ observations being pulled from various sources present in the SIMBAD database (Wenger et al., 2000)). For the *hk* measurements, the Twarog & Anthony-Twarog (1995) catalog of standards was used.

Of note is that no reddening correction was applied during the calibration process. This choice

Table 2.1. Photometric Observations

Run Date	No. Stars Observed	Telescope Used
05/2015	5	WIYN 0.9m
12/2015*	26	MLO 40”
02/2016	16	WIYN 0.9m
05/2016	9	WIYN 0.9m
08/2016	10	MLO 40”
10/2016	9	MLO 40”
01/2017*	24	MLO 40”
05/2017*	26	MLO 40”
10/2017*	29	MLO 40”
12/2017*	21	MLO 40”

Note. — The asterisks denote the runs dedicated to this project.

was made since the target stars are all nearby (< 100 pc) and the impact of reddening should be relatively small. Additionally, because single stars were observed, determining the reddening precisely is very difficult. After some discussion, the consensus was that applying an individual reddening correction for each star would likely inject uncertainties that outweighed the effect of a small systematic uncertainty due to an absence of such a correction.

2.4.2 Summary of Photometric Observations

The photometric observations occurred over 10 runs during the years 2015-2017. Of these runs, five (all on the MLO 40” telescope) were dedicated to this project, while for the others, the nights were shared with other projects. A summary of the runs can be found in Table 2.1.

For each run, the strategy for photometric observations was as follows. During the late afternoon/twilight on photometric (clear) nights, calibration images - biases, dome flats (for the 0.9m), and sky flats - were taken and later used to calibrate that night’s data. During the nights, standard stars were periodically observed between observations of target stars in a ratio of approximately

Table 2.2. Photometric Exposure Times

V mag:	7.5	8.0	8.3	9.0	9.7
			Exp. Time (s)		
y	1	1	2	4	8
b	1	1	2	10	11
v	2	3	7	15	20
Ca	5	5	10	30	40
Hβw	1	2	3	3	12
Hβn	5	7	20	45	60
u	5	7	15	40	60

1-2 standards per 3 program stars. Standards were drawn from the intersection of either the Olsen (1993) *uvby* catalog and the Twarog & Anthony-Twarog (1995) *Ca* filter extension or the Hauck & Mermilliod (1980) *uvbyH*β catalog and Twarog & Anthony-Twarog (1995) observations. Observable standard clusters (NGC 752 or NGC 6633) were observed at regular intervals for extinction correction and standardization purposes. The approximate exposure times used for each filter as a function of V magnitude are given in Table 2.2. In general, exposure times were chosen such that the sky background level was below 1% of the total measured flux. Since the two telescopes used for photometry are relatively similar, exposure times were kept the same between the two. Images were unguided due to the short exposure times. Generally, each star was observed on at least two nights in each filter. For the 0.9m frames, usually only a subset of filters was used each night (*uvbyCa* or *vbyCaH*β), while on the MLO 40", generally the full set of filters was used, in accordance with observer preference.

Over the 10 photometric runs, 116 unique stars were observed over $\sim$ 200 7-filter sets. 72 stars were observed at least twice. In general, the photometric targets were followed up with the spectroscopy detailed below. A summary of the number of frames per filter for each star can be found in Table 2.5.

2.4.3 Note on Photometry

In the original incarnation of this study, the photometry was to play a crucial role in the final analysis. At the time the project was started, it was assumed that ROBOSPECT (see Chapter 3) would provide the primary [Fe/H] determinations, while photometric [Fe/H] measures would be used in a supporting role. The use of ROBOSPECT for abundance analysis requires prior estimates of the primary atmospheric parameters - especially $T_{\rm eff}$, but also $log(g)$, [Fe/H], and v_t - and these were to have been derived from the photometric observations.

However, during the course of this project, ANNA (see Chapter 4) was developed. ANNA is capable of accurately determining $T_{\rm eff}$ and [Fe/H] from a spectrum alone. This substantially reduced the need for high-quality photometric observations of each target star. At the same time, several challenges were encountered during the collection of photometry, including a string of bad luck due to weather, the determination of non-negligible shutter effects on exposures under 4 seconds for MLO 40" images combined with somewhat inconsistent telescope pointing accuracy, and general time constraints leading to only one or two exposures for each filter per star. These things colluded to make the ANNA parameter determinations generally more reliable than the photometric ones.

Ultimately, the photometry was used in a secondary role for this project. It was decided that the ANNA temperatures and metallicities would be used as inputs to the atmospheric models used during the ROBOSPECT analysis. For gravities, many of the target stars in the Geneva-Copenhagen, N2K, and Hypatia catalogs already have estimates; these were adopted according to heirarchy discussed in Chapter 3. For the stars that had no available gravity measurements, the photometry was used to derive an estimate. The process by which this was done is also described in Chapter 3.

2.5 Spectroscopic Observations with WIYN/Hydra

The spectroscopic observations of metal-rich candidates were all carried out using the Hydra multifiber spectrograph (Barden et al., 1993) on the WIYN 3.5m telescope at KPNO. Hydra is a multi-

object, fiber-fed spectrograph capable of observing approximately ~ 90 objects simultaneously. For this study, the spectrograph was used with the 316@63.4 (316 lines/mm at a blaze angle of 63.4 degrees) grating at order 8 with the X19 filter. The spectra span wavelengths $6450 < \lambda < 6850$ Å, giving coverage of Hα at 6560 Å, the Li-Fe blend at 6708 Å, the strong Ca I line at 6717 Å, and a number of moderately strong, isolated Fe I lines. The "blue" cable was used which, in combination with the spectrograph setup, led to an effective resolution at the observed wavelengths of ~ 0.615, or $R \sim 13,000$. The STA1 detector was used, binned along the dispersion axis to yield a pixel scale of 0.205 Å per pixel.

2.5.1 Reduction and Calibration of Spectroscopy

The general process of calibrating and reducing the spectra began with bias subtraction, overscan correction, and flat-fielding, carried out using the same IRAF routines as used for the photometric reductions. Note that in contrast with the steps outlined in Lee-Brown et al. (2015), no correction for dark current was necessary due to the shorter exposure times used for this project. For the initial flat-fielding, well-exposed dome flats were used to correct for the pixel-to-pixel response variations. Once these basic steps were been carried out, the actual spectra were extracted from the CCD image. This process required tracing the spectrum apertures and collapsing them to 1-D spectra, correcting for scattered light, and dispersion correction/wavelength calibration through comparison with a set of ThAr lamp spectra taken over the course of each observing night. Again due to the shorter exposure times, no cosmic ray removal step was included during this portion of the reduction; cosmic rays were manually removed from the fully-processed spectra using IRAF's *splot* routine. Once the dispersion correction was completed, the spectra were throughput-corrected using uniformly illuminated daytime sky spectra. Background nighttime sky signal was subtracted using the signal recorded by unused fibers left on the focal plane during exposures. Finally, the heliocentric motion was removed from the spectra and each spectrum was continuum-fit, and multiple exposures of the same object were additively combined. An example fully-reduced Hydra spectrum is given in Figure 2.1.

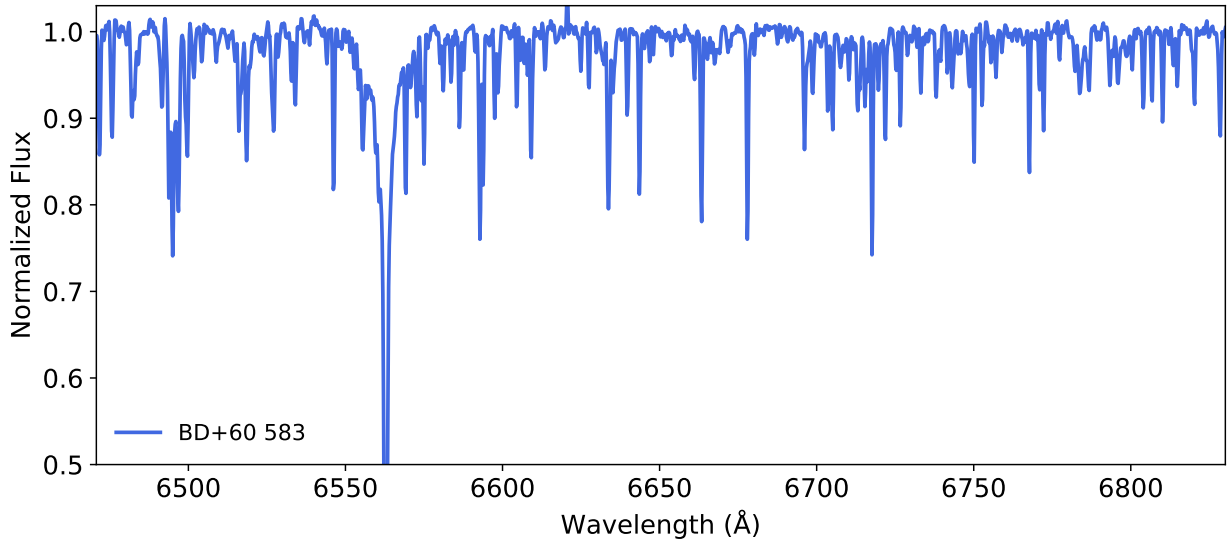

Figure 2.1: An example Hydra spectrum of metal-rich candidate BD+60 583.

2.5.2 Summary of Spectroscopic Observations

The spectroscopic observations for this project were carried out over 7 different runs spanning the years 2015-2017. Of these runs, two were awarded time by the National Optical Astronomy Observatory (NOAO) specifically for this project (proposal IDs: 16B-0132, 17B-0248, PI Lee-Brown). For the other runs, evening and morning twilight time unusable for the primary project was used to observe the brighter targets of this study. A summary of the run dates and number of stars observed can be found in Table 2.3.

Generally, when using Hydra, fibers are placed onto the focal plate in a pre-determined configuration, with some fibers placed to capture light from science targets, others placed to measure the sky background, and a few special guide fibers are used to precisely keep the telescope aligned with the target field. After configuring, the focal plate is warped to match the curvature of the true focal plane. This method allows for long exposure times and observation of multiple targets, but the process of reconfiguring the fiber placement can take as long as 25 minutes. As discussed previously, in order to gather as many observations as possible in an efficient manner, bright (V<10) stars were targeted for this study. For stars this bright, the typical exposure times, given in Table 2.4, are only a few hundred seconds. This means that time required for reconfiguration would

Table 2.3. Observations with Hydra

Run Date	No. Stars Observed
06/2015	16
01/2016	7
02/2016	8
03/2016	3
09/2016	9
02/2017*	26
10/2017*	33

Note. — The asterisks denote the runs corresponding to time awarded specifically for this project.

triple or quadruple the total time required to observe each metal-rich candidate. Furthermore, Hydra calibration images (especially the ThAr lamp images used for the dispersion correction) are generally configuration-specific, necessitating a separate set for each unique fiber configuration.

To avoid these hefty overhead penalties, Hydra was used in the following manner. At the beginning of the night, the spectrograph was configured once and a set of calibration images taken. For runs shared with other projects, the selected configuration was based on one to be used later in the night; for the runs dedicated to this project, a slightly modified "blue circle" configuration was used. In both cases, a fiber with high throughput was moved to the center of the focal plate before calibration images were taken. During the night, this central fiber was used to observe the metal-rich candidates, while the other deployed fibers were used to measure sky background. Exposures were unguided - each target was manually aligned with the central fiber. Testing indicated that the telescope's tracking was precise enough to maintain the pointing over the course of the exposure times used. Throughout the observations, the focal plate was left unwarped to further reduce overhead. This process significantly improved the efficiency of observations; the bulk of observing time could be spent on target, interrupted only by slewing the telescope, aligning the target, and

Table 2.4. Typical Hydra Exposure Times

V Mag.	Exposure Time (s)
7.0	150
7.5	200
8.0	300
8.5	400
9.0	400×2
9.5	400×3

Note. — These times are approximate and the actual length of individual exposures depended on seeing conditions and telescope focus.

occasional refocusing and comparison lamp observations.

For each target, two exposures following the Table 2.4 exposure times were collected to reach SN$\sim 150-200$ for each combined spectrum in order to adequately measure the relatively weak 6708 Å Li feature. In the interest of efficiency, these exposures were generally taken back-to-back before slewing to a new target, but in some cases this was not possible, leading to some stars being observed over multiple runs. In total, 94 unique stars were spectroscopically observed, generally overlapping with the photometric observations. A summary of total spectroscopic exposure time for each target can be found in Table 2.5.

2.6 Summary

Of the 94 unique stars observed spectroscopically for this project, 79 were also observed photometrically. Of these stars, 59 were observed at least twice both photometrically and spectroscopically. The median-stacked spectroscopic signal-to-noise, as determined by the ROBOSPECT-derived scatter about the continuum level over the relatively line-free 6680-6694 Å region, is SN=189.

The majority of the spectra have SN > 150; only 18 stars have SN < 150, while 35 have SN > 200. A summary of the photometric and spectroscopic observations, including spectroscopic SN, as well as coordinates for this project's targets, can be found below in Table 2.5.

Table 2.5. Total Photometric and Spectroscopic Observations

ID	V mag.	N_y	N_b	N_v	N_{Ca}	$N_{\beta w}$	$N_{\beta n}$	N_u	Spec. Exp. (s)	SN
HD 51356	7.54	2	2	2	2	2	2	2	300	324
HD 196199	7.76				2				250	311
HD 194510	8.22								350	300
HD 83616	7.87	3	3	3	3	3	3	3	400	280
HD 107087	8.04	3	3	3	3	3	3	3	1200	272
HD 91987	8.42	2	2	2	2	2	2	2	800	269
HD 4649	8.15	2	2	2	2	2	2	2	700	266
HD 220848	8.64								800	263
HD 129171	7.69	2	2	2	2	2	2	2	400	259
HD 27533	7.06	3	3	3	3	3	3	3	240	254
HD 119825	7.46	2	2	2	2	2	2	2	300	251
HD 112001	7.68	3	3	3	3	3	3	3	400	243
HD 220284	7.9	2	2	2	2	2	2	2	600	243
HD 14348	7.19	1	1	1	1	1	1	1	200	242
HD 78609	8.5								800	238
HD 1497	8.18	2	2	2	2	2	2	2	600	238
HD 13345	7.38	1	1	1	1	1	1	1	360	237
HD 144302	7.86	3	3	3	3	3	3	3	300	229
HD 76617	8.14	3	3	3	3	3	3	3	900	227
HD 154144	8.17								970	225
HD 100069	7.99	3	3	4	3	3	3	3	600	222
HD 30769	7.37	3	3	3	3	3	3	3	200	222
HD 13773	8.63	3	3	3	3	3	3	3	750	220
HD 106423	7.48	4	4	4	4	4	4	4	300	219
HD 94861		2	2	2	2	2	2	2	450	218
HD 149026	8.14	3	3	3	3	3	3	3	600	216
HD 97140		1	1	1	1	1	1	1	300	214
HD 130087	7.51	2	2	1	2	1	1	1	135	214
HD 16090	8.01	2	2	2	2	2	2	2	600	212
HD 147062	7.57	1	1	1	1	1	1	1	300	209
HD 180502	7.91								300	207
HD 103459	7.6	3	3	3	3	3	3	3	300	206
HD 124102	8.49	2	2	2	2	2	2	2	600	205

Note. — Key: N_x = number of exposures for a given filter x, Spec. Exp. = total spectroscopic exposure time. Spectroscopically observed stars without SN measurements were binaries or had atmospheric parameters that precluded an SN estimate using ROBOSPECT. V magnitudes are from the SIMBAD database (Wenger et al., 2000).

Table 2.6. Total Photometric and Spectroscopic Observations (continued I)

ID	V mag.	N_y	N_b	N_v	N_{Ca}	$N_{\beta w}$	$N_{\beta n}$	N_u	Spec. Exp. (s)	SN
HD 196674	7.79								250	205
HD 10211	7.39	1	1	1	1	1	1	1	600	204
HD 224882	8.02	2	2	2	2	2	2	2	600	199
HD 184295	8.13								325	198
HD 224543	7.84	1	1	1	1	1	1	1	250	198
HD 117302	8.01	3	3	3	3			3	300	197
HD 201529	8.72	2	2	2	2	2	2	2	340	197
HD 9729	8.62	1	1	1	1	1	1	1	800	196
HD 183490	8.21								350	195
HD 2330	7.54	2	2	2	2	2	2	2	200	194
HD 91988	8.38	1	1	1	1	1	1	1	420	192
HD 21313	8.16	1	1	1	1	1	1	1	400	189
HD 156016	8.93	2	2	2	2	2	2	2	1400	188
HD 105279	8.39	3	3	3	3	3	3	3	800	188
HD 218354	8.19	2	2	2	2	2	2	2	700	188
HD 7355	7.68	2	2	2	2	2	2	2	220	187
HD 110010	6.99	4	4	4	4	4	4	4	240	185
HD 2564	7.77	2	2	2	2	2	2	2	240	185
HD 113938	9.16	2	2	2	2	2	2	2	1200	184
HD 109929	7.65	3	3	3	3	3	3	3	400	183
HD 238069	9.16	3	3	3	3	3	3	3	1200	183
HD 104588	8.68	3	3	3	3	3	3	3	800	179
HD 192343	8.02								300	178
HD 78277	8.2	3	3	3	3	3	3	3	600	177
HD 11170	7.4	7	3	3	3	3	3	3	160	174
HD 26441	7.37	3	3	3	3	3	3	3	180	173
HD 11638	8.07	1	1	1	1	1	1	1	600	173
HD 3592	8.76	2	2	2	2	2	2	2	660	170
HD 82410	8.61								600	167
HD 449	8.57	2	2	2	2	2	2	2	800	163
HD 15866	8.01	1	1	1	1	1	1	1	600	162
HD 117243	8.34	5	5	3	5	2	2	3	480	159
HD 19961	8.6	2	2	2	2	2	2	2	800	159

Note. — Key: N_x = number of exposures for a given filter x, Spec. Exp. = total spectroscopic exposure time. Spectroscopically observed stars without SN measurements were binaries or had atmospheric parameters that precluded an SN estimate using ROBOSPECT. V magnitudes are from the SIMBAD database (Wenger et al., 2000).

Table 2.7. Total Photometric and Spectroscopic Observations (continued II)

ID	V mag.	N_y	N_b	N_v	N_{Ca}	$N_{\beta w}$	$N_{\beta n}$	N_u	Spec. Exp. (s)	SN
BD+60 583	8.41	3	3	3	3	4	3	3	800	154
HD 102196	8.16	3	3	3	3	3	3	3	340	154
HD 8446	8.14	2	2	2	2	2	2	2	360	154
HD 27831	8.22	3	3	3	3	3	3	3	1900	153
HD 107211	8.36	4	4	4	4	4	4	4	600	153
HD 47155	8.6	3	3	3	3	3	3	3	1200	150
HD 8328	8.28	2	2	2	2	2	2	2	720	148
HD 177985	8.66	2	2	2	2	2	2	2	500	147
HD 207418	8.67	2	2	2	2	2	2	2	340	146
HD 279527	9.22	3	3	3	3	3	3	3	1600	145
HD 126530	8.48	3	3	2	3	1	1	2	340	144
BD+39 2711	8.92	1	1	1	1	1	1	1	1000	139
HD 10766	8.72	1	1	1	1	1	1	1	800	133
HD 180556	8.09	2	2	2	2	2	2	2	400	132
HD 216027	8.44	2	2	2	2	2	2	2	500	128
HD 198483	7.67	3	3	3	3	3	3	3	460	122
HD 203557	8.6	2	2	2	2	2	2	2	340	122
HD 180318	9.03	2	2	2	2	2	2	2	800	117
HD 47218	7.54	3	3	3	3	3	3	3	800	116
HD 115954	8.35	3	3	2	3	1	1	2	300	114
HD 103012									300	103/126*
HD 199167	8.62								400	78
HD 205583	8.33	2	2	2	2	2	2	2	340	
HD 192833	8.07	7	4	4	4	4	4	4	1530	
HD 199744	8.66	2	2	2	2	2	2	2	340	
HD 2992	8.31	2	2	2	2	2	2	2	960	
HD 148511	7.45	2	2	2	2	2	2	2	300	
HD 1402	7.91	2	2	2	2	2	2	2	600	
HD 1949	9.15	1	1	1	1	1	1	1		
HD 4712	7.79	1	1	1	1	1	1	1		
HD 21496	8	1	1	1	1	1	1	1		
HD 23030	8.07	1	1	1	1	1	1	1		
HD 30854	8.46	1	1	1	1	1	1	1		
HD 36248	8.05	1	1	1	1	1	1	1		

Note. — Key: N_x = number of exposures for a given filter x, Spec. Exp. = total spectroscopic exposure time. Spectroscopically observed stars without SN measurements were binaries or had atmospheric parameters that precluded an SN estimate using ROBOSPECT. V magnitudes are from the SIMBAD database (Wenger et al., 2000). *Double star.

Table 2.8. Total Photometric and Spectroscopic Observations (continued III)

ID	V mag.	N_y	N_b	N_v	N_{Ca}	$N_{\beta w}$	$N_{\beta n}$	N_u	Spec. Exp. (s)	SN
HD 38400	8.22	1	1	1	1	1	1	1		
HD 42129	8.3	1	1	1	1	1	1	1		
HD 44414	8.32	1	1	1	1	1	1	1		
HD 44614	7.59	1	1	1	1	1	1	1		
HD 50688	7.74	1	1	1	1	1	1	1		
HD 60521	8	1	1	1	1	1	1	1		
HD 61663	8.77	1	1	1	1	1	1	1		
HD 61787	8.65	1	1	1	1	1	1	1		
HD 68988	8.19	1	1	1	1	1	1	1		
HD 69809	7.86	1	1	1	1	1	1	1		
HD 71053	8.27	1	1	1	1	1	1	1		
HD 73294	7.83	1	1	1	1	1	1	1		
HD 108942	7.91	1	1	1	1	1	1	1		
HD 117697	8.01	1	1	1	1	1	1	1		
HD 124244	8.45	1	1	1	1	1	1	1		
HD 126265	7.24	1	1	1	1	1	1	1		
HD 125960	8.26	1	1	1	1	1	1	1		
HD 112735	7.28	1	1	1	1	1	1	1		
HD 133460	7.28	1	1	1	1	1	1	1		
HD 151482	7.8									
BD+39 4559	8.27	2	2	2	2	2	2	2		
HD 213066	7.7	2	2	2	2	2	2	2		
HD 216083	8.51	2	2	2	2	2	2	2		
HD 137985	8.59	1	1	1	1	1	1	1		
HD 139907	8.66	1	1	1	1	1	1	1		
BD+36 2644	8.73	1	1	1	1	1	1	1		
HD 148284	9.02	1	1	1	1	1	1	1		
HD 42313	8.19	2	2	2	2	2	2	2		
HD 48141	8.48	3	3	3	3	3	3	3		
HD 203698	7.8	1	1	1	1	1	1	1		

Note. — Key: N_x = number of exposures for a given filter x, Spec. Exp. = total spectroscopic exposure time. Spectroscopically observed stars without SN measurements were binaries or had atmospheric parameters that precluded an SN estimate using ROBOSPECT. V magnitudes are from the SIMBAD database (Wenger et al., 2000).

Chapter 3

Spectroscopic Analysis Using ROBOSPECT

3.1 Introduction: Stellar Spectroscopy

The field of stellar spectroscopy is concerned with the translation between the observable features present in the spectrum of a star and one or more astrophysical parameters of interest. These parameters include the stellar surface temperature, relative chemical abundances, surface gravity, rotational velocity, and the kinematics of the corresponding star. Therefore, by studying stellar spectra, an observer can glean crucial information pertaining to stellar and galactic structure and evolution.

It is important to note that an observed stellar spectrum, strictly speaking, is not an observation of the entire star, but only of the outer layers of the stellar atmosphere. As the energy produced by nuclear fusion in the center regions of a star travels (in the form of photons) to the outer portions, it is absorbed and re-emitted many times by the atoms along its path. The observable features in a stellar spectrum are largely due to the the last few absorptions/emissions - the region of the atmosphere corresponding to these interactions is called the photosphere.

The principal challenge in spectroscopy is determining how to turn this incomplete picture of a star into astrophysically useful information. In this chapter, I will review one of the standard methods for accomplishing this process and its application to this study. The connection between the underlying physics of stellar atmospheres and spectroscopic observation will necessarily be addressed, but will be done so from the perspective of the observer and limited to topics relevant to this study. A more comprehensive and theoretical treatment of the subject can be found in Gray (1976).

3.2 Stellar Spectra

3.2.1 The Continuum Normalized Spectrum

The emission from the stellar photosphere generally consists of two intrinsic components. First, the continuum manifests itself as a smoothly varying, wavelength-dependent intensity profile, and is due to the emission produced by the many interacting atoms in the stellar atmosphere. The profile of the continuum, to first order, follows the standard blackbody emission law and is primarily temperature-dependent. Added to the continuum, as shown in Figure 3.1, are individual absorption lines corresponding to elements or molecules present in the stellar photosphere. Typically, stellar spectra are continum normalized, such that at every wavelength, the level of the local continuum is set to be 1.0. This process does discard the temperature information encoded in the stellar continuum, but greatly facilitates the measurement of spectral features and corrects for the wavelength-dependent instrumental response.

What is left after continuum normalization is a spectrum where deviations from the continuum level of 1.0 correspond to either measurement noise or real features - in the case of the stars observed for this study, these features are absorption lines. The strengths of these lines, as well as their specific profiles, depend on a number of factors. The factors considered most important for this study are listed below and illustrated in Figure 3.1 and Figure 3.2.

3.2.1.1 Surface Temperature

The stellar surface temperature plays the biggest role in the strength of spectral lines. For most metal lines in FGK stars, the temperature regulates line strength by controlling the ionization fraction (Gray, 1976). If more metals in the photosphere are ionized (or the layer in which un-ionized metals exist becomes smaller) then spectral line strengths are decreased due to fewer absorbers. This condition occurs as surface temperature increases - for example, the spectra of A-type stars have very weak metal lines due to their high surface temperatures. Conversely, as surface temperature decreases, metal line strengths increase as the number of absorbers rises.

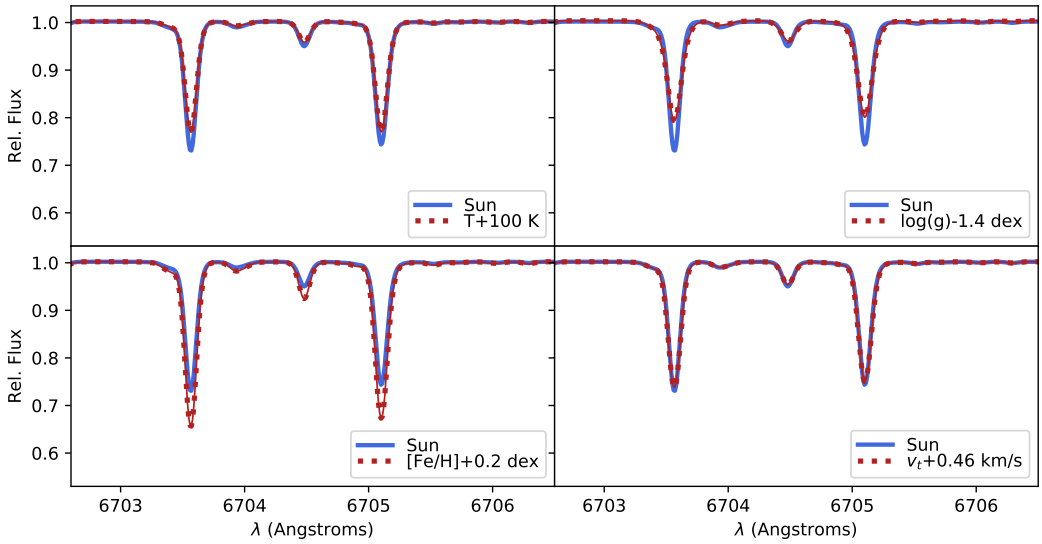

Figure 3.1: The effects on an observed spectrum due to - from upper left to lower right by row - temperature, gravity, metallicity, and microturbulent velocity. In each panel the blue line shows the original, high-resolution spectrum and the red dotted line indicates the altered spectrum.

3.2.1.2 Surface Gravity

Surface gravity is proportional to the photospheric pressure. Its effect on line strengths is somewhat complicated and depends on the ionization equilibrium in the stellar atmosphere, but in general, increasing surface gravity in main sequence stars makes their lines "wing-ier" while decreasing the maximum line depth (see Figure 3.1). However, as shown in Figure 3.1, for typical Fe I lines in solar-like stars, relatively drastic changes in surface gravity are necessary to significantly alter spectral line depth. The spectra of evolved stars are much more sensitive to changes in surface gravity due to these stars' extended, cool atmospheres.

3.2.1.3 [X/H]

The relative number of element X with respect to hydrogen has the most straightforward effect on the depth of any spectral line. As the number of X increases, then the line strength increases due to an increase in the number of absorbers. However, it is important to note that lines are still more sensitive to surface temperature than the abundance of X - the classic example is the spectrum of

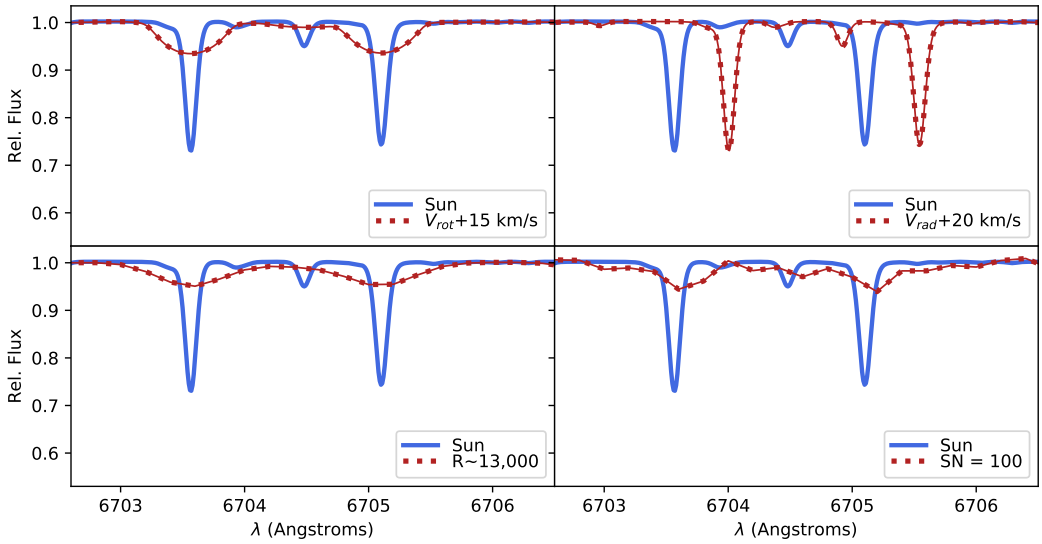

Figure 3.2: The effects on an observed spectrum due to - from upper left to lower right by row - rotational velocity, radial velocity, spectrograph resolution, and spectrograph resolution + random noise. In each panel the blue line shows the original, high-resolution spectrum and the red dotted line indicates the altered spectrum.

the Sun, with its deep Ca H and K lines.

3.2.1.4 Turbulent Velocity

The micro- and macroturbulent velocity both refer to the motion of atoms in the stellar photosphere - their effects are manifested in the broadening of spectral lines. The distinction between the two velocities is defined by the optical depth (and is therefore proportional to the photon mean free path). Microturbulence refers to velocities with scales less than the unit optical depth, while macroturbulence refers to velocities with scales larger than the unit optical depth. In both cases, typical estimates are on the order of a few km/s, and both conserve the overall line strength (Gray, 1976). For FGK stars, typical microturbulent velocities are 1-2 km/s and the lines present in the spectra of main sequence stars relatively insensitive to this parameter.

3.2.1.5 Rotational Velocity

Virtually all stars rotate to some degree; when this rotation extends to the photosphere then lines are Doppler broadened. The strength of this rotation depends on several factors, including initial angular momentum during star formation, mass, and evolutionary state. In general, main sequence FGK stars have rotational velocites around 5-30 km/s, while evolved FGK stars have very low rotational velocites, <5 km/s (see, e.g., Lee-Brown et al., 2015; Anthony-Twarog et al., 2018). On top of this intrinsic spread in rotation, measured rotational velocities depend on angle between the axis of rotation and the observer - if a star is observed along its axis of rotation, the inferred rotational velocity will be 0 km/s; if a star is observed perpendicular to this axis, then the true rotational velocity will be inferred. Generally when referring to rotational velocity V_{rot}, the number given is actually $V sini$, or the projected rotational velocity.

3.2.1.6 Radial Velocity

Radial velocity refers to the motion of the observed star in the radial direction relative to the observer. The effect of radial motion is a simple Doppler shift of the observed spectrum. For stars moving towards the observer, the spectrum is shifted to shorter wavelengths; for stars moving away, the spectrum is shifted towards redder wavelengths. The nearby stars observed as part of this study generally have radial velocities between -25 and 25 km/s, corresponding to maximum wavelength shift of $\sim \pm 1$.

3.2.1.7 Instrument/Measurement Effects

It is impossible to avoid the imprint of the spectrograph and camera used for the observation of spectra. The effect of finite slit widths, pixel size, and other considerations such as diffraction combine to generally broaden observed lines. This resolution degradation naturally impacts the ability to deblend closely-spaced spectral lines, and it significantly decreases the maximum depth of lines. It is also worth noting that the sensitivity and resolution of the spectrograph used are wavelength-dependent. Additionally, while the shape of the response curve of the instrument (i.e.,

the differences in total absolute flux due to wavelength-varying detector sensitivity) can be removed via continuum normalization, the increased fractional noise at lower sensitivities cannot. For example, the spectra analyzed for this study have $\sim 30\%$ lower signal-to-noise at the edges of the measured wavelength region. On top of this, for a multi-object spectrograph such as Hydra, the sensitivity is fiber-dependent as well; this can partially be corrected for during the calibration process, but variations in peak SN can be expected when comparing identical observations taken with different fibers.

3.3 From Spectra to Species: The Equivalent Width Method

It is clear from the section above that there are many factors influencing the appearance of a spectral line, and there is a fair amount of degeneracy in their effects - a deep spectral line can be caused by a high metallicity or low temperature, and line broadening could stem from a number of sources. Thus, there is no straightforward way to directly infer an atmospheric parameter (e.g., [Fe/H]) solely from a line measurement. The analysis method detailed below provides a workaround by dividing the process of parameterization into two stages. During the first stage, the lines in a spectrum are directly measured. Second, the measurements can be converted into the parameter of interest via a model that incorporates assumptions about the star being analyzed. In other words, if [Fe/H] is the parameter of interest, the model "fixes" the other major atmospheric parameters - surface temperature, gravity, turbulent velocity - and [Fe/H] can be determined from the line measures under the adopted model.

3.3.1 Measuring Spectral Lines

The standard way to directly measure the strength of stellar absorption lines is via their equivalent widths. The equivalent width (EW) is defined to be the width of the rectangle (in wavelength units) that extends from 0 to the continuum level and has the same area as the spectral line being measured. As spectral lines become deeper or broader, the equivalent width increases as well.

The principal advantage of the equivalent width is that in theory, it is line profile-agnostic. As detailed previously, there are many factors that can alter the specific profile of an absorption line. As long as the total flux absorbed by the line is unchanged, the EW is insensitive to these factors by only depending on the area enclosed by the line. In practice, EWs are often measured by fitting Gaussian profiles; this choice of fit may or may not accurately match the true line profile and can systematically bias EWs, as discussed in Chapter 4.

The main advantage of the EW can also be seen as a disadvantage. Because information about the line profile is discarded during the EW measurement process, parameters which manifest as alterations to the line profile cannot be inferred from EWs. This means that "flux-conserving" parameters such as turbulent velocity cannot be inferred at all from EWs, and profile-altering parameters like surface gravity are difficult to derive as well. This drawback is discussed in more detail in Chapter 4.

3.3.1.1 ROBOSPECT and the Linelist

The most straightforward way to measure EWs is to directly fit lines by eye, using, e.g., IRAF's *splot* routine. This approach works well for small samples, but quickly becomes impractical as the number of lines to measure grows, either by increasing the sample size or widening the spectral region. As modern spectrographs have become more capable in both wavelength coverage and number of simultaneously observed objects, several automated EW-measurement programs have been developed.

For this study, we used ROBOSPECT (Waters & Hollek, 2013). ROBOSPECT determines EWs via an iterative process, beginning with an initial continuum level estimate. Lines are identified using a user-supplied list of wavelengths or by significance relative to a local noise estimate, and subtracted from the spectrum. As real spectral features are identified and subtracted from the spectrum, the placement of the continuum is refined. Simultaneously, the estimate of the local noise level is improved as unidentified but real spectral features, which formerly contributed to the noise estimate, are removed from the spectrum. As the number of iterations increases, the

continuum and noise solutions converge to their correct values, and ROBOSPECT's EW estimates become more accurate.

ROBOSPECT provides the ability to adopt one of several line profiles to use during its iterative fitting process, and for computational simplicity we adopted a simple Gaussian profile. Practically speaking, this limits the lines for which ROBOSPECT returns accurate equivalent widths to low-to-medium strength features (EW$\sim 10-150$ mÅ) where the effect of non-Gaussian broadening is minimized. This limitation is relatively unimportant as the use of the curve of growth (see Section 3.3.2.1) during the equivalent width analysis imposes a similar restriction on the maximum measured line strength.

ROBOSPECT also provides the ability to deblend spectral features which are close together in wavelength space via a least-squares method. After testing, it was decided that ROBOSPECT's deblending capability would not be used due to its computational cost and sometimes inconsistent results, particularly for heavily blended lines. This imposed an additional restriction on the selection of lines to measure - only relatively isolated lines could be measured accurately. As this restriction was already being observed when measuring lines manually using *splot*, it does not reduce the utility of ROBOSPECT, compared with manual measurement.

With these restrictions in mind, a list of lines for ROBOSPECT to measure in a given spectrum was developed through visual inspection of the solar spectrum and comparison with the solar atlas of Wallace et al. (1998). ROBOSPECT only requires an estimate of the wavelength of each line, but as the atomic information associated with each line was needed later in the analysis process, lines were required to have atomic information recorded in the VALD database (Kupka et al., 2011). The final linelist contains 17 Fe I, 3 Ni I, 1 Ca I, and 1 Si I lines and is given in Table 3.1. Note that Li was not measured by ROBOSPECT - not only is this line relatively weak, but it is also blended with a neighboring Fe I line.

During testing of this linelist, it was determined that ROBOSPECT's continuum estimate in the region of lines of interest was not converging to the correct value. This was traced to the influence of neighboring weak lines, which had strengths below the local noise level and were not flagged

Table 3.1. ROBOSPECT Linelist

Species	Atomic Number	$\lambda(Angstroms)$	E.P (eV)	$log(gf)$
Si I	14	6721.85	5.86	-1.038
Ca I	20	6717.68	2.71	-0.226
Fe I	26	6597.56	4.8	-0.96
Fe I	26	6609.11	2.56	-2.47
Fe I	26	6609.68	0.99	-5.333
Fe I	26	6627.54	4.55	-1.597
Fe I	26	6646.93	2.61	-3.982
Fe I	26	6653.91	4.15	-2.475
Fe I	26	6677.99	2.69	-1.46
Fe I	26	6703.57	2.76	-3.062
Fe I	26	6710.32	1.49	-4.803
Fe I	26	6725.36	4.1	-2.321
Fe I	26	6726.67	4.61	-1.106
Fe I	26	6733.15	4.64	-1.539
Fe I	26	6750.15	2.42	-2.776
Fe I	26	6806.86	2.73	-3.198
Fe I	26	6810.27	4.61	-1.052
Fe I	26	6820.37	4.64	-1.177
Fe I	26	6837.01	4.59	-1.818
Ni I	28	6643.63	1.68	-1.898
Ni I	28	6767.77	1.83	-2.174
Ni I	28	6772.31	3.66	-0.958

Note. — Atomic parameters from the VALD database (Kupka et al., 2011); $log(gf)$ values are the solar-calibrated values.

by ROBOSPECT's automatic line identification routines, but nevertheless systematically lowered the local continuum placement. Thus, when running ROBOSPECT, any features identifiable in the Wallace et al. (1998) atlas within 0.5 Å were included in the linelist, which forced ROBOSPECT to fit and subtract these features when placing the continuum. The EWs corresponding to these features were then discarded before moving to the next stage of the analysis.

The ability of ROBOSPECT to accurately measure the lines in Table 3.1 was quantified by using ROBOSPECT to measure EWs in a sample of solar spectra of different SN. Four SN were tested - SN = 70, 95, 130, and 160. For each SN, 25 solar spectra were measured with ROBOSPECT. The mean standard deviation in EW - that is, the average of the 22 standard deviations (one for each line on the linelist) - was 11.1, 7.5, 4.7, and 4.2 mÅ for the different SN (lowest SN first). These results compare well with manual line measurement results, but ROBOSPECT performed its measurements many orders of magnitude faster. At all the tested SNs, there was no significant relation between the mean line EW and its uncertainty. Overall, our solar tests agree with the more extensive tests on a variety of stars by Waters & Hollek (2013).

Of note is that the ROBOSPECT EWs were systematically lower than the manually measured EWs by a nearly constant ~ 7.7 mÅ. This offset was addressed in Waters & Hollek (2013) as being largely due to a human observer's propensity to place the continuum artificially high relative to the true level. Regardless of the source, because our EW analysis is done differentially with respect to the Sun, as long as the systematic offset in EW is the same for the Sun and any object spectrum, there will be no appreciable difference between ROBOSPECT-derived and manual abundance determinations.

In order to correctly identify lines, ROBOSPECT requires a radial velocity for each input spectrum in order to correct the wavelength location of each entry in the linelist. Therefore, we also tested ROBOSPECT's sensitivity to the accuracy of the input radial velocity estimate. Typically, radial velocities estimated by either direct measurement of the wavelengths of known lines or by a more complicated cross-correlation method (IRAF's *fxcor* routine) are accurate to within 2.5 km/s. Applying this offset to a sample of solar spectra resulted in a mean deviation of 0.7 mÅ in

measured EW; a 5 km/s offset in radial velocity resulted in a deviation of 3.5 mÅ. In both cases, the offset in EW is relatively minor and has little impact on the overall abundance determination.

3.3.2 Translating EWs to Abundances

The adoption of ROBOSPECT greatly facilitates the EW measurement process, but once EWs are measured they must still be translated to abundance estimates. This itself is a two-stage process, detailed below.

3.3.2.1 The Curve of Growth

The first step in the translation is to convert the equivalent width of a spectral line into a more physically meaningful quantity. Logically, the strength of an absorption line should be proportional to the total number of absorbers, or more precisely the column density of the number of absorbers. As the column density increases, the strength of the absorption line and thus the EW should also increase. The relation between these two quantities forms what is known as the *curve of growth* (Gray, 1976).

The precise slope of the curve of growth is dependent on the optical depth at the central wavelength of the line (Gray, 1976). For thin optical depths, where most of the photons at the central wavelength escape without being absorbed or scattered, the EW of the line increases as a function of the column density (the "linear" portion of the curve of growth). At thicker optical depths, the absorption line saturates and very few photons at the center wavelength of the line make it to the observer. In this regime, further increasing the number of absorbers has little impact on the EW of the line, and the EW only grows as the logarithm of the column density. At very high optical depth, pressure broadening effects increase the optical depth at wavelengths around the central line wavelength and the EW again increases, this time as the square root of the column density.

It is obvious that the dependence of equivalent width on column density is most sensitive during the linear and square root portions of the curve of growth. However, because the pressure broadening during the super-saturated portion of the curve of growth increases the strength of the wings

of the line in a non-Gaussian manner, it is very difficult to accurately measure the EW of a line in this regime. Thus, the most effective EW analysis is conducted using weak lines corresponding to the linear portion of the curve of growth in order to maximize the sensitivity to the column density. This limits the analysis to lines of EW < 150 Å.

3.3.2.2 The Model Photosphere, LTE, and MOOG

The curve of growth is an important step towards finally deriving a chemical abundance estimate from an EW, but it is still insufficient. This is because the column density of the number of absorbers depends not only on the relative number of absorbers to hydrogen (this is the sought-after abundance X/H), but also on the interplay between atomic details of these absorbers - excitation potentials, oscillator strengths - and the properties of the stellar photosphere - chiefly temperature and pressure. The final step in the translation between EWs and chemical abundances is carried out using a model photosphere in conjunction with the necessary atomic parameters corresponding to each line being measured.

A computationally expendient model photosphere is the 1-D plane-parallel model. This model describes how the temperature, pressure, density, and particle velocity depend on radial depth in the photosphere. However, 3-D effects, namely convection, cannot be treated with this model, though there are approximate, empirically calibrated prescriptions such as radial mixing length theory (see, e.g., Roxburgh & Kupka (2007)). This means that 1-D models are generally inappropriate for stars dominated by convection, such as AGB stars or very low-mass dwarfs. They do still provide good results for the main sequence FGK and subgiant/giant branch stars analyzed in this work.

Another approximation that simplifies the model photosphere is the assumption of *local thermodynamic equilibrium* (LTE). Under this assumption, layers of the photosphere are assumed to be in approximate thermodynamic equilibrium with the layers above and below. This dramatically simplifies the calculations required to model the photosphere (Gray, 1976). Clearly, thermodynamic equilibrium cannot be even a reasonable approximation if the entire stellar atmosphere is considered, but for the photosphere the assumption of local thermodynamic equilibrium works rea-

sonably well for the stars analyzed in this work. Indeed, while the impact of non-LTE corrections depends on the element and increases in magnitude at lower metallicities (Ezzeddine et al., 2017), for the commonly-derived abundances (e.g., Fe) in solar-metallicity stars, switching to significantly more expensive non-LTE calculations has little impact (Mashonkina et al., 2011).

For this study, the popular pre-computed ATLAS grid of model photospheres was used (Kurucz, 2005). This grid is composed of 1-D, plane-parallel atmospheres computed under the LTE assumption, and spans a wide range in stellar metallicity, temperature, gravity, and micro/macroturbulence. When a model atmosphere is required, the user must supply at minimum the stellar surface temperature, gravity, and metallicity; micro/macroturbulence estimates may also be provided. The desired model atmosphere is then derived via interpolation onto the ATLAS grid.

Armed with EW measurements, a curve of growth, and a model photosphere, the desired chemical abundance estimates can finally be computed. This is done via solution of the stellar radiative transfer equation, which is a partial differential equation describing how radiative energy is transferred to the outermost layer of the photosphere. Solving this equation is a numerical endeavour, and for this study, the MOOG program was used (Sneden, 1973a). MOOG solves the transfer equation given a model photosphere and relevant atomic data, again assuming LTE for computational simplicity. Afer this, MOOG's *abfind* routine allows for an estimate of X/H given some input EW under the computed solution to the transfer equation.

There are a few quirks to this well-established analysis technique that deserve some discussion. First, to solve the transfer equation, MOOG requires a model photosphere; this photosphere in turn requires prior knowledge of the star being studied. At minimum, a relatively precise estimate of temperature and gravity must be supplied, as well as a reasonable guess of the stellar metallicity. This prior information can come from a variety of sources, such as photometric observations (see Section 3.4), literature sources, or directly from the spectra (see Chapter 4). It may seem strange to supply a metallicity during the photosphere calculation step when it is the parameter to be determined from the spectrum, but changes in metallicity do impact the structure of the photosphere (metallicity principally effects the opacity). However, the input metallicity needs only to be a

rough estimate; incorrect guesses on the order of $\sim 0.1 - 0.2$ dex have little impact on the derived abundance results.

Finally, it should be clear that any abundance determination via the equivalent width method is particularly sensitive to the adopted atomic parameters. This is particularly important for small line lists of the sort used for this study; an incorrect excitation potential for one or two lines, for example, can seriously bias any results. The workaround to this is to explicitly calculate any abundances differentially with respect to the solar abundances (i.e. [Fe/H] is calculated, rather than Fe/H). When this is done, assuming that the photosphere of the star being analyzed is somewhat similar in structure to that of the Sun, any offsets due to errors in atomic parameters will be present in the Sun and the target star. The differential chemical abundance [X/H] will therefore still be correct. This assumption holds less well for stars significantly different than the Sun.

For this study, the solar calibration was carried out by altering the adopted $log(gf)$ value (the oscillator strength) for each line, such that [X/H] derived from the ROBOSPECT solar EWs (from a sample of high-SN solar spectra) was forced to be 0 relative to the canonical solar abundances (Asplund et al., 2009). The adjusted $log(gf)$ values are given in Table 3.1. This method of calibration has the additional benefit of removing any systematic under- or over-measurement of equivalent width or systematic continuum placement offset by ROBOSPECT.

3.4 Science with ROBOSPECT and EWs: NGC 6819

A study of $\sim$ 300 main sequence, turnoff, and evolved stars in the open cluster NGC 6819 verified the ROBOSPECT+ATLAS+MOOG abundance analysis pipeline described above (see Lee-Brown et al. (2015) for full study details). NGC 6819 is a richly populated, old open cluster (age $\sim$2.3 Gyr, see Anthony-Twarog et al. (2014)) in the field of Cygnus. The kinematic properties of its members are well-known thanks to the radial velocities of Hole et al. (2009) and proper motions of Platais et al. (2013), making it relatively straightforward to identify cluster members. The field of the cluster has also been extensively imaged in broadband by several studies (see, e.g., Yang et al., 2013). Finally, the cluster was targeted by the *Kepler* mission, and the astroseismology enabled by

these observations provides precise $log(g)$ estimates (Gilliland et al., 2010).

Despite this wealth of observations, the cluster metallicity was poorly constrained before this study; the standard result of [Fe/H]$\sim +0.1$ came from the study of Bragaglia et al. (2001) and was determined via spectroscopic observation of 3 red clump stars. That a cluster of NGC 6819's age would have a moderately supersolar metallicity would be surprising, given that its thin-disk status would lead one to expect it to have a solar or slightly subsolar metallicity (see Anthony-Twarog et al., 2014; Lee-Brown et al., 2015). Indeed, the supersolar metallicity of Bragaglia et al. (2001) was called into question by the large-sample, intermediate-band photometric study of Anthony-Twarog et al. (2014), who found [Fe/H]=-0.06.

Thus, several hundred spectra of probable members of NGC 6819 were collected with WIYN/Hydra. Since the eventual goal of the program is to investigate Li patterns in this cluster, the spectra are of the Li-region - the same as the spectra observed for the study detailed in the present work. Therefore, ROBOSPECT's performance on these spectra should be representative of its performance on the SMR stars.

To carry out the analysis, the proven method outlined in Anthony-Twarog et al. (2009) for NGC 3680 was followed, with the exception of EWs from ROBOSPECT, rather than manual measurement. Atmospheric parameters used when generating the model photospheres were derived from the precision photometry given by Anthony-Twarog et al. (2014). For the surface gravity estimates, the *Kepler* and photometric values were in very good agreement (Lee-Brown et al., 2015).

The linelist used for the NGC 6819 study was the same as Table 3.1. Because the stars observed were in some cases significantly different than the Sun, a 3σ significance cut was imposed on the EW measurements; EWs within 3σ of the approximate noise level were discarded to prevent spurious noise spikes from being interpreted as real features. The SN used to impose this cut was estimated by examining the relatively line-free 6680-6695 Å region of each spectrum.

After eliminating probable non-members and binaries, abundances were measured for 247 stars - approximately 50 giants and 200 main sequence and turnoff dwarfs. The results of the abundance analysis are given in Figure 3.3 as a function of photometric surface temperature. For the giants,

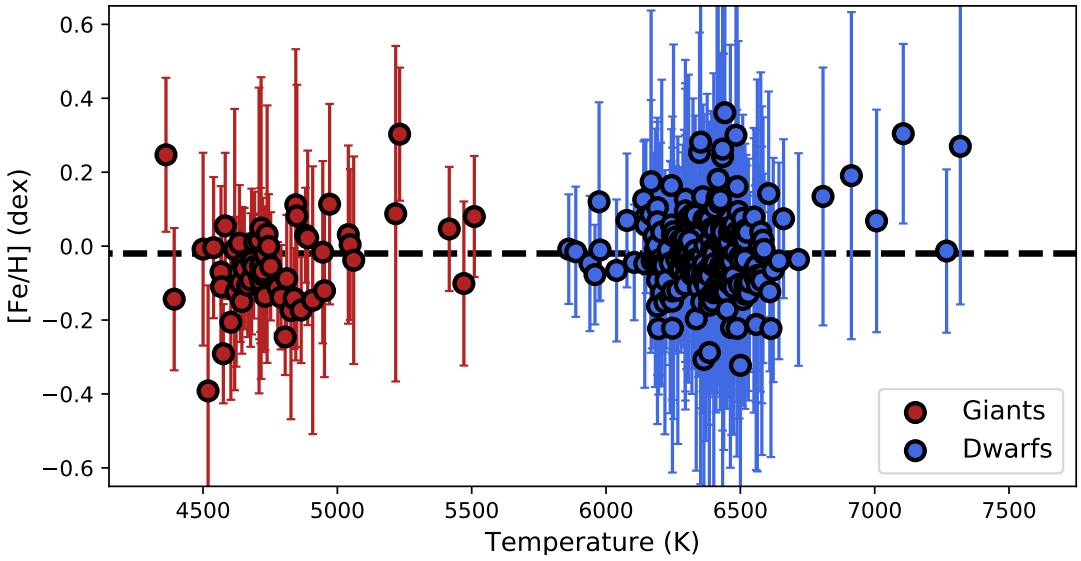

Figure 3.3: Derived [Fe/H] for the NGC 6819 sample of giants (red) and dwarfs (blue), with individual uncertainties indicated. The median cluster abundance of [Fe/H] = -0.02 dex is indicated by the black dashed line.

the median [Fe/H] was found to be -0.09 $\pm$ 0.05, and for the dwarfs, [Fe/H] = -0.02 $\pm$ 0.05. These results are statistically indistinguishable, indicating that the adopted atmospheric parameters are robust and that ROBOSPECT performs the same across the deeper-lined giant spectra, the solar-like stars, and the hotter, weaker-lined spectra near the turnoff. They are also in good agreement with the photometric results of Anthony-Twarog et al. (2014).

The large sample of the NGC 6819 study also afforded an opportunity to critically examine the adopted linelist. Ideally, there should be no variance when comparing the mean [Fe/H] from one line with that of another. This expectation is confirmed in Figure 3.4 - the [Fe/H] estimates from the different lines are statistically consistent with one another. It should be noted that the uncertainty varies from line to line; this is expected, as the lines are located in spectral regions with different SN, and have different typical strengths. Overall, each line's mean [Fe/H] is statistically consistent with the derived cluster [Fe/H].

Finally, while ROBOSPECT's sensitivity to SN was tested using solar spectra, the NGC 6819 sample was used to re-examine this as well. The standard deviation of each star's [Fe/H] estimates

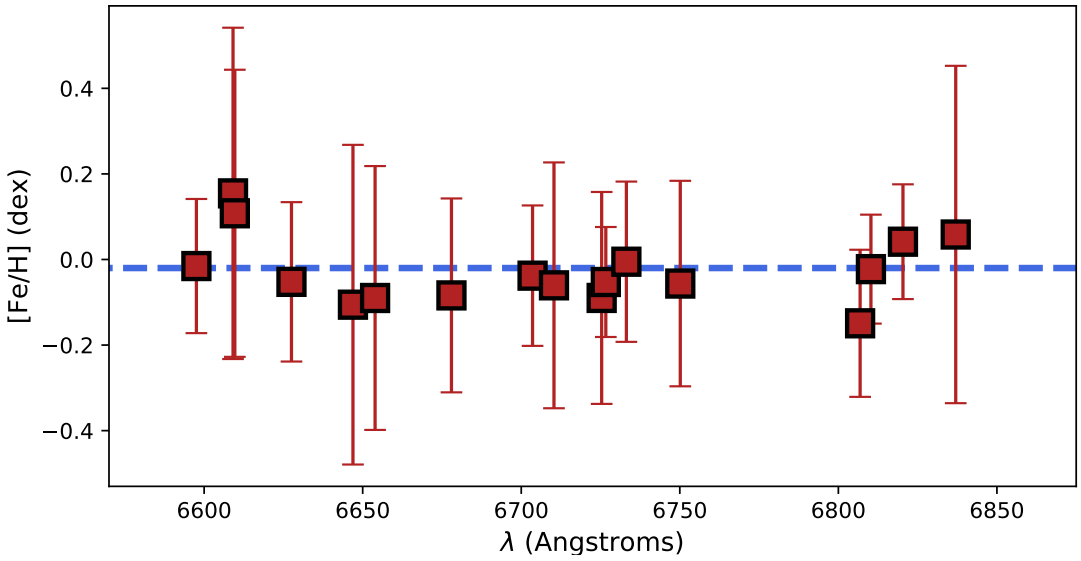

Figure 3.4: The average [Fe/H] for each Fe I line in the linelist as a function of wavelength. The error bars represent the standard deviation of all Fe I measurements for a given line. The cluster [Fe/H] of -0.02 dex is indicated by the dashed line.

is shown as a function of derived SN in Figure 3.5. The results are consistent with the solar testing; the σ[Fe/H]$\sim$0.3 at SN$\sim$ 100 corresponds to an uncertainty in EW of $\sim$13 mÅ. At high SN, $\sim$ 200, the [Fe/H] uncertainty corresponds to an EW error of 6-7 mÅ, slightly higher than the solar testing indicated but reasonably close; some of the difference may be driven by errors in, e.g., temperature, which would increase the scatter in Fe I estimates even if the EWs were precisely measured.

In summary, the study of NGC 6819 shows that ROBOSPECT returns reliable EWs across a wide range of stellar parameter space. ROBOSPECT-derived [Fe/H] results are consistent with photometric estimates, and are reliable at the high SNs of the SMR spectra, with typical uncertainties of $\pm$0.1 dex at SN$\sim$200. Additionally, the NGC 6819 study demonstrated the robust nature of the adopted linelist used with ROBOSPECT. This ground-truthing paves the way for it to be used straightforwardly to measure EWs in the SMR spectra.

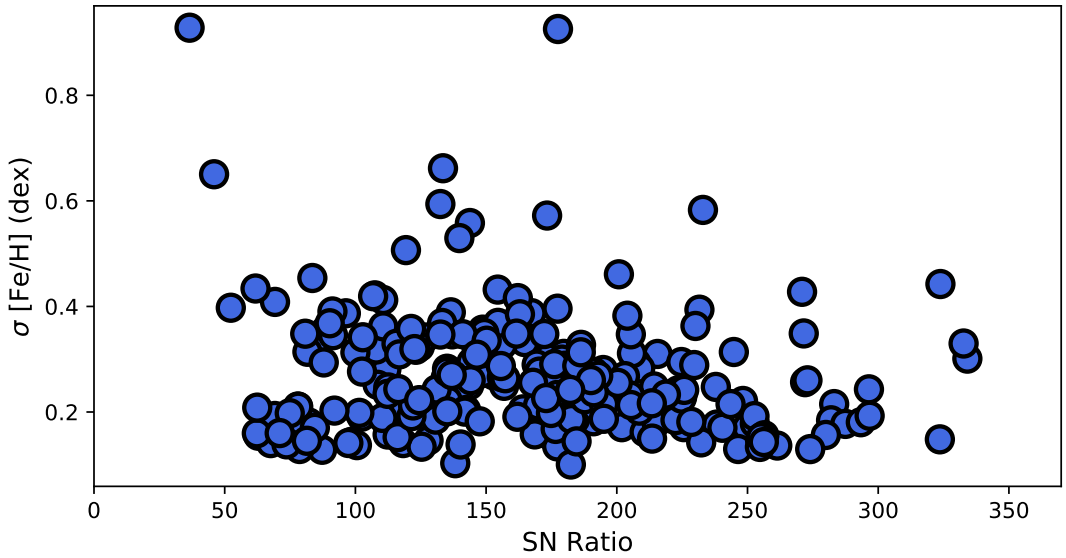

Figure 3.5: Standard deviation of the Fe I estimates for a given star as a function of derived SN ratio for the NGC 6819 sample.

3.5 Metallicities for the SMR Sample Using ROBOSPECT

In general, the procedure for determining [Fe/H] for the SMR candidate stars followed what has been outlined previously in this chapter. However, per the discussion regarding the quality of the photometric data collected for the SMR stars given in Chapter 2, atmospheric parameters to use when generating the model photospheres were obtained from other sources. Fortunately, since the sample of SMR candidates consists of bright, nearby stars, most of the sample already had gravity determinations, etc. from other studies, as described below.

3.5.1 The Atmospheric Parameters

For the temperatures, the purely spectroscopic ANNA temperatures detailed in Chapter 4 were adopted. Because of the target selection process outlined in Chapter 2, every SMR candidate has a temperature determination from a previous study. The ANNA temperatures are largely consistent with these results (see discussion in Chapter 4), and were adopted to avoid introducing any systematics by taking temperatures from a variety of sources - for example, as shown in Chapter 5, the

Geneva-Copenhagen temperature scale appears to run $\sim$ 50 K hotter than the Hypatia or ANNA scales.

ANNA, as trained for this study, does not provide accurate surface gravities, so these were adopted from a variety of sources. In order of priority, the literature sources used were the Hypatia catalog (Hinkel et al., 2014, 12 stars), the N2K catalog (Robinson et al., 2007, 26 stars), and the Geneva-Copenhagen Catalog (Casagrande et al., 2011, 27 stars). When an SMR candidate had gravity determinations in multiple catalogs, they typically agreed to within 0.1 dex. Unlike the temperatures, a small offset in $log(g)$ does not impact the metallicity determination significantly (see Lee-Brown et al. (2015)), so it is expected that any small systematics in the $log(g)$ values from different studies do not appreciably impact the final [Fe/H] results.

After this procedure, 25 stars still did not have gravity estimates. These were determined by computing the absolute V magnitude after using the Gaia DR2 parallaxes (Gaia Collaboration et al., 2016b,a; Lindegren et al., 2016) to determine distance moduli. Apparent V magnitudes were taken from the SIMBAD database (Wenger et al., 2000). Because the SMR stars are nearby, reddening should be very small ($\sim$ 0.1 dex in V) and was ignored. Once the values of M_V were computed, the stars with unknown $log(g)$ were compared with stars with known gravities, and a $log(g)$ estimated was derived via interpolation. This process leveraged the fact that the stars targeted for this study are all very close in temperature space and spectral class, so variations in M_V should be directly correlated with variations in $log(g)$. After this process, only three stars were without gravity estimates; these were excluded from the ROBOSPECT analysis.

For the metallicity estimates used during model atmosphere construction, the ANNA [Fe/H] determinations were adopted. These should be very close to the true [Fe/H] for each star and, as noted previously in this chapter, the [Fe/H] values used to generate the model photospheres only need to be approximately correct. Microturbulent velocities were computed according to the dwarf relation in Edvardsson et al. (1993). Radial velocities were estimated via determination of the 6715 Å Ca I line's location in each SMR candidate spectrum. As noted before, ROBOSPECT is relatively unaffected by small errors in radial velocity, so this crude method is sufficient for this

analysis.

Before running ROBOSPECT, several stars in addition to the three without $log(g)$ estimates were excluded. These included 5 stars with gravities consistent with giants, one star with a surface temperature of $\sim$ 7000 K whose spectrum is consistent with that of an A star, and several suspected binaries. After these cuts, 89 stars were analyzed with ROBOSPECT and MOOG.

3.5.2 Results

The distribution of EW-derived [Fe/H] estimates is given in Figure 3.6. The distribution is very similar in appearance to the ANNA [Fe/H] distribution shown in Chapter 4, with a general increase in number as a function of [Fe/H] with a peak around +0.2 dex. The EW and ANNA metallicities will be compared in more detail in Chapter 5. The full EW-derived results are given in Table 3.2.

In Figure 3.7, the EW metallicities are shown as a function of ANNA surface temperature. The average uncertainty in EW-derived [Fe/H] is $\pm$0.07 dex. Note that in Figure 3.7, the stars have different metallicities, so the scatter in the y-direction is expected. The takeaway from Figure 3.7 is that there is no obvious trend of [Fe/H] with surface temperature. This indicates that no serious systematics in temperature are biasing the EW-derived metallicities and, conversely, no systematic EW measurement errors as a function of temperature exist (due to, e.g., difficulty measuring EWs in hotter, weaker-lined stars).

The EW method with the linelist given in Table 3.1 also allows for estimates of [Ni/Fe], [Ca/Fe], and [Si/Fe]. These can be compared with the ratios for stars with [Fe/H] > +0.20 dex reported in López-Valdivia et al. (2017). For the SMR candidates with [Fe/H] > 0.20, [Ni/Fe], [Ca/Fe], and [Si/Fe] were found to be $+0.29 \pm 0.06$, -0.02 ± 0.04, and $+0.11 \pm 0.09$, respectively. The Ca and Si results are consistent with the López-Valdivia et al. (2017) results, but the [Ni/Fe] determination is significantly higher; López-Valdivia et al. (2017) report an essentially solar [Ni/Fe] for their SMR stars. Ultimately, however, it is difficult to draw conclusions given that only 3 Ni lines and a single Ca and Si line were measured by ROBOSPECT and the López-Valdivia et al. (2017) sample only contains 12 SMR stars.

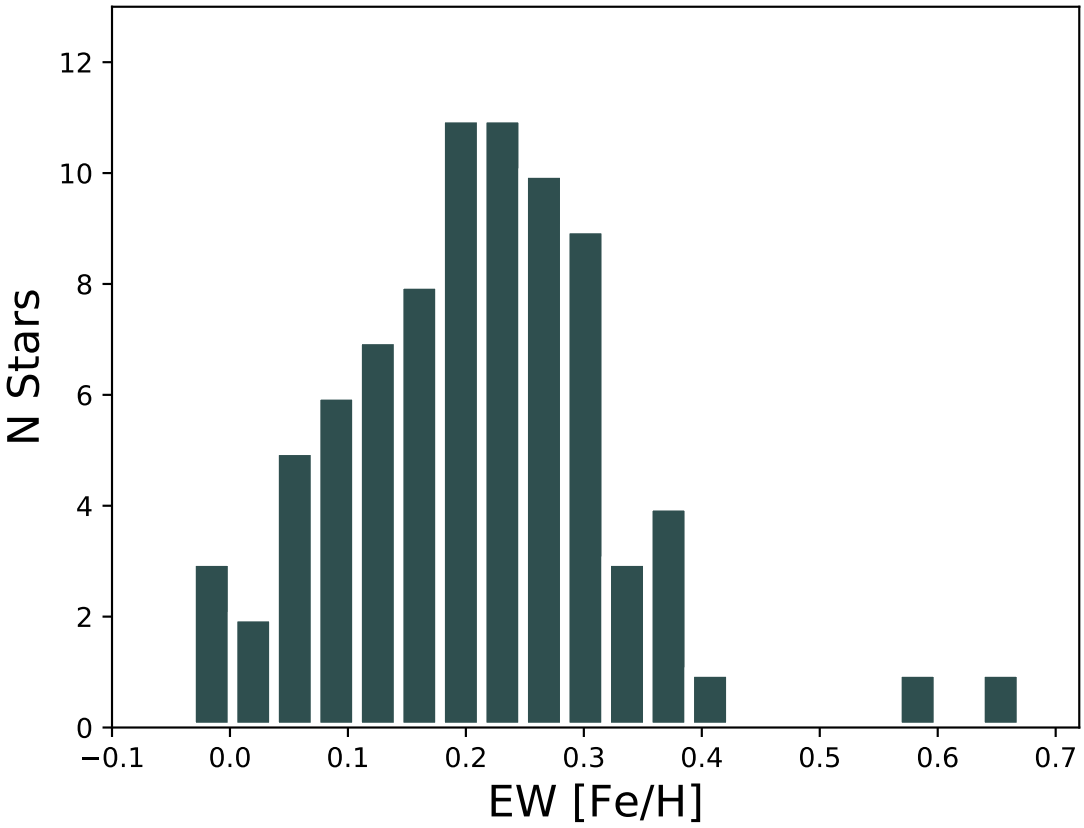

Figure 3.6: The distribution of [Fe/H] estimates from the EW analysis.

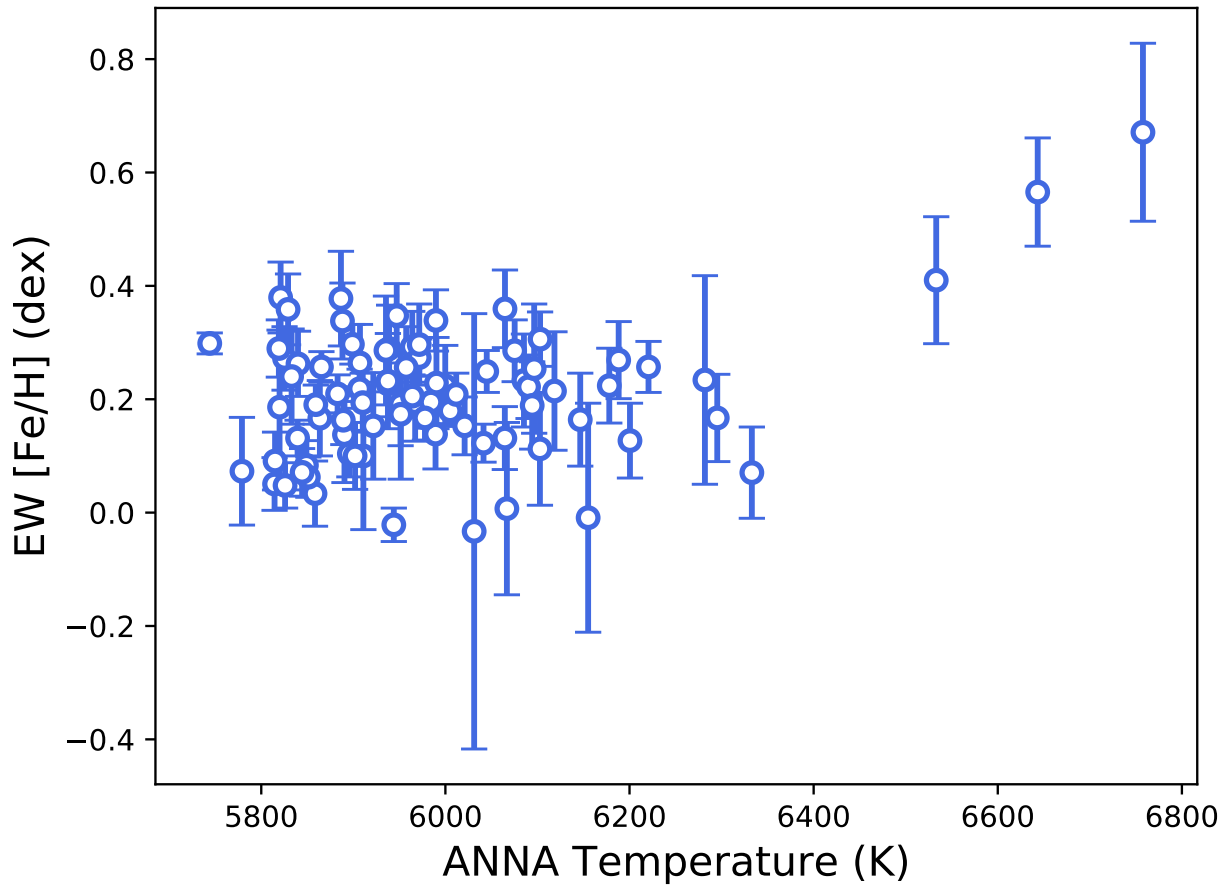

Figure 3.7: The EW-derived [Fe/H] estimates plotted against ANNA surface temperatures (see Chapter 4). The ANNA temperatures were used as the temperature estimates for model atmosphere construction as part of the EW analysis.

Table 3.2. EW Abundances

ID	$log(g)$	S_g	V_{rad}	[Fe/H]	σFe	[Ni/H]	σNi	[Si/H]	[Ca/H]
BD+39 2711	4.37	N	15.6	0.38	0.06	0.77	0.03	0.40	···
BD+60 583	4.20	N	-1.3	0.36	0.06	0.63	0.04	0.39	···
HD 100069	4.09	G	-14.7	0.05	0.05	0.38	0.06	0.06	0.09
HD 10211	3.92	G	-29.9	0.14	0.08	0.28	0.13	0.16	···
HD 102196	4.03	M	21.4	0.11	0.10	0.32	0.13	0.14	0.12
HD 103012	4.26	G	12.5	0.10	0.13	0.47	0.05	0.36	···
HD 103459	4.09	M	18.3	0.27	0.06	0.55	0.05	0.24	···
HD 104588	4.21	N	-9.4	0.30	0.02	0.63	0.01	0.36	···
HD 105279	4.20	N	-12.5	0.26	0.03	0.58	0.05	0.30	···
HD 106423	4.31	H	25.5	0.36	0.07	0.67	0.03	0.39	···
HD 107087	4.18	G	20.1	0.16	0.08	0.40	0.07	0.17	0.18
HD 107211	4.39	N	5.4	0.38	0.08	0.77	0.01	0.44	···
HD 10766	3.92	N	6.7	0.23	0.18	0.45	0.21	0.24	0.28
HD 109929	4.15	N	-9.8	0.29	0.05	0.57	0.05	0.36	···
HD 110010	4.58	H	-17.4	0.34	0.05	0.73	0.04	0.40	···
HD 11170	4.00	N	-9.4	0.22	0.07	0.43	0.05	0.25	···
HD 112001	4.26	H	-11.2	0.10	0.04	0.40	0.03	0.11	0.13
HD 113938	4.28	N	8.9	0.29	0.06	0.61	0.04	0.38	···
HD 115954	4.12	G	-6.7	0.19	0.14	0.48	0.08	0.20	···
HD 11638	4.21	N	11.6	0.29	0.08	0.54	0.03	0.30	···
HD 117243	4.36	H	-13.0	0.19	0.07	0.61	0.04	0.16	···
HD 117302	4.00	M	-16.1	0.10	0.06	0.40	0.08	0.08	0.08
HD 119825	4.18	G	13.8	0.12	0.03	0.41	0.05	0.09	0.17
HD 124102	4.04	G	-17.0	0.09	0.05	0.37	0.07	0.12	0.09
HD 126530	4.32	G	-26.3	0.23	0.06	0.53	0.04	0.26	···
HD 129171	4.27	G	-11.2	0.13	0.03	0.43	0.02	0.15	0.17
HD 130087	4.34	H	-16.5	0.20	0.05	0.56	0.02	0.28	0.19
HD 13345	4.21	M	22.8	0.22	0.07	0.47	0.09	0.26	0.19
HD 13773	4.14	M	10.3	0.27	0.07	0.51	0.11	0.32	0.34
HD 14348	4.09	G	-4.0	0.21	0.10	0.36	0.08	0.14	0.18
HD 144302	4.11	N	-38.9	0.22	0.03	0.50	0.06	0.34	···
HD 147062	4.08	G	-46.9	0.31	0.05	0.55	0.07	0.24	···
HD 149026	4.37	H	-17.9	0.25	0.04	0.57	0.05	0.27	···
HD 1497	4.25	G	-7.1	0.05	0.04	0.35	0.03	0.03	0.03

Note. — S_g indicates the source of the adopted $log(g)$ value: N = N2K (Robinson et al., 2007), G = Geneva-Copenhagen (Casagrande et al., 2011), H = Hypatia (Hinkel et al., 2014), M = Abs. Mag. (see Section 3.5.1). Radial velocities are in km/s. The solar abundances are from Asplund et al. (2009).

Table 3.3. EW Abundances (continued I)

ID	$log(g)$	S_g	V_{rad}	[Fe/H]	σFe	[Ni/H]	σNi	[Si/H]	[Ca/H]
HD 154144	4.18	N	-19.2	0.18	0.02	0.47	0.04	0.20	···
HD 156016	3.88	M	-29.5	0.19	0.05	0.42	0.11	0.22	···
HD 15866	4.00	H	-42.0	0.27	0.03	0.57	0.05	0.30	···
HD 16090	4.23	G	-6.3	0.15	0.05	0.46	0.10	0.21	0.24
HD 177985	4.05	M	-7.1	0.19	0.07	0.47	0.08	0.39	···
HD 180318	4.13	M	4.5	0.23	0.08	0.56	0.09	0.40	···
HD 180502	3.98	G	-6.7	0.17	0.07	0.43	0.02	0.19	0.18
HD 180556	4.19	G	-11.2	0.01	0.15	-0.06	0.09	0.23	0.12
HD 183490	4.30	M	-63.9	0.57	0.10	0.96	0.07	0.30	0.53
HD 192343	4.29	H	-0.4	0.26	0.06	0.60	0.00	0.18	···
HD 196199	3.82	N	-26.8	0.07	0.08	0.21	0.18	0.17	0.06
HD 196674	3.85	N	-48.7	0.17	0.08	0.38	0.09	0.11	0.28
HD 198483	4.30	G	-17.4	-0.01	0.20	0.29	0.04	0.44	···
HD 199167	3.84	M	-3.1	-0.03	0.38	-0.06	0.27	-0.03	-0.25
HD 19961	4.22	N	-11.2	0.34	0.07	0.65	0.04	0.40	···
HD 201529	4.19	M	-16.5	0.03	0.06	0.37	0.04	0.04	0.03
HD 203557	3.93	M	-19.2	0.23	0.08	0.45	0.10	0.17	···
HD 21313	4.30	H	-19.2	0.15	0.09	0.38	0.08	0.21	0.14
HD 216027	4.04	G	-21.0	0.07	0.10	0.36	0.07	0.01	···
HD 218354	4.11	G	-10.3	0.19	0.03	0.44	0.05	0.23	0.19
HD 220284	4.12	M	-14.7	0.08	0.04	0.36	0.03	0.08	0.13
HD 220848	3.90	G	-60.7	0.41	0.11	0.71	0.05	0.10	0.37
HD 224543	4.13	H	-41.5	0.21	0.04	0.49	0.09	0.18	0.14
HD 224882	3.87	M	-15.2	0.29	0.10	0.45	0.08	0.34	···
HD 2330	4.22	G	-7.1	0.14	0.06	0.39	0.02	0.14	0.14
HD 238069	4.02	N	-10.7	0.21	0.03	0.46	0.07	0.22	···
HD 2564	4.23	G	-18.8	0.26	0.04	0.56	0.05	0.39	···
HD 26441	4.04	G	25.0	0.26	0.07	0.47	0.06	0.30	···
HD 27533	3.90	M	-10.3	0.17	0.11	0.32	0.17	0.20	···
HD 279527	4.20	N	-71.5	0.67	0.16	1.02	0.11	0.55	···
HD 30769	4.01	M	-7.6	0.13	0.06	0.35	0.11	0.18	0.20
HD 3592	4.18	N	8.9	0.24	0.08	0.58	0.12	0.32	···
HD 449	4.22	N	28.6	0.35	0.06	0.66	0.03	0.42	···
HD 4649	4.10	G	-26.8	0.06	0.04	0.32	0.05	0.10	0.06

Note. — S_g indicates the source of the adopted $log(g)$ value: N = N2K (Robinson et al., 2007), G = Geneva-Copenhagen (Casagrande et al., 2011), H = Hypatia (Hinkel et al., 2014), M = Abs. Mag. (see Section 3.5.1). Radial velocities are in km/s. The solar abundances are from Asplund et al. (2009).

Table 3.4. EW Abundances (continued II)

ID	$log(g)$	S_g	V_{rad}	[Fe/H]	σFe	[Ni/H]	σNi	[Si/H]	[Ca/H]
HD 154144	4.18	N	-19.2	0.18	0.02	0.47	0.04	0.20	···
HD 156016	3.88	M	-29.5	0.19	0.05	0.42	0.11	0.22	···
HD 47155	4.03	M	9.8	0.13	0.07	0.40	0.07	0.09	0.14
HD 7355	3.99	N	-5.4	0.23	0.08	0.43	0.07	0.26	···
HD 76617	4.11	G	6.3	0.22	0.06	0.40	0.17	0.22	0.22
HD 78277	4.05	N	3.6	0.30	0.04	0.60	0.03	0.37	···
HD 78609	4.01	M	11.6	0.07	0.04	0.34	0.09	0.08	0.08
HD 82410	4.26	M	25.0	0.21	0.04	0.50	0.03	0.24	0.21
HD 8328	4.19	H	-2.7	0.29	0.05	0.65	0.02	0.37	···
HD 83616	4.01	N	-22.3	0.17	0.04	0.40	0.05	0.17	···
HD 8446	4.24	N	21.0	0.26	0.07	0.57	0.06	0.29	···
HD 91987	3.90	G	-24.1	-0.02	0.03	0.19	0.13	-0.07	0.01
HD 91988	4.01	H	45.1	0.25	0.11	0.42	0.08	0.19	0.26
HD 94861	4.15	G	-4.0	0.19	0.08	0.35	0.07	0.16	0.17
HD 97140	3.97	G	-32.6	0.16	0.04	0.42	0.11	0.20	0.17
HD 9729	4.24	N	25.0	0.30	0.07	0.55	0.12	0.24	···

Note. — S_g indicates the source of the adopted $log(g)$ value: N = N2K (Robinson et al., 2007), G = Geneva-Copenhagen (Casagrande et al., 2011), H = Hypatia (Hinkel et al., 2014), M = Abs. Mag. (see Section 3.5.1). Radial velocities are in km/s. The solar abundances are from Asplund et al. (2009).

Chapter 4

ANNA: A New Tool for Automated Spectroscopic Analysis

4.1 Introduction: The Limits of Current Spectroscopic Analysis Methods

The equivalent width (EW) based method of spectroscopic analysis detailed in Chapter 3 is a well-established, successfully employed technique in stellar spectroscopy. However, several limitations render the technique impractical and/or imprecise under certain conditions. In this chapter I will discuss these limitations in the context of new instrumentation and current or planned wide-field spectroscopic surveys, and present a new method for spectroscopic analysis that overcomes many of the problems associated with the EW method and other current techniques.

As shown in Figure 4.1, the ideal EW measurement is conducted on a line that meets four criteria. First, the line should be isolated, i.e., it should not be blended with another spectral feature, in order for a (typically) Gaussian profile to be fit. Second, the line should be low to moderate strength - this avoids saturation and deviations from non-Gaussianity, while ensuring the EW measurement corresponds to the linear portion of the curve-of-growth for the feature (see Chapter 3). Third, the strength of the line should be well above the local noise level - this is especially important when automatically measuring EWs using, e.g., ROBOSPECT, which can be "confused" into misidentifying neighboring noise features as lines of interest. Finally, EW measurements are quite sensitive to the local continuum placement - this placement also requires relative sparsity of spectral features in order for the continuum to be easily identified. The result of these requirements is that spectra used for an EW analysis must not only contain isolated lines, but also be of high signal-to-noise, relatively wide wavelength range, and medium-to-high spectral resolution in order for these lines to be measured accurately.

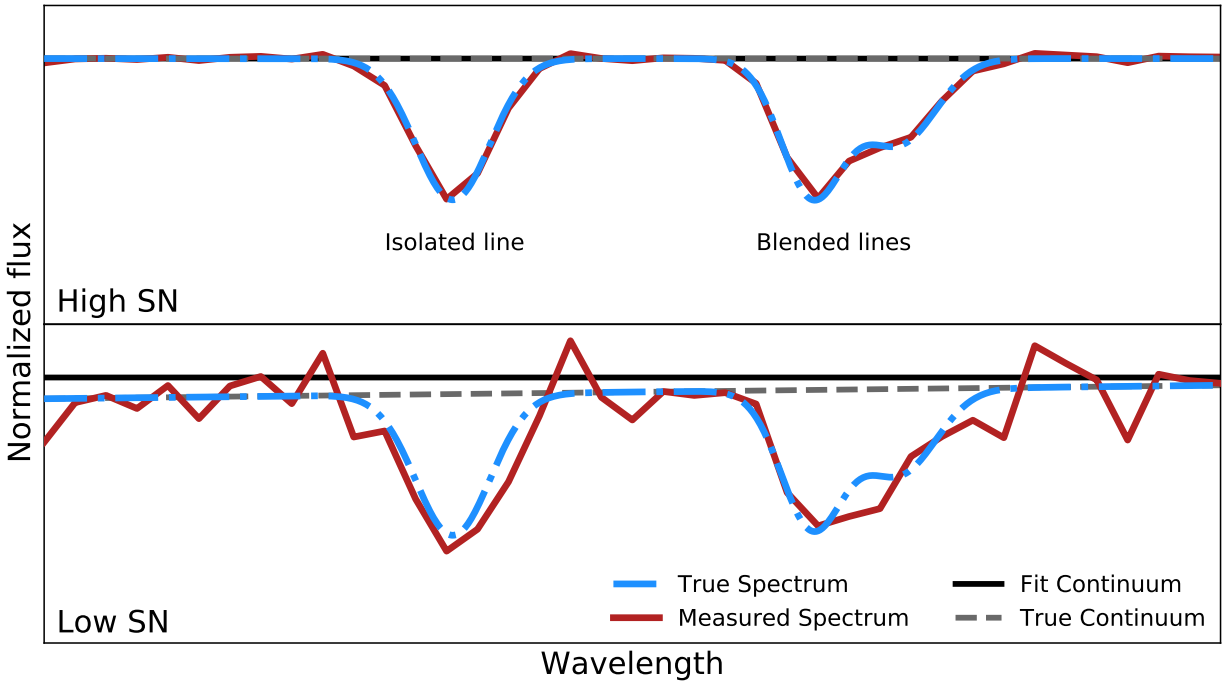

Figure 4.1: Illustration of the impact that spectrum signal-to-noise (SN) can have on the ability to accurately measure equivalent widths (EW). In both panels, the dashed blue line shows the true (simulated) spectrum, which is at very high resolution, and the solid red line indicates the lower-resolution spectrum that would typically be measured by a spectrograph. The dashed gray line indicates the true continuum level, while the black line shows the continuum placement derived via a fit to the measured spectrum. The top panel corresponds to high SN, while the bottom panel shows the same spectrum with a factor of 10 decrease in SN. For the high SN case, the measured spectrum closely tracks the true spectrum, and the derived continuum placement is at the true continuum level. The isolated line can be fit with a Gaussian to derive an EW, and even the blended lines can be deblended relatively easily. In the low SN case, the derived continuum placement is higher than the true continuum, and noise has increased the width of the isolated line - both these effects will result in an increase in measured EW. Additionally, the blend can no longer easily be deblended.

There are other considerations unrelated to the quality of the spectroscopy that impose additional limitations on the applicability of the EW method. First, translating between EW measures and chemical abundance estimates requires the construction of a model atmosphere corresponding to each spectrum. The parameters required to accurately construct this model - generally effective surface temperature, gravity, micro- and macro-turbulent velocities, and an estimate of the stellar metallicity - can in some cases be derived from the EW measures (see, e.g., the discussion in Gray 1996). However, this process requires a large number of line measurements in order to disentangle the similar effects these parameters have. For narrow wavelength regions (such as the ~ 200 Å covered by the Hydra spectra used in Section 4.4) there are too few clean spectral features to do this. Additionally, as the EW measurement discards information regarding line profile shape, parameters sensitive to profile shape such as microturbulent velocity cannot be determined from EWs, necessitating either photometric observations (as in Lee-Brown et al. 2015) or an alternate spectroscopic technique.

Second, the process of a full EW analysis is labor-intensive - while parts of the process can be automated, such as EW measurement, others cannot. For example, in Lee-Brown et al. (2015), automated EW measurement was followed by manual insertion of these measurements, along with a model atmosphere, into the MOOG spectroscopic analysis program. The need for manual interaction effectively imposes a maximum sample size of several hundred stars; larger samples quickly cause the EW method to become impractical.

Historically, the high cost of spectroscopic observations (see, e.g., Hill 1988) has generally limited individual spectroscopic chemical abundance studies to well below several hundred observations, but new or planned spectrographs and survey programs promise to change this. Contemporary multi-object spectrograph design, exemplified by instruments such as AAOmega on the AAT (400 fibers, Smith et al. 2004), MOONS on the VLT (1000 fibers, Cirasuolo et al. 2014), the PFS on Subaru (2400 fibers, Sugai et al. 2015), or DESI on the KPNO Mayall (5000 fibers, Flaugher & Bebek 2014), will afford large increases in spectroscopic sample size (note that some of these examples are not intended for stellar spectroscopy, but they serve to indicate the current state of

spectroscopic instrumentation). Next-generation spectroscopic surveys such as the Gaia mission (Recio-Blanco et al., 2016) or HERMES/GALAH (De Silva et al., 2015) will generate millions of high-quality spectra. Integral field spectrographs such as MUSE on the VLT (Henault et al., 2003) or SITELLE on the CFHT (Drissen et al., 2010) which produce spectra containing contributions from all sources within a small spatial area, will provide the means to efficiently measure many spectra, but these spectra will generally be heavily blended with few isolated spectral features. The sample sizes and data complexity enabled by these instruments and surveys will far exceed the limits of the EW method.

When confronted with the drawbacks associated with the EW method, the obvious path forward would be to rely on the other main spectroscopic analysis technique: spectral fitting. Rather than directly measuring the strength of spectral features, fitting methods generally seek to minimize the difference between a model or template spectrum and the observed spectrum (see, e.g., Valenti & Piskunov, 1996; Blanco-Cuaresma et al., 2014; Piskunov & Valenti, 2017). The parameters associated with the model or template of best fit are then adopted as the parameters of the observed spectrum. This method affords several advantages over the EW method. The technique is much more easily automated, tends to work better for feature-rich spectra, and is less sensitive to continuum placement errors. Additionally, it is easier to derive parameters other than chemical abundances using this technique (Blanco-Cuaresma et al., 2014), reducing the need for, e.g., separate photometric observations. These aspects make fitting particularly useful for analyzing the results from large surveys. Indeed, for the several hundred thousand spectra generated by the SDSS APOGEE spectroscopic survey, template fitting was adopted as the primary technique to derive reliable chemical abundances (García Pérez et al., 2016).

Unfortunately, fitting methods come with their own associated drawbacks. In particular, fitting methods tend to do no better than EW-based analyses at low SN (Recio-Blanco et al., 2016). This is because they generally rely on minimizing some metric of the difference between the observed and fit spectra (see, e.g., Valenti & Piskunov, 1996; Blanco-Cuaresma et al., 2014). At low SN or for observed spectra with few strong features, this metric can be more strongly a function of the noise

profile associated with the observed spectrum, rather than the true underlying signal, leading to inaccurate parameterizations. Fitting methods can also be computationally intensive, particularly as the wavelength coverage and/or resolution of the spectrum increases (Blanco-Cuaresma et al., 2014). For samples of many thousands of high-quality spectra, significant computing resources may be needed to derive stellar parameterizations in a timely manner.

4.1.1 A New Analysis Method: Design Challenges

It is clear that the limitations of standard spectroscopic analysis techniques will hamper our ability to fully leverage the outputs from next-generation instrumentation and surveys. Certainly improvements such as the development of ROBOSPECT help mitigate these limitations, but novel methods of analysis may be able to avoid them altogether. From the discussion in the preceding section, four key requirements for any new technique can be distilled:

1. The technique should be highly scalable - it should be possible to use this technique for samples of tens to millions of spectra. This means that excepting an initial period of setup, the technique should be entirely automated, requiring no per-spectrum action on the part of the user. On the other hand, it must not be so computationally intensive that analyzing large spectroscopic samples would outstrip practical computing power limitations.

2. Use of the method should not entail a great reduction in derived parameter precision relative to other methods. This means that for a typical spectrum of SN$\sim$200, uncertainties should be around 50-100 K for surface temperature and 0.05-0.10 dex for [Fe/H] and $log(g)$ determinations (Hinkel et al., 2016). Additionally, the method should at least result in temperature and metallicity determinations for a given spectrum (the same as an ideal EW analysis) but ideally would allow for other parameters to be determined as well.

3. The method should be more robust to high noise levels than template fitting or EW measurement. It should also return accurate results for spectra with few isolated features. It must

be relatively insensitive to typical artifacts in spectra - cosmic rays, continuum placement errors, etc.

4. As a final, practical matter, the method should be easy to use. That is, there should be some attention paid to user-friendliness and there cannot be an extensive period of tuning required for acceptable results. As an extension of (1) above, the method should not require special/expensive computer hardware or software to be used.

4.2 ANNA: Artificial Neural Network Abundances

4.2.1 Background

The need for algorithms that offer better scalability, precision, and computational efficiency than existing techniques is not unique to the problem of spectroscopic analysis. Certainly within astronomy, non-spectroscopic, next-generation surveys such as LSST and instruments like the SKA promise to push the limits of our computational resources and analysis capabilities by generating tera- and petabytes of imaging information that must be analyzed in as close to real-time as possible (Garofalo et al., 2017). However, from a broader perspective, the tremendous explosion in the volume of data collected by commercial, national, and research interests (see, e.g., Bhadani & Jothimani, 2017), combined with the need to analyze this data under time and accuracy sensitive conditions (e.g., autonomous driving), has meant that the scalability, precision, and efficiency challenges outlined in the previous section are replicated across a broad swath of disciplines. These near-universal issues have in turn catalyzed large investments in data analysis research that have yielded some very high-powered, cutting-edge techniques that have clear applications in astronomy. These techniques largely fall under the umbrella of machine learning.

Machine learning (ML) refers to a class of algorithms where the appropriate mapping between some input data and corresponding target outputs is inferred directly from the data (for a concise review of ML, see the introduction of Graff et al., 2014). As a simple example, linear regression is an instance of ML - from some sample of data, the slope and intercept of the line of best fit can be

inferred. More complex ML algorithms include support vector machines, clustering algorithms, and neural networks. These algorithms can be supervised, where the model encoding the mapping is derived using data corresponding to known target outputs (linear regression is an example of a supervised algorithm), or they can be unsupervised, in which case the target outputs are also inferred from the data (example: k-means clustering). In both cases, once the mapping between inputs and outputs has been derived, the "trained" ML model can be used to predict the target outputs corresponding to some input data.

One of the key advantages of ML algorithms is their scalability. A trained model is capable of rapidly computing target outputs with no interaction on the part of the end-user. The other key advantage of ML relates to precision. Complex ML algorithms such as neural networks or decision trees are capable of encoding nonlinearities and can be composed of millions of free parameters, resulting in the ability to map input data with accuracies exceeding the human eye or carefully tuned parametric methods. These two attributes clearly address most of the challenges posed in the previous section, and have led to a dramatic increase in interest in ML, both within and outside of astronomy, as shown in Figure 4.2. Recent examples of successful ML applications in astronomy include reconstruction of high-redshift sources (Schawinski et al., 2017), gravitational lens analysis (Hezaveh et al., 2017), star/galaxy classification (Kim & Brunner, 2017), transient detection (Cabrera-Vives et al., 2017), and redshift determination (Sadeh et al., 2016).

The advantages of ML in combination with its demonstrated success in astronomy make an ML-based approach a natural starting point for any new spectroscopic analysis tool. Indeed, several studies have focused in particular on the suitability of one ML algorithm, the artificial neural network (ANN) (Bailer-Jones et al., 1997; Allende Prieto et al., 2000; Snider et al., 2001; Bailer-Jones et al., 2002; Manteiga et al., 2010; Dafonte et al., 2016; Li et al., 2017). Overall, these studies have demonstrated that the ANN algorithm, when appropriately implemented, can return accurate stellar parameterizations orders of magnitude more rapidly than contemporary techniques (see, e.g., Li et al., 2017). However, these studies, especially the earlier ones, have tended to be exploratory or proof-of-concept in nature, and have highlighted several outstanding challenges with

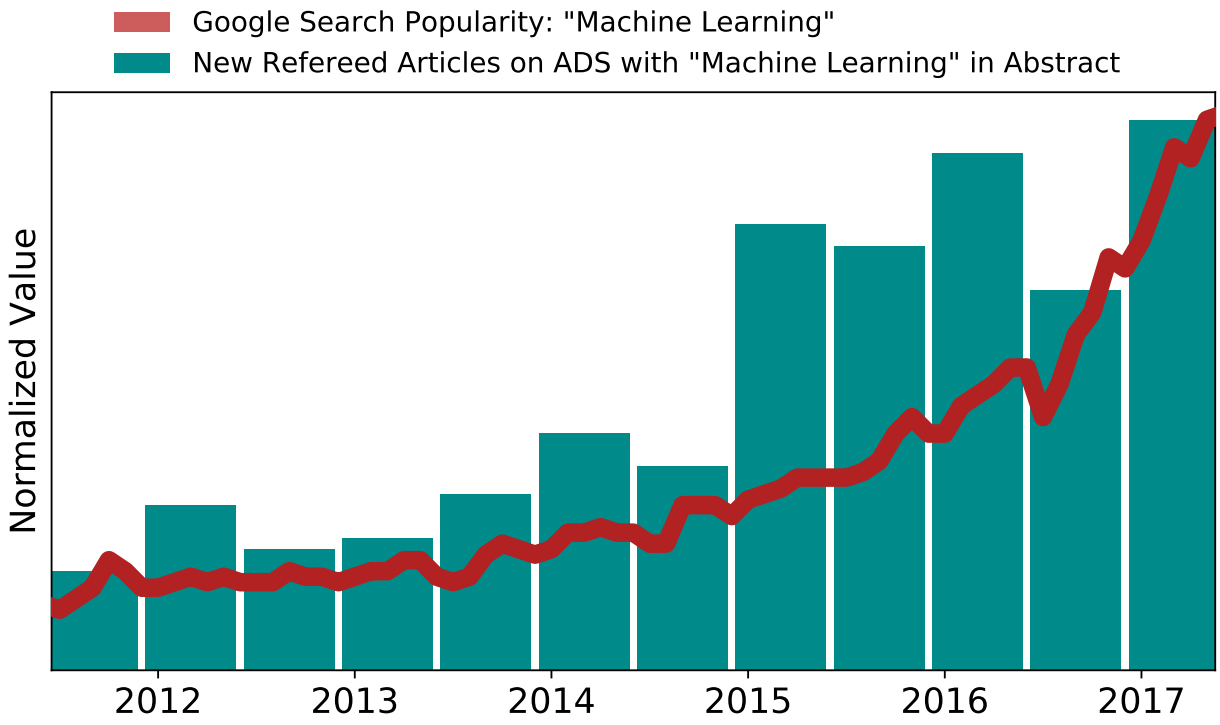

Figure 4.2: The rise in popularity of machine learning. In astronomy, the number of peer-reviewed, machine learning-related papers appearing every six months has increased by a factor of five since 2012. This trend mirrors the increase in popularity outside the field. Sources: NASA ADS, Google Trends.

the approach, namely the need for large training sets (Snider et al., 2001), the computational burden of training the ANN (Manteiga et al., 2010), and the intrinsic correlations between parameters governing stellar spectra (Bailer-Jones et al., 1997). While at least one large survey intends to use an ANN as part of its spectroscopic analysis pipeline (the Gaia mission, see Manteiga et al., 2010; Dafonte et al., 2016), there is as yet no ANN-based tool specifically for spectroscopic analysis available, and several of the challenges associated with the approach have not yet been fully resolved.

To this end, I have written a new, freely-available program, ANNA, which provides a convenient, easy-to-use framework for spectroscopic parameterization via an ANN. ANNA originally stood for Artificial Neural Network Abundances, as its original purpose was to derive metallicities from spectra; it has since been adapted to determine an arbitrary, user-specified number of atmospheric parameters (but the name stuck, so ANNA it is). Crucially, ANNA was designed from the start as a general-purpose tool and incorporates many features which reduce computational load, simplify the process of training a neural network, and increase parameterization accuracy and robustness. In the next sections, I will discuss the theory behind the ANN algorithm and detail its use in ANNA.

4.2.2 Neural Networks

An ANN is a non-linear computational model capable of mapping inputs to a set of outputs whose values are encoded in the inputs. This mapping is accomplished via a series of nested, interconnected mathematical operations whose organization was originally inspired by early models of biological nervous systems (see e.g., Haykin, 1998). It has been shown that ANNs, once trained, are "universal approximators" capable of approximating any well-defined function (see e.g., Bishop, 1995). Despite this undeniably useful property, for a considerable length of time, ANNs were relatively obscure, as their effective use was strongly limited by the computationally intensive process of training and the need for large training sets. However, the large growth in available computing power and data collection capability, combined with large efforts to improve

the computational and data efficiencies of ANNs, have significantly reduced these barriers. These developments, combined with freely-available ANN software libraries such as Google's Tensorflow (www.tensorflow.org), mean that ANNs have enjoyed a surge in popularity as it has become more feasible to implement them.

A simple ANN architecture is shown in Fig 4.3. The basic element of an ANN is a *node*, which represents a mathematical operation that transforms input data into an output, or "activation". Nodes are organized into layers, such that the nodes in one layer receive inputs from the preceding layer and pass their activations to the next layer. This structure of sequential layers is known as a feedforward neural network. If each node activation in one layer is dependent on every node activation in the preceding layer, then the network is *fully-connected*. Thus, the network shown in Fig 4.3 is a fully-connected, feedforward ANN (for a more comprehensive theoretical discussion of fully-connected networks, see Bishop, 1995). There are many other ANN variations, including the ubiquitous convolutional neural network (see Haykin, 1998), the autoencoder (Marivate et al., 2008), and the generative adversarial network (Creswell et al., 2018). While these different architectures offer significantly different functionality, at a high level, they all work similarly to the one given in Figure 4.3, in that they define a non-linear map between inputs and outputs via a series of simple, interconnected operations.

The *input layer* of a feedforward network is simply the input data (e.g., pixel values) to be analyzed. Each node in this layer simply passes an input datum to the nodes in the next layer. Following the input layer are one or more *hidden layers*. Each node in a hidden layer receives the outputs from the previous layer, each multiplied by some associated weight. These weighted inputs are then summed, and some non-linear function (the *activation function*) is applied to this sum and returned as the node activation. Thus, the activations of hidden layer nodes are non-linearly transformed sums of activations of the previous layer's nodes. In the network shown in Fig 4.3, there is a single hidden layer. Because the network in Fig 4.3 is fully-connected, the nodes in the hidden layer each receive weighted values from every node in the input layer.

The exception to the fully-connected network's rule of every node in a layer being connected

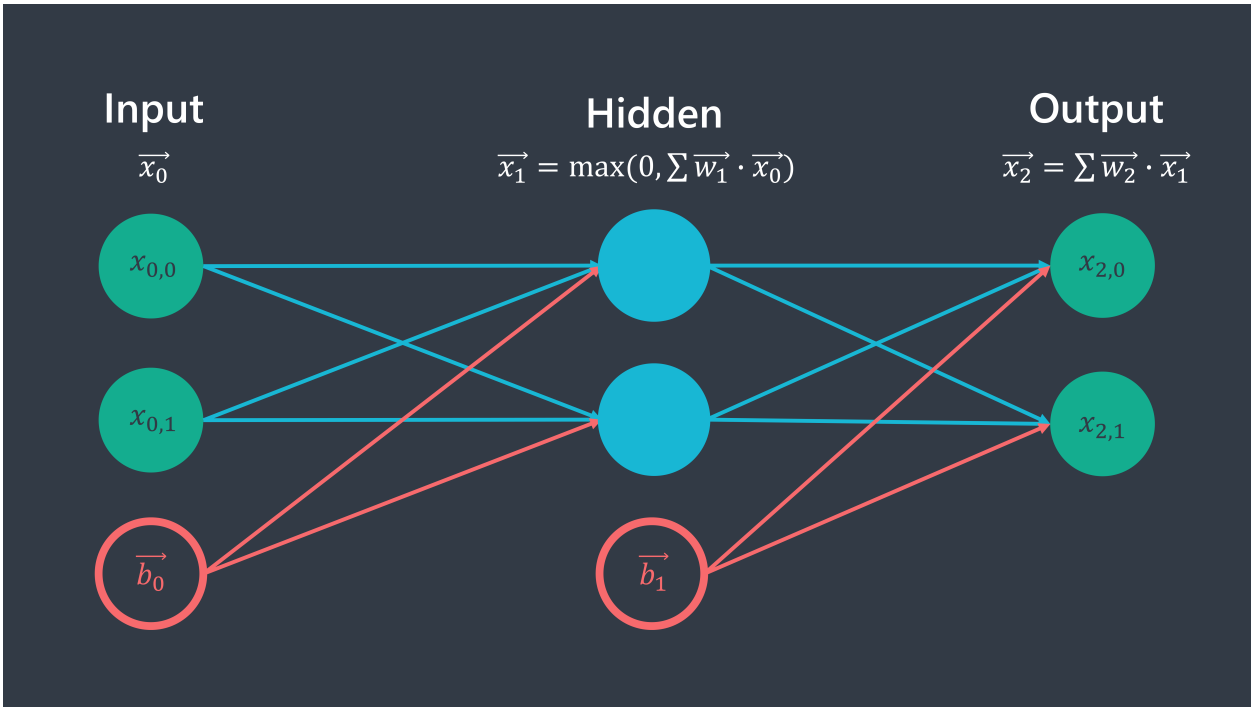

Figure 4.3: An example fully-connected ANN. The input layer consists of a vector $\vec{x_0}$ of input data and bias, $\vec{b_0}$, which are then propagated to the nodes in the next layer via weighted sums. The weighted sums are then activated - in this network the rectified linear unit (ReLU) is used, $\vec{x_1} = max(0, \Sigma \vec{w_1} \cdot \vec{x_0})$. The process is then repeated to reach the output layer whose node outputs $\vec{x_2}$ are the target outputs corresponding to the input data.

to one or more activations of the previous layer's nodes is the *bias node*. Unlike the other nodes in a layer, the bias node's activation does not depend on previous layer activations, and serves a role analogous to that of the constant b in the simple linear function $h(x) = ax + b$. As with the other activations, the bias node's activation is weighted and propogated to the next layer.

A common choice for the activation function is the sigmoid, defined as $f(\vec{w},\vec{x}) = \frac{1}{1+e^{-a\times\Sigma\vec{w}\cdot\vec{x}}}$, where $\vec{w}$ and $\vec{x}$ are the weights and associated activations from the previous layer and a is some constant. Another, less computationally demanding choice is the *rectified linear unit*, or ReLU, defined as $g(\vec{w},\vec{x}) = \max(0,\Sigma\vec{w}\cdot\vec{x})$. There are many other viable options as well (e.g., hyperbolic tangent) - the primary purpose of the activation function is to inject non-linearity into the ANN and particulars of how this is done are relatively unimportant for most applications (Bishop, 1995). For example, in the network shown in Fig 4.3, a ReLU activation function is used.

The final layer of the network is the *output layer*. Nodes in the output layer receive weighted activations from the preceding hidden layer, and depending on the application a non-linear activation function may also be applied to the sums of these inputs. The output layer activations are the outputs of the ANN; they correspond to whatever parameters the network was designed to infer from input data (e.g., probability of an image being of a particular object, stellar surface temperature, etc.). In other words, the values of the activations of the nodes in the output layer are of principal interest to anyone using a neural network to analyze data.

As can be seen, once the number of nodes and layers have been set and an activation function has been chosen, the only free parameters in an ANN are the weight values. Thus, defining the particular mapping that correctly translates between inputs and outputs boils down to carefully choosing these weights. Since ANNs often contain many thousands (or even millions or billions) of individual weights, correctly choosing weight values is necessarily a task for computers.

During training, the ANN hyperparameters (number of nodes and layers) are set, and the network is given a number of example inputs whose outputs are known via some other method (i.e., this is an example of supervised learning). The weights in the network are set to their initial values (usually small, random numbers), and the training examples are fed through the network, produc-

ing outputs. These inferred outputs $\vec{x}$ can then be quantitatively compared with the the known output values $\vec{y}$ via a *cost function*, $J(\vec{x},\vec{y})$, where $\vec{x}$ is itself a function of the network weights and inputs. The specific form of the cost function depends on what the network is being used to do (e.g., classify, produce continuous-valued outputs, etc.).

Once the cost has been calculated, training the network is reduced to solving a minimization problem, where the function to be minimized is $J(\vec{x},\vec{y})$. The most straightforward method of doing this is to calculate the gradient of the cost function with respect to each weight in the network. This gradient can be used to update each weight with the magnitude of the update controlled by a parameter known as the network *learning rate*. Once the weights have been updated, training data can again be fed through the network and another weight update performed. Over many update steps, the network weights will converge to their optimal values and the ANN will be capable of correctly translating between inputs and outputs. Naturally, it is critically important that the training examples (and their known outputs) be representative of the data the network will be used to analyze.

This processing of training the network is known as *backpropagation*. While straightforward to understand, it is computationally expensive in its most naive implementation (termed gradient descent) due to the large number of gradient calculations required and static learning rate; newer training algorithms operate using the same general principle but employ various schemes to speed up the weight update process (see examples in, e.g., Simonyan & Zisserman, 2015). It is also crucial to have sufficient training data; the network weights are effectively free parameters that must be carefully tuned, so the training data must be sufficiently comprehensive to allow the network to map out (using the weights) the relations between inputs and outputs. Again, there has been significant work to address this issue as well (through processes such as data augmentation, e.g., Chrysos et al., 2018).

This is but a basic overview of neural networks - the information regarding choice of activation function and architecture, as well as the terminology used, is drawn variously from Bishop (1995) and Haykin (1998). For more comprehensive discussions, interested readers are referred to these

references. For a comprehensive - albeit somewhat dated - discussion of neural networks in the context of astronomy, see Bailer-Jones et al. (2002). Some practical working examples of different neural network architectures and their applications can be found at www.tensorflow.org.

4.2.3 ANNA: Architecture

ANNA was largely inspired by the examples set by previous explorations of neural networks as tools for spectroscopic analysis (e.g., Bailer-Jones et al., 1997), but incorporates several modern developments in ANN design that improve upon previous studies. ANNA is written in Python, and uses the Python version of Google's TensorFlow deep learning library for the ANN-related parts of the code. The use of TensorFlow greatly simplifies ANN design and parallelization, and provides easy access to important features discussed below.

The neural network at the core of ANNA is a *convolutional* neural network (CNN), an ANN variant that has enjoyed significant success in solving computer vision problems (see Simonyan & Zisserman, 2015). In contrast to the simple fully-connected networks described in the previous section, a CNN contains one or more hidden layers that apply one or more convolutional kernels to the layer inputs. These convolutional kernels, or filters, can be thought of as a small collection of nodes that only receive inputs from a small, localized subsample of inputs, as shown in Fig 4.4. The filters are "slid" across the entire range of inputs to the layer, such that every input is connected to the convolutional filter at some point, but only its neighboring inputs are connected to the filter at the same time.

The convolutional layer ensures that within such layers, a CNN only "sees" correlations between neighboring inputs. This property is ideal for a program such as ANNA, since widely spaced pixel values likely have little to do with one another, but spectral lines or line complexes form localized regions of highly correlated pixel values whose variance contains important atmospheric information. While a fully-connected network can eventually be trained to recognize these localized regions as well, the much larger number of free parameters in a fully-connected layer vs. a convolutional layer results in longer training times to achieve the same accuracy as a CNN.

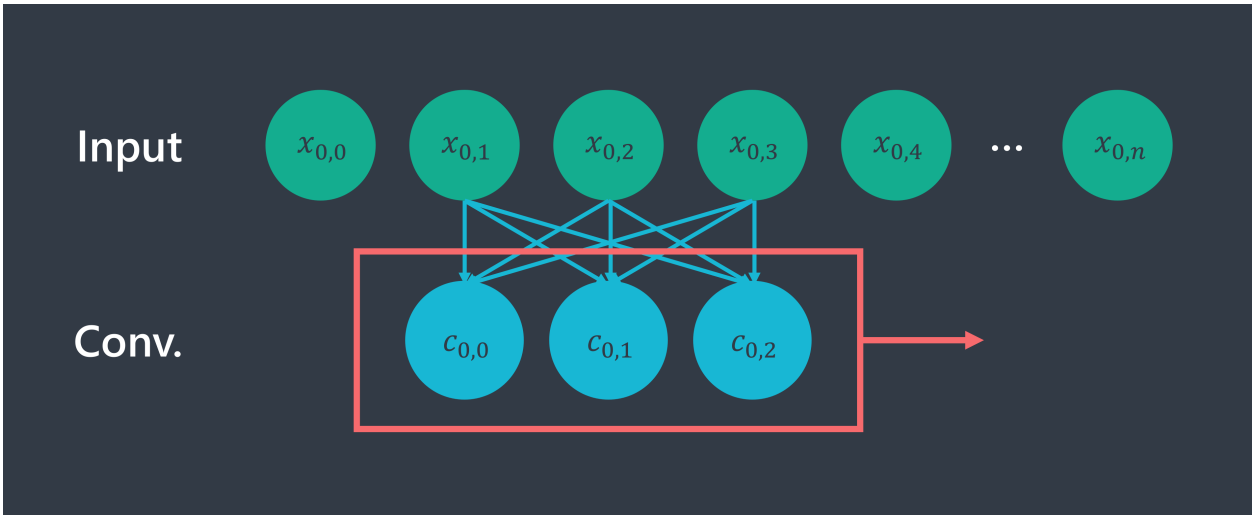

Figure 4.4: Diagram illustrating how a convolutional layer works. The convolutional filter, or kernel, (lower blue circles) is fully-connected to a localized region of the previous layer. The filter then "slides" across the previous layer, such that a series of outputs, each responsive to a localized region of the previous layer, are computed.

ANNA contains a convolutional layer as the first hidden layer. The outputs of the convolutional layer are then used as inputs into two sequential fully-connected layers, as shown in Fig 4.5. This means that the network is still free to learn correlations between widely spaced spectral regions, but the convolutional layer provides a computationally inexpensive way to capture correlations between localized regions. In other words, the convolutional layer in ANNA acts like a filter, passing a series of outputs based on local correlations to a fully-connected network which handles global correlations. The user is free to determine the number of nodes and filters in all three hidden layers of ANNA.

Between the fully-connected layers, ANNA employs dropout, a mechanism to prevent overfitting (Srivastava et al., 2014). Dropout involves randomly selecting nodes (according to a user-specified probability) to ignore during a training step. Nodes flagged in this way are re-initialized. This process of randomly resetting nodes during training helps avoid the problem of the network becoming overly-dependent on the activations of a few nodes, and improves the network's resiliance to overfitting (i.e., dropout is a regularization technique). Importantly, dropout is computationally cheap and requires minimal tuning to be effective.

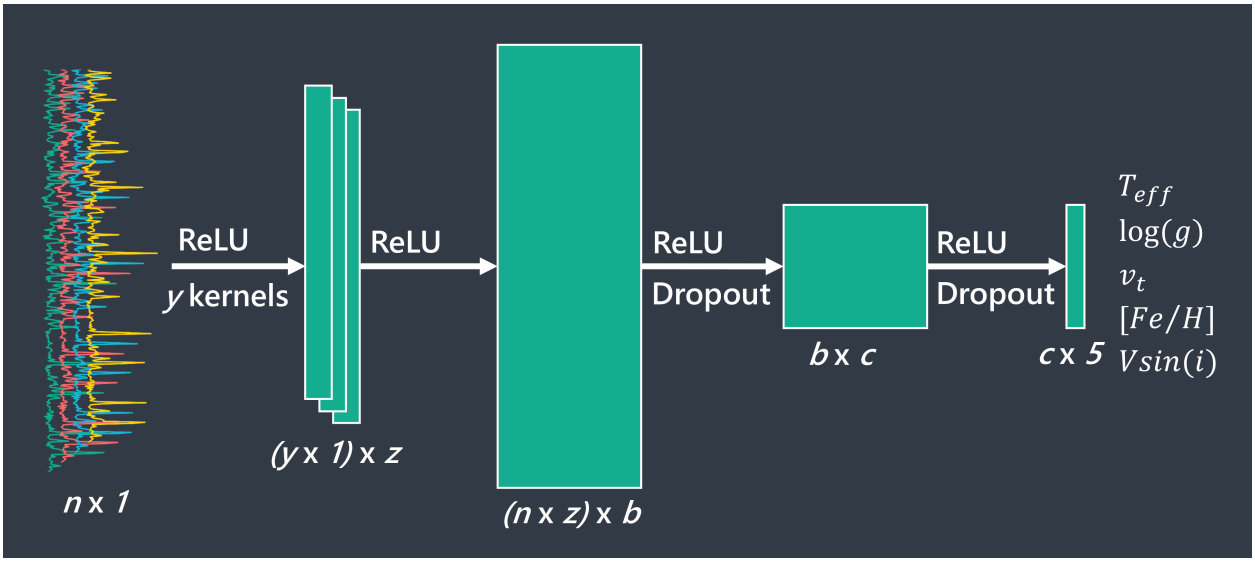

Figure 4.5: ANNA's architecture. For the input layer, one or more 1-D spectra are fed in. These are then passed to outputs via a convolutional layer and two fully-connected layers. The convolutional layer consists of y filters (or kernels), and the outputs from the filters are concatenated before they are passed to the fully-connected layers. The activation function used throughout is the rectified linear unit (ReLU, $f(x) = max(0,x)$. Dropout is employed between the fully-connected layers. The outputs of the network are a number of user-specified atmospheric parameters.

The activation function used throughout ANNA is the ReLU, defined in the previous section. This choice of activation function affords a computational advantage relative to more complex activation functions such as the sigmoid, with no appreciable loss in accuracy - as noted previously, the particular choice of activation is generally unimportant as its purpose is to introduce generic non-linearity into the network. The only exception is the output layer of the network, which consists of weighted sums of the layer inputs with no ReLU activation (i.e. the layer uses the identity function, $f(x) = x$, as its activation).

During training, ANNA first initializes the network weights according to the scheme outlined in He et al. (2015). The adopted weight initialization improves the ability of the weights to converge to the optimal solution during training, and was specifically developed for the case of ReLU activation functions. The bias units in the network are initialized to 0.

The cost function adopted for training the network is the squared error, $\Sigma(\vec{y} - \vec{y}')^2$, where $\vec{y}$ and $\vec{y}'$ are the true and inferred parameters, respectively. This cost function was chosen as it is similar to the commonly adopted function to be minimized during regression problems. It is also guaranteed

to be convex with respect to each parameter, helping prevent the network from converging to a local, rather than global, minimum in the cost function.

ANNA uses mini-batching during training. In the most naive implementation of neural network training, the entire training set is used during each training step. This is inefficient, as it requires that every training example be examined by the network before the weights are updated. A much faster training method is to randomly sample from the entire training set and feed a small number of training examples into the network during each weight update step (see discussion and references in Ruder, 2016). Over many training steps, the network will be exposed to the entire training sample, but will be allowed to update its weights during that process. This results in some stochasticity in the cost function with respect to training step, as one mini-batch may be better fit by the current network weights than a different mini-batch, but results in significantly faster training.

The weight optimizer used during training is the Adam optimizer, a stochastic gradient-based algorithm (Kingma & Ba, 2014). Adam incorporates several features that have been shown to significantly increase training speed, including momentum (Nesterov, 1983), and was designed to be computationally efficient. Empirical tests with ANNA have shown that Adam leads to significantly faster weight convergence when compared with other gradient-based optimization methods.

4.2.4 ANNA: User Features

In keeping with the original design goals for ANNA, many features were incorporated into the code to facilitate its use and efficiency. In contrast with the architectural aspects of ANNA detailed above, many of these features are user-controllable and optional, as they may require additional data, computational resources, or may not be applicable to all use cases. The major features are described below; a more comprehensive description of all features can be found in the ANNA documentation (see Section 4.5).

Perhaps the most useful feature of ANNA is its ability to be trained to extract a user-specified collection of target parameters from input spectra. For example, a user wishing only to use ANNA to determine surface temperatures may do so, while a user wishing to determine surface tempera-

tures, gravities, microturbulent velocities, etc. may also do so. Naturally, the more features a user wishes to extract from a spectrum, the more complicated the model defining the extraction should be. Thus, as noted previously, ANNA allows the number of convolutional filters and nodes in each layer to be modified.

The process of training an ANN is significantly more computationally intensive than running inference, and care was taken during the design process to ensure that ANNA is capable of being trained using modest hardware. In order to reduce I/O costs, the code was written to use a compact binary format for the training data set. This allows even relatively large ($\sim$100,000 examples) training sets to be stored entirely in a typical computer's RAM during training. Additionally, because ANNA was built using TensorFlow, a supported Nvidia graphics processing unit (GPU) can be used during training if one is available, leading to orders of magnitude faster training times. If no GPU is available, ANNA will use all available CPU cores during training.

During training, ANNA supports the use of a *cross-validation* dataset and early stopping. A cross-validation dataset is kept separate from the main pool of training data. At user-defined intervals, the network pauses training to run inference on this data, computing the cross-validation cost. The training then continues until the cross-validation cost has not improved for a user-defined number of iterations. At this point, the network stops training (early stopping), as the cross-validation error is minimized and further decreases in the cost function during training are likely due to overfitting of the training data.

ANNA also supports an optional, second training stage. This means that the user can run training with an initial set of network learning parameters, and when the cost is minimized during this stage of training or the end of the specified iterations is reached, training can continue with a second set of learning parameters. This allows the user, e.g., to adopt a high initial learning rate or small batch size to quickly and approximately converge the network weights, then switch to a smaller learning rate or larger batch size to "fine-tune" the weights.

The program includes the ability to preprocess training inputs, along with TensorFlow's queue method for importing data. Preprocessing includes the optional addition of random noise to input

examples as they are read in for training. The noise solution added to each spectrum is computed according to a user-supplied, wavelength-dependent template, and it is re-generated every time an example is read in. This allows ANNA to be trained using synthetic spectra while ensuring two things. First, since it is important to ensure that the training data are representative of real data, adding noise when training using synthetic spectra ensures that the network is exposed to the wavelength-dependent response of the spectrograph and prevents over-reliance on small spectral features below the typical spectrum SN (Seghouane et al., 2002). Second, since noise is added on-the-fly, synthetic training examples can be re-used without ANNA "memorizing" the noise associated with each example. Preprocessing in this manner does incur a computational cost, but due to the use of the queue method, preprocessing is assigned its own hardware resources that can execute independently of the weight updating process.

ANNA makes use of TensorFlow's TensorBoard utility to visualize neural network performance, allowing users to monitor how training progresses and visually confirm that things are working as expected. The most relevant TensorBoard feature, the ability to visualize how the cost function changes after each training iteration in near real-time, is shown in Figure 4.6. Conveniently, TensorBoard allows this visualization to be viewed in a standard web browser. The TensorBoard implementation in ANNA also provides visualizations of how each layer responds during training, as well as a detailed block diagram of the entire code.

Once a model is trained, it can be saved in a self-contained, compact, hardware-agnostic form. The upshot of this is that ANNA can be trained on one computer, and then the trained model can simply be transferred to another computer, and used for inference, provided the second machine has ANNA installed. Since inference is significantly faster to execute than training, this means that training could be carried out on a more powerful machine (perhaps GPU-equipped), and then the trained model can be sent to one or more less powerful machines for inference use. Naturally, the saved model is still only applicable to data similar to what was used during training.

After training, ANNA can (optionally) test the trained model if it is supplied with data corresponding to parameterizations known *a priori*. This data can simply be a separate set of synthetic

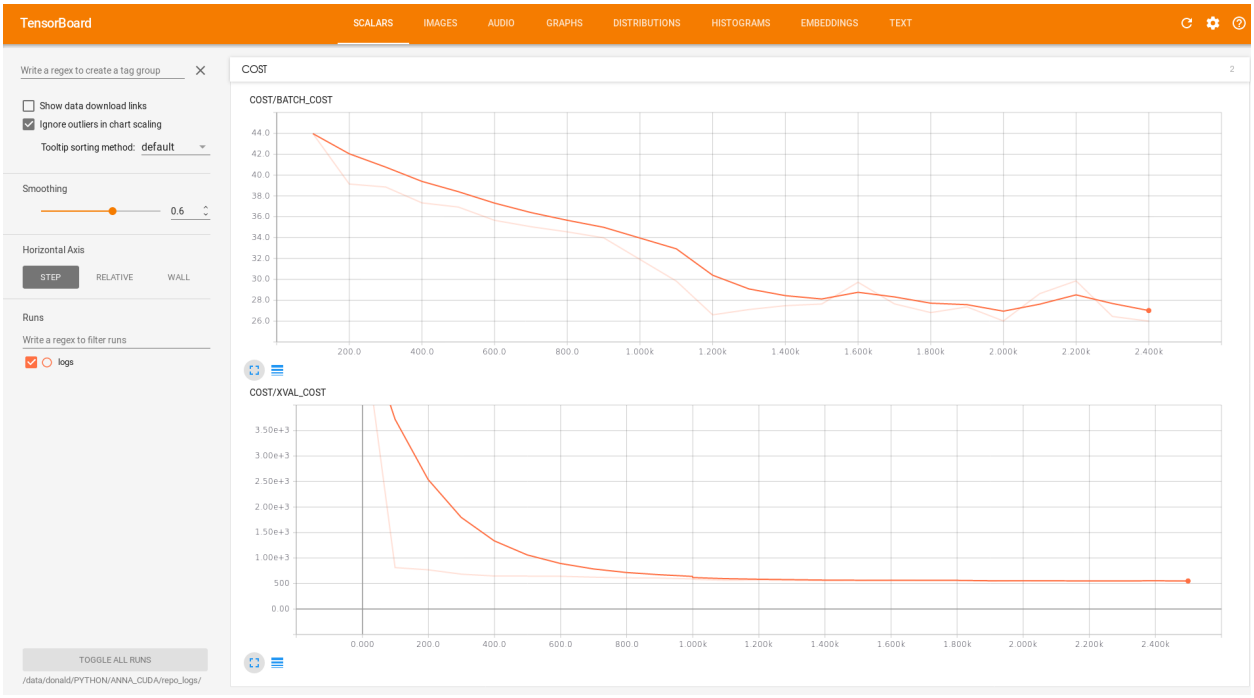

Figure 4.6: Screenshot of the cost graphs in TensorBoard. The upper plot shows the cost associated with each individual batch as a function of weight update iteration, and the bottom plot shows the same except for the cross-validation set.

spectra, if ANNA was trained using synthetic data, in which case the test set can be preprocessed in the same way as the training data. Alternately, the trained model can be tested using real, benchmark spectra (e.g., of the sun) in order to ensure that the training data did not inject any systematics into the ability of the model to infer parameters from real spectra. In either case, ANNA will output a file comparing the parameters it inferred from the test spectra to those provided.

Finally, when running inference, ANNA supports a variety of inputs. For very large spectroscopic samples, the same compact binary form used for training could be supplied. For most use cases, spectra will be in FITS format; ANNA includes a routine to handle multispec FITS files. Simple text file read-in is also supported.

4.3 ANNA Results

4.3.1 Training ANNA

In order to use ANNA to infer stellar parameters from WIYN/Hydra data and verify its capabilities before deployment on real data, including the SMR candidate spectra, a Python-based pipeline to generate synthetic training examples was written. Synthetic training examples were used because the training sample size required to adequately train ANNA far outstrips the capabilities of Hydra; typically a training set of $\sim 100,000+$ is desired, where the examples span a wide range in the parameters to be extracted - temperature, gravity, metallicity, and microturbulent velocity. As a point of comparison, a "large" Hydra project consists of a sample of several hundred spectra (Lee-Brown et al., 2015).

The program selected to generate the model spectra was SPECTRUM (Gray & Corbally, 1994). SPECTRUM is a synthesis program that functions similarly to MOOG's *synth* routine (Sneden, 1973b) - the user provides a one-dimensional, plane-parallel approximation of a stellar atmosphere along with a list of absorption lines and their accompanying atomic parameters, and with these inputs the program solves the stellar radiative transfer equation and returns a continuum-normalized, one-dimensional model spectrum. SPECTRUM was selected for two reasons: it is easily run in batch mode and can be called from within a Python program with minimal effort, and it includes many post-processing capabilities such as treatment of macroturbulent velocity and resolution downsampling.

For the model atmospheres used as inputs to SPECTRUM, the standard ATLAS one-dimensional model atmosphere grid (Kurucz, 2005) is used. The linelist used is the standard output from the VALD database (Kupka et al., 2011) for the wavelength range 6600 Å$<\lambda<$6900 Å, converted to the format SPECTRUM requires. The linelist was mildly tuned using a Hydra solar spectrum as a reference - lines that were present in a synthesized solar spectrum but completely absent from the actual solar spectrum were removed from the linelist (the final linelist used for this project contains $\sim$31,000 lines and so is not reproduced here, but is available upon request).

Around the core functionality provided by SPECTRUM, the ATLAS models, and the VALD linelist, a Python framework was built; it is illustrated in Figure 4.11. The framework generates ready-to-use, continuum-normalized spectra in the following manner. First, appropriate ranges for the various atmospheric parameters are selected. These are then randomly sampled over for a specified number of iterations. At each iteration, the randomly selected parameter values are used to generate a plane-parallel atmospheric model which is then used with SPECTRUM to generated a synthetic, continuum normalized spectrum of very high resolution ($R > 500,000$). Approximately 10^4 such models are generated. These models are then randomly selected (with repetition) for post-processing in order to include various line-broadening effects and radial velocity. The post-processed models are then degraded to the target output resolution ($R \sim 10,000$); approximately 10^5 post-processed models are created. Finally, these models are packaged into the compact, RAM-efficient binary format used by ANNA during training. The process of post-processing from original high-resolution models is carried out twice for each ANNA run discussed later in this chapter - once to generate the large 10^5 member training sample, and once to generate a separate 10^3 member sample to use in a cross-validation capacity during training.

Once the training examples have been generated and packaged into the binary format, they are ready to be used to train ANNA. At this point, the synthetic examples have the appropriate resolution, but are infinite SN and have perfect continuum placement. While such qualities would be quite nice for the real Hydra spectra, reality conspires against the desires of mortals. As discussed in Section 4.2.4, failure to model SN at all would result in ANNA placing too much emphasis on weak features below the noise level in a typical Hydra spectrum. Additionally, Hydra, as with any spectrograph, has a wavelength-dependent response, such that the SN at 6625 Å is only $\sim 65\%$ of the SN at 6750 Å. Omission of this effect would result in ANNA placing too much weight on features in noisy regions of the real spectra. Similarly, modeling continuum placement errors is important as it effectively forces ANNA to rely more on flux values relative to one another, rather than absolute normalized flux values which would be systematically impacted if the continuum was misplaced.

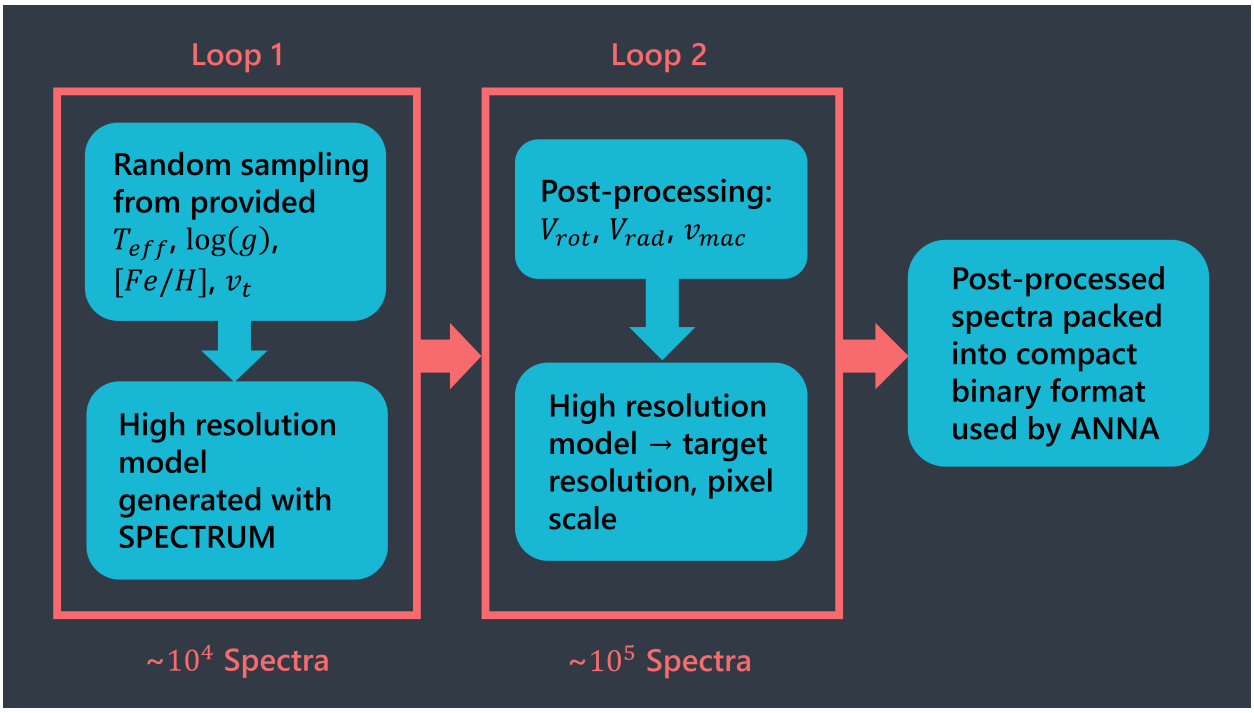

Figure 4.7: The pipeline for building synthetic sets of spectra used to train ANNA.

Thus, the preprocessing functionality of ANNA described in Section 4.2.4 was used during training. For the wavelength-dependent relative SN profile specific to Hydra, ROBOSPECT was used to extract all identifiable lines from a sample of very high resolution (SN>250) solar spectra, leaving only the noise (convolved with any remaining weak lines) behind. The SN at each pixel was then estimated and normalized relative to the SN level near the 6708 Å lithium line. This normalized SN profile is then provided to ANNA during training. Each time an example is read in during training, ANNA randomly assigns the spectrum a peak SN value within a range provided via the main ANNA parameter file, Gaussian noise is added according to the provided SN profile, and the continuum placement is randomly altered as well.

After some testing, it was decided to train ANNA using spectra covering the wavelength range 6625 Å< λ < 6825 Å and enforce the same wavelength range on the input Hydra data. This step was taken after observing that the models and real spectra were particularly deviant from one another in the region of Hα ($\sim$ 6560 Å). On the model side, the profile of the strong hydrogen lines is difficult to reproduce. On the Hydra data side, the spectroscopic calibration process occasionally

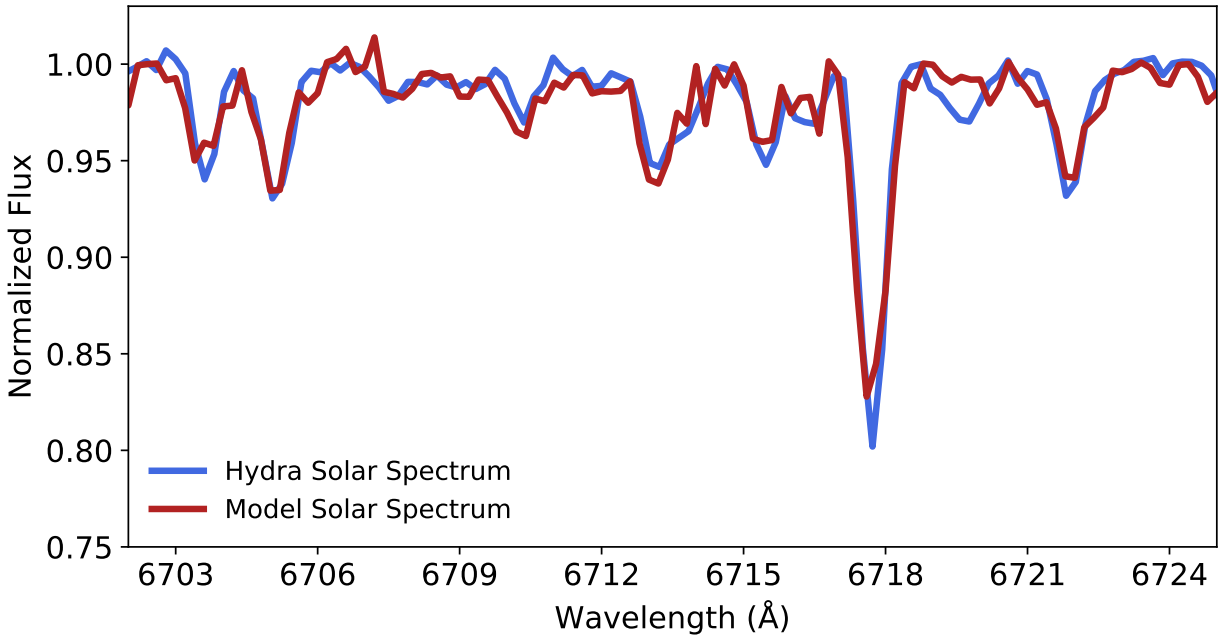

Figure 4.8: A model solar spectrum after postprocessing and uncertainty modeling compared with a real Hydra solar spectrum in the region of the $\sim$ 6615 Å Ca I line.

introduces artifacts (e.g., large spikes) into the region of Hα, and the strong line often drags the continuum placement artificially low.

As an example of the final results from this pipeline, a portion of a synthetic solar spectrum of SN$\sim$ 150 is shown with a real solar spectrum of identical SN in Figure 4.8. The synthetic spectrum is nearly indistinguishable from the actual solar spectrum. Additionally, as expected, the low-SN portions of the synthetic spectrum match the low-SN portions of the solar spectrum.

4.3.2 Testing ANNA

In Figure 4.9, the residuals from comparing the ground-truth T_{eff}, $log(g)$, and [Fe/H] values with those inferred by a trained ANNA model are shown against the values of the ground-truth parameters. For these results, ANNA was trained according to the parameters given in Table 4.1. The synthetic test set, which contained 5000 spectra, was treated in the same way in terms of uncertainty modeling as the training data, and was drawn from the same region of atmospheric parameter space as the training set.

It is immediately clear that ANNA is capable of making reasonable estimations of the three parameters shown in Figure 4.9. The average deviations in T_{eff}, $log(g)$, and [Fe/H] for the test set were 55 K, 0.14 dex, and 0.03 dex, respectively. These errors are well below the ranges the parameters were drawn from, and are comparable to those reported in Li et al. (2017) for SDSS/SEGUE spectra, which are reasonably similar to the Hydra data in terms of total number of pixels.

Of note is that ANNA is able to reliably infer T_{eff}, $log(g)$, and [Fe/H] from a 200 Å-wide spectral region at medium resolution ($\sim$ 1000 pixels). In contrast, it is impossible to infer accurate temperatures or gravities from the same data via an EW-based analysis. This can largely be attributed to the fact that when conducting an EW-based analysis, nearly 90% of the pixel data are discarded in favor of keeping only the most easily measured features; ANNA uses all available data, including heavily blended lines.

As seen in Figure 4.9, there are mild systematic trends in the parameter determinations. Interestingly, testing indicates that increasing the complexity of ANNA (i.e., increasing the number of weights per neural network layer) or training for additional iterations does not completely remove these trends. It may be that the narrow wavelength region causes these trends - variances in T_{eff}, $log(g)$, and [Fe/H] may be difficult to disentangle from one another since they must all be inferred from the relatively small number of features in this wavelength region. Ultimately, however, these trends are well-below the level of scatter; correcting for them does not materially change the results within the uncertainty. However, it is reasonable to expect that if the spectral region were larger or contained more strong features (the $\sim$ 6700 Å region was chosen because it contains the 6708 Å Li line and, in general, the region is relatively sparsely populated by strong features), then the ANNA-inferred parameters would be more precisely determined.

Regarding the relative accuracies of the different inferred parameters, it is apparent that ANNA is best at determining temperature and metallicity. This agrees with expectations; these two parameters have the most influence on the appearance and depth of a spectral feature. Unsurprising as well is that the $log(g)$ determinations are somewhat poorly constrained, with typical errors $\sim$ 10% of the input range. Surface gravity is most easily determined by examining lines corresponding to

the second ionization state for a species (e.g., Fe II); these features are sensitive to the ionization equilibrium which is itself driven by surface gravity (which ultimately depends on the photospheric pressure) (Mortier et al., 2014). The spectral region tested here contains very few second ionization features and those that do exist are very weak, leading to imprecise $log(g)$ estimations.

ANNA's performance as a function of SN compared with the EW-based method outlined in the previous chapter is given in Figure 4.10. For this test, a number of solar models were generated and passed through the SPECTRUM+post-processing+uncertainty modeling pipeline in order to mimic Hydra-produced spectra. These spectra were then analyzed using the standard EW/ROBOSPECT method and five ANNA models. The ANNA models were trained using the parameters given in Table 4.1 except that the training SN was changed each run to match the different solar model SN levels.

Since the EW analysis only produces metallicities, the only point of comparison between the two methods is [Fe/H], but it is striking how performant ANNA is relative to the EW method. Both methods show an expected degradation in accuracy as SN is decreased, but while the EW method becomes essentially useless at low SN, the ANNA results remain surprisingly precise. At high SN, EW measurement results in reliable [Fe/H] determinations, though in relative terms it is still appreciably outperformed by ANNA. Worth noting is that this is the "best case scenario" for the EW-method. The linelist, ROBOSPECT, and MOOG portions of the EW analysis were all tuned using the solar spectrum and thus the accuracies in Figure 4.10 should be taken to be lower limits when considering stars of different temperature, etc. In contrast, the only portion of the ANNA method tuned using the sun was the linelist, and this tuning was relatively mild (see Section 4.3.1).

Figure 4.10 also demonstrates the importance of realistic uncertainty modeling when training ANNA. Fixing the SN during training to a value much higher than that of the input spectra leads poorly determined [Fe/H] values, relative to the models trained with representative SN levels. This is likely due to the higher-SN model placing more weight on weak spectral features which fall below the noise level in lower SN spectra (see previous discussion in Section 4.2.4). On the other hand, a model trained at lower SN will ignore these features when inferring [Fe/H]. Still, it is

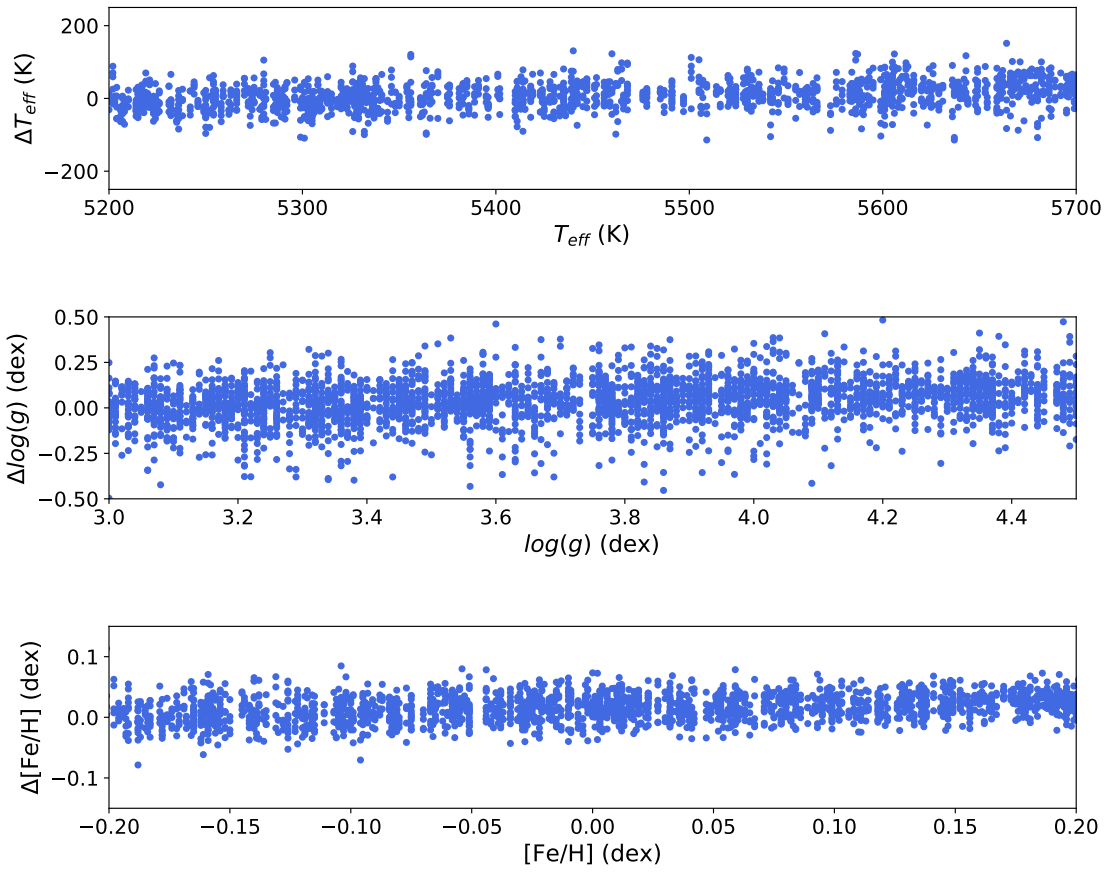

Figure 4.9: Plots of ANNA's post-training performance inferring the three main stellar atmospheric parameters - T_{eff}, $log(g)$, and [Fe/H] - for a synthetic test set. The vertical axis of each plot shows the deviation of the inferred parameter from its true value, and the horizontal axis is the ground-truth parameter value.

Table 4.1. Training Set and ANNA Parameters Used for the ANNA Tests

Parameter	Value/Range
T_{eff} (K)	5200, 6000
$log(g)$ (dex)	3.0, 4.5
[Fe/H] (dex)	-0.2, +0.2
v_t (kms^{-1})	1.0, 2.5
V_{rot} (kms^{-1})	0.0, 50.0
V_{rad} (kms^{-1})	-25.0, 25.0
Resolution (Å)	0.615
SN	150.0, 250.0
ΔC	-0.010, 0.010
w_{fc}	384
I_1	150,000
I_2	50,000
D_1	0.90
D_2	1.0
L_1	5×10^{-5}
L_2	1×10^{-6}

Note. — Abbreviations: SN = signal-to-noise, ΔC = continuum placement error, w_{fc} = outputs from each fully-connected hidden layer, I_1, I_2 = iterations for first and second training stages, D_1, D_2 = node retention probability, L_1, L_2 = learning rate for each stage

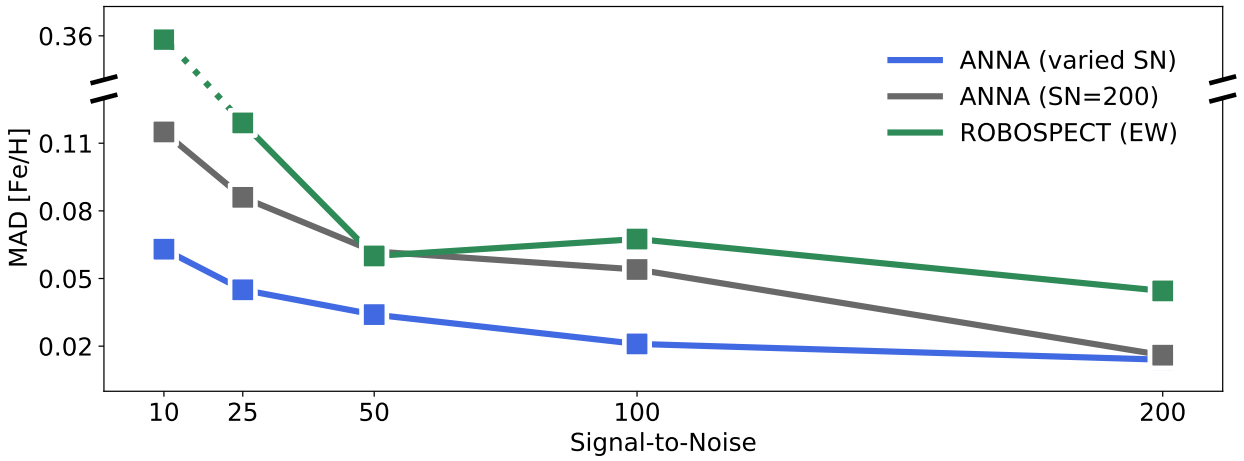

Figure 4.10: Comparison of the precision (as measured using the MAD statistic) of ANNA-derived [Fe/H] and EW (via ROBOSPECT) results as a function of SN for a sample synthetic spectra of varying atmospheric parameters. At all SN, the two ANNA models are super to the EW methods. The ANNA model trained on data with SN matching the test data performs better at all SN than the ANNA model trained using spectra of one SN level.

worth re-emphasizing that even if ANNA were trained using the single SN value, it would still outperform EW analysis at all tested SN.

Figure 4.10 does not show results for template fitting, since it is not used in our research group. However, from Recio-Blanco et al. (2016), which compared the ANN and template fitting approaches for model Gaia spectra, some qualitative predictions can be made. At high SN (>200), it is expected that template fitting would outperform ANNA, though at this SN ANNA, ROBOSPECT, and template fitting are all precise enough that the total error budget will start to be dominated by systematics. At lower SN (<50), however, template fitting becomes increasingly unreliable, as noted in Section 4.1. This is because most template fitting algorithms seek to minimize some goodness-of-fit error (e.g., χ^2; see Valenti & Piskunov, 1996; Blanco-Cuaresma et al., 2014). As the noise level increases, it begins to dominate this metric, and precision decreases. ANNA performs its parameterizations in a fundamentally different manner, and as can be seen in Figure 4.10, is much less impacted by high noise levels.

It is interesting to examine the sources of ANNA's improved inference ability - early studies involving neural networks (e.g., Snider et al., 2001) were only able to achieve temperature and

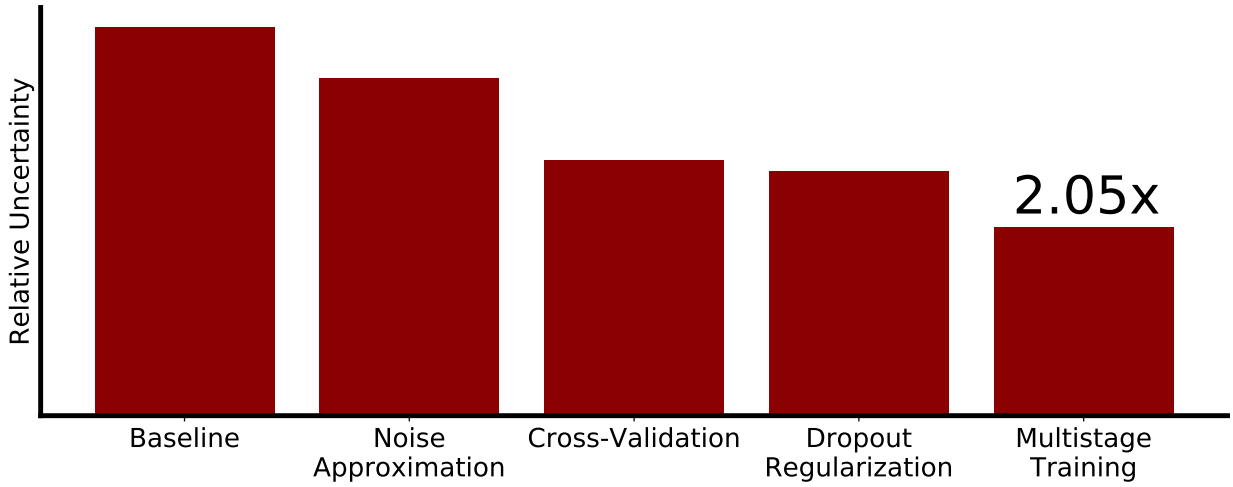

Figure 4.11: Impact of various ANNA features on trained network inference accuracy. The baseline result was set to be a standard fully-connected network of the type described in. e.g., and Snider et al. (2001), Manteiga et al. (2010).

metallicity accuracies of $\sim$ 130 K and $\sim$ 0.20 dex. Which of the optimizations outlined in Section 4.2.3 and Section 4.2.4 contribute most to ANNA's ability to parameterize spectra a factor of $\sim$ 2 more precisely? In Figure 4.11, a neural network of the simple, fully-connected type with basic gradient descent optimization is fixed as the baseline result with relative accuracy fixed to 1.0 - this neural network architecture is representative of early efforts to apply ANNs to stellar parameterization. The subsequent items in the chart show how the addition of various features (in a cumulative sense, i.e., each successive entry contains all the previous optimizations) improve the final parameterization capability, as measured by the minimum quadratic cost associated with a fixed test sample. The largest gains in final parameterization accuracy come from the uncertainty modeling, cross-validation+early stopping, and multistage training, with a lesser benefit from dropout regularization. In particular, the addition of cross-validation provides about 50% of the total improvement by stopping training before the network begins to overfit the training data.

The $\sim 2\times$ improvement in accuracy relative to previous ANN efforts is certainly valuable from a scientific standpoint, but this gain looks relatively modest when compared with the very large decrease in computational expense ANNA provides. In Figure 4.12, the simple fully-connected network architecture is again set to be the baseline result with a relative training time of 1.0. The

minimum test cost associated with the baseline was set to be the target cost for the other entries in the figure, in that the training time for each entry in Figure 4.12 was measured to be the time required to reach this cost.

The gains from CPU parallelization and GPU utilization are hardware-dependent, but the overall picture is clear - for a typical quad-core-equipped desktop (with no GPU), ANNA is at least $5\times$ faster than the baseline result. In particular, the switch to a multilayer CNN architecture instead of a simple fully-connected network halves the training time, and this speedup is hardware-independent. Worth noting is that the switch also greatly decreases the memory footprint - fully-connected layers are significantly more memory-hungry than convolutional layers for a fixed target accuracy.

If a GPU is available, the network training time becomes nearly negligible. For the tests in Figure 4.12, ANNA was trained using an Intel i5 quad-core system (3.1 GHz) with 8 GB of RAM and an Nvidia GTX 1060 GPU. Training using just the CPU, ANNA reached target accuracy in several hours. With the GPU enabled, ANNA finished training in several minutes. These times will vary, of course, depending on the complexity of the input data and specific hardware used, but the $\sim 40\times$ speedup using even this modest hardware means that ANNA can be trained on virtually any computer - in contrast, a cluster of high-performance CPUs was used to train the ANN in Manteiga et al. (2010).

The final test of ANNA is to determine whether or not it can accurately infer parameters from Hydra-produced spectra. Since it has already been demonstrated that ANNA is capable of parameterizing synthetic spectra, this is more a test of how well the atmospheric models, SPECTRUM, post-processing, and uncertainty modeling combine to mimic the Hydra spectra. In particular, it is important to determine that after training using synthetic tests, no serious systematics are present when using the trained model to parameterize real spectra.

To this end, ANNA was tested on a variety of spectra gathered with Hydra. The first test was on a sample of 89 solar spectra of high SN (~ 200) originally gathered for calibration purposes. For these spectra, the trained ANNA model returns an average $T_{\rm eff} = 5780 \pm 77$ K, and average

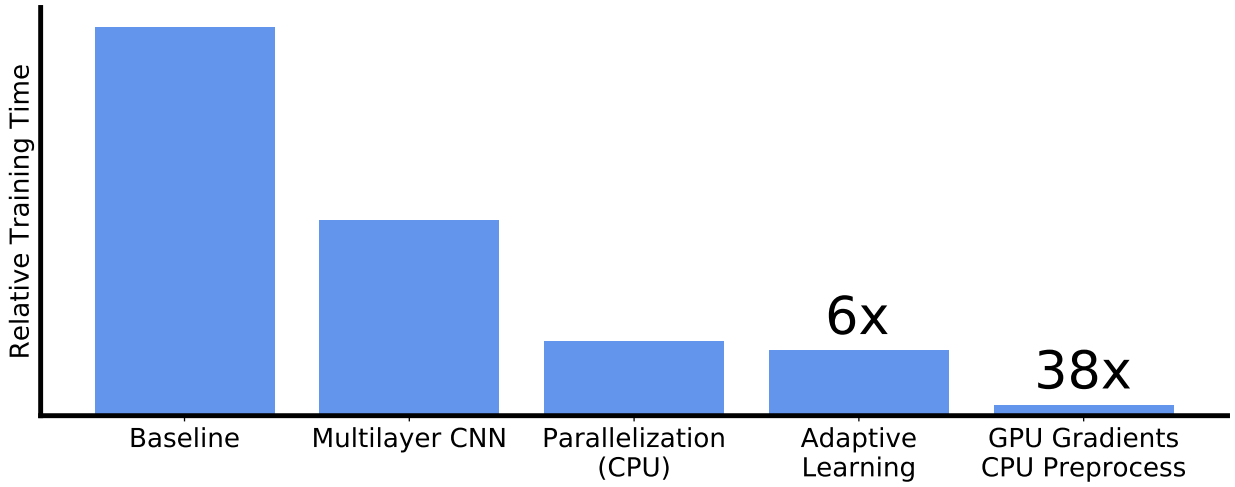

Figure 4.12: Impact of various ANNA features on overall training time.The baseline result was set to be a standard fully-connected network of the type descripted in e.g., and Snider et al. (2001), Manteiga et al. (2010).

[Fe/H] = 0.04 $\pm$0.03 dex. These results indicate that at least for the solar spectrum, ANNA is able to determine temperature and metallicity no worse than it could for model solar spectra.

Unfortunately, the $log(g)$ reported by ANNA for the solar spectrum is systematically high by $\sim$ 0.30 dex. This offset was later found to be approximately constant regardless of whether the input spectra were of a solar-type MS star or evolved giant. Since the effects of surface gravity primarily affect the width of the line profile, this systematic offset indicates that the synthetic training data imperfectly reproduce the broadening effects present in real data and/or the Hydra line-spread function. Microturbulent velocity, V_t and rotational velocity V_{rot} are also profile width sensitive, and as a test ANNA was also used to infer these parameters from the real spectra. As expected, these parameters are also systematically off, confirming the suspicion that the training data do not accurately reproduce the line profiles. Ultimately, the profile-dependent parameters ($log(g)$, V_t, and V_{rot}) produced by ANNA are ignored; these are of secondary interest for the purposes of the studies detailed later in this chapter. However, the temperatures and metallicities appear to be reliable - the assumption is that ANNA essentially does a line-depth ratio analysis to determine these parameters, so profile shapes are unimportant for these parameters.

Several open cluster data sets consisting of stars spanning a range in temperature and evolu-

tionary state were also parameterized with ANNA. For the sample of 37 giants and 184 dwarfs analyzed using the EW-method in Lee-Brown et al. (2015), ANNA returns [Fe/H]=-0.01 $\pm$0.09 and [Fe/H] = -0.06 $\pm$0.08, respectively. These determinations are in agreement with the overall cluster [Fe/H]=-0.03$\pm$0.09 derived in Lee-Brown et al. (2015). For a smaller sample of Hyades spectra, ANNA determines [Fe/H] = 0.17 $\pm$0.05, in excellent agreement with the generally accepted metallicity of [Fe/H] $\sim$ 0.15 (Cummings et al., 2017). These results, taken together, indicate that the ANNA results for the solar spectrum are not a fluke - ANNA is capable of accurately determining [Fe/H] over a wide range in stellar properties after being trained using model spectra. Crucially for the SMR study, this ability extends to high metallicities as evidenced by the Hyades results.

During testing with the open cluster spectra, one (unsurprising) limitation of ANNA was discovered. For stars with surface temperatures greater than 6500 K, ANNA's results become increasingly erratic, both for temperature and metallicity. This is likely because above this temperature, spectroscopic features in the wavelength region of the Hydra Li configuration become very weak and begin to drop below the typical noise level. Thus, ANNA cannot accurately translate these features into parameters.

During the testing of the NGC 6819 data, it was discovered that ANNA's temperatures were $\sim$ 150 K lower than previously published results. That the published temperatures (see, e.g., Lee-Brown et al., 2015) are incorrect is unlikely, as this would require a relatively drastic change to the cluster reddening, which is well-determined (Anthony-Twarog et al., 2014). It is unclear what is driving this systematic offset, as ANNA's temperatures were reliable for the Hyades and solar spectra (as well as NGC 2506, see Section 4.3.3) for the same ANNA model. The most likely answer may lie with how the NGC 6819 spectra were calibrated, though this was not tested. However, the correct metallicity for NGC 6819, despite this offset in temperature, indicates that ANNA's temperature and metallity determinations are relatively decoupled, in that an incorrect temperature determination does not imply a similarly incorrect metallicity estimate. This is useful information, since it means that at least to first order, the determinations of temperature and metallicity are independent, which greatly simplifies the uncertainty estimation and model ensembling technique

used in Section 4.4.

To summarize before discussing ANNA's application to science cases, testing indicates that ANNA meets the design criteria outlined in Section 4.1.1. In particular, ANNA is theoretically capable of reliably determining the main stellar atmospheric parameters - surface temperature, gravity, and metallicity - from spectra covering as little as 200 Å. These determinations are significantly more robust to noise than template fitting or EW measurement. Importantly, ANNA is extremely fast. Training its neural network, which is typically the most computationally challenging part of using an ANN, is completed many times faster than previous ANN efforts. Also demonstrated is the ability to train ANNA using synthetic spectra and subsequently infer accurate parameters from real Hydra spectra. Key to this is careful uncertainty modeling. The major caveat to this approach is that the models must be representative of the actual spectra - during testing it was determined that line profile-dependent parameters such as surface gravity were unable to be reliably inferred by ANNA for the real Hydra spectra due to the particular modeling scheme used. However, ANNA is still capable of determining temperature and metallicity for real spectra up to surface temperatures of 6500 K, above which the ANNA results become unreliable due to the absence of strong spectral features.

4.3.3 Science with ANNA: NGC 2506

NGC 2506 is an old ($\sim$ 2 Gyr, (Salaris et al., 2004)), metal-poor ([Fe/H]$\sim$ -0.4, (Anthony-Twarog et al., 2016)) open cluster located in the direction of the galactic anticenter. Its age falls between the less evolved NGC 7789 ($\sim$ 1.6 Gyr, (Gim et al., 1998)) and the older NGC 6819 ($\sim$2.3 Gyr, (Anthony-Twarog et al., 2014)). Because of its age, it is an ideal test of the increasingly robust correlation between rotational spindown and surface lithium depletion as stars warmer than the Li dip evolve along the subgiant branch (Lee-Brown et al., 2015; Anthony-Twarog et al., 2018, Deliyannis et al., 2018, *in prep*). Thus, NGC 2506 was selected for a detailed study following the same proven method used for NGC 3680 (Anthony-Twarog et al., 2009) and NGC 6819 (Lee-Brown et al., 2015): precision intermediate-band Stromgren photometry anchors the cluster metallicity,

distance, and age, ultimately leading to estimates of the key atmospheric parameters of T_{eff}, $log(g)$, [Fe/H], and V_t, while high-dispersion spectroscopic followup of a large sample of likely members refines the adopted cluster metallicity and allows the Li evolution patterns in the cluster to be accurately traced.

The NGC 2506 study (Anthony-Twarog et al., 2018) presented an ideal opportunity for the first science use of ANNA. At the time ANNA was completed, an EW analysis of approximately ~ 70 spectroscopic targets had just been finished. As in NGC 6819 (Lee-Brown et al., 2015), the NGC 2506 sample contains many stars that have low V_{rot}, the cluster reddening is well-constrained, and the spectra are of good quality, so aside from the metal-poor status of the cluster, the extensively-tested EW-based results should be robust. Therefore, ANNA was used to provide a semi-independent estimate of cluster [Fe/H] as well as independent measures of T_{eff}, and the EW-derived [Fe/H] values served as a meaningful check of these results.

The ANNA model used for NGC 2506 was trained according to the same process outlined in Section 4.3.1: a large number of high-resolution synthetic models were generated, postprocessed, and degraded to the resolution of Hydra. This synthetic training data was then used to train an ANNA model iteratively until the minimum error as measured using a cross-validation sample was reached. During training, the input examples were noised according to the wavelength-dependent response of Hydra, and typical continuum-fitting errors were randomly added. The full set of training parameters is given in Table 4.2.

Once the ANNA model was trained, the Hydra spectra to be parameterized were interpolated onto the same wavelength grid used for training. Of note is that while the pixel scale of this wavelength grid is essentially the same as the spectra from Hydra (0.200 Å/px vs ~ 0.205 Å/px), the resolution of the training data was significantly lower than Hydra's resolution at this wavelength ($R \sim 9,000$ vs. $R \sim 13,000$). The lower training resolution was selected during testing because it minimized the RMS deviation between the synthetic and real spectra. As noted previously, the synthetic spectra imperfectly represent the full suite of broadening effects present in the real data and so ANNA has difficulty determining line profile-dependent parameters such as $log(g)$ after being

Table 4.2. Training Set and ANNA Parameters Used for the NGC 2506 Analysis

Parameter	Value/Range
T_{eff} (K)	3500, 7500
$log(g)$ (dex)	2.0, 4.5
[Fe/H] (dex)	-1.0, +0.00
v_t (kms^{-1})	1.0, 2.5
V_{rot} (kms^{-1})	0.0, 50.0
V_{rad} (kms^{-1})	-10.0, 95.0
Resolution (Å)	0.739
SN	100.0, 250.0
ΔC	-0.010, 0.010
w_{fc}	384
I_1	150,000
I_2	50,000
D_1	0.90
D_2	1.0
L_1	5×10^{-5}
L_2	1×10^{-6}

Note. — Abbreviations: SN = signal-to-noise, ΔC = continuum placement error, w_{fc} = outputs from each fully-connected hidden layer, I_1, I_2 = iterations for first and second training stages, D_1, D_2 = node retention probability, L_1, L_2 = learning rate for each stage

trained using synthetic spectra. Lowering the training resolution approximates these broadening effects. Ultimately, the profile-dependent parameters inferred by ANNA were judged to be unreliable anyway and not used, but testing indicated that ANNA's T_{eff} and [Fe/H] determinations were unaffected by the specific choice of resolution, likely due to the sensitivity of these parameters to line depth ratios, rather than the specific form of the line profiles. Thus, the lower-than-actual resolution was kept.

Before using ANNA to infer NGC 2506 member parameters, the trained model was tested on a set of 89 high SN (~ 200) solar spectra. These test spectra were treated in the same way in terms of calibration and input into ANNA as the NGC 2506 spectra. From these spectra, ANNA infers results that are consistent with the canonical solar values of $T_{eff} = 5770$ K and [Fe/H]$= 0.00$ dex and indicate that, barring any systematic error that has a strong dependence on parameter value, the temperatures and metallicities ANNA infers from the NGC 2506 spectra should be reliable and free of any strong systematics.

The ANNA [Fe/H] results for approximately 60 NGC 2506 targets are shown in Figure 4.13, plotted against the photometric T_{eff} values. Omitted from the plot are several stars with surface temperatures greater than $T_{eff} = 6500$ K and a single star with temperature less than $T_{eff} = 4000$ K; on the hot side ANNA cannot reliably determine temperatures and metallicity due to a lack of strong spectral features, and on the cool side the synthetic models fail to reproduce the complicated line complexes observed in the spectra of cooler stars. The residuals resulting from the comparison of ANNA [Fe/H] values with EW-derived ones is shown in the bottom plot of the figure.

From ANNA, a metallicity estimate for NGC 2506 of [Fe/H]$= -0.27 \pm 0.03$ dex can be derived, where the reported uncertainty is the median absolute deviation statistic. From Figure 4.13, it can be seen that the star-by-star results agree quite well with the EW-derived ones. Indeed, from the EW-analysis, a cluster metallicity of [Fe/H]$= -0.27 \pm 0.07$ dex is calculated - this value is identical to that derived using ANNA but, in-line with the tests presented in Section 4.3.2, is less precise due to larger star-to-star scatter in [Fe/H]. Both spectroscopic results agree quite well with the photometric metallicity of [Fe/H]$= -0.32 \pm 0.03$ dex.

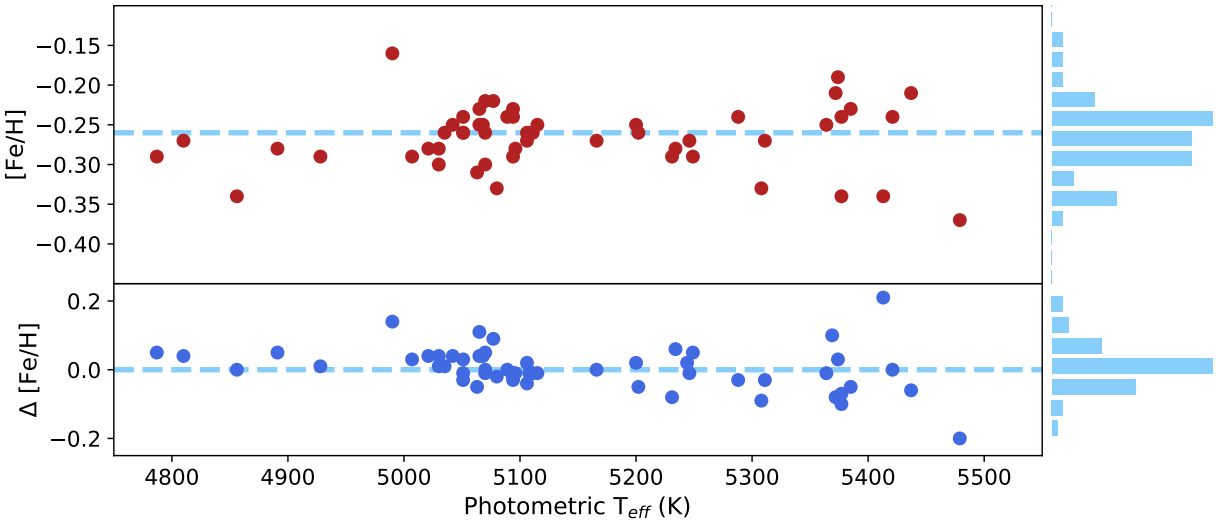

Figure 4.13: Metallicity results from NGC 2506 illustrating the agreement between the ANNA and equivalent-width (EW) analyses. In the top panel, the ANNA [Fe/H] results are plotted against the photometric effective surface temperature. The dashed blue line indicates the median [Fe/H] value of -0.27 dex. Some scatter is observed but as can be seen by the distribution on the right-hand side of the panel the results are well-clustered around the median [Fe/H]. In the bottom panel the differences between the ANNA [Fe/H] values and the EW-derived values are shown. There is no systematic difference between the two sets of measures. Note that stars with temperatures $T_{\rm eff} > 6500$ K are excluded from the plot as they cannot be reliably parameterized by ANNA.

The ANNA temperatures are largely in agreement with the photometric ones, with the exception of the cooler giants with $B-V > 0.7$. For these stars, the temperatures produced by ANNA were judged to be more precise than the ones derived using the color-temperature calibration of Ramírez & Meléndez (2005). Adoption of the ANNA temperatures for these stars and the photometric ones for the hotter dwarfs results in a flat relation between EW-derived [Fe/H] and adopted T_{eff}; if the photometric temperatures alone are used then the giants have systematically high EW-derived temperatures. Again, it is stressed that the EW-based analysis over this narrow wavelength range cannot be used to derive temperatures, so this correction to the photometric results is enabled by ANNA.

4.4 Application of ANNA to the SMR study

It is clear from the sections above that ANNA is capable of accurately parameterizing stellar spectra, and that these parameterizations can be achieved after training with synthetic spectra. Additionally, ANNA comes with several important advantages over the EW-based method: it does not require additional data, it is more robust against the random noise present in a spectrum, and it is capable of deriving more than [Fe/H]. These features along with its demonstrated accuracy make ANNA an ideal tool for analyzing the SMR candidate spectra.

In some ways, the analysis of the SMR spectra can be seen as more challenging than, for example, the NGC 2506 data. In the latter case, the principal parameter of interest was cluster [Fe/H]. Since this is a global quantity, in that every member of an open cluster should have the same metallicity, ensemble statistics could be used to derive a mean [Fe/H] for NGC 2506. Practically speaking, this meant that the accuracy of any one [Fe/H] measurement was of secondary concern, since the large number of spectra analyzed would reduce the statistical error associated with mean [Fe/H] (population statistical error goes as $1/\sqrt{N}$, where N is the sample size). For similar reasons, accurately quantifying the uncertainty associated with any one [Fe/H] measurement was also of lesser importance.

In contrast, each SMR candidate will have a different [Fe/H], and it is critically important to

determine this value as precisely as possible in order to confirm/deny each star's SMR status. In addition to precise [Fe/H] estimates, is also important to accurately determine T_{eff} in order to trace the lithium plateau for the confirmed SMR stars. Thus, the analysis of the SMR stars requires some extra care, relative to the NGC 2506 analysis.

4.4.1 Estimating Uncertainties

Measuring precise [Fe/H] and T_{eff} values necessarily entails an accurate quantification of the uncertainty accompanying each measurement. The total uncertainty δ_T associated with an ANNA parameterization can be represented as a sum of three sources, i.e., $\delta_T = \sqrt{(}\delta_1^2 + \delta_2^2 + \delta_3^2)$. The first component, δ_1, is due to random noise and is a function of the spectrum SN. The second component, δ_2, is introduced by the neural network used to model the mapping between inputs and target outputs; this uncertainty varies as the underlying neural network is changed or retrained. Finally, the last source of uncertainty, δ_3, is due to systematic errors associated with the underlying examples used to train ANNA (or systematics in the way the target outputs were derived from these examples). Since δ_1, δ_2, and δ_3 are independent functions of different variables, their impact on the total uncertainty will go as the square root of the sum of their squares.

For the NGC 2506 study (Section 4.3.3), since the input spectra were of moderate SN, it can be expected that δ_1 is the largest contributor to the uncertainty associated with the ANNA parameterizations. As the NGC 2506 spectra ostensibly all correspond to identical [Fe/H] determinations, a comparison of ANNA-derived [Fe/H] values vs. those given by EW measurement provides an easy way to confirm this. If the scatter in ANNA results is significantly larger than that of the ROBOSPECT results, then the implication is that δ_2 and/or δ_3 are non-negligible. Similarly, if the ANNA-derived [Fe/H] results are significantly deviant from the EW-derived [Fe/H] measures then it is likely some unaccounted-for source of error drives those differences. Since the scatter in ANNA-derived [Fe/H] is in-line with the EW results, and both methods result in an identical cluster metallicity, δ_1 can be assumed to be the dominant source of uncertainty for the NGC 2506 study.

For the SMR study, several important differences from the NGC 2506 study can be identified that complicate the uncertainty estimation. First, the SMR candidate spectra are all of very high SN (generally SN$>$ 200), which reduces δ_1 and increases the relative importance of δ_2 and/or δ_3. Second, the stars do not have identical [Fe/H] values, so parameterizing the scatter in [Fe/H] is not particularly illuminating. Finally, for the SMR stars, ANNA is the primary method of analysis for both [Fe/H] and T_{eff}. The EW results are used as a check for catastrophic parameterizations but are not independent determinations since they rely on ANNA-derived atmospheric parameters during the MOOG analysis, while the photometric temperatures are relatively uncertain and, like the EW-based [Fe/H] results, serve as a check of the ANNA results.

4.4.2 Ensemble modeling

The strategy adopted to address the aforementioned challenges associated with the SMR analysis is *ensemble modeling*. Ensemble modeling is a common technique in ML that first involves the training of several different models. For a given input, the set of outputs returned by the different models are then combined in some fashion to form a final prediction. In a sense, then, ensemble modeling is analogous to a voting system where the outcome is decided by majority vote - the assumption is that the more votes an outcome receives, the more likely it is to be the correct outcome.

There are two key advantages to this approach relevant to the SMR analysis. First and foremost, it has been demonstrated repeatedly that ensemble modeling generally results in more accurate outcome estimates (see, e.g. Ju et al., 2017, and references therein). Intuitively, this makes a great deal of sense; in principle, there should exist an ideal combination of model parameters, input data, training parameters, etc. that result in a perfect mapping between inputs and outputs. In practice, such a combination is very difficult to identify, and any given combination adopted for an ML model will likely inject some model-dependent error into any prediction. The simple workaround to this is to sample from the distribution of all model parameters. The variance in prediction introduced by these varying parameters can then be averaged out.

The second advantage of ensemble modeling is that the uncertainty due to the choice of model can be quantified. As noted in Section 4.4.1, as spectrum SN increases and error due to random noise decreases (δ_1) decreases, then the error due to the adopted model parameters (δ_2) becomes a larger part of the overall error budget. Training multiple models allows for an estimation of this uncertainty via examination of the scatter in output values when identical inputs are used.

To this end, 6 distinct ANNA models were trained for the SMR analysis. The various parameters adopted are given in Table 4.3. Both the input spectroscopic training sample and the neural network hyperparameters were altered between runs. It is also important to note that in addition to the changes listed in Table 4.3, the initial values for the network weights were changed between runs as they were randomly reinitialized.

Once the 6 models were trained, they were tested on a sample of $\sim$50 solar spectra of SN comparable to the SMR candidate spectra. The results of these tests are given in Table 4.4. With the exception of Model 2, the individual models produced reasonable solar T_{eff} and [Fe/H] estimates, slightly biased towards supersolar temperatures and metallicities. The scatter in T_{eff} and [Fe/H] is essentially the same for each model; this is likely the scatter induced by the SN level of the spectra (δ_1).

The crudest way to combine the results from the 6 trained models would be to take a simple arithmetic mean of their outputs, but since the models tend towards supersolar results, this would result in a systematically biased ensemble model. Instead, a slightly more elegant approach was adopted where the models were weighted according their deviation from the canonical solar values (T_{eff} = 5770 K and [Fe/H] = 0.00 dex), i.e., each model's (unnormalized) weight was calculated according to $1/|dev|$. This scheme ensures that the most accurate models are assigned the largest weights. The NGC 2506 analysis demonstrated that ANNA surface temperature and metallicity estimates are largely decoupled from one another, so this weighting was done independently for T_{eff} and [Fe/H]. The weights are given in Table 4.4.

As a check, these derived weights were then used to estimate the weighted solar surface temperature and metallicity. These results are given in Table 4.5. It is immediately apparent that the

Table 4.3. Parameters/Ranges Used for the ANNA Model Ensemble

Parameter	Model 1	2	3	4	5	6
T_{eff} (K)	5250, 6500	"	5000, 6500	"	"	"
$log(g)$ (dex)	3.8, 5.0	"	2.5, 5.0	"	"	"
[Fe/H] (dex)	-0.15, +0.50	"	-0.25, +0.50	"	-0.50, +0.50	"
v_t (kms^{-1})	1.0, 1.5	"	"	"	"	"
V_{rot} (kms^{-1})	0.0, 15.0	"	"	"	"	"
V_{rad} (kms^{-1})	-20.0, 20.0	"	"	"	"	"
Resolution (Å)	0.739	"	"	0.615	"	0.739
SN	150.0, 250.0	"	"	"	"	"
ΔC	-0.010, 0.010	"	"	"	"	"
w_{fc}	512	"	768	"	"	"
I_1	150,000	"	"	"	"	"
I_2	10,000	50,000	"	"	"	"
D_1	0.90	"	"	"	"	"
D_2	0.99	"	1.0	"	"	"
L_1	5×10^{-5}	"	"	"	"	"
L_2	1×10^{-6}	"	"	"	"	"

Note. — When two values are given for each parameter, they indicate the boundaries used when generating the synthetic training data or preprocessing training examples. The " indicate values identical to those used in the model to the immediate left. For all ANNA models, the pixel scale was set to 0.200 Å, but the effective spectroscopic resolution was altered according to the table above. Abbreviations: SN = signal-to-noise, ΔC = continuum placement error, w_{fc} = number of outputs from each fully-connected hidden layer, I_1 and I_2 = number of iterations for first and second training stages, respectively (mini-batch sizes of 100 used throughout), D_1 and D_2 = probability to retain a node in the fully-connected hidden layers during first and second training stages, L_1 and L_2 = learning rate used during first and second training stages.

Table 4.4. ANNA Ensemble Solar Results and Derived Weights

Quantity	Model 1	2	3	4	5	6
T_{eff} (K)	5843	6016	5811	5772	5752	5726
σT_{eff} (K)	43	42	47	46	54	38
[Fe/H] (dex)	0.088	0.170	0.108	-0.030	0.015	0.122
σ[Fe/H] (dex)	0.029	0.032	0.029	0.030	0.034	0.033
Weight T_{eff}	0.027	0.008	0.048	0.768	0.106	0.044
Weight [Fe/H]	0.085	0.044	0.069	0.243	0.499	0.061

Note. — Weights determined by the model's inverse absolute mean deviation from the canonical solar values, T_{eff} = 5770 K, [Fe/H] = 0.00. Because of rounding, the weights for each parameter may not sum to 1.0.

ensemble model results reproduce the canonical solar T_{eff} and [Fe/H] better than any one ANNA model. Provided that any systematic offset in these parameters does not depend strongly on the parameter values themselves, it is also readily apparent that any systematic offset between the ensemble-derived parameters and the true spectroscopic parameters is well below the level of the statistical scatter. Assuming that any systematic difference between the inferred and true parameters for the solar spectra is due to problems with the training data (e.g., the plane-parallel model atmospheres used to generate the synthetic training spectra result in systematically low line depths for a given surface temperature), this means that δ_3 can be neglected in the uncertainty calculations for each SMR star.

To derive the uncertainties associated with the ensemble model, the statistical uncertainties in temperature and metallicity (δ_1) are taken to be the weighted combination of σT_{eff} or σ[Fe/H] values from Table 4.4. Since the tested solar spectra are of comparable SN to the SMR spectra, and the tests in Section 4.3.2 indicate that at the SN typical of the SMR spectra, the uncertainty due to random noise is relatively flat with respect to small changes in SN, this choice for δ_1 should be representative of the statistical uncertainty associated with the SMR spectra. This assumption is

Table 4.5. Weighted Solar Results

Quantity	Value	δ_1	δ_2	δ_T
T_{eff} (K)	5774	46	31	56
[Fe/H] (dex)	0.015	0.032	0.019	0.037

Note. — Total uncertainty calculated by the square root of the sum of squared individual uncertainties.

strengthened by the fact that the SMR spectra are of similar spectral type as the sun, and so should be relatively similar in terms of number and strength of features.

To determine the uncertainty due to the neural network parameters (δ_2), the weighted standard deviation of the different model results is adopted. This weighted standard deviation is calculated according to the standard formula:

$$\sigma_w = \sqrt{\frac{\Sigma w_i (x_i - \bar{x})^2}{\frac{N-1}{N}}} \tag{4.1}$$

where w_i are the weight values given in Table 4.4, x_i is the parameter returned by the i-th model, $\bar{x}$ is the weighted mean value for that parameter considering all 6 models, and N is the number of models (6). This formula is similar to the normal corrected standard deviation except for an adjustment to take into account the weight values.

The results of this error estimation process for the solar spectra are given in Table 4.5. While the random noise in each spectrum still makes up the majority of the overall uncertainty, at the high SN of the solar/SMR spectra, the model-induced uncertainty clearly plays a non-negligible role. The combination of these two sources of uncertainty results in 1σ precisions of ± 56 K and ± 0.037 dex for the solar temperature and metallicity, respectively.

As a final note, for the SMR stars, a portion of the differences between the various ANNA models will be due to the random noise present in each spectrum. Unlike the solar tests discussed above, this noise cannot be averaged out, as only one spectrum exists for each SMR star. Thus, the overall parameter uncertainty attached to each SMR star should be a conservative estimate, as the impact of random noise will be partially double-counted.

4.4.3 SMR candidate results: a first look

The 93 SMR candidate spectra were parameterized using the ensemble of ANNA models and uncertainties estimated according to the procedure outlined above. The results of this process are given in Table 4.6. As a sanity check, the distributions of determined T_{eff} and [Fe/H] were inspected visually; these distributions are given in Figures 4.14 and 4.15. As expected, the distributions largely lie within the original target sample selection bounds (see Chapter 2). Another encouraging sign is that both distributions have shapes consistent with simple expectations resulting from the sample selection process. For example, considering metallicity, the distribution is nearly flat above [Fe/H] = 0.15; this is due to the fact that although the expectation is that super metal-rich stars should be increasingly rare in the solar neighborhood as metallicity increases, stars with high estimated metallicities were prioritized during target selection and should be over-represented in the final sample.

In Figure 4.16, the ensemble-derived metallicities are plotted against surface temperature, with associated uncertainties. It is immediately apparent that the largest outliers tend to have poorly constrained parameters. Visual inspection of the spectra corresponding to these outliers reveals that HD 151482, which has a well-constrained surface temperature of 6670 ± 51 K, actually appears to be an A-star, consistent with the ANNA temperature determination. The lack of strong spectral features for this hotter star likely drives the poorly constrained metallicity estimate. The two stars (HD 196674 and HD 52356) with sub-solar metallicities and well-constrained T_{eff} and [Fe/H] have weaker-lined spectra consistent with a *bona fide* metal-poor status. The other strong outliers, HD 220848, HD 183490, HD 279527, and HD 27831 (see Table 4.6), do not have easily

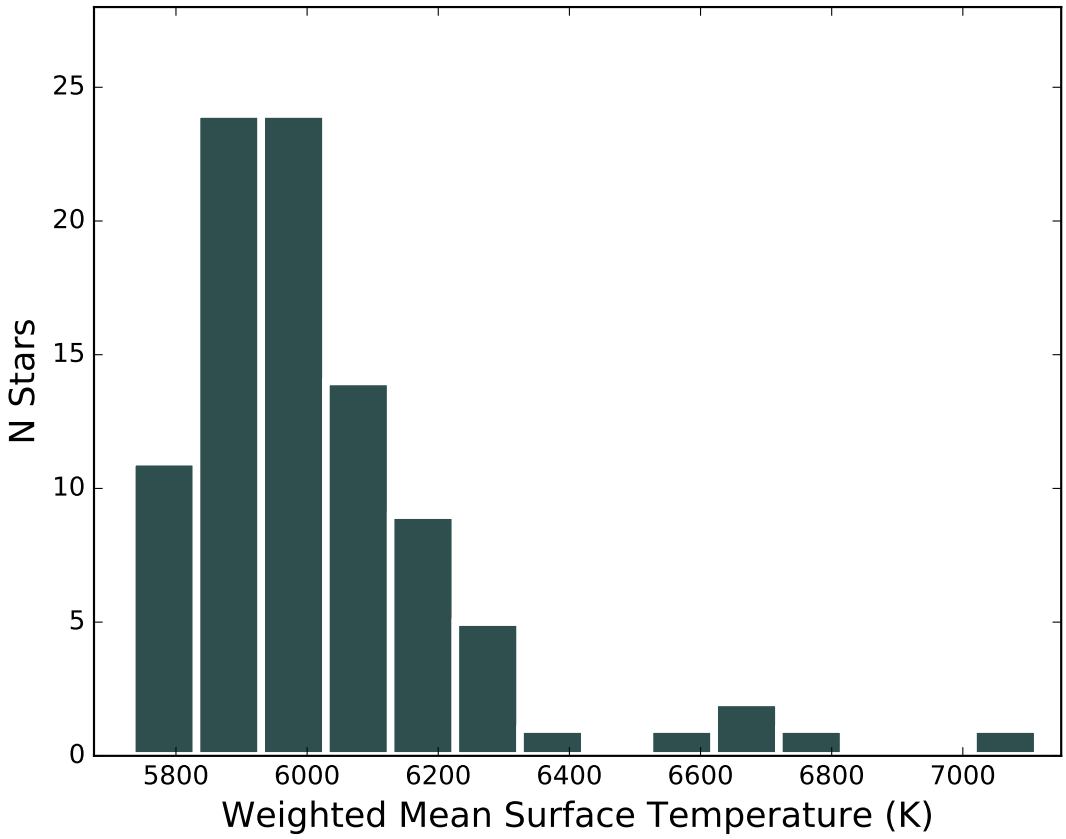

Figure 4.14: Distribution of weighted ANNA T_{eff} values for the SMR candidates.

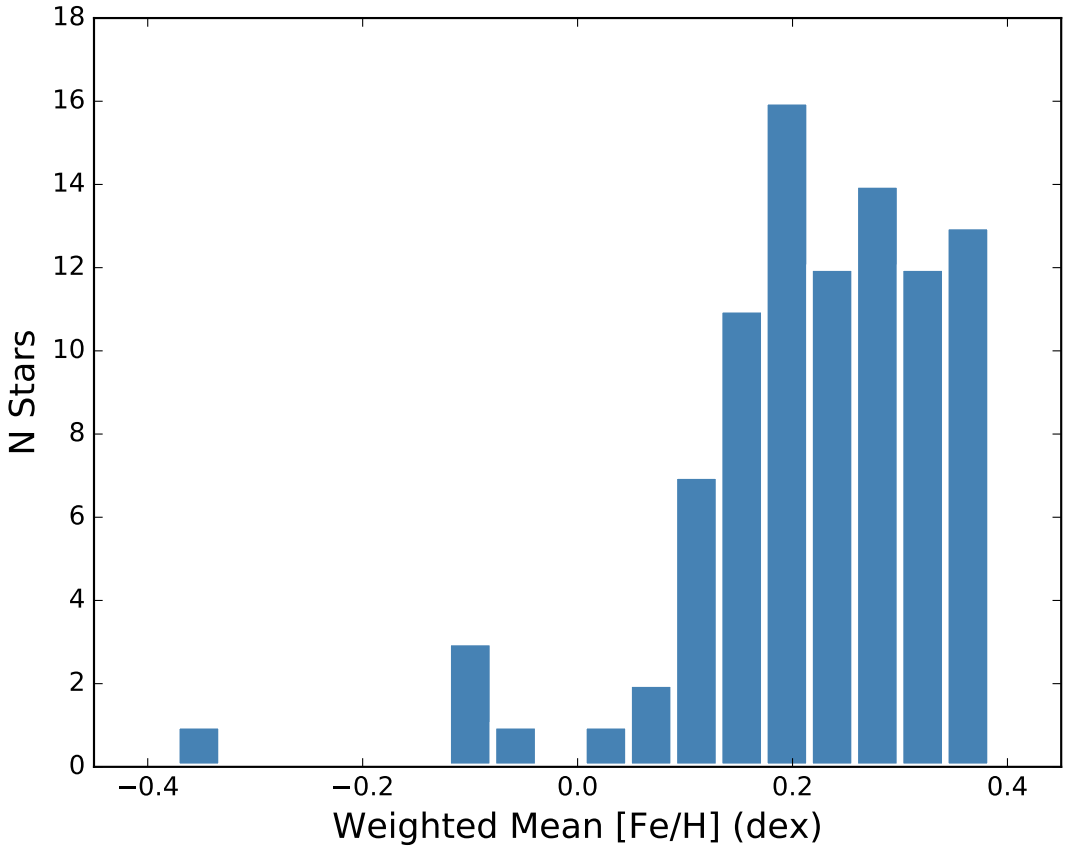

Figure 4.15: Distribution of weighted ANNA [Fe/H] values for the SMR candidates.

identifiable features that would explain their poorly constrained parameterizations. These stars will be discussed further in light of their EW-derived results in the next chapter.

The great majority of SMR candidates have well-constrained parameterizations, as evidenced in Table 4.6 and, as already seen in the temperature and metallicity distributions, occupy a small region in T_{eff}-[Fe/H] space. The median uncertainty is 57 K for surface temperature and 0.071 dex for metallicity, comparable to the uncertainties derived for the solar spectra. Importantly, as seen in Figure 4.17, there is no correlation between temperature and metallicity. The existence of such a correlation would run counter to expectations based on the sample selection and would indicate that ANNA was unable to reliably disentangle the two parameters.

Looking at the uncertainties, and excluding outliers, there is a relation between $\delta_{[Fe/H]}$ and $\delta_{T_{eff}}$. As seen in Figure 4.18, stars with near-median temperature uncertainties also have near-median metallicity uncertainties, and in general these increase with one another, such that stars with temperature uncertainties of $\sim$ 70 K have accompanying metallicity uncertainties of 0.10 dex. Such a correlation is not entirely unexpected, given that both parameters are most strongly a function of relative line strengths; e.g., if the spectrum SN is lower or the lines present are weaker, both temperature and metallicity determinations should suffer. Of course, the nominal SN-induced uncertainty for the SMR stars was fixed based on a sample of solar spectra, but any "extra" uncertainty due to, e.g., lower-than-assumed SN, would still make it into the final uncertainty estimate via the scatter present in the different model results.

In Section 4.3.2 it was asserted that ANNA's temperature and metallicity estimates appear to be independent, and it is stressed here that the SMR results do not contradict this. What is shown here is that the *uncertainties* are correlated, not the parameter determinations themselves. If the data quality is driving the uncertainties, then it is reasonable to expect that both temperature and metallicity determinations would suffer in tandem, even though the parameter determinations are uncorrelated.

As a final, qualitative check of the ANNA parameterizations for the SMR stars, individual spectra were visually examined. In Figure 4.19, a portion of the SMR candidate BD+60 583 spec-

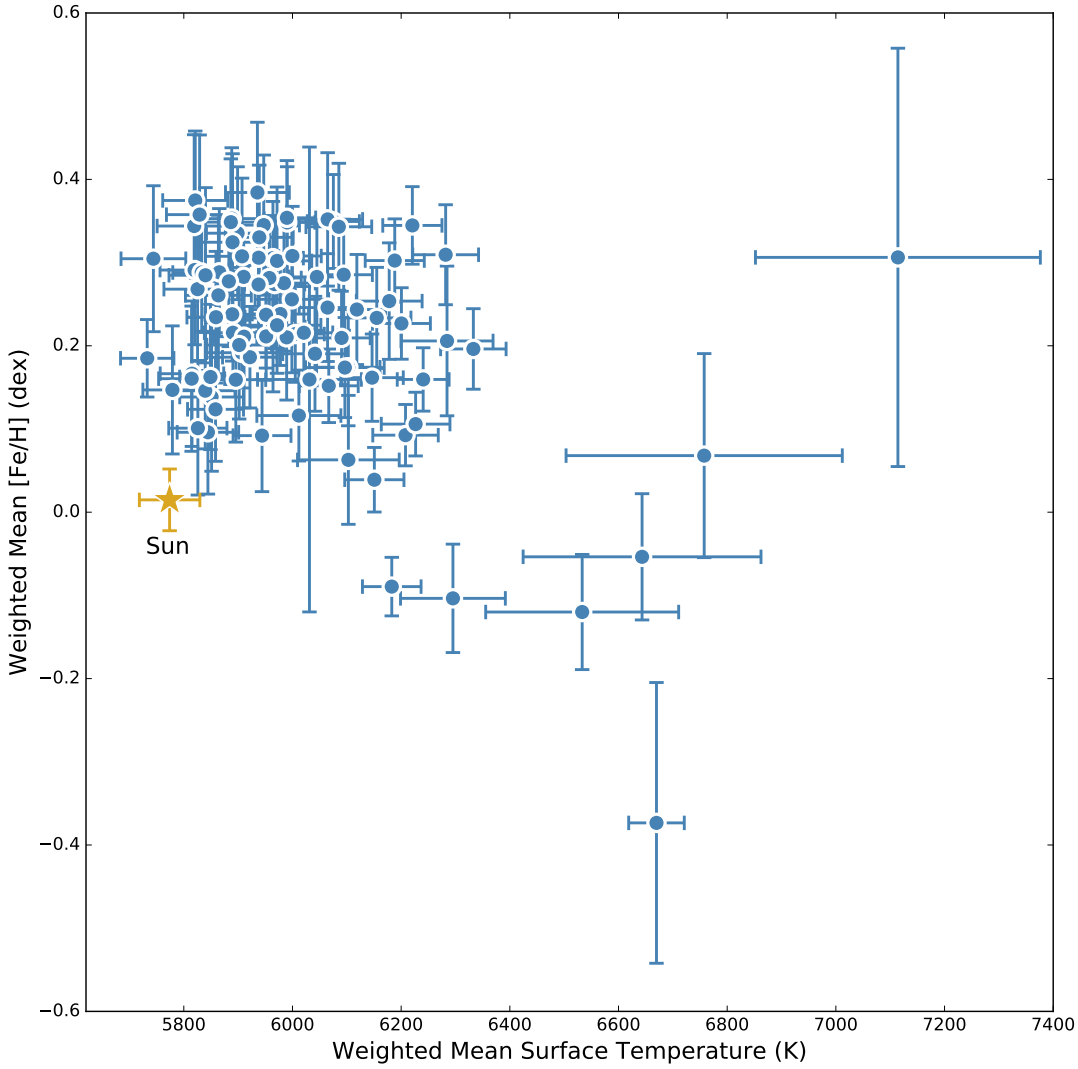

Figure 4.16: The SMR candidate [Fe/H] values plotted against T_{eff}, with associated total uncertainties. The solar values with derived uncertainties are indicated with the star.

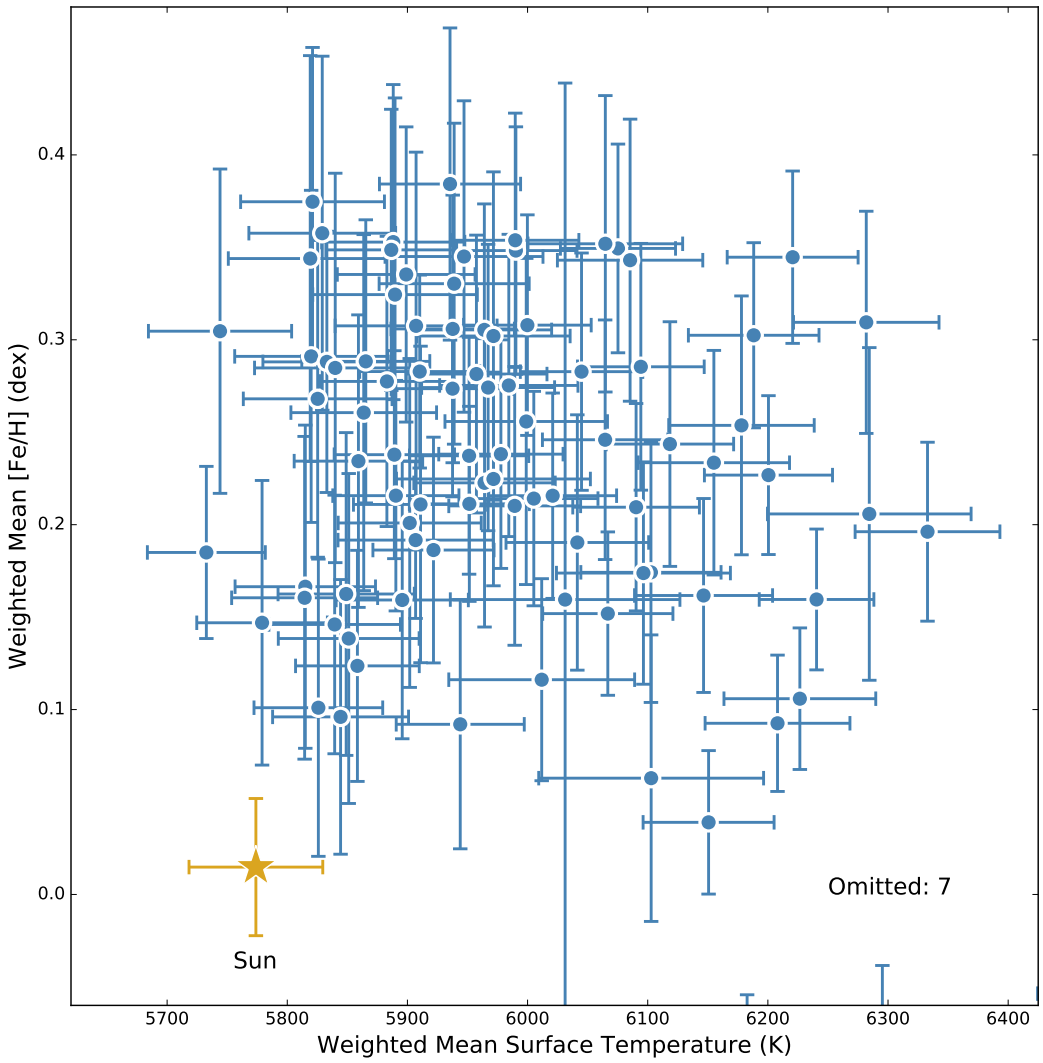

Figure 4.17: Same as Figure 4.16, but with the 7 largest outliers omitted. There is no clear correlation between [Fe/H] and T_{eff}, as expected.

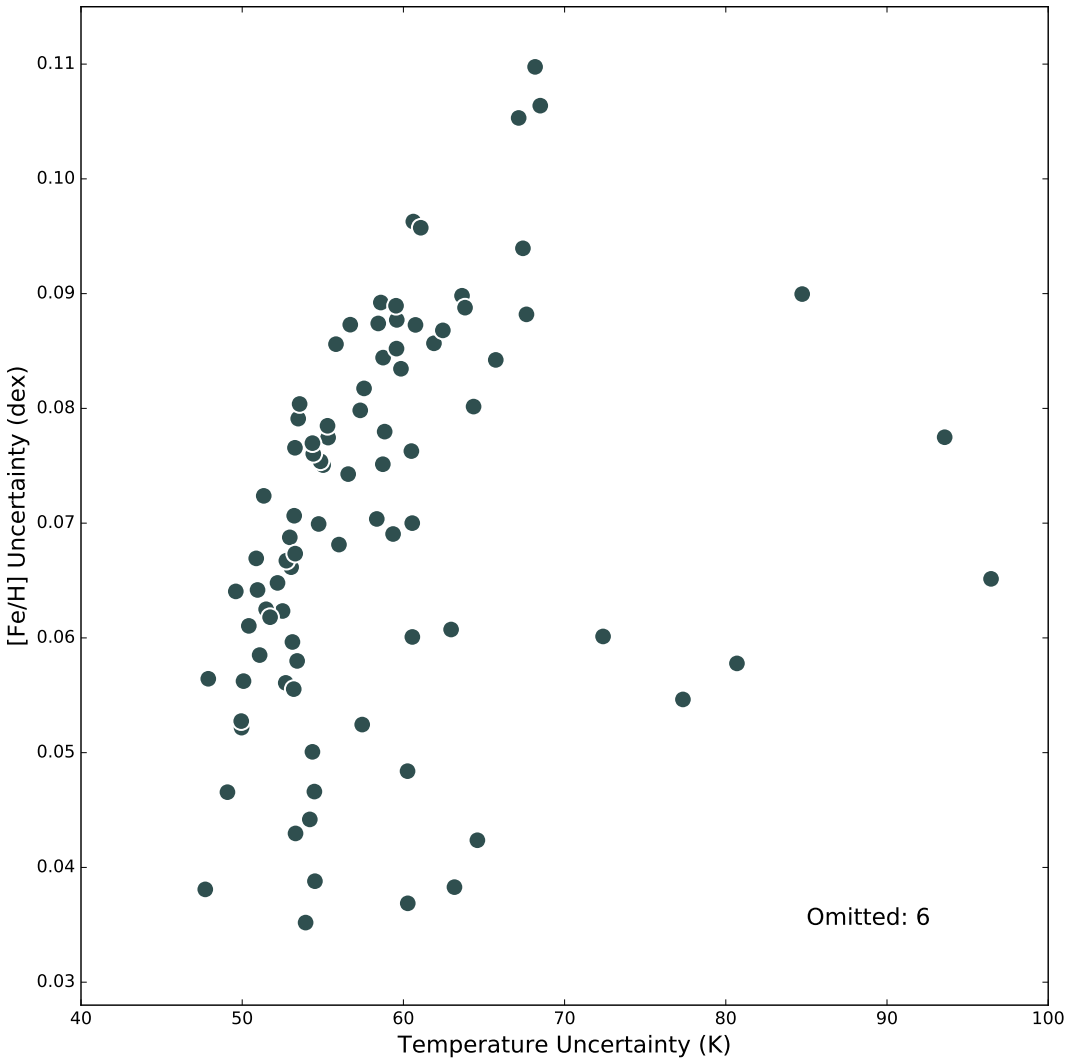

Figure 4.18: Uncertainties in [Fe/H] plotted against uncertainties in T_{eff} for the SMR candidates. The correlation between the two uncertainties is a result of the degeneracy between temperature and metallicity in stellar spectra. 6 strong outliers have been omitted from the plot.

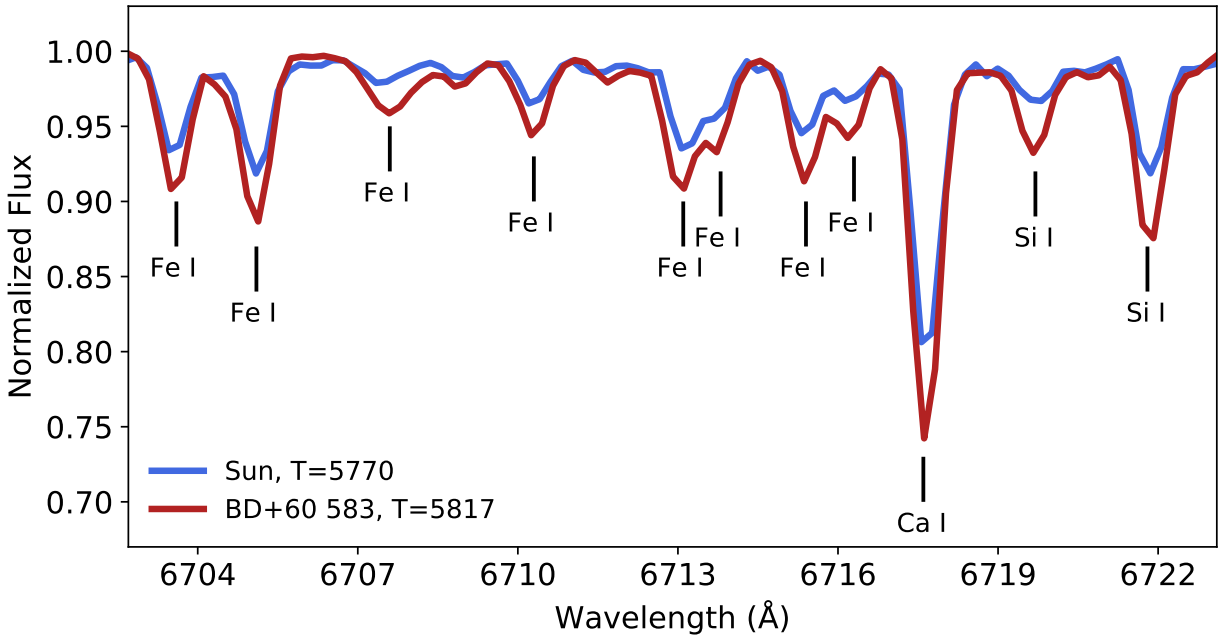

Figure 4.19: An example super-metal-rich (SMR) candidate spectrum snippet (BD+60 583) plotted against the solar spectrum, with spectral features labeled. The temperatures of the two stars are similar, indicating that the difference in line depths is likely due to metallicity effects, with the SMR candidate being higher metallicity. The ANNA ensemble returns T_{eff}=5829±61 K and metallicity [Fe/H]=+0.357±0.096

trum is shown along with the solar spectrum. This star has a literature surface temperature (see Chapter 5) derived from narrow-band photometry of T_{eff}=5817 K and a metallicity estimate of [Fe/H]=+0.465, which means that its spectrum should be similar in appearance to the solar spectrum except the lines should be much deeper due to metallicity effects. Indeed, visual inspection reveals that the SMR candidate spectrum lines are much deeper than in the sun, and the ANNA ensemble returns a temperature of 5829±61 K and metallicity [Fe/H]=+0.357±0.096. A more detailed comparison of the ANNA parameters versus literature results will be presented in the next chapter, but it is heartening to see that the ANNA results are in good qualitiative agreement with what can be seen visually in the SMR candidate spectra.

4.5 Conclusion

In this chapter, I presented a novel tool - ANNA - for parameterizing stellar spectra via a convolutional neural network. ANNA was built to address several shortcomings of standard spectroscopic analysis techniques, namely scalability and resilience to noise. ANNA also simultaneously sought to address some of the issues impacting previous efforts to use neural networks to parameterize spectra, including computational expense and the need for an adequate number of training examples.

To this end, ANNA was developed to be as resource-efficient and use-friendly as possible while simultaneously outperforming the capabilities of standard techniques. The code leverages recent developments in ML and relies heavily on Google's TensorFlow deep learning library to greatly improve computational speed over previous neural network efforts. It also includes diagnostic and visualization features which allow the user to easily monitor the accuracy of the network. A preprocessing pipeline allows for realistic noise modelling and permits the use of synthetic spectra for network training, solving the issue of training sample size.

Tests using synthetic data indicate that at high SN, ANNA is competitive with techniques such as template fitting or EW-based parameter estimation. At low SN, ANNA clearly outperforms these techniques. It is also extremely fast when inferring parameters, operating up to millions of times faster than standard methods. On top of this, it is capable of inferring parameters such as $T_{\rm eff}$ from spectral regions too narrow for techniques such as EW measurement to work.

After training ANNA using synthetic spectra, the surface temperatures and metallicities it infers from real spectra compare favorably with the results from our well-established EW-based method, indicating that training the network using model spectra is a viable strategy. On the other hand, ANNA was unable to accurately reproduce line profile-dependent features such as surface gravity or microturbulent velocity, so if measurements of these parameters are desired, some care must be taken when modeling the spectra used for training. Further testing showed that ANNA is capable of accurately reproducing the [Fe/H] of several open clusters, and returns reasonable $T_{\rm eff}$ estimates for the cluster members. Its ability to infer these parameters only seriously degrades for the feature-

sparse spectra of hotter stars.

For its first science application, ANNA was used to infer T_{eff} and [Fe/H] for ~ 60 members of NGC 2506. These results were compared with precision photometric results as well as EW-derived metallicities. All three, semi-independent analysis methods yielded a cluster metallicity of [Fe/H]~ -0.27 dex, in line with other studies. As with the tests touched on previously, ANNA returned reliable T_{eff} and [Fe/H] estimates for most of the NGC 2506 sample, only failing for stars of temperature $T_{eff} \sim 6500$ and greater.

Finally, ANNA was used as the primary means to derive T_{eff} and [Fe/H] for the 93 SMR candidates. For this analysis, an ensemble of six different ANNA models trained under different conditions were combined in order to arrive at more accurate parameterizations as well as better quantify the uncertainty attached to each parameter determination. Using the solar spectrum as a benchmark, use of the ensemble was shown to improve the quality of the derived parameters, relative to the use of a single ANNA model. For the SMR candidates, the derived parameters appear to be reliable, as the distributions of temperature and metallicity mirror the original sample selection criteria, and are uncorrelated with one another as expected. Typical (conservative) uncertainties in T_{eff} and [Fe/H] were found to be 57 K and 0.071 dex, respectively.

The next chapter will cover the final selection of the truly SMR sample, and detail the measurement of surface Li for these stars. The version of ANNA used for this work, as well as the most recent version of the code, can be found on my Github at www.github.com/dleebrown/ANNA. A user manual and working example are also included in the repository.

Table 4.6. ANNA SMR Results

ID	T_{eff} (K)	σT_{eff}	[Fe/H] (dex)	σ[Fe/H]
BD+39 2711	5821	60	0.375	0.083
BD+60 583	5829	61	0.358	0.096
HD 100069	5814	61	0.160	0.087
HD 10211	5890	53	0.216	0.062
HD 102196	6103	58	0.174	0.070
HD 103012A	5911	56	0.211	0.086
HD 103012B	5999	68	0.256	0.088
HD 103459	5825	62	0.268	0.086
HD 104588	5744	60	0.305	0.088
HD 105279	5865	53	0.288	0.077
HD 106423	6065	64	0.352	0.080
HD 107087	6146	57	0.162	0.052
HD 107211	5887	54	0.349	0.076
HD 10766	6282	61	0.309	0.060
HD 109929	6075	48	0.349	0.056
HD 110010	5990	53	0.354	0.069
HD 11170	6000	53	0.308	0.060
HD 112001	5896	55	0.159	0.075
HD 113938	5964	56	0.305	0.068
HD 115954	5820	64	0.291	0.090
HD 11638	5939	62	0.330	0.087
HD 117243	5967	55	0.274	0.077
HD 117302	5902	60	0.201	0.089
HD 119825	6041	59	0.190	0.069
HD 124102	5815	58	0.166	0.087
HD 126530	5938	51	0.306	0.072
HD 129171	5839	55	0.146	0.070
HD 130087	5984	58	0.275	0.082
HD 13345	6178	61	0.254	0.070
HD 13773	6188	54	0.302	0.050
HD 1402	6208	60	0.093	0.037
HD 14348	6118	53	0.244	0.066
HD 144302	5907	65	0.192	0.042
HD 147062	6103	94	0.063	0.077

Note. — Results are from the weighted ensemble of ANNA models discussed in Section 4.4.2.

Table 4.7. ANNA SMR Results (continued I)

ID	T_{eff} (K)	σT_{eff}	[Fe/H] (dex)	σ[Fe/H]
HD 149026	6045	51	0.283	0.064
HD 1497	5826	54	0.101	0.080
HD 151482	6670	51	-0.373	0.169
HD 154144	6005	53	0.214	0.058
HD 156016	5910	50	0.283	0.052
HD 15866	5972	81	0.225	0.058
HD 16090	6021	53	0.216	0.056
HD 177985	5951	50	0.237	0.064
HD 180318	5938	51	0.274	0.059
HD 180502	5864	61	0.261	0.096
HD 180556	6067	54	0.152	0.044
HD 183490	6643	219	-0.054	0.076
HD 184295	5733	49	0.185	0.047
HD 192343	5840	67	0.285	0.105
HD 194510	6241	48	0.160	0.038
HD 196199	6333	60	0.196	0.048
HD 196674	6295	96	-0.104	0.065
HD 198483	6155	63	0.234	0.061
HD 199167	6031	96	0.159	0.279
HD 19961	5888	60	0.353	0.085
HD 199744	6284	85	0.206	0.090
HD 201529	5858	51	0.124	0.062
HD 203557	5990	51	0.348	0.067
HD 205583	6151	55	0.039	0.039
HD 207418	6227	63	0.106	0.038
HD 21313	5922	50	0.186	0.061
HD 216027	5779	54	0.147	0.077
HD 218354	5859	53	0.234	0.079
HD 220284	5849	57	0.163	0.087
HD 220848	6533	178	-0.120	0.069
HD 224543	6012	77	0.116	0.055
HD 224882	5935	59	0.384	0.084
HD 2330	5989	55	0.210	0.075
HD 238069	5883	55	0.277	0.078

Note. — Results are from the weighted ensemble of ANNA models discussed in Section 4.4.2.

Table 4.8. ANNA SMR Results (continued II)

ID	T_{eff} (K)	σT_{eff}	[Fe/H] (dex)	σ[Fe/H]
HD 2564	6221	54	0.345	0.047
HD 26441	5957	59	0.281	0.075
HD 27533	5952	50	0.211	0.053
HD 27831	7114	262	0.306	0.251
HD 279527	6758	254	0.068	0.123
HD 30769	6065	52	0.246	0.065
HD 3592	5833	53	0.288	0.071
HD 449	5947	66	0.345	0.084
HD 4649	5851	59	0.138	0.089
HD 47155	6200	53	0.227	0.043
HD 47218	5890	68	0.324	0.106
HD 51356	6183	54	-0.089	0.035
HD 7355	6085	60	0.343	0.076
HD 76617	6090	53	0.209	0.056
HD 78277	5899	57	0.335	0.080
HD 78609	5844	57	0.096	0.074
HD 82410	5964	59	0.223	0.078
HD 8328	5819	68	0.344	0.110
HD 83616	5978	52	0.238	0.062
HD 8446	5907	67	0.308	0.094
HD 91987	5944	53	0.092	0.067
HD 91988	6096	72	0.174	0.060
HD 94861	6094	53	0.285	0.067
HD 97140	5889	50	0.238	0.056
HD 9729	5972	64	0.302	0.089

Note. — Results are from the weighted ensemble of ANNA models discussed in Section 4.4.2.

Chapter 5

The SMR Sample and Li Measurements

5.1 Testing ANNA's Results and Selecting the SMR Sample

Armed with the two semi-independent determinations of [Fe/H] detailed in Chapter 3 and Chapter 4, the final SMR sample was selected. This selection process first involved comparison of the ANNA and ROBOSPECT [Fe/H] results with each other and available determinations from the literature. This was followed by a series of quality cuts to exclude, e.g., stars with poorly constrained parameterizations.

5.1.1 ANNA Temperatures

First, the ANNA temperature determinations were compared with available values from the catalogs the SMR candidates were selected from. As detailed in Chapter 4, ANNA's temperatures are apparently relatively independent from its [Fe/H] determinations (unlike other analysis methods). However, understanding any systematics in temperature is critically important because the Li measurement process detailed later in this chapter is temperature-sensitive and in particular, systematics in the temperatures can bias A(Li) results. Note that there were no temperatures derived from EWs for this study, so only the ANNA temperatures can be compared with the literature.

Every star in the SMR candidate sample has a temperature value from one of the three parent catalogs (Geneva-Copenhagen, N2K, and Hypatia), and these values were adopted in the following manner. If a star had a spectroscopic temperature listed in the Hypatia catalog, this was used. If no Hypatia temperature was available, then the N2K temperature, if available, was adopted; otherwise the Geneva-Copenhagen temperature was used. This process ensured that spectroscopic

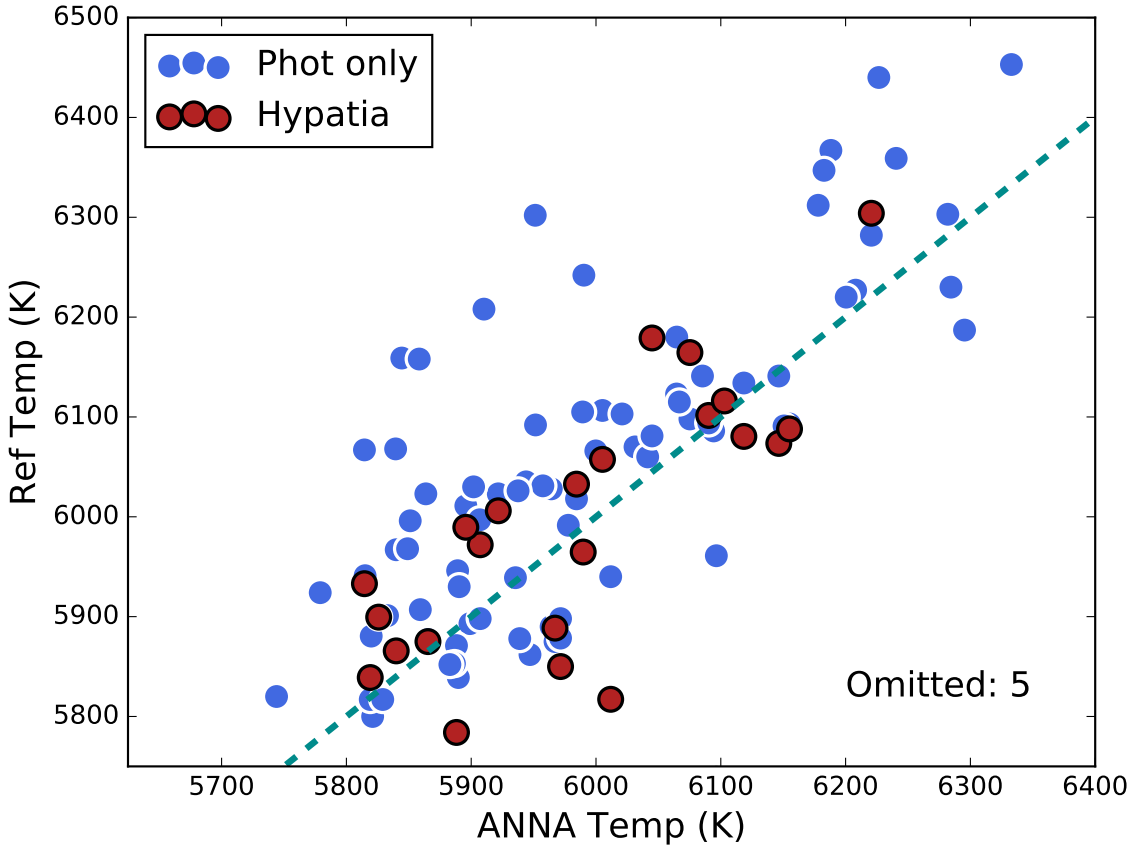

Figure 5.1: Comparison of ANNA-derived surface temperatures (x-axis) and those from a variety of literature studies (y-axis). Literature temperatures derived from photometry (either the Geneva-Copenhagen survey (Casagrande et al., 2011) or the N2K catalog (Robinson et al., 2007)) are plotted as blue circles, while spectroscopic temperatures from the Hypatia catalog (Hinkel et al., 2014) are represented by solid-outlined red circles. The dotted line indicates the line of 1:1 correspondence.

temperatures were preferred over photometric ones.

A comparison of the ANNA temperatures with the adopted literature values can be found in Figure 5.1. Here, the stars have been subdivided into two categories - spectroscopic and photometric. The N2K temperatures, while based on low-resolution spectroscopic data, have been included in the photometric sample due to the use of Lick indices as temperature indicators (Robinson et al., 2007).

In general, the ANNA and literature values agree quite well. 26 SMR candidates have Hypatia temperatures; omitting two stars with extremely discrepant temperatures ($\Delta T \sim 400$ K), the average

deviation between the ANNA and Hypatia temperatures (in the sense ANNA - Hypatia) is 10 K $\pm$85 K. Given that the average temperature uncertainty for the ANNA values alone is 57 K, the scatter about this average deviation is perfectly reasonable. Thus, it can be concluded that the Hypatia and ANNA temperatures are in agreement with one another within their uncertainties.

Comparing the ANNA and photometric temperatures, and again excluding the contribution from large outliers, the ANNA temperatures are on average 76 K lower than the photometric ones. The scatter about this mean offset (again, ANNA - photometric) is 126 K, which is reasonable given that the photometric temperatures come from two different data sets and may be less well-determined than the spectroscopic ones. Examining these results further, the 76 K deviation is largely due to the Geneva-Copenhagen temperatures. From Figure 5.1, it can be seen that the deviation is constant across the (admittedly narrow) temperature range, suggesting that the offset is due to a zeropoint difference. The N2K temperatures largely agree with the ANNA temperatures.

5.1.2 ANNA and EW Metallicities

Both ANNA and the EW measurements provide an estimate of [Fe/H], and these can be compared with each other. It should be noted before discussing the results that the two methods are only semi-independent, since the EW determinations relied on ANNA temperatures and initial metallicity estimates, and both used the same photospheric models (ANNA for training, and the EW method during the MOOG analysis). The EW [Fe/H] measurements as a function of ANNA [Fe/H] are shown in Figure 5.2.

It is apparent that there is a zeropoint offset in [Fe/H] when comparing the two methods, with the ANNA metallicities being on average 0.05 dex higher than the EW ones. The scatter about this mean offset is $\pm$0.05, well within the expected range, given that the uncertainty on any one [Fe/H] value for either method is $\sim$ 0.07 dex. Ultimately, the specific source of this offset was not pursued further as it is actually relatively small; typically systematics due to calibrations or differences in measurement technique result in offsets in [Fe/H] on the order of $\pm$0.1 dex (see, e.g., Lee-Brown et al., 2015; Hinkel et al., 2016). The more important takeaway from the ANNA/EW comparison

is that aside from the zeropoint offset, the two methods agree extremely well with one another - a metal-rich star determination from one method is echoed by the other.

The ANNA [Fe/H] results can also be compared with the catalog [Fe/H] measurements. The results of this comparison are given in Figure 5.3, where the stars have again been subdivided into a sample with spectroscopic [Fe/H] determinations from Hypatia and a sample with photometric [Fe/H] estimates. Slightly more stars - 34, or 33 after excluding an outlier - have spectroscopic [Fe/H] determinations than have spectroscopic temperatures.

Figure 5.3 perfectly demonstrates why the systematic offset between the ANNA and EW [Fe/H] temperatures was deemed acceptable! Comparing the ANNA and Hypatia [Fe/H] values, the ANNA values are on average 0.05 dex *lower* than the Hypatia ones. As before, this is a constant offset with respect to [Fe/H], indicating a zeropoint difference due to systematics. Aside from this offset, the Hypatia and ANNA results are consistent with their respective uncertainties, with the scatter about the mean deviation determined to be ± 0.06 dex.

Comparing the ANNA [Fe/H] with photometric values reveals that the photometric [Fe/H] are even more discrepant - the ANNA values are on average ~ 0.08 dex lower than the photometric ones. However, the difference between ANNA and the photometric results can again be traced to the Geneva-Copenhagen metallicity estimates, and explained according to the temperature offset between ANNA and the GC catalog. In Lee-Brown et al. (2015) it was shown that for main sequence stars, a temperature offset of 100 K would systematically bias determined [Fe/H] by ~ 0.06 dex. This is because temperature and metallicity effects are degenerate; spectral features can be made deeper by either lowering temperature or increasing metallicity, either of which would increase the EW. Thus, the ~ 76 K hotter Geneva-Copenhagen temperatures imply that the GC metallicities should be ~ 0.04 higher to compensate for this offset. This is in-line with the offset in [Fe/H] relative to the spectroscopic results. Aside from the zeropoint offset between ANNA and the photometric [Fe/H], the scatter in average deviation is ~ 0.1 dex, in-line with expectations stemming from the uncertainties.

The EW and literature [Fe/H] values are both plotted as a function of ANNA [Fe/H] in Fig-

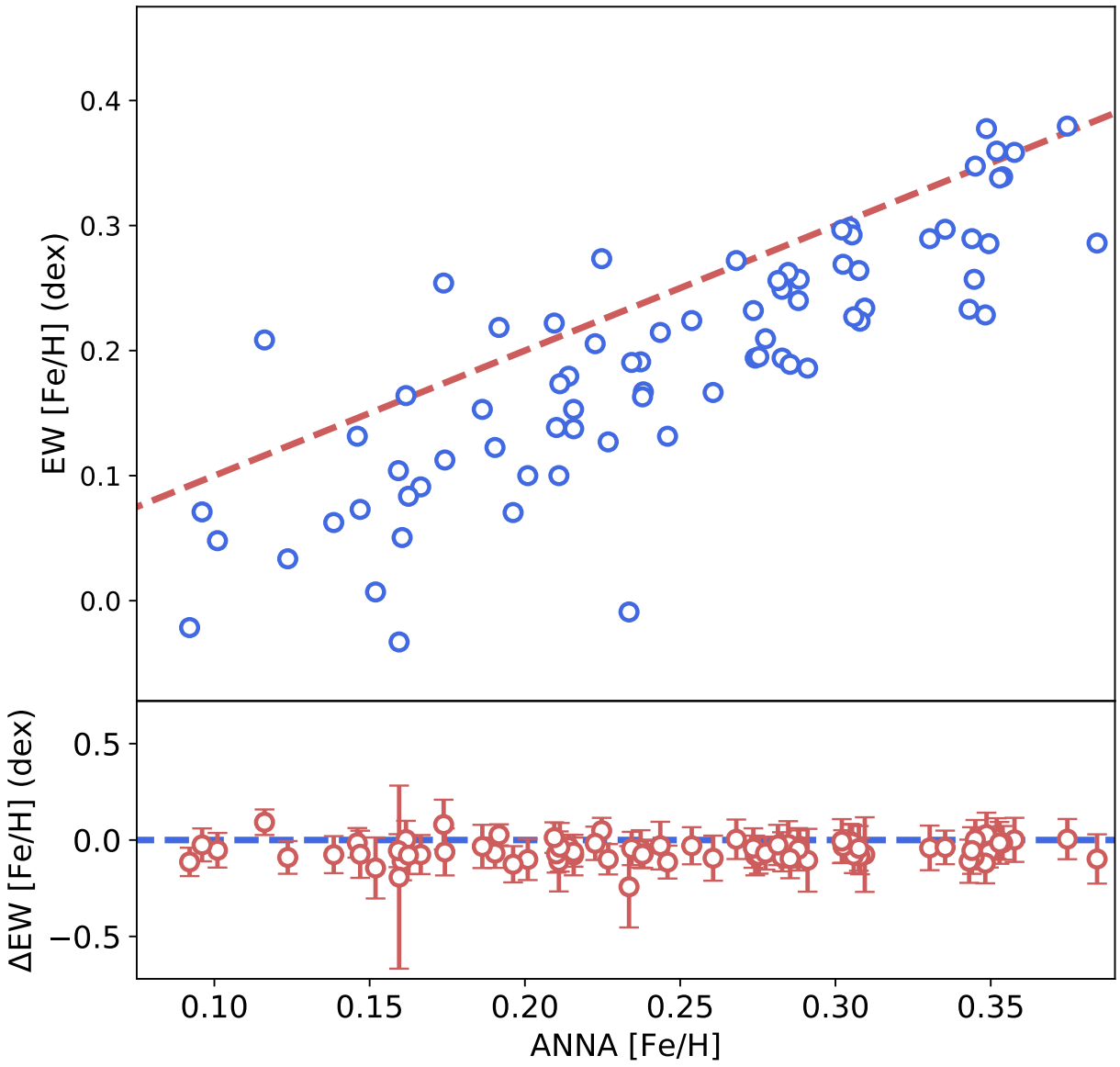

Figure 5.2: Comparison of ANNA and EW [Fe/H] estimates. In the top panel, the dotted line indicates the line of 1:1 correspondence. The bottom panel shows the residuals after computing $[\mathrm{Fe/H}]_{EW} - [\mathrm{Fe/H}]_{ANNA}$. The dashed blue line indicates a residual of 0.

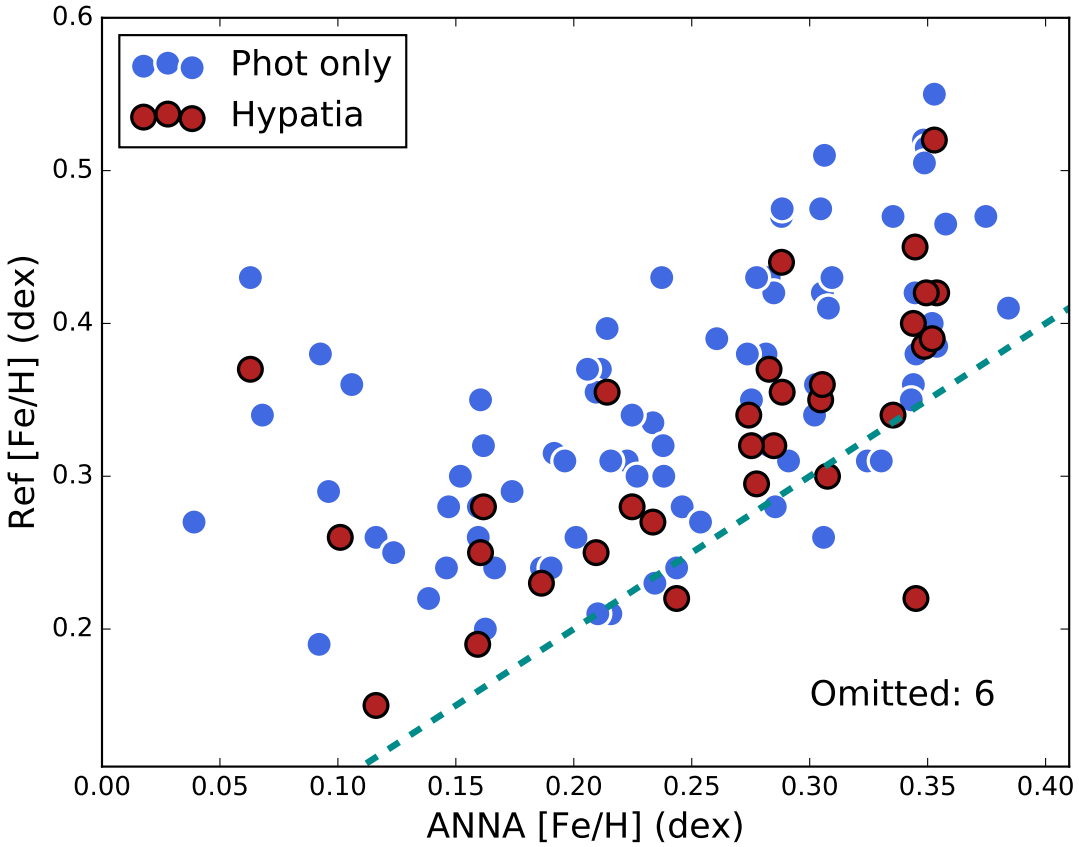

Figure 5.3: Comparison of ANNA-derived [Fe/H] estimates (x-axis) and those from a variety of literature studies (y-axis). The color codes and line are the same as in Figure 5.1.

ure 5.4. Comparing the four different metallicity determinations - ANNA, photometric, EW, and Hypatia - it is clear that all are correlated with one another. The scatter when comparing the different results is substantial due to the different [Fe/H] zeropoints, but again it is noted that if the Geneva-Copenhagen and spectroscopic temperatures were placed on the same scale, the Geneva-Copenhagen [Fe/H] values would likely be consistent with the Hypatia ones. Once this was done, the ANNA [Fe/H] results would essentially lie at the midpoint between the Hypatia/corrected GC values and the EW-derived ones, and on an individual star basis would be statistically consistent with either estimate.

To briefly summarize, the ANNA and literature temperatures and ANNA, EW, and literature metallicities agree with one another, aside from some minor systematic offsets. These results first show that ANNA's temperature determinations are certainly good enough to map out the Li plateau. Secondly, and more importantly, the widespread agreement between the different [Fe/H] determinations indicates that the truly SMR stars in the sample can be robustly identified.

5.1.3 The Final SMR Sample

With ANNA's temperatures and metallicities verified, the final SMR sample was selected. This process first involved excluding problematic stars - e.g., binaries - via visual inspection of the spectra or through their ANNA parameterizations. Additionally, stars with severely discrepant ANNA and EW [Fe/H] ($> 3\sigma$) were also excluded. The stars excluded and the reasons for exclusion were:

1. HD 110010: Classified as a spectroscopic binary (see Frankowski et al. (2007))
2. HD 126530: Visually identified as a binary.
3. HD 1402: Visually identified as a binary.
4. HD 183490: Discrepant ANNA and EW [Fe/H].
5. HD 199167: Discrepant ANNA and EW [Fe/H].
6. HD 199744: Visually identified as a binary.

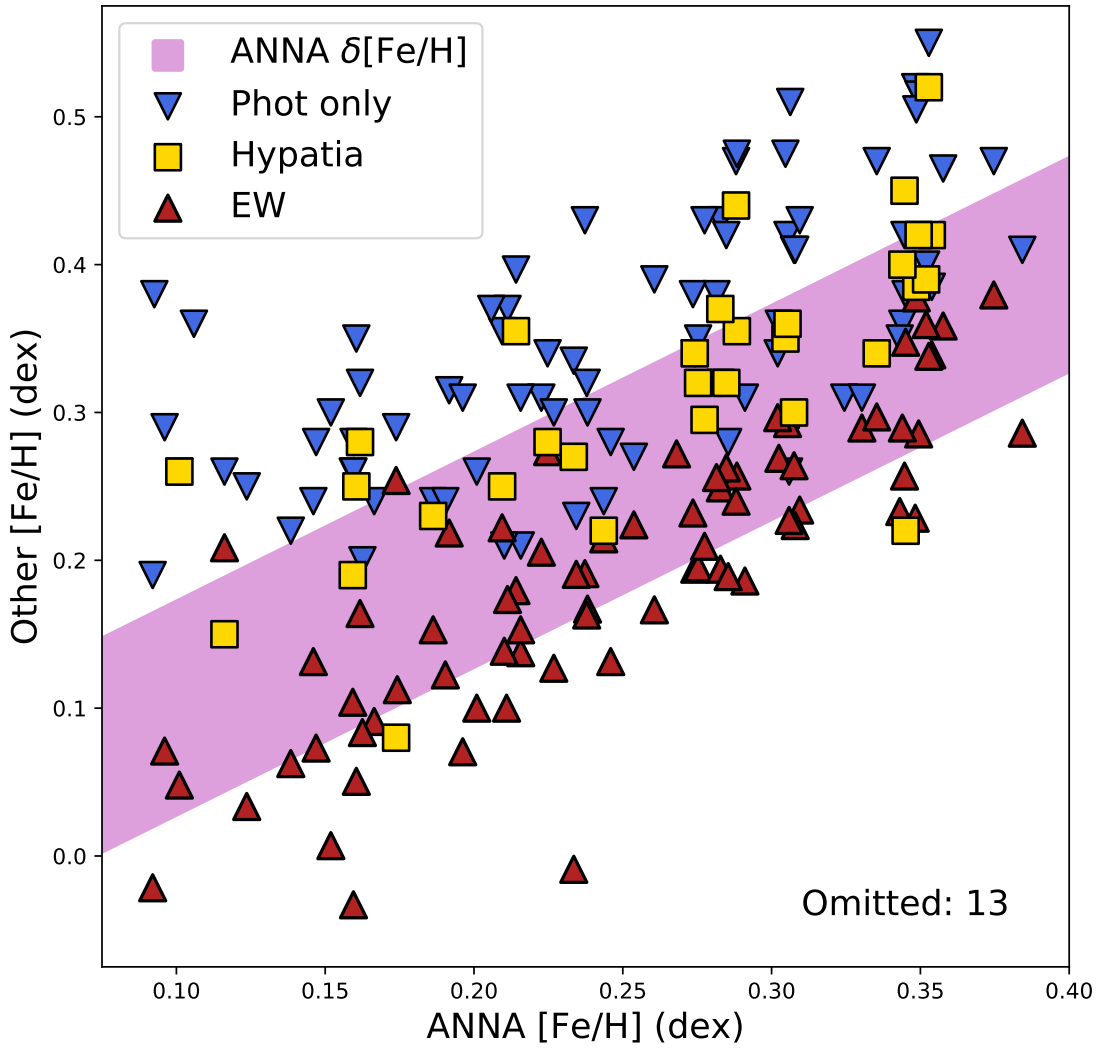

Figure 5.4: Comparison of ANNA-derived [Fe/H] estimates with those from an EW-analysis using ROBOSPECT, as well as available literature values. Blue inverted triangles and yellow squares indicate the literature values for [Fe/H] derived from photometry and spectroscopy, respectively, and are the same as in Figure 5.3. The red triangles indicate the [Fe/H] estimates derived from the EW analysis. The lavender band indicates the line of 1:1 correspondence, and its width indicates the typical uncertainty attached to each ANNA [Fe/H] measurement.

7. HD 205583: Visually identified as a binary.

8. HD 220848: Discrepant ANNA and EW [Fe/H].

9. HD 27831: Poorly-constrained ANNA parameterization.

10. HD 279527: Poorly-constrained ANNA parameterization.

After this, a further three stars (HD 47218, HD 199744, and HD 103012B) were excluded as they did not have a $log(g)$ estimate, which was required for the A(Li) measurement. An additional 9 stars with $log(g) < 4$ dex were excluded as they are likely evolved stars and of no use to this study (see Table 3.2). Finally, 4 stars with temperatures outside the plateau region were excluded (HD 104588, HD 151482, HD 184295, and HD 216027).

After these initial cuts, the final SMR sample was selected by requiring the ANNA [Fe/H] to be greater than +0.20 dex. This cut follows the standard definition of an SMR star (see, e.g., McWilliam, 1997). The final SMR sample contains 44 stars, in line with what was deemed necessary when designing the study (see Chapter 2). The parameters for the SMR stars, including absolute V magnitudes calculated as outlined in Chapter 3, are given in Table 5.1. The stars in the sample with good parameterizations but sub-SMR metallicities will be used as a low-metallicity comparison sample in Chapter 6.

5.2 Measuring Li in the SMR Stars

With the SMR sample finalized, Li was measured for each star in the sample. As noted in Chapter 3, the 6708 Å line is blended with an Fe I line, so ROBOSPECT cannot be used to measure its EW accurately. While manual measurement (using IRAF's *splot* utility) of the Li/Fe blend's EW followed by a prescription to subtract the contribution of the Fe line was used in Anthony-Twarog et al. (2009), this process becomes difficult at higher [Fe/H] where the Fe line makes a greater contribution to the blend (Cummings et al., 2012).

Therefore, MOOG's *synth* routine was used to visually fit a synthetic spectrum to the region of the Li doublet and derive an estimate of A(Li). In many ways, this process is similar to that used with the *abfind* MOOG routine described in Chapter 3. The user provides a model photosphere, and MOOG solves the radiative transfer equation (in LTE) to compute a synthetic spectrum. The major difference is that instead of providing EWs which are combined with a curve of growth, the user can tweak any of the major stellar parameters in order to match the synthetic spectrum generated by MOOG to the observed spectrum. The best-fit synthetic parameters are then adopted as the parameters for the observed spectrum. This process is essentially a manual version of the template fitting method described in Chapter 4.

For this analysis, the synthetic spectra generated by MOOG were matched to the observed spectra using the wavelength region 6700 Å $< \lambda <$ 6715 Å. The linelist used during the process was taken from the VALD database (Kupka et al., 2011). The parameters adopted for the photospheric models were the same as used during the EW [Fe/H] analysis. The solar limb darkening coefficient was set to be 0.4.

When manually fitting, the following procedure was used for each star. First, the radial velocity-induced shift was altered until the synthetic line centers overlapped with the observed ones. Second, the synthetic continuum level was adjusted until the line-free regions of the two spectra matched. Third, the rotational velocity was tweaked until the wings of the synthetic lines matched those of the observed lines. These steps were followed in this order for each star to minimize the impact of visually-induced systematics from, for example, matching maximum line strengths by increasing rotational velocity first rather than adjusting the continuum level.

Once the synthetic and observed spectra were calibrated in this way, Li was measured for each star. This was done by altering A(Li) and regenerating the synthetic spectrum while keeping the other parameters constant. The visually identified A(Li) of best fit was then recorded as the Li abundance for each star. Figure 5.5 illustrates the impact of various changes to A(Li) on the synthetic spectrum for a typical SMR star. As a final check on the A(Li) results from synthesis, an EW-based method was also used to measure Li in the SMR stars. This process, as detailed in

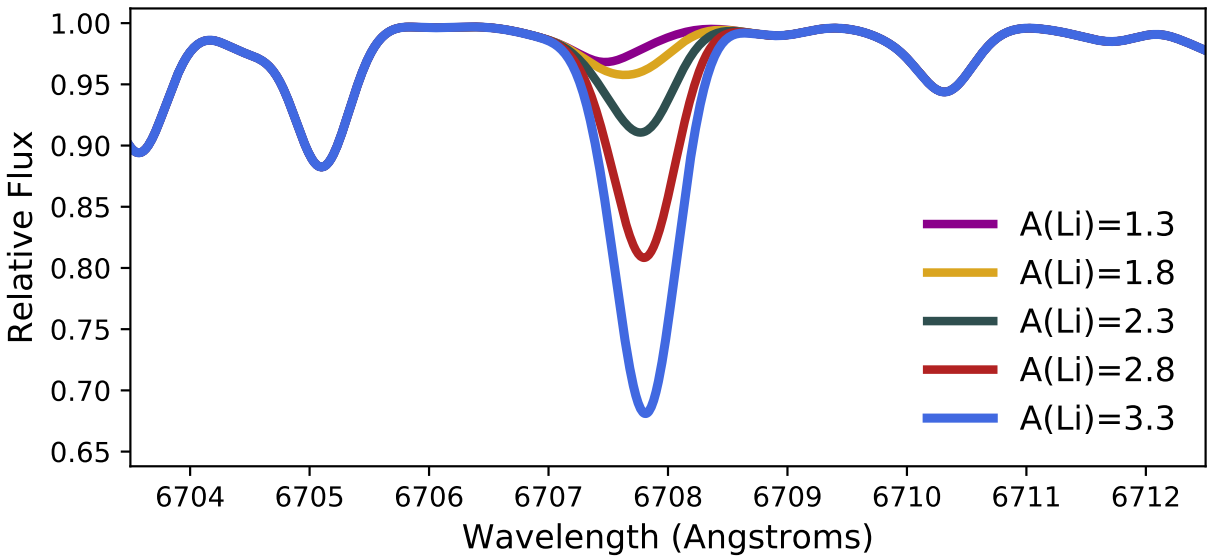

Figure 5.5: Synthetic spectra illustrating the effect of changing the Li abundance. The spectrum parameters are typical of one of the SMR spectra, T= 5850 K, [Fe/H]=+0.38.

(Anthony-Twarog et al., 2009), subtracts the expected Fe contribution to the Li-Fe blend, and then uses a curve of growth to compute the resultant Li abundance. The EW-derived Li abundances are consistent with the results from synthesis.

From Figure 5.5, it can be noted that the largest apparent changes in the Li line occur at high A(Li), e.g., the visual difference when going from A(Li) = 3.3 to 2.8 dex is much greater than the difference when going from A(Li) = 1.8 to 1.3 dex. As A(Li) is reported as a logarithmic abundance this is unsurprising, but it means that at low Li, the precise value of A(Li) becomes difficult to determine. As a conservative measure, A(Li) determinations below 2.0 dex are treated as upper limits, as below this value large changes in A(Li) are required to significantly change the line's appearance. While this specific cutoff was chosen somewhat arbitrarily, it actually coincides quite well with the upper limit boundary calculated more formally by Cummings et al. (2012) for the metal-rich cluster NGC 6253.

Accurately quantifying the uncertainty associated with each A(Li) measurement is non-trivial, due to the reliance on measurement via visual inspection. In Cummings et al. (2012), the statistical uncertainty associated with each A(Li) estimate was calculated according to the Cayrel de Strobel

& Spite (1988) formula (as given in Deliyannis et al. (1993)), which depends on the telescope plate-scale, local SN, and full width half max of the spectral line. For this study, such a calculation would result in a statistical uncertainty of < 0.03 dex for each Li measurement, due to the high SN of the spectra. This uncertainty is far below the uncertainty expected due to, e.g., errors in temperature or metallicity, as well as the uncertainty due to visual measurement.

Ultimately, a relatively conservative ± 0.15 dex uncertainty was adopted for each A(Li) measurement. The primary driver of this uncertainty is the temperature uncertainty; based on Cummings et al. (2012); Lee-Brown et al. (2015), the typical T_{eff} uncertainty of $\sim \pm 60$ K for the SMR stars should result in Δ A(Li) $\sim \pm 0.1$ dex. In contrast with the two studies just mentioned, where the uncertainty in temperature was systematic due to the dependence on reddening, the temperature uncertainties for the SMR stars are random. The remainder of the uncertainty budget was estimated based on the metallicity uncertainty (which has a smaller effect on the Li uncertainty), as well as the smallest ΔA(Li) that could be easily detected by eye when generating synthetic spectra (for stars with A(Li) > 2.0 dex). The uncertainty is approximately constant across the SMR stars due to to the relatively constant σT_{eff} and σ[Fe/H].

The A(Li) measurements are given in Table 5.1. After the Li measurement procedure, each confirmed SMR star has a well-constrained determination of T_{eff}, $log(g)$, [Fe/H], A(Li), and M_V. The relations between these parameters and an investigation of the Li plateau in SMR stars will be given in the next chapter.

Table 5.1. Final SMR Sample Li Measurements

ID	M_V	T_{eff}	σT_{eff}	[Fe/H]	σ[Fe/H]	A(Li)	Type
BD+39 2711	4.19	5821	60	0.375	0.083	1.60	UL
BD+60 583	4.03	5829	61	0.358	0.096	1.80	UL
HD 103012A	2.07	5911	56	0.211	0.086	2.55	M
HD 103459	3.61	5825	62	0.268	0.086	2.10	M
HD 105279	3.64	5865	53	0.288	0.077	2.20	M
HD 106423	3.91	6065	64	0.352	0.080	2.78	M
HD 107211	4.14	5887	54	0.349	0.076	2.15	M
HD 109929	3.33	6075	48	0.349	0.056	1.70	UL
HD 11170	2.46	6000	53	0.308	0.060	1.40	UL
HD 113938	3.87	5964	56	0.305	0.068	2.57	M
HD 115954	3.62	5820	64	0.291	0.090	2.65	M
HD 11638	4.33	5939	62	0.330	0.087	2.05	M
HD 117243	4.11	5967	55	0.274	0.077	2.31	M
HD 117302	3.19	5902	60	0.201	0.089	2.46	M
HD 130087	3.76	5984	58	0.275	0.082	2.60	M
HD 13345	3.66	6178	61	0.254	0.070	2.58	M
HD 13773	3.46	6188	54	0.302	0.050	2.63	M
HD 14348	3.28	6118	53	0.244	0.066	1.40	UL
HD 149026	3.73	6045	51	0.283	0.064	2.40	M
HD 154144	3.40	6005	53	0.214	0.058	2.55	M
HD 15866	3.11	5972	81	0.225	0.058	2.12	M
HD 16090	3.25	6021	53	0.216	0.056	2.25	M
HD 177985	3.37	5951	50	0.237	0.064	2.60	M
HD 180318	3.85	5938	51	0.274	0.059	2.64	M
HD 192343	4.02	5840	67	0.285	0.105	1.75	UL
HD 198483	4.16	6155	63	0.234	0.061	2.94	M
HD 218354	3.59	5859	53	0.234	0.079	1.45	UL
HD 224882	2.74	5935	59	0.384	0.084	1.45	UL
HD 2330	3.61	5989	55	0.210	0.075	2.77	M
HD 238069	3.68	5883	55	0.277	0.078	2.32	M
HD 2564	2.60	6221	54	0.345	0.047	1.60	UL

Note. — Absolute V magnitudes are described in Chapter 3. Temperatures and [Fe/H] values are from ANNA. The Type column indicates whether the Li measurement is UL = Upper Limit or M = Measurement.

Table 5.2. Final SMR Sample Li Measurements (continued)

ID	M_V	T_{eff}	σT_{eff}	[Fe/H]	σ[Fe/H]	A(Li)	Type
HD 26441	3.31	5957	59	0.281	0.075	2.45	M
HD 30769	3.03	6065	52	0.246	0.065	1.40	UL
HD 3592	4.07	5833	53	0.288	0.071	1.95	UL
HD 449	3.94	5947	66	0.345	0.084	2.62	M
HD 47155	3.03	6200	53	0.227	0.043	1.70	UL
HD 76617	3.41	6090	53	0.209	0.056	2.88	M
HD 78277	3.45	5899	57	0.335	0.080	2.68	M
HD 82410	4.06	5964	59	0.223	0.078	2.56	M
HD 8328	3.70	5819	68	0.344	0.110	2.22	M
HD 83616	2.55	5978	52	0.238	0.062	1.56	UL
HD 8446	3.87	5907	67	0.308	0.094	2.74	M
HD 94861	3.33	6094	53	0.285	0.067	1.80	UL
HD 9729	3.41	5972	64	0.302	0.089	2.39	M

Note. — Absolute V magnitudes are described in Chapter 3. Temperatures and [Fe/H] values are from ANNA. The Type column indicates whether the Li measurement is UL = Upper Limit or M = Measurement.

Chapter 6

Results and Discussion

In this chapter the main results of this study will be presented and discussed. In Section 6.1, a likely Li-dip origin for some of the SMR stars will be detailed. The initial A(Li) abundances of the remaining SMR stars will be considered in Section 6.2, followed by a discussion of the Li plateau in Section 6.3. Finally, the possible origins of the stars in the SMR sample will be explored in Section 6.4.

6.1 SMR Stars with no Detected Li: Evidence for a Li-Dip Origin

In Figure 6.1, the A(Li) measurements are plotted as a function of surface temperature. Included in the plot are the measurements for SMR stars from Ramírez et al. (2012), López-Valdivia et al. (2015), and Fu et al. (2018). Upper limits (i.e. Li non-detections) are indicated with triangles. The four sets of plotted data all tell a similar story. Below 5900 K, there is an increase in the number of stars with low/non-detected A(Li); depletion below this temperature is observed in a wide range in clusters (see, e.g., Cummings et al., 2012, 2017) and is predicted by standard models that include convection, though the magnitude at fixed age is typically underestimated (see Pinsonneault, 1997; Cummings et al., 2017).

Above 5900 K, excluding the lower limits, A(Li) is relatively constant for all samples, with a slight increase from 2.25 dex to 2.6 dex by 6200 K. Of note is the so-called "lithium desert" identified by Ramírez et al. (2012), indicated by the lavender box in Figure 6.1. In this region, across a wide range in [Fe/H], there are no Li detections in the SMR sample, only upper limits. The López-Valdivia et al. (2015) study found one star with A(Li) and temperature that placed it in

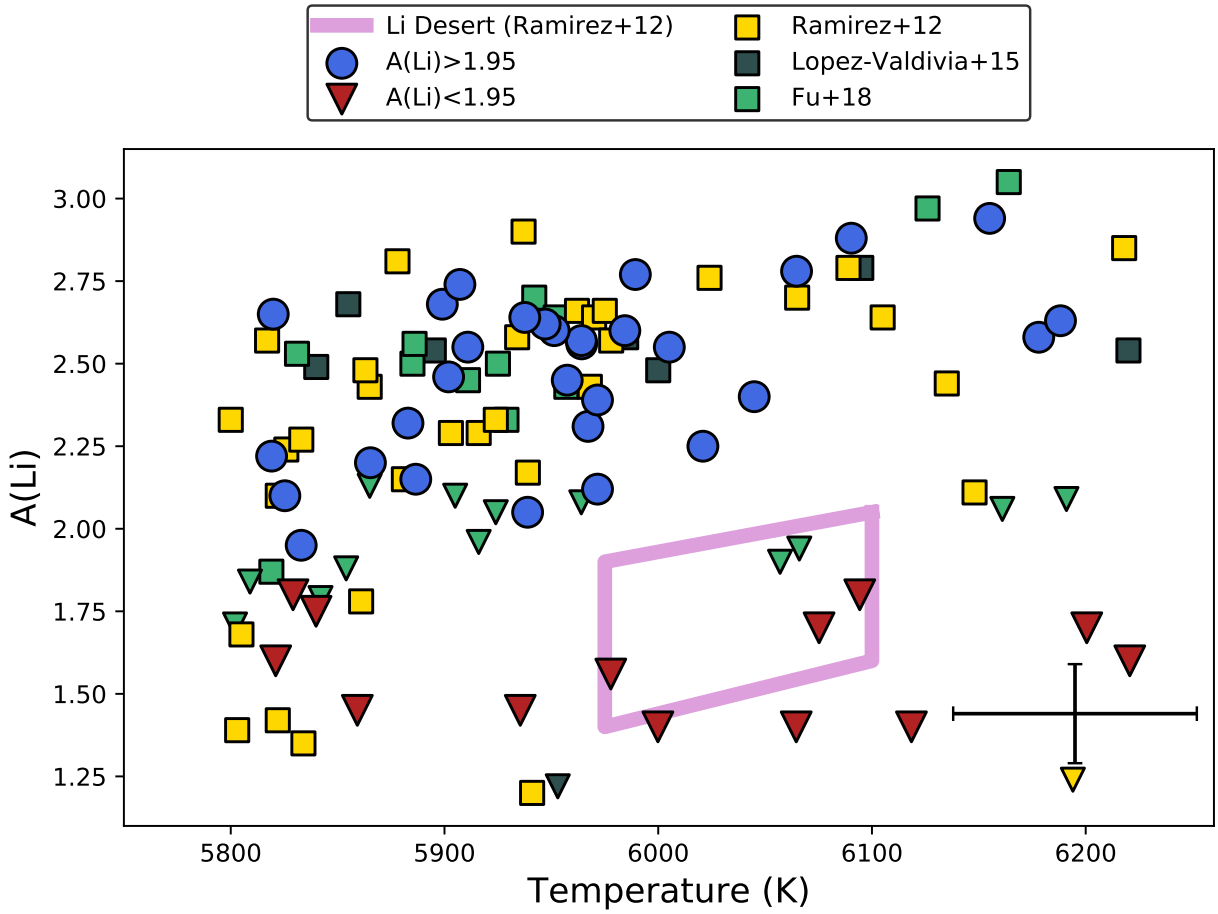

Figure 6.1: Measured A(Li) vs. surface temperature for the stars observed as part of this study (blue circles and red triangles for high and low A(Li) subsamples, respectively), Ramírez et al. (2012) (yellow squares), López-Valdivia et al. (2015) (dark squares/triangles), and Fu et al. (2018) (green squares/triangles). The box in the central part of the figure indicates the location of the "lithium desert" reported in Ramírez et al. (2012). Typical uncertainties are indicated by the errorbars in the lower right portion of the figure.

the region of the desert, but it is not a SMR star.

It is apparent that stars with no detected Li exist in all four data sets plotted in Figure 6.1 across the entire temperature range. Even taking into account the temperature uncertainties, this means that these non-detections are not merely stars with low surface temperatures below the convection-induced depletion boundary. It is stressed that the non-detections plotted in Figure 6.1 are upper limits only, so the gap between the high and low lithium populations (which defines the lithium desert) may be larger than portrayed in the figure.

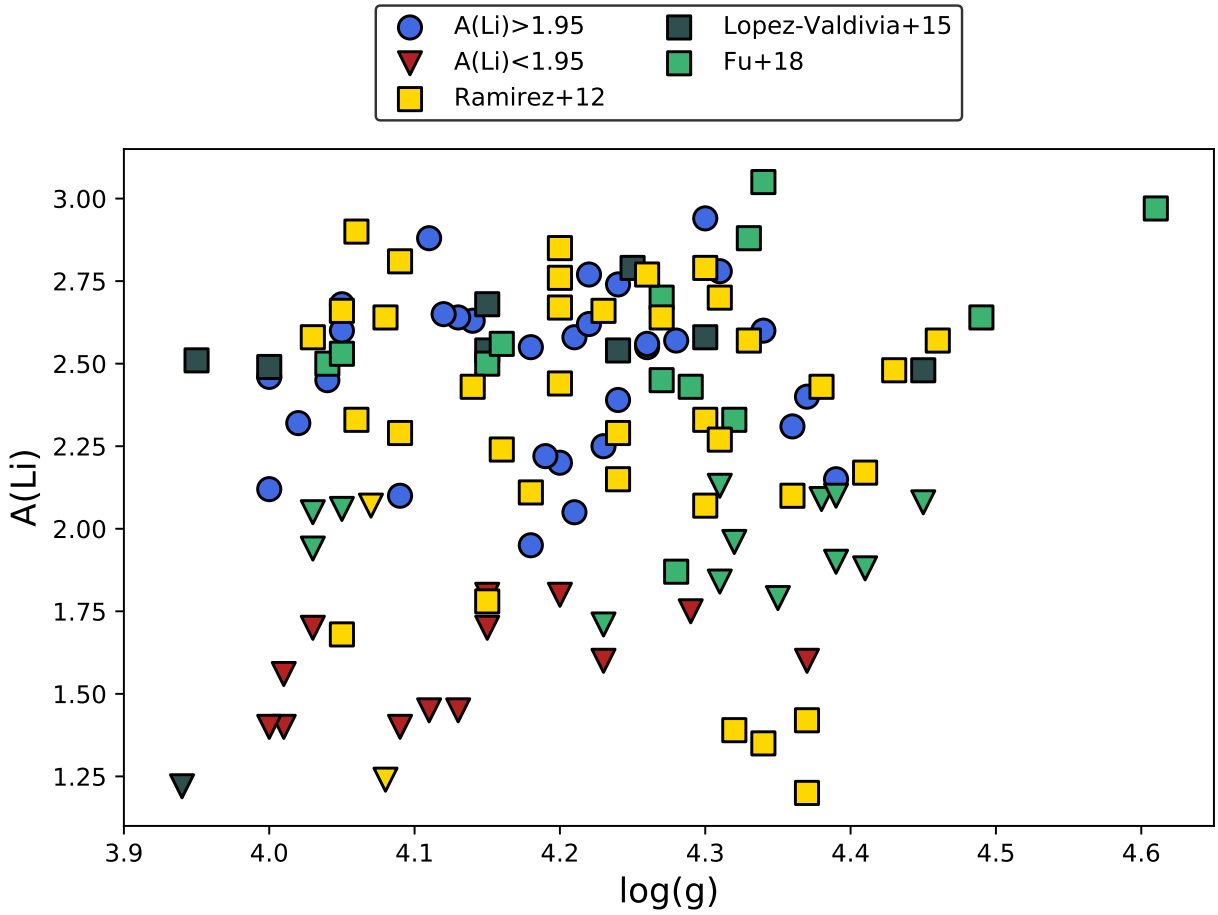

Figure 6.2: Measured A(Li) vs. surface gravity, where the color codes/symbols used are the same as Figure 6.1.

In Figure 6.2, the measured lithium abundances are shown as a function of $log(g)$, with the measurements for SMR stars from the three previously-mentioned studies shown as well. The $log(g)$ values are consistent with non-evolved stars, which of course is expected for this study's sample, as a cut in $log(g)$ was applied to explicitly exclude evolved stars. What Figure 6.2 does show is that the low-Li subpopulation is relatively evenly distributed across the range in $log(g)$.

Finally, in Figure 6.3, A(Li) is shown as a function of [Fe/H]. There appears to be the possibility of a decrease in average Li as a function of metallicity. However, it is important to note that the large scatter in the diagram and the significant uncertainty in [Fe/H] mean that the data are consistent with a flat trend of A(Li) with metallicity as well, once lower limits are excluded. In keeping with the theme established by previous plots, the low-lithium subpopulation is distributed

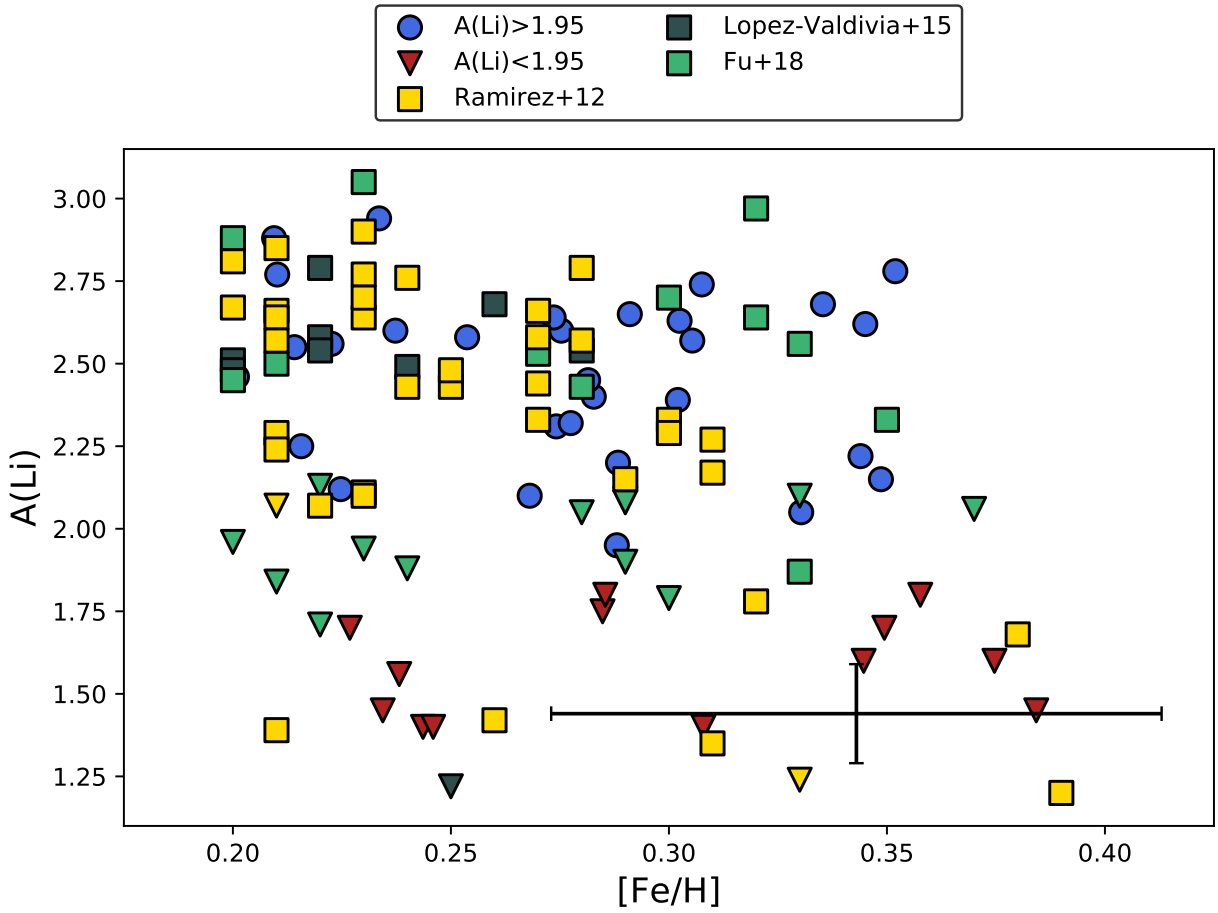

Figure 6.3: Measured A(Li) vs. [Fe/H], where the color codes/symbols used are the same as Figure 6.1 and Figure 6.2. Typical uncertainties are indicated by the errorbars in the lower right portion of the figure.

across the entire metallicity range.

The presence of stars with low A(Li) in the plateau temperature range has been examined by several studies. While the "lithium desert" moniker was coined in Ramírez et al. (2012) and subsequently adopted by López-Valdivia et al. (2015), the presence of plateau stars with low A(Li) can be observed in virtually all studies of Li in field stars (e.g., Chen et al., 2001; Ramírez et al., 2012; López-Valdivia et al., 2015; Guiglion et al., 2016). This pattern persists across a wide range in metallicity, from the sub-solar and solar metallicities contained in the aforementioned studies to the highly enriched stars of this study.

The original explanation for this pattern, given in Chen et al. (2001), was that the low-Li sub-

population was composed of evolved Li-dip stars. Under this explanation, these stars depleted their lithium on the MS per the usual (but unknown) mechanism causing the dip, and due to the decrease in their surface temperatures after evolving off the main sequence towards the subgiant branch, fall into the temperature range of the Li plateau. This conclusion was justified by determining that the masses of the low-Li stars either corresponded to lower-mass stars expected to deplete on the MS or more evolved stars with masses consistent with the Li dip, especially considering the apparent metallicity dependence of the mass of the Li dip. A similar pattern and explanation (though with less consideration paid to metallicity due to sample size) can be found in Lambert et al. (1991).

However, Ramírez et al. (2012) suggested an alternate explanation for the presence of the lithium desert. Based on a much larger sample of field stars ($\sim 4\times$ larger), the authors determined that the mass-metallicity relation from Chen et al. (2001) for dip stars could be observed in both the high and low Li subpopulations, indicating a possible selection effect, rather than a Li dip origin for the low-Li stars. They do not discount that some of the low-Li stars originated from the dip, but suggest that an unknown mechanism may rapidly deplete Li in some stars during the MS or early subgiant phases of evolution. A possible connection to the presence of giant planets is noted, as stars in the temperature range of the lithium desert with confirmed giant planets are confined to the high-Li population.

More recently, Aguilera-Gómez et al. (2018) presented a detailed analysis of the lithium desert identified in Ramírez et al. (2012). Via an analysis of Li in ~ 230 stars, they find that plateau-temperature stars across a range in metallicity exhibit a bimodality in Li directly connected to their evolutionary state. On the basis of their large sample size, they rule out statistical chance as being the cause of the lithium desert, as suggested by López-Valdivia et al. (2015). By comparing the masses and core hydrogen fractions of the high and low Li subpopulations, Aguilera-Gómez et al. (2018) find that the low-lithium stars are generally consistent with being higher-mass stars that have already left the main sequence and have plateau-like temperatures due to the cooling of their outer layers as they evolve onto/along the subgiant branch. Comparing the low-lithium stars with MS stars of similar mass, the main conclusion of the study is that the low end of the lithium desert

is composed of evolved Li-dip stars.

The controversy over the origin of the Li desert can be addressed by leveraging the absolute V magnitudes and precise ANNA temperatures for the SMR stars. In Figure 6.4, the absolute magnitudes of the SMR stars (as derived from Gaia DR2 parallaxes - see Chapter 3) are plotted as a function of their surface temperatures. Stars are colored by their metallicity, and upper limits are noted with triangles. Additionally, a series of PARSEC isochrones (Bressan et al., 2012) is shown spanning a range in age and with [Fe/H]=0.29, the midpoint of the metallicity range spanned by the SMR stars.

What can be seen from the (almost) Hertzsprung-Russell diagram is that the low-Li stars primarily populate one of two regions in M_V-T_{eff} space. There is a population at cool temperatures - considering the temperature uncertainties ($\sim$ 60 K), these are stars consistent with being stars well into the region corresponding to extensive MS Li depletion. The rest of the low-Li stars are clustered in the upper left portion of the diagram, at bright M_V and/or hotter temperatures. This pattern is similar to that seen in Chen et al. (2001) and Lambert & Reddy (2004), and similarly lends support to the idea that the hotter low-Li stars may indeed be evolved dip stars.

Further evidence for a Li-dip origin can be found by determining the mass location of the cool side of the lithium dip for the SMR stars. Several open cluster studies have confirmed the mass-metallicity relation for the lithium dip boundary suggested by Chen et al. (2001) for metallicities up to [Fe/H]=+0.4 (NGC 6253), (Anthony-Twarog et al., 2009; Cummings et al., 2012, 2017). From these results, the cool boundary of the dip was estimated to be 1.31 $M_{\odot}$ for a star with [Fe/H] = +0.29, the midpoint of the range spanned by the SMR stars. This mass is indicated by the stars on each isochrone in Figure 6.4.

Excluding the cool stars, which as noted before are expected to deplete Li on the MS, all of the low-Li stars are consistent with being Li dip stars, based on their HR diagram positions relative to the Li dip mass boundary. Conversely, very few of the stars with detected Li lie above this boundary. Taken together, the implication is that the SMR population studied here is consistent with the original Chen et al. (2001) explanation for the low-Li subpopulation. A more exotic

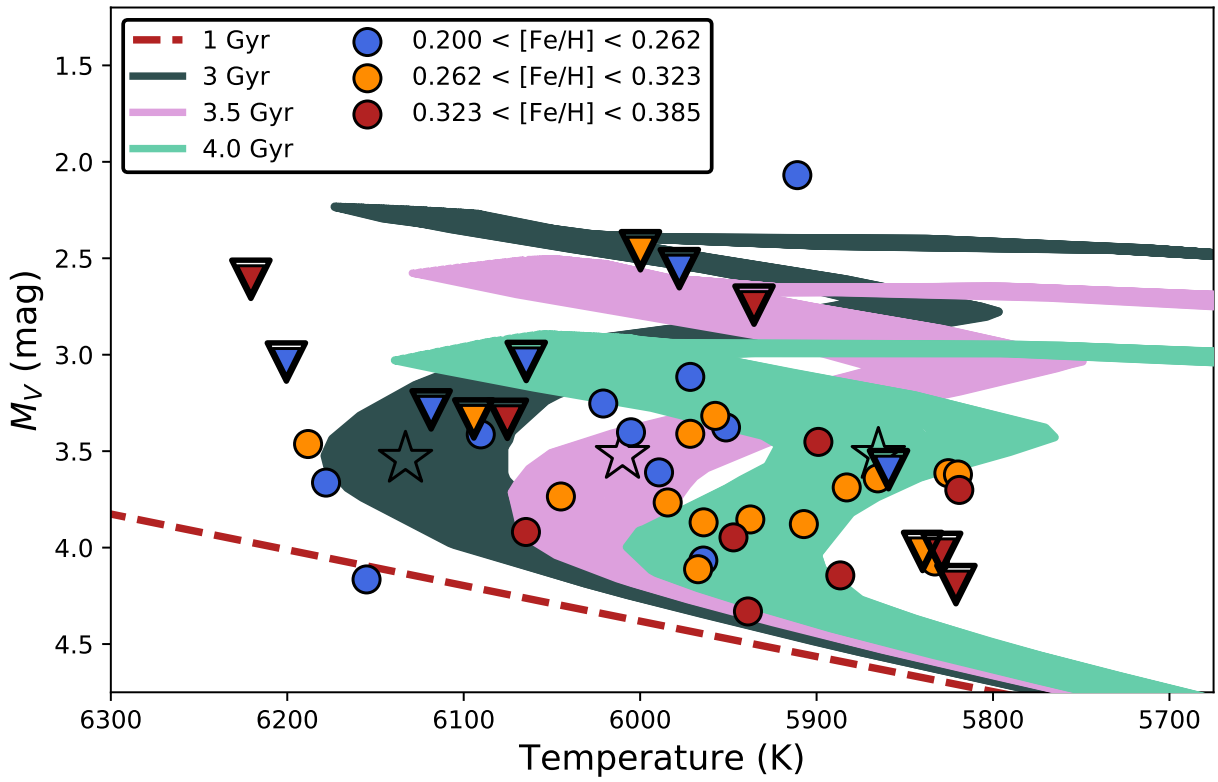

Figure 6.4: Hertzsprung-Russell diagram for the stars in this study. Absolute V magnitudes were calculated according to the procedure given in Chapter 3 using Gaia DR2 parallaxes. The stars are color-coded by metallicity; blue, orange, and red points correspond to membership in equal-size metallicity bins from [Fe/H]=+0.20 to [Fe/H]=+0.385 (in increasing fashion). Triangles indicate the low A(Li) subsample. The filled tracks indicate PARSEC isochrones (Bressan et al., 2012) of three ages: 3.0 Gyr (dark green), 3.5 Gyr (lavender) and 4.0 Gyr (teal) and metallicities spanning the range +0.20 < [Fe/H] < +0.385, such that the lowest metallicity corresponds to the leftmost edge of the filled track. The dotted red line indicates a PARSEC isochrone of age 1 Gyr and metallicity [Fe/H]=0.29. The starred positions on each isochrone track indicate the location of a [Fe/H]=+0.29 star with mass corresponding to the cool-side edge of the Li-dip, $1.27 M_{\odot}$, extrapolated from Cummings et al. (2012).

physical mechanism operating in these stars (i.e. the Ramírez et al. (2012) interpretation) cannot strictly be ruled, out, but it should be noted that aside from their position in the HR diagram, there is nothing immediately unusual about the low-Li stars considering the information gathered by this study. Thus, the simpler explanation of a Li dip origin for some stars as being the driver of their low A(Li) is favored over invoking new physics.

Considering possible systematics that could impact this conclusion, the Li dip's location in mass is metallicity-dependent, as discussed above, but a dip mass for a single [Fe/H] was adopted here. However, for stars of metallicity of NGC 6253, the dip mass is 1.34 $M_{\odot}$, while for Hyades-metallicity stars it is 1.27 $M_{\odot}$ (Cummings et al., 2012). The majority of the evolved low-Li sub-population is well away from the 1.31 $M_{\odot}$ mass adoped here, so these small changes in dip mass (which would translate to small changes in the locations of the starred points in Figure 6.4) would not alter the conclusion made above. Temperature uncertainties would leave the conclusions unchanged as well, as the mass boundary shown in Figure 6.4 occurs at nearly fixed M_V and so has little temperature dependence. Uncertainties in M_V, as discussed in Section 6.2, are mostly driven by reddening considerations and should be relatively small, $\delta M_V < 0.1$, and would not impact the results.

6.2 The Initial A(Li) in SMR Stars

There are no SMR stars in this study's sample with measured A(Li) > 3.0 dex; the maximum A(Li) is 2.94 dex. This value is similar to the SMR upper limit found by Ramírez et al. (2012), Delgado Mena et al. (2015), López-Valdivia et al. (2015), Guiglion et al. (2016), and Fu et al. (2018), and is significantly lower than what is observed in young (<650 Myr), solar-metallicity or slightly super-solar open clusters (Sestito & Randich, 2005). This sub-Hyades upper bound for A(Li) has been previously interpreted as a signature of decreasing initial Li at super-solar metallicities by Delgado Mena et al. (2015), Guiglion et al. (2016), and Fu et al. (2018).

Figure 6.4 may provide an alternate explanation for the apparent downturn in maximum recorded A(Li) at super-solar metallicities shown in Ramírez et al. (2012), Delgado Mena et al. (2015),

Guiglion et al. (2016), and Fu et al. (2018). The initial A(Li)-[Fe/H] anticorrelation for [Fe/H]>0.0 was interpreted by Guiglion et al. (2016) and Fu et al. (2018) to be a signature of decreasing initial Li abundance in metal-rich stars. This would be at odds with the predictions of many Galactic chemical enrichment models (see, e.g., Romano et al., 1999; Travaglio et al., 2001; Prantzos, 2012) - few of these models explicitly extend to the [Fe/H] of the SMR stars, but extrapolation of the e.g., Prantzos (2012) model implies a flat [Li/Fe] relation above [Fe/H]=+0.20.

As discussed in Fu et al. (2018), a decrease in Li at high metallicities could be a result of, e.g., clumpy star formation in the past few Gyr in the solar neighborhood. This clumpiness could occur under certain self-regulating star formation scenarios (due to a critical gas density threshold for star formation) as shown in the models of Chiappini et al. (1997) and subsequently Romano et al. (2001). Under the right conditions, Li would increase over a short period of time (due to the contributions of AGB and supernovae), and then be followed by long periods of low star formation during which Li is destroyed by internal mixing processes in lower-mass stars. Li-depleted material would then be returned to the ISM and incorporated into the next generation of stars, thereby lowering their initial A(Li) while continuing to increase [Fe/H] (Romano et al., 2001).

However, the interpretation of the decrease in measured A(Li) as a function of [Fe/H] is dependent on the assumption that the currently observed upper limit of A(Li) at a given metallicity is indicative of the characteristic, undepleted Li abundance at that metallicity (e.g., Romano et al., 2001; Guiglion et al., 2016). However, as shown in Figure 1.3 and discussed several times during this work, open cluster Li observations indicate that in the plateau stars, initial Li is depleted relatively rapidly over the first $\sim$ 2 Gyr of MS evolution before reaching a more or less constant value of 2.4 - 2.6 dex (Sestito & Randich, 2005; Randich et al., 2009; Cummings et al., 2012, 2017). Thus, implicit in the use of the upper limit of A(Li) as indicative of the initial Li abundance is the assumption that a sample of stars at a given [Fe/H] will include relatively young stars with ages less than $\sim$ 1 Gyr. It is worth noting that even this assumption may be suspect, as models predict that pre-MS Li depletion in stars is metallicity-dependent (Somers & Pinsonneault, 2014).

What Figure 6.4 shows is that the sample of SMR stars examined by this study are all consistent with being turnoff/subgiant stars with ages greater than $\sim$ 3 Gyr. This raises the possibility that the reason for the apparent turnover in A(Li) at high [Fe/H] is due to an age effect, rather than one of chemical evolution. If there are no (or very few) SMR stars in the solar neighborhood, then any upper limit inferred from them will reflect a depleted value due to the same non-standard MS depletion observed open clusters, rather than an initial one. Certainly this interpretation would be more consistent with the predictions of most chemical evolution models, as under this scenario SMR stars could have started with the predicted A(Li), $\sim$3.3-3.5 dex, and then depleted over the first few Gyr to their present level, $\sim 2.5 - 2.6$ dex.

The natural question that can be asked if this interpretation is correct, then, is why aren't there any young SMR stars in the solar neighborhood? Star forming regions in the solar neighborhood only extend up to [Fe/H]$\sim +0.15$ dex for the Hyades (Cummings et al., 2017). If the SMR stars formed elsewhere in the Galaxy and migrated to the solar neighborhood, their older ages could be a natural result of the timescale required for this migration. The origins of the SMR stars will be investigated further in Section 6.4.

It is worth considering the impact of possible systematics due to, e.g., selection or measurement effects, on the interpretation of the SMR stars as having ages greater than $\sim$ 3 Gyr. On the measurement side, either the temperatures or absolute magnitudes could impact the results. The temperatures are an unlikely culprit, as the ANNA temperatures would need to be systematically $\sim 150 - 200$ K too cool in order to shift the stars shown in Figure 6.4 onto the 1 Gyr main sequence track. However, as shown in Chapter 5, the ANNA temperatures compare quite favorably with the Hypatia catalog temperatures, which are based on a variety of spectroscopic analysis methods.

The absolute magnitudes are only approximate, since they are unreddened, but applying a reddening correction would actually *strengthen* the conclusion that the SMR stars are > 3 Gyr old. Removing the reddening would increase the apparent brightness of the SMR stars; at a fixed distance this would increase the absolute brightness of the stars. Thus, correcting for reddening would increase the distance between the SMR stars and the 1 Gyr isochrone shown in Figure 6.4. How-

ever, since these stars are relatively close, reddening values should be very small - approximately < 0.1 in V.

The selection of the SMR stars was essentially magnitude-limited - this could plausibly bias the sample, as the brighter turnoff stars would be preferentially selected for observation. The impact of this effect can be estimated by converting the absolute magnitudes of MS stars along the 1 Gyr isochrone in Figure 6.4 to apparent magnitudes using the distance moduli of the actual SMR sample, and comparing the distribution of these apparent magnitudes to the actual V magnitude distribution of the SMR stars. The range of absolute magnitudes of 1 Gyr old plateau-region stars is $4.0 < M_V < 4.5$, and the average distance modulus for the actual SMR sample is 4.52 ± 0.67. Thus, the average apparent V for 1 Gyr stars would be 8.5-9.0 ± 0.67. This can be compared with the actual average apparent V of 8.12. These two values are within 1σ of one another; it can therefore be expected that approximately 15-20% the SMR sample (or 5-10 stars) would be stars on the MS. However, from Figure 6.4, it can be seen that virtually none of the stars are close to the unevolved MS track; the handful of stars that are reasonably close are in the lowest metallicity bin which, given the typical metallicity uncertainties, could imply that they are lower-metallicity, Hyades-like stars. None of the most metal-rich stars in the SMR sample are close to the MS.

Thus, selection effects are highly unlikely to be responsible for the lack of young SMR stars. This conclusion is strengthened by the fact that the above calculations are conservative - the average distance modulus used to calculate the apparent V of any MS SMR stars is likely an overestimate as it was derived from brighter turnoff stars, which would in turn imply that the average apparent V magnitude of a MS population would be brighter than calculated. Additionally, the calculations of an expected 15-20% MS population assumed a uniform parent distribution in V. This results in an overestimate of the number of turnoff stars relative to MS, because the parent distribution should be biased towards lower V due to an expected 3 Gyr MS lifetime vs. $\sim$1 Gyr spent on the turnoff. In other words, the fraction of MS stars expected, assuming a uniform star formation rate, should be somewhat higher than the 15-20% figure calculated above.

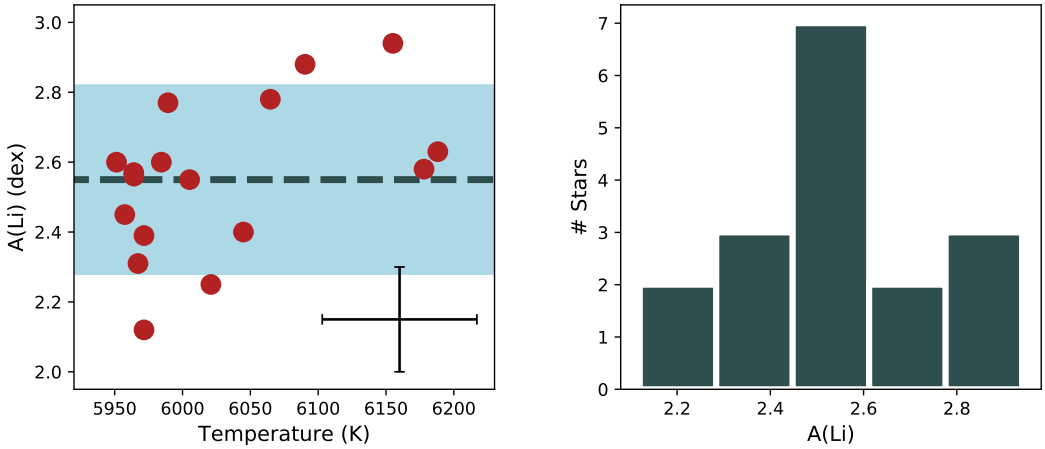

Figure 6.5: Left panel: A(Li) as a function of surface temperature for plateau stars, where the boundaries of the plateau were set to be 5950 K and 6200 K, as determined from the results given in Cummings et al. (2012). Lower limit measurements are excluded from the plot. The dotted line indicates the mean A(Li) for the plotted points, A(Li)=2.55 dex, and the band around this line indicates the standard deviation, σ=0.21 dex. The errorbars in the lower right corner of the plot indicate the typical uncertainties. Right panel: the distribution of Li for the plateau stars shown in the left panel. Bin width was selected to be the adopted σA(Li), $\pm$0.15 dex.

6.3 The Lithium Plateau

In Figure 6.5, A(Li) for stars from this study in the lithium plateau region are shown as a function of temperature. The lower-temperature boundary defining this region was taken to be 5950 K, approximately 1σ (temperature uncertainty for the SMR stars) from the boundary defining standard convection-induced depletion. Stars without Li detections above this temperature boundary were also excluded, as they are likely evolved Li-dip stars (see Section 6.1). The resultant distribution of A(Li) measurements for the remaining SMR stars is shown in the right panel of Figure 6.5.

From the stars shown in Figure 6.5, a mean A(Li) of 2.55 $\pm$0.21 dex can be derived. The specific temperature boundary chosen to define the true plateau stars has little impact on the plateau Li abundance; a temperature cutoff of 5900 K or 6000 K still results in a plateau value of A(Li)$\sim 2.5-2.6$ dex. The width of the distribution is similar to the typical uncertainty assigned to each A(Li) measurement, δA(Li)$=0.15$ dex; the implication is that the A(Li) measurements in Figure 6.5 are all consistent with the identified peak in A(Li).

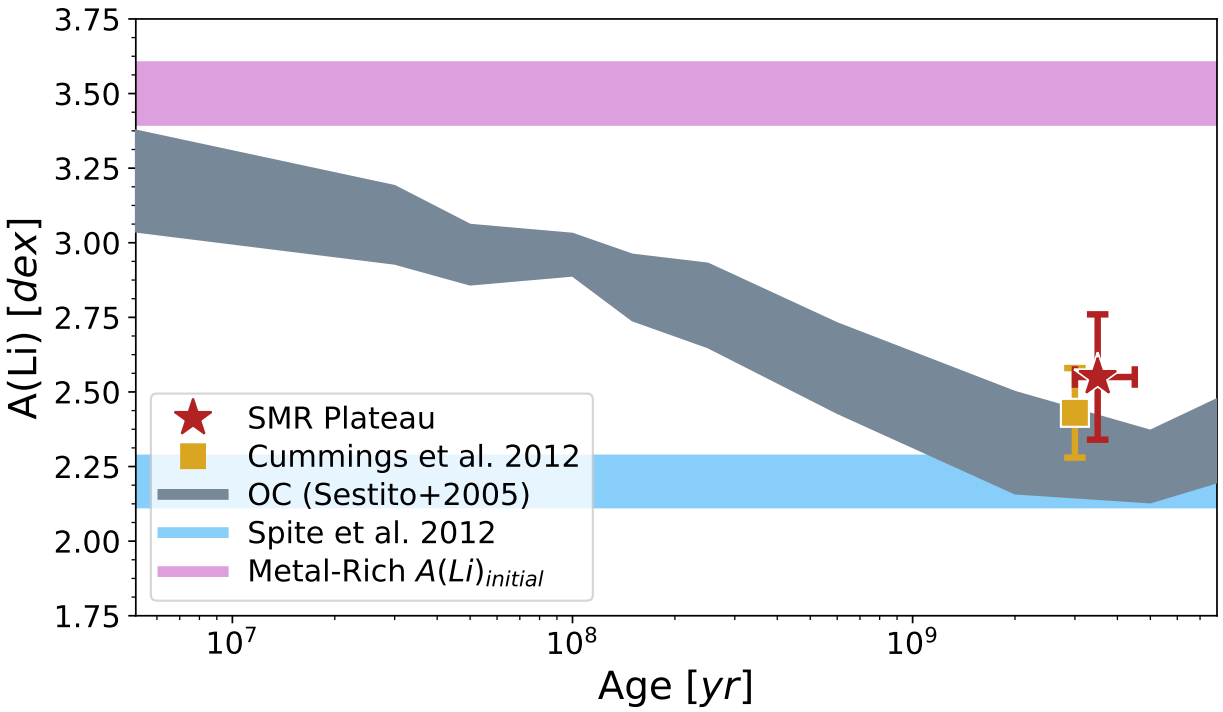

Figure 6.6: Plateau-temperature SMR A(Li) and age. The violet shaded horizontal line is the initial SMR Li estimated from the results of Ramírez et al. (2012). The blue horizontal line is the halo star plateau abundance from Spite et al. (2012). The gray line traces the open cluster Li plateau abundance as given in Sestito & Randich (2005). The gold point indicates the position of NGC 6253 on the diagram Cummings et al. (2012).

The derived Li plateau value of A(Li) of 2.55 dex is entirely consistent with the $>$ 2 Gyr aged open clusters shown in Figure 1.3. Indeed, as discussed in the previous section, the implication of Figure 6.4 is that the SMR stars all have ages between 3-4.5 Gyr. These two pieces of information are shown together in Figure 6.6.

From Figure 6.6, it is apparent that the mean plateau abundance for the SMR stars is entirely consistent with what is seen in the similarly metal-rich NGC 6253 (Cummings et al., 2012). Indeed, like NGC 6253, the SMR stars fit neatly into the position in A(Li)-age space expected from the trend of decreasing plateau Li with increasing age in lower metallicity open clusters (Sestito & Randich, 2005). This is particularly interesting since the implication is that by 3 Gyr, the mean plateau abundance is more or less the same across stars spanning a sizeable metallicity range, from the metal-poor ([Fe/H]$\sim$-0.4) NGC 2243 (François et al., 2013) to the level of NGC 6253 and the

SMR stars, [Fe/H]$\sim +0.4$. This is at odds with the predictions of standard models, which indicate a strong metallicity dependence (due to opacity effects) on the rate of Li depletion (Swenson et al., 1994; Pinsonneault, 1997), though this may primarily impact early MS evolution (Somers & Pinsonneault, 2014).

Certainly the disagreement with standard evolution models should be unsurprising, given the typically poor job they do matching any observed Li features (see Chapter 1). In Sestito & Randich (2005), it was demonstrated that open clusters spanning a range in age signal the existence of two discontinous periods of Li depletion for plateau stars: depletion on the order of 0.1-0.2 dex during the pre-main sequence phase, followed by a period of very little or no depletion until $\sim 150-250$ Myr, after which main sequence depletion commences for 1-2 Gyr. After the MS depletion phase, depletion slows or ceases, and the Li plateau observed in older open clusters remains constant at a level of $2.4-2.6$ dex. As noted in Chapter 1, this latter depletion especially is entirely unpredicted by standard models, which predict constant A(Li) in MS plateau region stars (Deliyannis et al., 1990; Pinsonneault, 1997; Somers & Pinsonneault, 2014).

However, even considering models that take into account non-standard physics, the failure of theory to match observations persists. In particular, the discontinous depletion has proven challenging to model. In Sestito & Randich (2005), it was observed that models including processes such as diffusion and rotational mixing (such as those of Chaboyer et al. (1995)) reproduced the pre-main sequence and early main sequence Li plateau evolution reasonably well, including the pause in Li depletion for the first few hundred Myr spent on the MS. However, for clusters older than the Hyades (600 Myr), the models increasingly *overpredicted* Li depletion for plateau stars, as they did not reproduce the cessation of depletion by 2 Gyr.

The apparent end of MS depletion may be tied to the rotation evolution of the plateau stars. It has been known for some time that rotation strongly evolves with age for F and G dwarfs (Skumanich, 1972), and that this evolution impacts Li depletion (see, e.g., Deliyannis et al., 1994). Indeed, the observed spread in ZAMS rotation rate may be tied to the scatter observed in Li in cooler stars (Stauffer et al., 1984; Stauffer, 2004), and the rotational spindown timescale for plateau stars

is very similar to the timescale of MS depletion (Stauffer, 2004; Sestito & Randich, 2005; Lanzafame & Spada, 2015). Further evidence for the connection between rotational spindown and Li depletion can be found in open cluster studies as well (Anthony-Twarog et al., 2018). However, current models that incorporate rotation, as noted above, do not yet match the observations.

It should also be noted that there is no model that can reproduce all Li depletion patterns even over the first few hundred Myr of evolution. As discussed in Cummings et al. (2017), while models including phenomena such as rotation and diffusion do better than standard models in predicting A(Li) for young clusters, especially for plateau stars, there are still apparent discrepancies. For example, cool stars (G and later) tend to be more depleted than models predict, and there is a large scatter in A(Li) for these stars that is not matched by model predictions. A satisfactory model of stellar structure and evolution will need to reproduce these features as well as match the plateau patterns.

It is clear that there is much work to be done on the theoretical side in order to reconcile models with observations, but how can the SMR stars help with this? What the results in Figure 6.6 show is that NGC 6253 is not an anomaly. That is, the high-metallicity plateau is indeed at virtually the same level as in metal-poor clusters. The implication, as noted previously, is that the Li plateau is metallicity-insensitive after ~ 2 Gyr, at least within the current observational uncertainties. This provides a strong constraint on any MS depletion mechanism - not only must it stop or slow by 2-3 Gyr, but it must also deplete a metallicity-dependent ZAMS Li abundance to a uniform value by this time.

A caveat to this interpretation is that it can be seen in Figure 6.6 that a moderately enhanced Li plateau cannot be ruled out for the SMR stars. Both NGC 6253 and the SMR stars are consistent with being enhanced by $\sim 0.1 - 0.2$ dex above the level traced by the more metal-poor clusters. This level of enhancement is coincident with the difference in inferred initial A(Li) for the SMR stars relative to the young metal-poor clusters. More observations are needed to be able to confirm or deny the possiblity of a slightly enhanced Li plateau in metal-rich stars.

On the other hand, it also worth considering the possiblity that SMR stars have lower initial

A(Li) as posited by, e.g. Guiglion et al. (2016) and discussed at length in the previous section. It is unlikely that the SMR stars had initial A(Li) as low as the plateau value given their present ages and the wealth of observations indicating MS depletion, but as there are no young SMR stars in this study's sample a lower initial Li for these stars cannot strictly be ruled out. However, the general constraint provided by the SMR stars remains intact - by 2-3 Gyr, stars must deplete to the observed plateau value, which is apparently insensitive to metallicity.

6.4 The Origins of the SMR Stars

As discussed in Chapter 1, there is some uncertainty regarding the origin of SMR stars. In general, studies have found that many SMR stars are consistent with being members of the Galactic thin disk (McWilliam & Rich, 1994; Castro et al., 1997; Feltzing & Gustafsson, 1998; Grenon, 1999; Feltzing & Gonzalez, 2001; Barbuy et al., 2010; Pereira et al., 2011), but there are also SMR stars which appear to have a bulge or inner thin disk origin (Barbuy & Grenon, 1990; Barbuy et al., 2010; Trevisan et al., 2010, 2011). The two populations are distinguishable by their abundance ratios - the older population has, for example, [O/Fe] consistent with formation in the regions of the Galaxy that underwent rapid chemical enrichment - [O/Fe]$\sim$+0.2 to +0.3 dex (Barbuy & Grenon, 1990; Trevisan et al., 2010, 2011). There are also kinematic signatures - the older SMR population has galactocentric velocities and orbital eccentricities consistent with inner Galaxy stars that were ejected via, e.g., interactions with the bar (Raboud et al., 1998; Grenon, 1999).

Thus, Grenon (1999) suggested two main sources for SMR stars. First, an intermediate-age (3-5 Gyr) population that formed in the thin disk inside the solar radius from gradually enriched molecular clouds - this population should have kinematics consistent with a thin-disk formation inside the solar circle and abundance ratios typical of the thin disk. Second, an old (10-11 Gyr) population from the bulge or far inner thin disk, characterized by unusual kinematics and abundance ratios atypical of the thin disk.

The implication of Figure 6.4 is that this study's sample of SMR stars is almost entirely composed of the intermediate-age, thin-disk SMR stars, as the ages inferred from the isochrone fits are

in the 3-5 Gyr range. Additionally, the peak in measured A(Li) at $\sim 2.5-2.6$ dex is also indicative of an intermediate age population, as discussed in Section 6.3. It should be noted that bulge stars are not expected in this sample, as the age of the typical bulge star is $\sim 10+$ Gyr (Grenon, 1999). However, stars at the low end of the plateau temperature range evolve off the MS by ~ 8 Gyr. Thus, any SMR bulge stars in the solar neighborhood would be too cool to be included in the sample selected for this study.

While detailed abundance ratios are unavailable for most of this study's SMR stars due to the narrow spectral region studied, the kinematics of the stars can be compared to the values expected given their presumed origin. In Figure 6.7, the U and V space velocities (which indicate the stars' motion relative to the Galactic center in the radial (U) and azimuthal (V) directions) are shown for the SMR stars, as well as the subset of stars observed for this study that have lower [Fe/H], typically 0.0 < [Fe/H] < +0.20. The velocities were taken from the Geneva-Copenhagen (Casagrande et al., 2011) and Hypatia catalogs (Hinkel et al., 2014), and were therefore derived primarily from *Hipparcos* parallaxes in combination with radial velocities from a variety of sources. These velocities do not reflect the Gaia DR2 results, but for the relatively bright, nearby stars examined as part of this study, the *Hipparcos* and *Gaia* parallaxes are in good agreement with one another and using Gaia DR2 parallaxes would not significantly change the velocity results.

From Figure 6.7, several conclusions can be drawn. First, the SMR stars are not kinematically distinct from the lower [Fe/H] stars used as a thin disk control sample. Both populations have on average negative V, indicating they lag the rotation of the galaxy; this suggests formation interior to the solar circle (Grenon, 1999; Pereira et al., 2011), and is supported by their min/max orbital radii, 6.81 ± 0.802 kpc (min) and 8.23 ± 0.24 kpc (max) for the SMR stars and 6.54 ± 0.83 kpc (min) and 8.25 ± 0.31 kpc (max) for the lower-[Fe/H] stars. Given that even the lower-[Fe/H] sample is on average composed of super-solar metallicity stars, this result is unsurprising. Note that the orbital radii are the same for both populations, consistent with the statistically identical eccentricities (0.012 ± 0.050 and 0.025 ± 0.054 for the SMR and non-SMR stars, respectively). These results show that the SMR stars are kinematically similar to the control sample, supporting the notion that

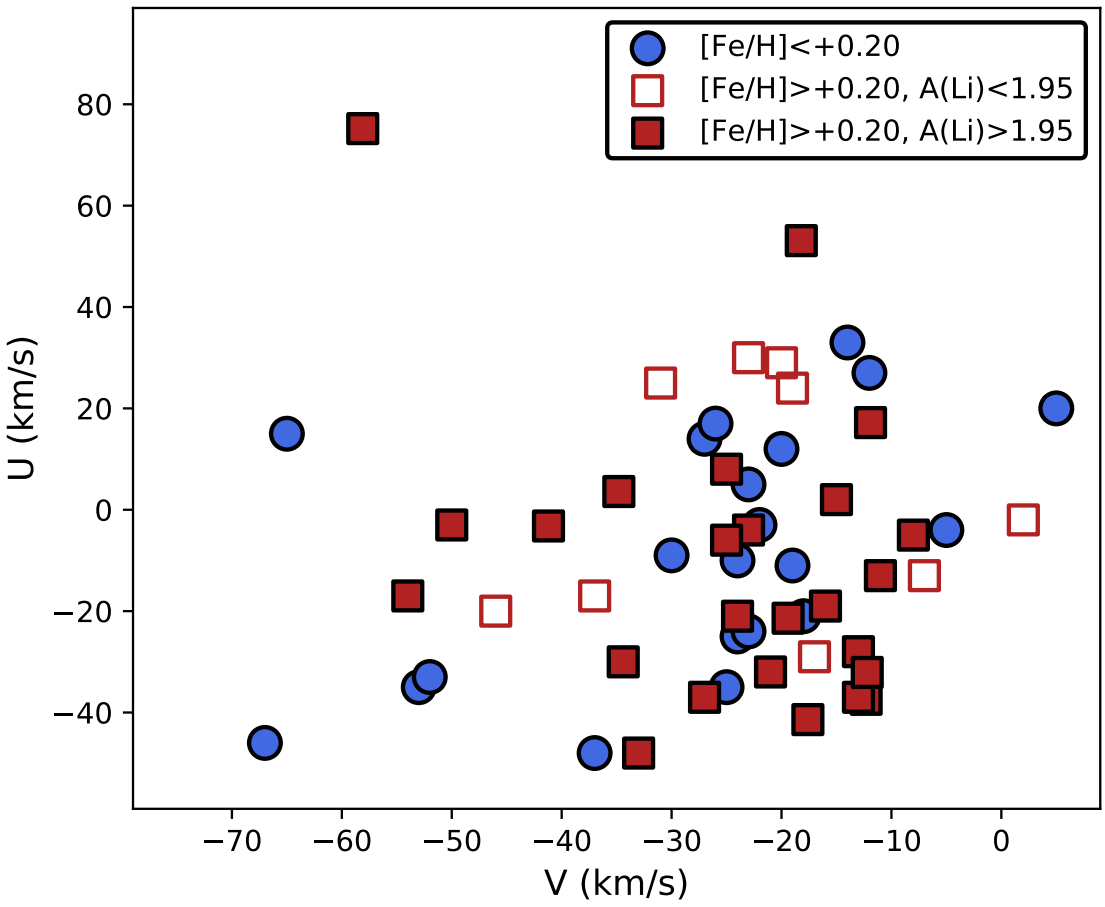

Figure 6.7: *UV* plane for the observed stars - blue circles indicate the low-[Fe/H] sample and red squares denote the SMR stars. The velocities are with respect to the local standard of rest.

they represent the high-metallicity tail of the thin disk.

Comparing these results to other SMR studies further supports the thin disk origin scenario. The positions of the SMR stars in the U-V plane are consistent with those of the disk population identified in Grenon (1999) and Pereira et al. (2011). The dispersions in U and V for the SMR stars are consistent with those of the thin disk SMR stars analyzed by Feltzing & Gonzalez (2001).

As a final check of the SMR kinematics, a Toomre diagram is given in Figure 6.8. The dashed line indicates the boundary established in Nissen (2004) to separate thin and disk components. As with the U-V diagram, it can be seen that the SMR and lower [Fe/H] populations do not lie in different regions of the diagram. Both populations, with the exception of a single outlier each, lie well within the kinematic boundary defining the thin disk.

Taken together, the kinematics of the SMR stars confirm what their ages suggest: they represent a sample of the thin disk SMR population. Support for this comes from internal comparisons (to a sample of lower-[Fe/H] stars) as well as comparison to other stellar population studies. Only one of the SMR stars is consistent with a potential thick disk association.

A final piece of support in favor of the thin disk origin for some of the SMR stars can be found by examining their oxygen abundances as a proxy for alpha abundance. Observations indicate that bulge stars show alpha element enhancements, consistent with the picture of rapid chemical enrichment which resulted in an overabundance of alpha elements relative to iron due to the longer timescales required for supernovae type Ia enrichment (see, e.g., Johnson et al., 2011). As shown in Trevisan et al. (2010), bulge-like SMR stars show enhanced [O/Fe], while metal-rich thin disk stars have [O/Fe] consistent with the observed inverse relation between [O/Fe] and [Fe/H] for lower metallicity thin disk stars (see also McWilliam & Rich, 1994; Feltzing & Gustafsson, 1998; Pereira et al., 2011).

In Figure 6.9, [O/Fe] as a function of [Fe/H] is shown for the 25 stars in the full observed sample (including non-SMR stars) with reported [O/H] in the Hypatia catalog (Hinkel et al., 2014). One star with a poorly constrained [O/H] was omitted from the plot. The Fe abundances used are from this study and were adjusted to the Hypatia metallicity scale (which is ~ 0.05 dex higher than the

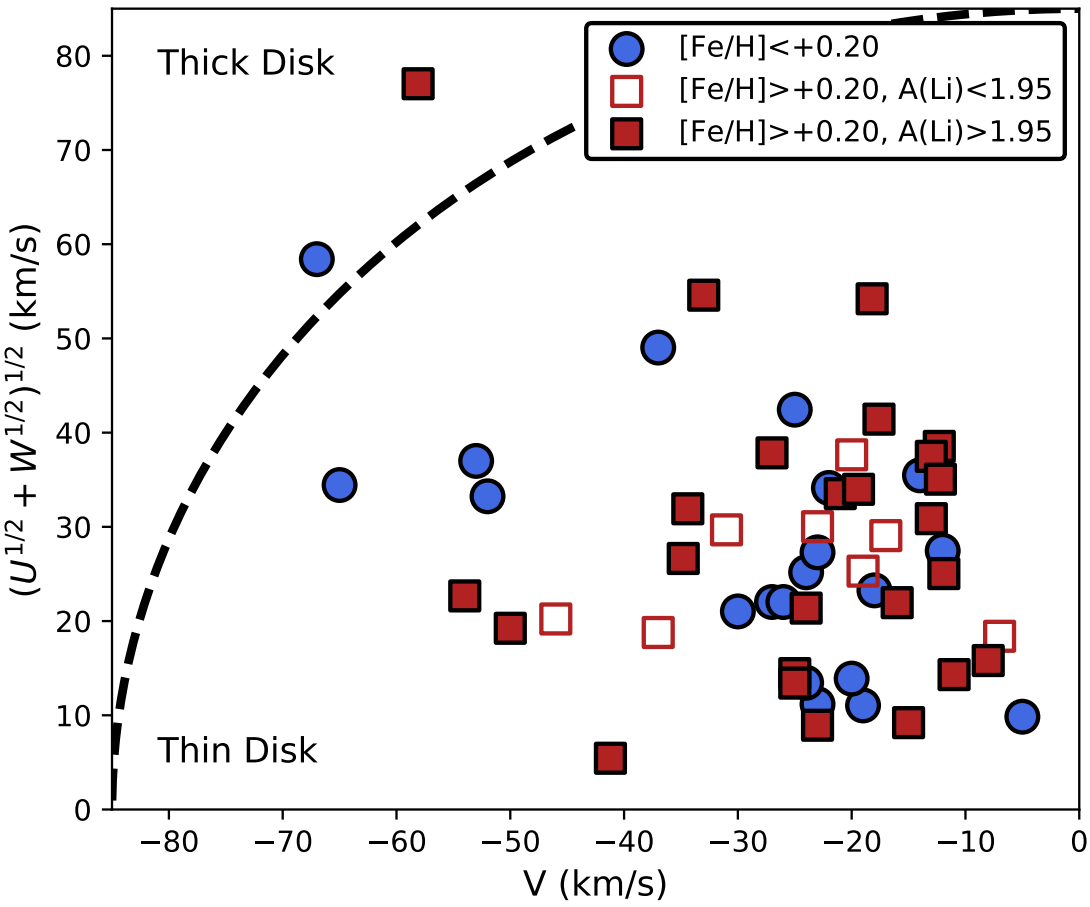

Figure 6.8: Toomre diagram for the stars observed as part of this study. *UVW* measurements are largely from the Geneva-Copenhagen catalog (Casagrande et al., 2011) (using Tycho2 and Hipparcos measurements in addition to GCS radial-velocity measurements), though some are drawn from the Hypatia catalog (Hinkel et al., 2014), and are with respect to the local standard of rest. The filled circles indicate stars with [Fe/H]<+0.20, the unfilled squares indicate stars with [Fe/H]>+0.20 and A(Li)<1.95, and the filled squares represent stars with [Fe/H]>+0.20 and A(Li)>1.95. The dotted line indicates the kinematic boundary between thick and thin disks as defined in Nissen (2004).

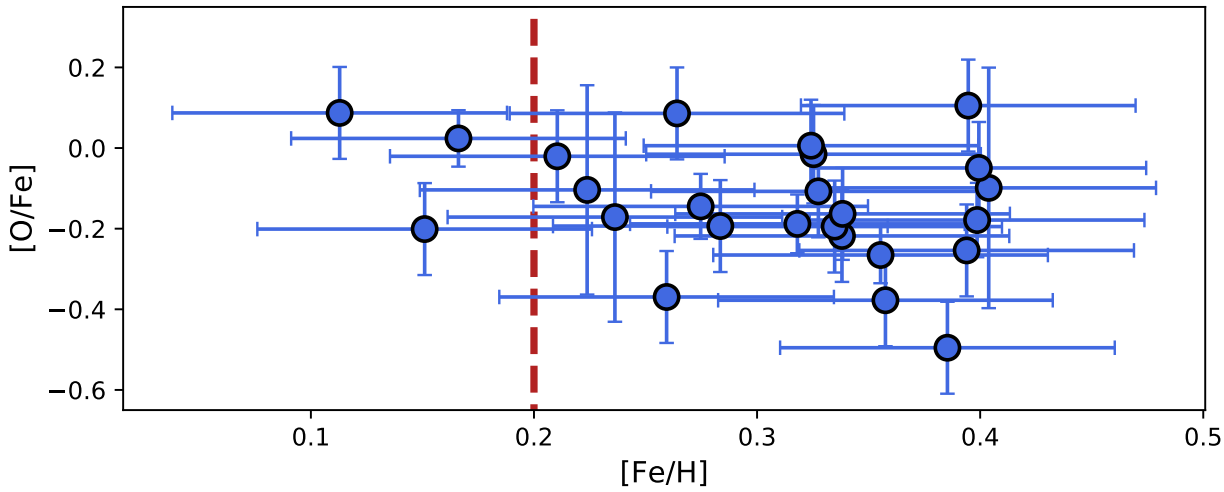

Figure 6.9: [O/Fe] versus [Fe/H] for all stars in the sample with [O/H] reported in the Hypatia catalog (Hinkel et al., 2014). The vertical dashed line indicates the SMR [Fe/H] criterion. The ANNA [Fe/H] measurements used were adjusted to the Hypatia [Fe/H] scale for this figure.

ANNA scale, see Chapter 5).

From Figure 6.9, despite the large uncertainties, it can be seen that the majority of the SMR stars have sub-solar [O/Fe], consistent with the trend of decreasing [O/Fe] as a function of [Fe/H] observed in the local thin disk (see, e.g., Johnson et al., 2011). This can be contrasted with the pattern observed by Trevisan et al. (2010) for a sample of bulge-like SMR stars, where [O/Fe] was found to be supersolar. Unfortunately, oxygen abundances are only available for a small subset of this sample's SMR stars, but for those that do have [O/H] measurements available, the thin disk origin is again favored over inner thin disk or thick disk formation.

Chapter 7

Conclusion

7.1 Summary

The overarching goal of this project was to investigate Li depletion patterns in a sample of super metal-rich ([Fe/H] > +0.20) field stars with temperatures in the region of the F and G dwarf Li plateau. The plateau region in particular was selected because while standard stellar models predict no MS depletion in this temperature range, a number of studies have indicated that MS depletion does occur. However, despite these observations, updated models have been unable to reproduce the depletion and the apparent metallicity insensitivity of the depleted plateau abundance that appears after 2 Gyr of main sequence evolution. SMR stars represent the extreme end of Galactic chemical evolution but have been poorly studied, and therefore represent a valuable opportunity to constrain our understanding of anomalous MS lithium depletion.

Photometric and spectroscopic surveys of the solar neighborhood were used to construct a sample of SMR stars for observation. In total, 100 stars were observed spectroscopically with the Hydra spectrograph on the WIYN 3.5m telescope during the years 2015 – 2017. Most targets were also observed photometrically in the Strömgren $uvbyCaH\beta$ system using the WIYN 0.9m and MLO 40" telescopes at KPNO and Mt. Laguna Observatory, respectively. The typical SN value for the spectra was ~ 200, which enables precise metallicity and Li measurements.

Two methods were used to confirm the metallicity of each SMR candidate. First, a novel tool using an artificial neural network, ANNA, was developed and used to parameterize the SMR candidate spectra. Second, a more traditional EW-based analysis was performed using atmospheric parameters from literature sources or the photometric observations. The results from these semi-

independent analyses compare favorably with one another and with available literature estimates for each star's [Fe/H] and temperature, and allowed an accurate selection of SMR stars.

Using this assortment of data, 44 single, plateau-temperature stars were selected as being bona fide SMR stars with [Fe/H]>+0.20. Li was measured for these stars using the spectrum synthesis method, and Li measurements were confirmed via a second, EW-based method. After measuring Li in the SMR stars the main conclusions of this study are as follows:

1. Consistent with other Li studies, the SMR stars studied here either have measurable Li and A(Li)>2.0 or upper limits only and A(Li) < 2.0. Explanations for this phenomenon from previous studies include evolved dip stars or some as-yet unknown rapid depletion mechanism. On the basis of the low-Li subpopulation's position in an HR diagram, the conclusion of this study is that the low-Li stars are likely evolved Li dip stars that have cooled into the temperature range of the plateau.

2. Considering the upper limit of the SMR stars' Li measurements, there are no stars with A(Li) > 3.0. Galactic chemical evolution models predict a positive correlation between A(Li) and [Fe/H], so the expectation is that SMR stars should have the highest A(Li) abundances. Given that solar-metallicity stars have initial Li of approximately 3.1 – 3.3 dex, SMR stars should have initial A(Li) up to 3.5-3.7 dex. Previous studies in this metallicity regime have suggested that the lower-than-expected A(Li) for SMR stars indicates a possible turnover in the A(Li)-[Fe/H] trend, a conclusion that runs counter to most chemical evolution models. However, given that significant Li depletion has been observed in open cluster plateau stars over the first 2 Gyr of stellar evolution, the use of the upper limit of A(Li) as a tracer of initial Li for a given metallicity requires the inclusion of young (<1 Gyr) stars in the examined sample. Based on the SMR stars' positions in the HR diagram relative to a series of isochrones, all of the SMR stars in this study are consistent with ages in the range 3-4.5 Gyr, i.e they have ages that suggest significant Li depletion has occurred. Ruling out selection effects as a possible reason for the selection of only older SMR stars, the conclusion is that the apparent turnover in A(Li) at high metallicities is most likely due to a lack of young SMR stars in

the solar neighborhood. This conclusion is strengthened by the fact that observations of star formation regions and young open clusters in the solar neighborhood only find metallicities up to [Fe/H]>+0.15, again indicating a general lack of young SMR stars.

3. There is a peak in the distribution of A(Li) in the SMR stars at A(Li) = 2.55$\pm$ 0.21. Given that the SMR stars are relatively close in age and metallicity to one another, this was taken to be the typical plateau value for the sample. Comparing this value with the open cluster NGC 6253, which has similar age and metallicity, this study's SMR plateau is consistent with the plateau in NGC 6253. Comparing with the general trend observed in lower-metallicity open clusters, it is apparent that plateau stars over a wide range in metallicity all deplete their Li from the metallicity-dependent ZAMS value to 2.4-2.6 dex by 2-3 Gyr. The rate of depletion then slows or ceases for the next $\sim$5 Gyr at least. The physical processes responsible for the initial depletion and subsequent stable, metallicity-insensitive plateau are unclear – while rotation is favored by many studies, no models can reproduce the specific depletion patterns.

4. The SMR stars examined by this study are consistent with being typical thin-disk stars with enhanced [Fe/H]. Studies attempting to explain the origins of SMR stars have suggested that SMR stars belong to one or more of several stellar subpopulations: the inner thin disk, the thick disk, or the galactic bulge. The bulge origin for the SMR stars examined by this study is disfavored by the sample selection process – stars with ages > 7 Gyr would not have been selected for observation by this study as they would have already evolved out of the plateau temperature region. Using the stellar kinematic measurements from a variety of sources, the population of SMR stars is kinematically indistinguishable from a lower-metallicity thin-disk dominated control sample. Oxygen abundances, used as a proxy for alpha element abundances, are also consistent with a thin-disk origin. This origin for the SMR stars is consistent with at least one study which suggest that an intermediate-age SMR population may have formed from enriched molecular gas clouds in the inner thin disk and then migrated to the solar neighborhood.

In addition to the science results, ANNA, the Python-based tool for spectroscopic analysis developed during this project, has been made publicly available. ANNA uses a convolutional neural network, a machine learning algorithm, to determine a user-specified set of parameters from an input spectrum after a period of training. The training may be done with either synthetic spectra or real spectra; ANNA provides the ability to pre-process training data, including on-the-fly error modeling. Testing indicates that ANNA is capable of returning parameters at least as accurate as existing methods over a wide range in signal-to-noise and, unlike e.g., the EW method, is capable of inferring parameters solely from spectra and does not require prior information derived from other observations. ANNA is also extremely fast – once trained, it typically performs its classifications in a fraction of a second per spectrum. This latter property especially makes ANNA a useful tool as new instrumentation and surveys dramatically increase the amount of available spectroscopic data.

7.2 Implications and Future Work

This work provides further evidence for a metallicity-independent Li plateau in intermediate-age stars (2-7 Gyr). This surprising result is now anchored by NGC 2243 on the low-metallicity end (François et al., 2013), a number of studies of solar or nearly-solar stars (Deliyannis et al., 1994; Anthony-Twarog et al., 2009; Sestito et al., 2004; Soderblom et al., 1993; Boesgaard et al., 1988), and NGC 6253 (Cummings et al., 2012) as well as this study's SMR stars at high metallicities. Taken together, these results show that the intermediate-age A(Li)=2.6 plateau can be identified in both field stars and clusters.

The metallicity-insensitivity of the Li plateau certainly poses challenges to our models of stellar structure and evolution. Virtually all Li depletion models predict metallicity-dependent Li destruction (Swenson et al., 1994; Pinsonneault, 1997). More fundamentally, our basic understanding of stellar atmospheres indicates that metallicity plays a role in controlling the depth of the surface convection zone in stars via its impact on opacity (e.g., Mowlavi et al., 1998). Thus, regardless of the proposed source of extra mixing responsible for non-SSET Li depletion, it is perplexing that

the intermediate-age plateau is insensitive to [Fe/H].

While this study only strengthens this tension, it does suggest several possible explanations and paves the way for future observational work. As noted above, it is difficult to reconcile the basic expectation that metallicity plays some role in Li depletion with the metallicity-insensitive plateau that appears after a certain age. A possible resolution to this is that metallicity *does* in fact play a role in Li depletion, but that different initial Li abundances obfuscate its effects.

A separate conclusion of this study is that the observed turnover in A(Li) at supersolar [Fe/H] (Delgado Mena et al., 2015; Guiglion et al., 2016; Fu et al., 2018) may be due a lack of young SMR stars in the solar neighborhood. If only older (2+ Gyr) SMR stars can be found in the solar neighborhood, as suggested by this study, then the upper limit of A(Li) in SMR stars would reflect main sequence depletion. If this is true, then initial Li may in fact monotonically increase with [Fe/H], as predicted by models of galactic Li evolution (Travaglio et al., 2001; Prantzos, 2012).

Under such a scenario, metallicity may still play a role in Li plateau depletion, in that higher [Fe/H] results in more rapid depletion over the first few Gyr of stellar evolution, as suggested by standard models (e.g., Pinsonneault, 1997). If the depletion was tied to, e.g., the core-envelope coupling timescales (see e.g., Lanzafame & Spada, 2015), then after several Gyr the depletion would slow or cease. The metallicity-insensitive plateau after this point may merely be a coincidence; higher metallicity stars with higher Li depletion rates but higher initial Li reached the same plateau abundance as lower-metallicity, lower initial Li stars before the mechanism responsible for depletion shuts off. While this coincidence may seem far-fetched at first glance, it is important to note that under the current observational uncertainties, there is still room for a difference of 0.2-0.3 dex between the NGC 2243 and NGC 6253/SMR plateau values. Thus, the scenario suggested above need only deplete Li to approximately the same plateau value; small trends with metallicity consistent with the observational uncertainties cannot be ruled out.

Future observations should be able to further investigate the intermediate-age plateau and test the above suggestion. The two main sources of uncertainty impacting this study are the inferred stellar ages and the uncertainties in plateau value due to small sample sizes. Both of these limi-

tations will be addressed by Gaia. As demonstrated in this study, the precise distances from Gaia allow for reasonable age estimates for field stars via their positions on a temperature-absolute magnitude diagram. Additionally, Gaia will provide an unprecedented number of precise spectroscopic temperature determinations as well as metallicity estimates – these together should enable a much greater sample of plateau stars across a wide range in metallicity to be selected for further observation, as well as improve the likelihood that a selected candidate is indeed a bona fide plateau star. While Gaia will not directly help with the final step of any future studies – measuring Li abundances – it will provide the means to carry out such a study more efficiently, thereby increasing possible sample sizes.

The age estimates enabled by Gaia should allow for a better understanding of the plateau depletion patterns as a function of metallicity over the first few Gyr of stellar evolution. While it may be that no young SMR stars exist in the solar neighborhood, at lower metallicities (slightly subsolar to solar) stars span a range in age (e.g. Sestito & Randich, 2005). Mapping Li depletion in these stars and examining the metallicity-dependence of this depletion, as well as the precise age at which depletion slows, should help shed light on the intermediate-age plateau. This procedure has already been done with solar-like stars (Thévenin et al., 2017) – the task now is to expand the range of metallicities studied.

With these additional observational results, our understanding of the underlying mechanisms responsible for Li depletion should improve. In particular, the tantalizing coincidence between predicted stellar rotational spindown/coupling timescales and the age at which the Li plateau reaches its constant value can be investigated further. The connection between spindown and the Li dip has been suggested observationally by several studies (Balachandran, 1995; Anthony-Twarog et al., 2018). Can observations of a similar pattern in the plateau region edge us closer to a comprehensive understanding of the physics behind non-SSET Li depletion?

Future studies, especially ones leveraging Gaia results, should also be able to shed light on the poorly understood origins of the SMR stars in the solar neighborhood. In this study, the SMR stars were found to be consistent with an inner thin disk formation scenario on the basis of their

kinematics. However, it remains unclear where exactly in the inner thin disk these stars could have formed, and how they subsequently migrated to the solar neighborhood.

A resolution to these unknowns requires both a precise understanding of our Galaxy's chemodynamical history as well as direct observations of the inner regions of the thin disk. Both of these requirements are challenging; observations of the inner thin disk suffer from the extreme dust extinction present in the plane of the Galaxy, and constraining chemodynamical models requires precision kinematics for large populations of stars. Fortunately, Gaia results and other upcoming surveys promise advancements on both these fronts.

On the subject of observations of the inner galactic disk, a particularly useful technique for identifying stars is via observations of Cepheids and other variables. Armed with period-luminosity relations, distances can be derived even when parallaxes are unavailable, and several recent studies have leveraged this technique to shed light on the characteristics of the inner disk (Martin et al., 2015; Inno et al., 2018). Sample sizes are still very small, but the larger samples enabled by future surveys (including Gaia as well as LSST) should help pinpoint where in our Galaxy SMR stars can form. Abundance ratio matching with the SMR stars in the solar neighborhood would also strengthen any link between inner disk SMR stars and those found nearby.

These observational results can then be compared with the predictions of precision chemodynamical models (Robin et al., 2003; Just & Rybizki, 2016). Notable questions to test include: Do chemodynamical model predictions match the kinematic, age, and abundance characteristics of SMR stars in the solar neighborhood? Do observations of inner thin-disk stars match the abundance trends predicted by chemical evolution models? The importance of Gaia in answering these questions cannot be overstated; the exquisite precision and massive sample size enabled by the mission promises to revolutionize our understanding of our galaxy's chemical and dynamical history.

In conclusion, this study supplies enhanced boundary conditions for our understanding of stellar structure and the evolution of internal mixing processes by providing the largest self-contained sample of Li plateau observations for SMR stars. These observations serve to confirm patterns

observed by previous efforts – notably the metallicity-insensitive intermediate-age Li plateau. Simultaneously, they pose new questions for future studies – what are the origins of SMR stars in the solar neighborhood and why are there no or very few nearby, young, SMR stars? Answers to these questions, combined with the conclusions from this work and studies before it, will advance our knowledge of the Galaxy and stars within it.

7.3 Facility, Software and Grant Support

The author used the WIYN 0.9m and 3.5m telescopes as a visiting astronomer at Kitt Peak National Observatory, National Optical Astronomy Observatory, which is operated by the Association of Universities for Research in Astronomy (AURA) under a cooperative agreement with the National Science Foundation. The WIYN Observatory is a joint facility of the University of Wisconsin-Madison, Indiana University, the National Optical Astronomy Observatory and the University of Missouri.

This work has made use of data from the European Space Agency (ESA) mission *Gaia*, processed by the *Gaia* Data Processing and Analysis Consortium (DPAC). Funding for the DPAC has been provided by national institutions, in particular the institutions participating in the *Gaia* Multilateral Agreement.

The author gratefully acknowledges support for this project under National Science Foundation grant AST-1211621 and a University of Kansas Graduate Summer Research Scholarship.

Additional software support was provided by the TOPCAT suite (http://www.star.bristol.ac.uk/mbt/topcat/), the Vienna VALD (Kupka et al., 1999), ROBOSPECT Waters & Hollek (2013), and MOOG (Sneden, 1973a).

This research has made use of the SIMBAD database, operated at CDS, Strasbourg, France.

TensorFlow, the TensorFlow logo and any related markes are trademarks of Google, Inc.

References

Aguilera-Gómez, C., Ramírez, I., & Chanamé, J. (2018). Lithium abundance patterns of late-F stars: an in-depth analysis of the lithium desert. *Accepted for publication, A&A, ArXiv e-prints: 1803.05922*.

Allende Prieto, C., Rebolo, R., García López, R. J., Serra-Ricart, M., Beers, T. C., Rossi, S., Bonifacio, P., & Molaro, P. (2000). The INT Search for Metal-Poor Stars: Spectroscopic Observations and Classification via Artificial Neural Networks. *The Astronomical Journal*, 120, 1516–1531.

Anthony-Twarog, B. J., Deliyannis, C. P., Rich, E., & Twarog, B. A. (2013). A Lithium-rich Red Giant Below the Clump in the Kepler Cluster, NGC 6819. *ApJ*, 767, L19.

Anthony-Twarog, B. J., Deliyannis, C. P., & Twarog, B. A. (2014). A uvbyCaHβ Analysis of the Old Open Cluster, NGC 6819. *AJ*, 148, 51.

Anthony-Twarog, B. J., Deliyannis, C. P., & Twarog, B. A. (2016). WIYN Open Cluster Study. LXXII. A uvbyCaHβ CCD Analysis of the Metal-deficient Open Cluster NGC 2506. *AJ*, 152, 192.

Anthony-Twarog, B. J., Deliyannis, C. P., Twarog, B. A., Croxall, K. V., & Cummings, J. D. (2009). Lithium in the Intermediate-Age Open Cluster, NGC 3680. *AJ*, 138, 1171–1191.

Anthony-Twarog, B. J., Lee-Brown, D. B., Deliyannis, C. P., & Twarog, B. A. (2018). WIYN Open Cluster Study. LXXVI. Li Evolution Among Stars of Low/Intermediate Mass: The Metal-deficient Open Cluster NGC 2506. *AJ*, 155, 138.

Arnould, M. & Norgaard, H. (1975). The Explosive Thermonuclear Formation of 7Li and 11B. *A&A*, 42, 55.

Asplund, M., Grevesse, N., Sauval, A. J., & Scott, P. (2009). The Chemical Composition of the Sun. *ARA&A*, 47, 481–522.

Bailer-Jones, C. A. L., Gupta, R., & Singh, H. P. (2002). An Introduction to Artificial Neural Networks. In R. Gupta, H. P. Singh, & C. A. L. Bailer-Jones (Eds.), *Automated Data Analysis in Astronomy* (pp.5̃1).

Bailer-Jones, C. A. L., Irwin, M., Gilmore, G., & von Hippel, T. (1997). Physical parametrization of stellar spectra - The neural network approach. *Monthly Notices of the Royal Astronomical Society*, 292, 157.

Bailly, S. (2011). Gravitino dark matter and the lithium primordial abundance within a pre-BBN modified expansion. *JCAP*, 3, 022.

Balachandran, S. (1995). The Lithium Dip in M67: Comparison with the Hyades, Praesepe, and NGC 752 Clusters. *ApJ*, 446, 203.

Barbuy, B. & Grenon, M. (1990). Oxygen in bulge-like super-metal-rich stars. In B. J. Jarvis & D. M. Terndrup (Eds.), *European Southern Observatory Conference and Workshop Proceedings*, volume 35 of *European Southern Observatory Conference and Workshop Proceedings* (pp. 83–86).

Barbuy, B., Trevisan, M., Gustafsson, B., Eriksson, K., Grenon, M., & Pompéia, L. (2010). Lithium abundances in Bulge-like SMR stars. In C. Charbonnel, M. Tosi, F. Primas, & C. Chiappini (Eds.), *Light Elements in the Universe*, volume 268 of *IAU Symposium* (pp. 325–326).

Barden, S. C., Armandroff, T., Massey, P., Groves, L., Rudeen, A. C., Vaughnn, D., & Muller, G. (1993). Hydra - Kitt Peak Multi-Object Spectroscopic System. In P. M. Gray (Ed.), *Fiber Optics in Astronomy II*, volume 37 of *Astronomical Society of the Pacific Conference Series* (pp. 185).

Baumann, P., Ramírez, I., Meléndez, J., Asplund, M., & Lind, K. (2010). Lithium depletion in solar-like stars: no planet connection. *A&A*, 519, A87.

Bhadani, A. & Jothimani, D. (2017). Big Data: Challenges, Opportunities and Realities. *Effective Big Data Management and Opportunities for Implementation*, (pp. 1–24).

Bishop, C. M. (1995). *Neural Networks for Pattern Recognition*. New York, NY, USA: Oxford University Press, Inc.

Blanco-Cuaresma, S., Soubiran, C., Heiter, U., & Jofré, P. (2014). Determining stellar atmospheric parameters and chemical abundances of FGK stars with iSpec. *A&A*, 569, A111.

Boesgaard, A. M. (1976). Stellar abundances of lithium, beryllium, and boron. *PASP*, 88, 353–366.

Boesgaard, A. M., Armengaud, E., King, J. R., Deliyannis, C. P., & Stephens, A. (2004). The Correlation of Lithium and Beryllium in F and G Field and Cluster Dwarf Stars. *ApJ*, 613, 1202–1212.

Boesgaard, A. M., Budge, K. G., & Ramsay, M. E. (1988). Lithium in the Pleiades and Alpha Persei clusters. *ApJ*, 327, 389–398.

Boesgaard, A. M. & King, J. R. (2002). Beryllium in the Hyades F and G Dwarfs from Keck HIRES Spectra. *ApJ*, 565, 587–597.

Boesgaard, A. M., Lum, M. G., & Deliyannis, C. P. (2015). The Old, Super-metal-rich Open Cluster, NGC 6791: Elemental Abundances in Turn-off Stars from Keck/HIRES Spectra. *ApJ*, 799, 202.

Boesgaard, A. M., Lum, M. G., Deliyannis, C. P., King, J. R., Pinsonneault, M. H., & Somers, G. (2016). Boron Abundances Across the Li-Be Dip in the Hyades Cluster. *ApJ*, 830, 49.

Boesgaard, A. M. & Tripicco, M. J. (1986). Lithium in the Hyades Cluster. *ApJ*, 302, L49–L53.

Bragaglia, A., Carretta, E., Gratton, R. G., Tosi, M., Bonanno, G., Bruno, P., Calì, A., Claudi, R., Cosentino, R., Desidera, S., Farisato, G., Rebeschini, M., & Scuderi, S. (2001). Metal Abundances of Red Clump Stars in Open Clusters. I. NGC 6819. *AJ*, 121, 327–336.

Bressan, A., Marigo, P., Girardi, L., Salasnich, B., Dal Cero, C., Rubele, S., & Nanni, A. (2012). PARSEC: stellar tracks and isochrones with the PAdova and TRieste Stellar Evolution Code. *MNRAS*, 427, 127–145.

Burkhart, C. & Coupry, M. F. (2000). The Pleiades, Coma, Hyades, and Praesepe open clusters: Li, Al, Si, S, Fe, Ni, and Eu abundances compared in A stars. *A&A*, 354, 216–228.

Butler, R. P., Tinney, C. G., Marcy, G. W., Jones, H. R. A., Penny, A. J., & Apps, K. (2001). Two New Planets from the Anglo-Australian Planet Search. *ApJ*, 555, 410–417.

Cabrera-Vives, G., Reyes, I., Förster, F., Estévez, P. A., & Maureira, J.-C. (2017). Deep-HiTS: Rotation Invariant Convolutional Neural Network for Transient Detection. *ApJ*, 836, 97.

Cameron, A. G. W. & Fowler, W. A. (1971). Lithium and the s-PROCESS in Red-Giant Stars. *ApJ*, 164, 111.

Casagrande, L., Ramírez, I., Meléndez, J., Bessell, M., & Asplund, M. (2010). An absolutely calibrated T_{eff} scale from the infrared flux method. Dwarfs and subgiants. *A&A*, 512, A54.

Casagrande, L., Schönrich, R., Asplund, M., Cassisi, S., Ramírez, I., Meléndez, J., Bensby, T., & Feltzing, S. (2011). New constraints on the chemical evolution of the solar neighbourhood and Galactic disc(s). Improved astrophysical parameters for the Geneva-Copenhagen Survey. *A&A*, 530, A138.

Castro, S., Rich, R. M., Grenon, M., Barbuy, B., & McCarthy, J. K. (1997). High-Resolution Abundance Analysis of Very Metal-rich Stars in the Solar Neighborhood. *AJ*, 114, 376–387.

Cayrel de Strobel, G. & Spite, M., Eds. (1988). *The impact of very high S/N spectroscopy on stellar physics: proceedings of the 132nd Symposium of the International Astronomical Union held in Paris, France, June 29-July 3, 1987.*, volume 132 of *IAU Symposium*.

Chaboyer, B., Demarque, P., & Pinsonneault, M. H. (1995). Stellar models with microscopic diffusion and rotational mixing. 2: Application to open clusters. *ApJ*, 441, 876–885.

Charbonnel, C. & Talon, S. (2005). Influence of Gravity Waves on the Internal Rotation and Li Abundance of Solar-Type Stars. *Science*, 309, 2189–2191.

Charbonnel, C. & Zahn, J.-P. (2007). Thermohaline mixing: a physical mechanism governing the photospheric composition of low-mass giants. *A&A*, 467, L15–L18.

Chen, Y. Q., Nissen, P. E., Benoni, T., & Zhao, G. (2001). Lithium abundances for 185 main-sequence stars: Galactic evolution and stellar depletion of lithium. *A&A*, 371, 943–951.

Chiappini, C., Matteucci, F., & Gratton, R. (1997). The Chemical Evolution of the Galaxy: The Two-Infall Model. *ApJ*, 477, 765–780.

Chrysos, G. G., Panagakis, Y., & Zafeiriou, S. (2018). Visual Data Augmentation through Learning. *ArXiv e-prints: 1801.06665*.

Cirasuolo, M., Afonso, J., Carollo, M., Flores, H., Maiolino, R., Oliva, E., Paltani, S., Vanzi, L., Evans, C., Abreu, M., Atkinson, D., Babusiaux, C., Beard, S., Bauer, F., Bellazzini, M., Bender, R., Best, P., Bezawada, N., Bonifacio, P., Bragaglia, A., Bryson, I., Busher, D., Cabral, A., Caputi, K., Centrone, M., Chemla, F., Cimatti, A., Cioni, M.-R., Clementini, G., Coelho, J., Crnojevic, D., Daddi, E., Dunlop, J., Eales, S., Feltzing, S., Ferguson, A., Fisher, M., Fontana, A., Fynbo, J., Garilli, B., Gilmore, G., Glauser, A., Guinouard, I., Hammer, F., Hastings, P., Hess, A., Ivison, R., Jagourel, P., Jarvis, M., Kaper, L., Kauffman, G., Kitching, A. T., Lawrence, A., Lee, D., Lemasle, B., Licausi, G., Lilly, S., Lorenzetti, D., Lunney, D., Maiolino, R., Mannucci, F., McLure, R., Minniti, D., Montgomery, D., Muschielok, B., Nandra, K., Navarro, R., Norberg, P., Oliver, S., Origlia, L., Padilla, N., Peacock, J., Pedichini, F., Peng, J., Pentericci, L., Pragt, J., Puech, M., Randich, S., Rees, P., Renzini, A., Ryde, N., Rodrigues, M., Roseboom, I., Royer, F., Saglia, R., Sanchez, A., Schiavon, R., Schnetler, H., Sobral, D., Speziali, R., Sun, D., Stuik, R., Taylor, A., Taylor, W., Todd, S., Tolstoy, E., Torres, M., Tosi, M., Vanzella, E., Venema, L., Vitali, F., Wegner, M., Wells, M., Wild, V., Wright, G., Zamorani, G., & Zoccali, M. (2014). MOONS: the Multi-Object Optical and Near-infrared Spectrograph for the VLT. In

Ground-based and Airborne Instrumentation for Astronomy V, volume 9147 of *Proc. SPIE* (pp. 91470N).

Coc, A., Goriely, S., Xu, Y., Saimpert, M., & Vangioni, E. (2012). Standard Big Bang Nucleosynthesis up to CNO with an Improved Extended Nuclear Network. *ApJ*, 744, 158.

Coc, A., Uzan, J.-P., & Vangioni, E. (2014). Standard big bang nucleosynthesis and primordial CNO abundances after Planck. *JCAP*, 10, 050.

Creswell, A., White, T., Dumoulin, V., Arulkumaran, K., Sengupta, B., & Bharath, A. A. (2018). Generative adversarial networks: An overview. *IEEE Signal Processing Magazine*, 35(1), 53–65.

Cummings, J. D., Deliyannis, C. P., Anthony-Twarog, B., Twarog, B., & Maderak, R. M. (2012). Lithium Abundances of the Super-metal-rich Open Cluster NGC 6253. *AJ*, 144, 137.

Cummings, J. D., Deliyannis, C. P., Maderak, R. M., & Steinhauer, A. (2017). WIYN Open Cluster Study. LXXV. Testing the Metallicity Dependence of Stellar Lithium Depletion Using Hyades-aged Clusters. I. Hyades and Praesepe. *AJ*, 153, 128.

Dafonte, C., Fustes, D., Manteiga, M., Garabato, D., Álvarez, M. A., Ulla, A., & Allende Prieto, C. (2016). On the estimation of stellar parameters with uncertainty prediction from Generative Artificial Neural Networks: application to Gaia RVS simulated spectra. *Astronomy & Astrophysics*, 594, A68.

De Silva, G. M., Freeman, K. C., Bland-Hawthorn, J., Martell, S., de Boer, E. W., Asplund, M., Keller, S., Sharma, S., Zucker, D. B., Zwitter, T., Anguiano, B., Bacigalupo, C., Bayliss, D., Beavis, M. A., Bergemann, M., Campbell, S., Cannon, R., Carollo, D., Casagrande, L., Casey, A. R., Da Costa, G., D'Orazi, V., Dotter, A., Duong, L., Heger, A., Ireland, M. J., Kafle, P. R., Kos, J., Lattanzio, J., Lewis, G. F., Lin, J., Lind, K., Munari, U., Nataf, D. M., O'Toole, S., Parker, Q., Reid, W., Schlesinger, K. J., Sheinis, A., Simpson, J. D., Stello, D., Ting, Y.-S.,

Traven, G., Watson, F., Wittenmyer, R., Yong, D., & Žerjal, M. (2015). The GALAH survey: scientific motivation. *MNRAS*, 449, 2604–2617.

Dearborn, D. S. P., Schramm, D. N., Steigman, G., & Truran, J. (1989). The shocking development of lithium (and boron) in supernovae. *ApJ*, 347, 455–460.

Delgado Mena, E., Bertrán de Lis, S., Adibekyan, V. Z., Sousa, S. G., Figueira, P., Mortier, A., González Hernández, J. I., Tsantaki, M., Israelian, G., & Santos, N. C. (2015). Li abundances in F stars: planets, rotation, and Galactic evolution. *A&A*, 576, A69.

Deliyannis, C. P., Demarque, P., & Kawaler, S. D. (1990). Lithium in halo stars from standard stellar evolution. *ApJS*, 73, 21–65.

Deliyannis, C. P., King, J. R., Boesgaard, A. M., & Ryan, S. G. (1994). Lithium in a short-period tidally locked binary of M67: Implications for stellar evolution, Galactic Lithium evolution, and cosmology. *ApJ*, 434, L71–L74.

Deliyannis, C. P. & Pinsonneault, M. H. (1997). 110 Herculis: A Possible Prototype for Simultaneous Lithium and Beryllium Depletion, and Implications for Stellar Interiors. *ApJ*, 488, 836–840.

Deliyannis, C. P., Pinsonneault, M. H., & Duncan, D. K. (1993). Evidence for a dispersion in the lithium abundances of extreme halo stars. *ApJ*, 414, 740–758.

Do Nascimento, J. D., da Costa, J. S., & de Medeiros, J. R. (2010). Rotation and lithium abundance of solar-analog stars. Theoretical analysis of observations. *A&A*, 519, A101.

Drissen, L., Bernier, A.-P., Rousseau-Nepton, L., Alarie, A., Robert, C., Joncas, G., Thibault, S., & Grandmont, F. (2010). SITELLE: a wide-field imaging Fourier transform spectrometer for the Canada-France-Hawaii Telescope. In *Ground-based and Airborne Instrumentation for Astronomy III*, volume 7735 of *Proc. SPIE* (pp. 77350B).

Edvardsson, B., Andersen, J., Gustafsson, B., Lambert, D. L., Nissen, P. E., & Tomkin, J. (1993). The Chemical Evolution of the Galactic Disk - Part One - Analysis and Results. *A&A*, 275, 101.

Eggenberger, P., Maeder, A., & Meynet, G. (2010). Effects of rotation and magnetic fields on the lithium abundance and asteroseismic properties of exoplanet-host stars. *A&A*, 519, L2.

Ezzeddine, R., Frebel, A., & Plez, B. (2017). Ultra-metal-poor Stars: Spectroscopic Determination of Stellar Atmospheric Parameters Using Iron Non-LTE Line Abundances. *ApJ*, 847, 142.

Feltzing, S. & Gonzalez, G. (2001). The nature of super-metal-rich stars. Detailed abundance analysis of 8 super-metal-rich star candidates. *A&A*, 367, 253–265.

Feltzing, S. & Gustafsson, B. (1998). Abundances in metal-rich stars. Detailed abundance analysis of 47 G and K dwarf stars with [Me/H] > 0.10 dex. *A&AS*, 129, 237–266.

Fields, B. D. & Olive, K. A. (1999). The Revival of Galactic Cosmic-Ray Nucleosynthesis? *ApJ*, 516, 797–810.

Fischer, D. A. & Valenti, J. (2005). The Planet-Metallicity Correlation. *ApJ*, 622, 1102–1117.

Flaugher, B. & Bebek, C. (2014). The Dark Energy Spectroscopic Instrument (DESI). In *Ground-based and Airborne Instrumentation for Astronomy V*, volume 9147 of *Proc. SPIE* (pp. 91470S).

François, P., Pasquini, L., Biazzo, K., Bonifacio, P., & Palsa, R. (2013). Lithium abundance in the metal-poor open cluster NGC 2243 . *A&A*, 552, A136.

Frankowski, A., Jancart, S., & Jorissen, A. (2007). Proper-motion binaries in the Hipparcos catalogue. Comparison with radial velocity data. *A&A*, 464, 377–392.

Fu, X., Romano, D., Bragaglia, A., Mucciarelli, A., Lind, K., Delgado Mena, E., Sousa, S. G., Randich, S., Bressan, A., Sbordone, L., Martell, S., Korn, A. J., Abia, C., Smiljanic, R., Jofré, P., Pancino, E., Tautvaišienė, G., Tang, B., Magrini, L., Lanzafame, A. C., Carraro, G., Bensby, T., Damiani, F., Alfaro, E. J., Flaccomio, E., Morbidelli, L., Zaggia, S., Lardo, C., Monaco, L., Frasca, A., Donati, P., Drazdauskas, A., Chorniy, Y., Bayo, A., & Kordopatis, G. (2018). The Gaia-ESO Survey: Lithium enrichment histories of the Galactic thick and thin disc. *A&A*, 610, A38.

Gaia Collaboration, Brown, A. G. A., Vallenari, A., Prusti, T., de Bruijne, J. H. J., Mignard, F., Drimmel, R., Babusiaux, C., Bailer-Jones, C. A. L., Bastian, U., & et al. (2016a). Gaia Data Release 1. Summary of the astrometric, photometric, and survey properties. *A&A*, 595, A2.

Gaia Collaboration, Prusti, T., de Bruijne, J. H. J., Brown, A. G. A., Vallenari, A., Babusiaux, C., Bailer-Jones, C. A. L., Bastian, U., Biermann, M., Evans, D. W., & et al. (2016b). The Gaia mission. *A&A*, 595, A1.

García-Hernández, D. A., Zamora, O., Yagüe, A., Uttenthaler, S., Karakas, A. I., Lugaro, M., Ventura, P., & Lambert, D. L. (2013). Hot bottom burning and s-process nucleosynthesis in massive AGB stars at the beginning of the thermally-pulsing phase. *A&A*, 555, L3.

Garcia Lopez, R. J. & Spruit, H. C. (1991). Li depletion in F stars by internal gravity waves. *ApJ*, 377, 268–277.

García Pérez, A. E., Allende Prieto, C., Holtzman, J. A., Shetrone, M., Mészáros, S., Bizyaev, D., Carrera, R., Cunha, K., García-Hernández, D. A., Johnson, J. A., Majewski, S. R., Nidever, D. L., Schiavon, R. P., Shane, N., Smith, V. V., Sobeck, J., Troup, N., Zamora, O., Weinberg, D. H., Bovy, J., Eisenstein, D. J., Feuillet, D., Frinchaboy, P. M., Hayden, M. R., Hearty, F. R., Nguyen, D. C., O'Connell, R. W., Pinsonneault, M. H., Wilson, J. C., & Zasowski, G. (2016). ASPCAP: The APOGEE Stellar Parameter and Chemical Abundances Pipeline. *AJ*, 151, 144.

Garofalo, M., Botta, A., & Ventre, G. (2017). Astrophysics and Big Data: Challenges, Methods, and Tools. In M. Brescia, S. G. Djorgovski, E. D. Feigelson, G. Longo, & S. Cavuoti (Eds.), *Astroinformatics*, volume 325 of *IAU Symposium* (pp. 345–348).

Ghezzi, L., Cunha, K., Smith, V. V., & de la Reza, R. (2010). Lithium Abundances in a Sample of Planet-hosting Dwarfs. *ApJ*, 724, 154–164.

Gilliland, R. L., Brown, T. M., Christensen-Dalsgaard, J., Kjeldsen, H., Aerts, C., Appourchaux, T., Basu, S., Bedding, T. R., Chaplin, W. J., Cunha, M. S., De Cat, P., De Ridder, J., Guzik,

J. A., Handler, G., Kawaler, S., Kiss, L., Kolenberg, K., Kurtz, D. W., Metcalfe, T. S., Monteiro, M. J. P. F. G., Szabó, R., Arentoft, T., Balona, L., Debosscher, J., Elsworth, Y. P., Quirion, P.-O., Stello, D., Suárez, J. C., Borucki, W. J., Jenkins, J. M., Koch, D., Kondo, Y., Latham, D. W., Rowe, J. F., & Steffen, J. H. (2010). Kepler Asteroseismology Program: Introduction and First Results. *PASP*, 122, 131.

Gim, M., Vandenberg, D. A., Stetson, P. B., Hesser, J. E., & Zurek, D. R. (1998). The Open Cluster NGC 7789. II. CCD VI Photometry. *PASP*, 110, 1318–1335.

Gonzalez, G. & Laws, C. (2000). Parent Stars of Extrasolar Planets. V. HD 75289. *AJ*, 119, 390–396.

Graff, P., Feroz, F., Hobson, M. P., & Lasenby, A. (2014). SKYNET: an efficient and robust neural network training tool for machine learning in astronomy. *MNRAS*, 441, 1741–1759.

Gray, D. F. (1976). *The observation and analysis of stellar photospheres*.

Gray, D. F. (1996). The determination of temperature from spectral lines. In K. G. Strassmeier & J. L. Linsky (Eds.), *Stellar Surface Structure*, volume 176 of *IAU Symposium* (pp. 227).

Gray, R. O. & Corbally, C. J. (1994). The calibration of MK spectral classes using spectral synthesis. 1: The effective temperature calibration of dwarf stars. *AJ*, 107, 742–746.

Grenon, M. (1999). The Kinematics and Origin of smr Stars. *Ap&SS*, 265, 331–336.

Guiglion, G., de Laverny, P., Recio-Blanco, A., Worley, C. C., De Pascale, M., Masseron, T., Prantzos, N., & Mikolaitis, Š. (2016). The AMBRE project: Constraining the lithium evolution in the Milky Way. *A&A*, 595, A18.

Hartmann, D., Myers, J., Woosley, S., Hoffman, R., & Haxton, W. (1999). Neutrino Process Contributions to LiBeB Nucleosynthesis. In R. Ramaty, E. Vangioni-Flam, M. Cassé, & K. Olive (Eds.), *LiBeB Cosmic Rays, and Related X- and Gamma-Rays*, volume 171 of *Astronomical Society of the Pacific Conference Series* (pp. 235).

Hauck, B. & Mermilliod, M. (1980). Uvbybeta photoelectric photometric catalogue. *A&AS*, 40, 1–32.

Haykin, S. (1998). *Neural Networks: A Comprehensive Foundation*. Upper Saddle River, NJ, USA: Prentice Hall PTR, 2nd edition.

He, K., Zhang, X., Ren, S., & Sun, J. (2015). Delving deep into rectifiers: Surpassing human-level performance on imagenet classification. In *The IEEE International Conference on Computer Vision (ICCV)*.

Henault, F., Bacon, R., Bonneville, C., Boudon, D., Davies, R. L., Ferruit, P., Gilmore, G. F., Le Fèvre, O., Lemonnier, J.-P., Lilly, S., Morris, S. L., Prieto, E., Steinmetz, M., & de Zeeuw, P. T. (2003). MUSE: a second-generation integral-field spectrograph for the VLT. In M. Iye & A. F. M. Moorwood (Eds.), *Instrument Design and Performance for Optical/Infrared Ground-based Telescopes*, volume 4841 of *Proc. SPIE* (pp. 1096–1107).

Hezaveh, Y. D., Levasseur, L. P., & Marshall, P. J. (2017). Fast automated analysis of strong gravitational lenses with convolutional neural networks. *Nature*, 548, 555–557.

Hill, J. M. (1988). The History of Multiobject Fiber Spectroscopy. In S. C. Barden (Ed.), *Fiber Optics in Astronomy*, volume 3 of *Astronomical Society of the Pacific Conference Series* (pp.̃77).

Hinkel, N. R., Mamajek, E. E., Turnbull, M. C., Osby, E., Shkolnik, E. L., Smith, G. H., Klimasewski, A., Somers, G., & Desch, S. J. (2017). A Catalog of Stellar Unified Properties (CATSUP) for 951 FGK-Stars within 30 pc. *ApJ*, 848, 34.

Hinkel, N. R., Timmes, F. X., Young, P. A., Pagano, M. D., & Turnbull, M. C. (2014). Stellar Abundances in the Solar Neighborhood: The Hypatia Catalog. *AJ*, 148, 54.

Hinkel, N. R., Young, P. A., Pagano, M. D., Desch, S. J., Anbar, A. D., Adibekyan, V., Blanco-Cuaresma, S., Carlberg, J. K., Delgado Mena, E., Liu, F., Nordlander, T., Sousa, S. G., Korn,

A., Gruyters, P., Heiter, U., Jofré, P., Santos, N. C., & Soubiran, C. (2016). A Comparison of Stellar Elemental Abundance Techniques and Measurements. *ApJS*, 226, 4.

Hobbs, L. M. & Pilachowski, C. (1988). Lithium in old open clusters - NGC 188. *ApJ*, 334, 734–745.

Hole, K. T., Geller, A. M., Mathieu, R. D., Platais, I., Meibom, S., & Latham, D. W. (2009). WIYN Open Cluster Study. XXIV. Stellar Radial-Velocity Measurements in NGC 6819. *AJ*, 138, 159–168.

Inno, L., Urbaneja, M. A., Matsunaga, N., Bono, G., Nonino, M., Debattista, V. P., Sormani, M., Bergemann, M., da Silva, R., Lemasle, B., Romaniello, M., & Rix, H. (2018). First metallicity determination from Near-Infrared spectra for five obscured Cepheids discovered in the inner Disk. *ArXiv e-prints: 1805.03212*.

Iocco, F., Mangano, G., Miele, G., Pisanti, O., & Serpico, P. D. (2007). Path to metallicity: Synthesis of CNO elements in standard BBN. *Phys. Rev. D*, 75(8), 087304.

Israelian, G., Delgado Mena, E., Santos, N. C., Sousa, S. G., Mayor, M., Udry, S., Domínguez Cerdeña, C., Rebolo, R., & Randich, S. (2009). Enhanced lithium depletion in Sun-like stars with orbiting planets. *Nature*, 462, 189–191.

Jeffries, R. D. (2000). Lithium depletion in open clusters. In R. Pallavicini, G. Micela, & S. Sciortino (Eds.), *Stellar Clusters and Associations: Convection, Rotation, and Dynamos*, volume 198 of *Astronomical Society of the Pacific Conference Series* (pp. 245).

Jeffries, R. D., Totten, E. J., Harmer, S., & Deliyannis, C. P. (2002). Membership, metallicity and lithium abundances for solar-type stars in NGC 6633. *MNRAS*, 336, 1109–1128.

Johnson, C. I., Rich, R. M., Fulbright, J. P., Valenti, E., & McWilliam, A. (2011). Alpha Enhancement and the Metallicity Distribution Function of Plaut's Window. *ApJ*, 732, 108.

Ju, C., Bibaut, A., & van der Laan, M. J. (2017). The Relative Performance of Ensemble Methods with Deep Convolutional Neural Networks for Image Classification. *ArXiv e-prints: 1704.01664*.

Just, A. & Rybizki, J. (2016). Dynamical and chemical evolution of the thin disc. *Astronomische Nachrichten*, 337, 880.

Kang, M.-m., Hu, Y., Hu, H.-b., & Zhu, S.-h. (2012). Cosmic rays during BBN as origin of Lithium problem. *JCAP*, 5, 011.

Kim, E. J. & Brunner, R. J. (2017). Star-galaxy classification using deep convolutional neural networks. *MNRAS*, 464, 4463–4475.

Kingma, D. P. & Ba, J. (2014). Adam: A method for stochastic optimization. In *Proceedings of the 3rd International Conference on Learning Representations (ICLR)*.

Kirby, E. N., Guhathakurta, P., Zhang, A. J., Hong, J., Guo, M., Guo, R., Cohen, J. G., & Cunha, K. (2016). Lithium-rich Giants in Globular Clusters. *ApJ*, 819, 135.

Knauth, D. C., Federman, S. R., Lambert, D. L., & Crane, P. (2000). Newly synthesized lithium in the interstellar medium. *Nature*, 405, 656–658.

Komatsu, E., Smith, K. M., Dunkley, J., Bennett, C. L., Gold, B., Hinshaw, G., Jarosik, N., Larson, D., Nolta, M. R., Page, L., Spergel, D. N., Halpern, M., Hill, R. S., Kogut, A., Limon, M., Meyer, S. S., Odegard, N., Tucker, G. S., Weiland, J. L., Wollack, E., & Wright, E. L. (2011). Seven-year Wilkinson Microwave Anisotropy Probe (WMAP) Observations: Cosmological Interpretation. *ApJS*, 192, 18.

Kraft, R. P., Peterson, R. C., Guhathakurta, P., Sneden, C., Fulbright, J. P., & Langer, G. E. (1999). An Extremely Lithium-rich Bright Red Giant in the Globular Cluster M3. *ApJ*, 518, L53–L56.

Kumar, Y. B. & Reddy, B. E. (2009). HD 77361: A New Case of Super Li-Rich K Giant with Anomalous Low $^{12}C/^{13}C$ Ratio. *ApJ*, 703, L46–L50.

Kumar, Y. B., Reddy, B. E., & Lambert, D. L. (2011). Origin of Lithium Enrichment in K Giants. *ApJ*, 730, L12.

Kupka, F., Dubernet, M.-L., & VAMDC Collaboration (2011). Vamdc as a Resource for Atomic and Molecular Data and the New Release of Vald. *Baltic Astronomy*, 20, 503–510.

Kupka, F., Piskunov, N., Ryabchikova, T. A., Stempels, H. C., & Weiss, W. W. (1999). VALD-2: Progress of the Vienna Atomic Line Data Base. *A&AS*, 138, 119–133.

Kurucz, R. L. (2005). ATLAS12, SYNTHE, ATLAS9, WIDTH9, et cetera. *Memorie della Societa Astronomica Italiana Supplementi*, 8, 14.

Lambert, D. L., Heath, J. E., & Edvardsson, B. (1991). Lithium abundances for 81 F dwarfs. *MNRAS*, 253, 610–618.

Lambert, D. L. & Reddy, B. E. (2004). Lithium abundances of the local thin disc stars. *MNRAS*, 349, 757–767.

Lanzafame, A. C. & Spada, F. (2015). Rotational evolution of slow-rotator sequence stars. *A&A*, 584, A30.

Larson, D., Dunkley, J., Hinshaw, G., Komatsu, E., Nolta, M. R., Bennett, C. L., Gold, B., Halpern, M., Hill, R. S., Jarosik, N., Kogut, A., Limon, M., Meyer, S. S., Odegard, N., Page, L., Smith, K. M., Spergel, D. N., Tucker, G. S., Weiland, J. L., Wollack, E., & Wright, E. L. (2011). Seven-year Wilkinson Microwave Anisotropy Probe (WMAP) Observations: Power Spectra and WMAP-derived Parameters. *ApJS*, 192, 16.

Lattanzio, J. C., Siess, L., Church, R. P., Angelou, G., Stancliffe, R. J., Doherty, C. L., Stephen, T., & Campbell, S. W. (2015). On the numerical treatment and dependence of thermohaline mixing in red giants. *MNRAS*, 446, 2673–2688.

Lee-Brown, D. B., Anthony-Twarog, B. J., Deliyannis, C. P., Rich, E., & Twarog, B. A. (2015). Spectroscopic Abundances in the Open Cluster NGC 6819. *AJ*, 149, 121.

Li, X.-R., Pan, R.-Y., & Duan, F.-Q. (2017). Parameterizing stellar spectra using deep neural networks. *Research in Astronomy and Astrophysics*, 17(4), 036.

Lindegren, L., Lammers, U., Bastian, U., Hernández, J., Klioner, S., Hobbs, D., Bombrun, A., Michalik, D., Ramos-Lerate, M., Butkevich, A., Comoretto, G., Joliet, E., Holl, B., Hutton, A., Parsons, P., Steidelmüller, H., Abbas, U., Altmann, M., Andrei, A., Anton, S., Bach, N., Barache, C., Becciani, U., Berthier, J., Bianchi, L., Biermann, M., Bouquillon, S., Bourda, G., Brüsemeister, T., Bucciarelli, B., Busonero, D., Carlucci, T., Castañeda, J., Charlot, P., Clotet, M., Crosta, M., Davidson, M., de Felice, F., Drimmel, R., Fabricius, C., Fienga, A., Figueras, F., Fraile, E., Gai, M., Garralda, N., Geyer, R., González-Vidal, J. J., Guerra, R., Hambly, N. C., Hauser, M., Jordan, S., Lattanzi, M. G., Lenhardt, H., Liao, S., Löffler, W., McMillan, P. J., Mignard, F., Mora, A., Morbidelli, R., Portell, J., Riva, A., Sarasso, M., Serraller, I., Siddiqui, H., Smart, R., Spagna, A., Stampa, U., Steele, I., Taris, F., Torra, J., van Reeven, W., Vecchiato, A., Zschocke, S., de Bruijne, J., Gracia, G., Raison, F., Lister, T., Marchant, J., Messineo, R., Soffel, M., Osorio, J., de Torres, A., & O'Mullane, W. (2016). Gaia Data Release 1. Astrometry: one billion positions, two million proper motions and parallaxes. *A&A*, 595, A4.

Lodders, K., Palme, H., & Gail, H.-P. (2009). Abundances of the Elements in the Solar System. *Landolt Börnstein*.

López-Valdivia, R., Bertone, E., & Chávez, M. (2017). Mg, Al, Si, Ca, Ti, Fe, and Ni abundance for a sample of solar analogues. *MNRAS*, 467, 2412–2420.

López-Valdivia, R., Hernández-Águila, J. B., Bertone, E., Chávez, M., Cruz-Saenz de Miera, F., & Amazo-Gómez, E. M. (2015). Lithium abundance in a sample of solar-like stars. *MNRAS*, 451, 4368–4374.

Malagnini, M. L., Morossi, C., Buzzoni, A., & Chavez, M. (2000). Observations and Atmospheric Parameters of Super-Metal-rich Candidates. *PASP*, 112, 1455–1466.

Manteiga, M., Ordóñez, D., Dafonte, C., & Arcay, B. (2010). ANNs and Wavelets: A Strategy for

Gaia RVS Low S/N Stellar Spectra Parameterization. *Publications of the Astronomical Society of the Pacific*, 122, 608.

Marivate, V. N., Nelwamondo, F. V., & Marwala, T. (2008). Investigation into the use of autoencoder neural networks, principal component analysis and support vector regression in estimating missing hiv data. *IFAC Proceedings Volumes*, 41(2), 682 – 689. 17th IFAC World Congress.

Martin, R. P., Andrievsky, S. M., Kovtyukh, V. V., Korotin, S. A., Yegorova, I. A., & Saviane, I. (2015). Oxygen, α-element and iron abundance distributions in the inner part of the Galactic thin disc. *MNRAS*, 449, 4071–4078.

Mashonkina, L., Gehren, T., Shi, J.-R., Korn, A. J., & Grupp, F. (2011). A non-LTE study of neutral and singly-ionized iron line spectra in 1D models of the Sun and selected late-type stars. *A&A*, 528, A87.

McWilliam, A. (1997). Abundance Ratios and Galactic Chemical Evolution. *ARA&A*, 35, 503–556.

McWilliam, A. & Rich, R. M. (1994). The first detailed abundance analysis of Galactic bulge K giants in Baade's window. *ApJS*, 91, 749–791.

Meibom, S., Grundahl, F., Clausen, J. V., Mathieu, R. D., Frandsen, S., Pigulski, A., Narwid, A., Steslicki, M., & Lefever, K. (2009). Age and Distance for the Old Open Cluster NGC 188 from the Eclipsing Binary Member V 12. *AJ*, 137, 5086–5098.

Meléndez, J., Ramírez, I., Casagrande, L., Asplund, M., Gustafsson, B., Yong, D., Do Nascimento, J. D., Castro, M., & Bazot, M. (2010). The solar, exoplanet and cosmological lithium problems. *Ap&SS*, 328, 193–200.

Mishenina, T., Kovtyukh, V., Soubiran, C., & Adibekyan, V. Z. (2016). Behaviour of elements from lithium to europium in stars with and without planets. *MNRAS*, 462, 1563–1576.

Montalbán, J. & Schatzman, E. (2000). Mixing by internal waves. III. Li and Be abundance dependence on spectral type, age and rotation. *A&A*, 354, 943–959.

Mortier, A., Sousa, S. G., Adibekyan, V. Z., Brandão, I. M., & Santos, N. C. (2014). Correcting the spectroscopic surface gravity using transits and asteroseismology. No significant effect on temperatures or metallicities with ARES and MOOG in local thermodynamic equilibrium. *A&A*, 572, A95.

Mowlavi, N., Meynet, G., Maeder, A., Schaerer, D., & Charbonnel, C. (1998). On some properties of very metal-rich stars. *A&A*, 335, 573–582.

Nesterov, Y. (1983). A method of solving a convex programming problem with convergence rate o (1/k2). In *Soviet Mathematics Doklady*, volume 27 (pp. 372–376).

Nissen, P. E. (2004). Thin and Thick Galactic Disks. *Origin and Evolution of the Elements*, (pp. 154).

Nordström, B., Mayor, M., Andersen, J., Holmberg, J., Pont, F., Jørgensen, B. R., Olsen, E. H., Udry, S., & Mowlavi, N. (2004). The Geneva-Copenhagen survey of the Solar neighbourhood. Ages, metallicities, and kinematic properties of 14 000 F and G dwarfs. *A&A*, 418, 989–1019.

Olsen, E. H. (1983). Four-colour UVBY and H-beta photometry of A5 to G0 stars brighter than 8.3 M. *A&AS*, 54, 55–134.

Olsen, E. H. (1993). Stromgren Four-Colour UVBY Photometry of G5-TYPE Hd-Stars Brighter than MV=8.6. *A&AS*, 102, 89.

Olsen, E. H. (1994). Stroemgren photometry of F- and G-type stars brighter than V = 9.6. I. UVBY photometry. *A&AS*, 106, 257–266.

Pasquini, L., Randich, S., & Pallavicini, R. (1997). Lithium in M 67: evidence for spread in a solar age cluster. *A&A*, 325, 535–541.

Pereira, C. B., Sales Silva, J. V., Chavero, C., Roig, F., & Jilinski, E. (2011). Chemical abundances and kinematics of a sample of metal-rich barium stars. *A&A*, 533, A51.

Pinsonneault, M. (1997). Mixing in Stars. *ARA&A*, 35, 557–605.

Pinsonneault, M. H. (2010). Rotational mixing and Lithium depletion. In C. Charbonnel, M. Tosi, F. Primas, & C. Chiappini (Eds.), *Light Elements in the Universe*, volume 268 of *IAU Symposium* (pp. 375–380).

Pinsonneault, M. H., Kawaler, S. D., & Demarque, P. (1990). Rotation of low-mass stars - A new probe of stellar evolution. *ApJS*, 74, 501–550.

Piskunov, N. & Valenti, J. A. (2017). Spectroscopy Made Easy: Evolution. *A&A*, 597, A16.

Planck Collaboration, Ade, P. A. R., Aghanim, N., Armitage-Caplan, C., Arnaud, M., Ashdown, M., Atrio-Barandela, F., Aumont, J., Baccigalupi, C., Banday, A. J., & et al. (2014). Planck 2013 results. XVI. Cosmological parameters. *A&A*, 571, A16.

Platais, I., Gosnell, N. M., Meibom, S., Kozhurina-Platais, V., Bellini, A., Veillet, C., & Burkhead, M. S. (2013). WIYN Open Cluster Study. LV. Astrometry and Membership in NGC 6819. *AJ*, 146, 43.

Prantzos, N. (2012). Production and evolution of Li, Be, and B isotopes in the Galaxy. *A&A*, 542, A67.

Raboud, D., Grenon, M., Martinet, L., Fux, R., & Udry, S. (1998). Evidence for a signature of the galactic bar in the solar neighbourhood. *A&A*, 335, L61–L64.

Ramírez, I., Fish, J. R., Lambert, D. L., & Allende Prieto, C. (2012). Lithium Abundances in nearby FGK Dwarf and Subgiant Stars: Internal Destruction, Galactic Chemical Evolution, and Exoplanets. *ApJ*, 756, 46.

Ramírez, I. & Meléndez, J. (2005). The Effective Temperature Scale of FGK Stars. II. T_{eff}:Color:[Fe/H] Calibrations. *ApJ*, 626, 465–485.

Randich, S., Aharpour, N., Pallavicini, R., Prosser, C. F., & Stauffer, J. R. (1997). Lithium abundances in the young open cluster IC 2602. *A&A*, 323, 86–97.

Randich, S., Pace, G., Pastori, L., & Bragaglia, A. (2009). Membership and lithium in the old, metal-poor open cluster Berkeley 32. *A&A*, 496, 441–451.

Rebolo, R. (1989). The galactic evolution of lithium. *Ap&SS*, 157, 47–54.

Recio-Blanco, A., de Laverny, P., Allende Prieto, C., Fustes, D., Manteiga, M., Arcay, B., Bijaoui, A., Dafonte, C., Ordenovic, C., & Ordoñez Blanco, D. (2016). Stellar parametrization from Gaia RVS spectra. *A&A*, 585, A93.

Reeves, H. (1970). Galactic Cosmic Ray Origin of Li, Be and B in Stars. *Nature*, 226, 727–729.

Richard, O., Michaud, G., & Richer, J. (2005). Implications of WMAP Observations on Li Abundance and Stellar Evolution Models. *ApJ*, 619, 538–548.

Richer, J. & Michaud, G. (1993). Diffusion of Lithium and Beryllium in Evolving, Nonrotating Main-Sequence A and F Stars. *ApJ*, 416, 312.

Robin, A. C., Reylé, C., Derrière, S., & Picaud, S. (2003). A synthetic view on structure and evolution of the Milky Way. *A&A*, 409, 523–540.

Robinson, S. E., Ammons, S. M., Kretke, K. A., Strader, J., Wertheimer, J. G., Fischer, D. A., & Laughlin, G. (2007). The N2K Consortium. VII. Atmospheric Parameters of 1907 Metal-rich Stars: Finding Planet-Search Targets. *ApJS*, 169, 430–438.

Romano, D., Matteucci, F., Molaro, P., & Bonifacio, P. (1999). The galactic lithium evolution revisited. *A&A*, 352, 117–128.

Romano, D., Matteucci, F., Ventura, P., & D'Antona, F. (2001). The stellar origin of ^{7}Li. Do AGB stars contribute a substantial fraction of the local Galactic lithium abundance? *A&A*, 374, 646–655.

Roxburgh, I. W. & Kupka, F. (2007). Mixing length model of convection in stellar cores. In F. Kupka, I. Roxburgh, & K. L. Chan (Eds.), *Convection in Astrophysics*, volume 239 of *IAU Symposium* (pp. 98–99).

Ruchti, G. R., Fulbright, J. P., Wyse, R. F. G., Gilmore, G. F., Grebel, E. K., Bienaymé, O., Bland-Hawthorn, J., Freeman, K. C., Gibson, B. K., Munari, U., Navarro, J. F., Parker, Q. A., Reid, W., Seabroke, G. M., Siebert, A., Siviero, A., Steinmetz, M., Watson, F. G., Williams, M., & Zwitter, T. (2011). Metal-poor Lithium-rich Giants in the Radial Velocity Experiment Survey. *ApJ*, 743, 107.

Ruder, S. (2016). An overview of gradient descent optimization algorithms. *ArXiv e-prints: 1609.04747*.

Ryan, S. G., Kajino, T., Beers, T. C., Suzuki, T. K., Romano, D., Matteucci, F., & Rosolankova, K. (2001). Abundances and Evolution of Lithium in the Galactic Halo and Disk. *ApJ*, 549, 55–71.

Sackmann, I.-J. & Boothroyd, A. I. (1992). The creation of superrich lithium giants. *ApJ*, 392, L71–L74.

Sackmann, I.-J. & Boothroyd, A. I. (1999). Creation of ^{7}Li and Destruction of ^{3}He, ^{9}Be, ^{10}B, and ^{11}B in Low-Mass Red Giants, Due to Deep Circulation. *ApJ*, 510, 217–231.

Sadeh, I., Abdalla, F. B., & Lahav, O. (2016). ANNz2: Photometric Redshift and Probability Distribution Function Estimation using Machine Learning. *PASP*, 128(10), 104502.

Salaris, M., Weiss, A., & Percival, S. M. (2004). The age of the oldest Open Clusters. *A&A*, 414, 163–174.

Sato, B., Fischer, D. A., Henry, G. W., Laughlin, G., Butler, R. P., Marcy, G. W., Vogt, S. S., Bodenheimer, P., Ida, S., Toyota, E., Wolf, A., Valenti, J. A., Boyd, L. J., Johnson, J. A., Wright, J. T., Ammons, M., Robinson, S., Strader, J., McCarthy, C., Tah, K. L., & Minniti, D. (2005).

The N2K Consortium. II. A Transiting Hot Saturn around HD 149026 with a Large Dense Core. *ApJ*, 633, 465–473.

Schawinski, K., Zhang, C., Zhang, H., Fowler, L., & Santhanam, G. K. (2017). Generative adversarial networks recover features in astrophysical images of galaxies beyond the deconvolution limit. *MNRAS*, 467, L110–L114.

Schramm, D. N., Steigman, G., & Dearborn, D. S. P. (1990). Main-sequence mass loss and the lithium dip. *ApJ*, 359, L55–L58.

Seghouane, A. K., Moudden, Y., & Fleury, G. (2002). On learning feedforward neural networks with noise injection into inputs. In *Proceedings of the 12th IEEE Workshop on Neural Networks for Signal Processing* (pp. 149–158).

Sestito, P. & Randich, S. (2005). Time scales of Li evolution: a homogeneous analysis of open clusters from ZAMS to late-MS. *A&A*, 442, 615–627.

Sestito, P., Randich, S., & Pallavicini, R. (2004). Lithium evolution in intermediate age and old open clusters: NGC 752 revisited. *A&A*, 426, 809–817.

Sills, A. & Deliyannis, C. P. (2000). WIYN Open Cluster Study. VI. Interpretive Models of Light-Element Depletion from M67 Subgiants. *ApJ*, 544, 944–952.

Simonyan, K. & Zisserman, A. (2015). Very deep convolutional networks for large-scale image recognition. *International Conference on Learning Representations 2015 (retrieved from arXiv:1409.1556)*.

Skumanich, A. (1972). Time Scales for CA II Emission Decay, Rotational Braking, and Lithium Depletion. *ApJ*, 171, 565.

Smith, G. A., Saunders, W., Bridges, T., Churilov, V., Lankshear, A., Dawson, J., Correll, D., Waller, L., Haynes, R., & Frost, G. (2004). AAOmega: a multipurpose fiber-fed spectrograph for

the AAT. In A. F. M. Moorwood & M. Iye (Eds.), *Ground-based Instrumentation for Astronomy*, volume 5492 of *Proc. SPIE* (pp. 410–420).

Smith, V. V., Shetrone, M. D., & Keane, M. J. (1999). Lithium in a Cool Red Giant Member of the Globular Cluster NGC 362. *ApJ*, 516, L73–L76.

Sneden, C. (1973a). The nitrogen abundance of the very metal-poor star HD 122563. *ApJ*, 184, 839–849.

Sneden, C. (1973b). The nitrogen abundance of the very metal-poor star HD 122563. *ApJ*, 184, 839–849.

Snider, S., Allende Prieto, C., von Hippel, T., Beers, T. C., Sneden, C., Qu, Y., & Rossi, S. (2001). Three-dimensional Spectral Classification of Low-Metallicity Stars Using Artificial Neural Networks. *The Astrophysical Journal*, 562, 528–548.

Soderblom, D. R., Fedele, S. B., Jones, B. F., Stauffer, J. R., & Prosser, C. F. (1993). The evolution of the lithium abundances of solar-type stars. IV - Praesepe. *AJ*, 106, 1080–1086.

Somers, G. & Pinsonneault, M. H. (2014). A Tale of Two Anomalies: Depletion, Dispersion, and the Connection between the Stellar Lithium Spread and Inflated Radii on the Pre-main Sequence. *ApJ*, 790, 72.

Soubiran, C., Le Campion, J.-F., Brouillet, N., & Chemin, L. (2016). The PASTEL catalogue: 2016 version. *A&A*, 591, A118.

Sousa, S. G., Fernandes, J., Israelian, G., & Santos, N. C. (2010). Higher depletion of lithium in planet host stars: no age and mass effect. *A&A*, 512, L5.

Spite, F. & Spite, M. (1982). Abundance of lithium in unevolved halo stars and old disk stars - Interpretation and consequences. *A&A*, 115, 357–366.

Spite, M., Spite, F., & Bonifacio, P. (2012). The cosmic lithium problem . an observer's perspective. *Memorie della Societa Astronomica Italiana Supplementi*, 22, 9.

Srivastava, N., Hinton, G. E., Krizhevsky, A., Sutskever, I., & Salakhutdinov, R. (2014). Dropout: a simple way to prevent neural networks from overfitting. *Journal of machine learning research*, 15(1), 1929–1958.

Stauffer, J. R. (2004). Rotational Evolution of Intermediate and Low Mass Main Sequence Stars (Invited Review). In A. Maeder & P. Eenens (Eds.), *Stellar Rotation*, volume 215 of *IAU Symposium* (pp. 127).

Stauffer, J. R., Hartmann, L., Soderblom, D. R., & Burnham, N. (1984). Rotational velocities of low-mass stars in the Pleiades. *ApJ*, 280, 202–212.

Steinmetz, M., Zwitter, T., Siebert, A., Watson, F. G., Freeman, K. C., Munari, U., Campbell, R., Williams, M., Seabroke, G. M., Wyse, R. F. G., Parker, Q. A., Bienaymé, O., Roeser, S., Gibson, B. K., Gilmore, G., Grebel, E. K., Helmi, A., Navarro, J. F., Burton, D., Cass, C. J. P., Dawe, J. A., Fiegert, K., Hartley, M., Russell, K. S., Saunders, W., Enke, H., Bailin, J., Binney, J., Bland-Hawthorn, J., Boeche, C., Dehnen, W., Eisenstein, D. J., Evans, N. W., Fiorucci, M., Fulbright, J. P., Gerhard, O., Jauregi, U., Kelz, A., Mijović, L., Minchev, I., Parmentier, G., Peñarrubia, J., Quillen, A. C., Read, M. A., Ruchti, G., Scholz, R.-D., Siviero, A., Smith, M. C., Sordo, R., Veltz, L., Vidrih, S., von Berlepsch, R., Boyle, B. J., & Schilbach, E. (2006). The Radial Velocity Experiment (RAVE): First Data Release. *AJ*, 132, 1645–1668.

Stephens, A., Boesgaard, A. M., King, J. R., & Deliyannis, C. P. (1997). Beryllium in Lithium-deficient F and G Stars. *ApJ*, 491, 339–358.

Sugai, H., Tamura, N., Karoji, H., Shimono, A., Takato, N., Kimura, M., Ohyama, Y., Ueda, A., Aghazarian, H., de Arruda, M. V., Barkhouser, R. H., Bennett, C. L., Bickerton, S., Bozier, A., Braun, D. F., Bui, K., Capocasale, C. M., Carr, M. A., Castilho, B., Chang, Y.-C., Chen, H.-Y., Chou, R. C. Y., Dawson, O. R., Dekany, R. G., Ek, E. M., Ellis, R. S., English, R. J., Ferrand, D., Ferreira, D., Fisher, C. D., Golebiowski, M., Gunn, J. E., Hart, M., Heckman, T. M., Ho, P. T. P., Hope, S., Hovland, L. E., Hsu, S.-F., Hu, Y.-S., Huang, P. J., Jaquet, M., Karr, J. E., Kempenaar,

J. G., King, M. E., le Fèvre, O., Mignant, D. L., Ling, H.-H., Loomis, C., Lupton, R. H., Madec, F., Mao, P., Souza Marrara, L., Ménard, B., Morantz, C., Murayama, H., Murray, G. J., Cesar de Oliveira, A., Mendes de Oliveira, C., Souza de Oliveira, L., Orndorff, J. D., de Paiva Vilaça, R., Partos, E. J., Pascal, S., Pegot-Ogier, T., Reiley, D. J., Riddle, R., Santos, L., dos Santos, J. B., Schwochert, M. A., Seiffert, M. D., Smee, S. A., Smith, R. M., Steinkraus, R. E., Sodré, L., Spergel, D. N., Surace, C., Tresse, L., Vidal, C., Vives, S., Wang, S.-Y., Wen, C.-Y., Wu, A. C., Wyse, R., & Yan, C.-H. (2015). Prime Focus Spectrograph for the Subaru telescope: massively multiplexed optical and near-infrared fiber spectrograph. *Journal of Astronomical Telescopes, Instruments, and Systems*, 1(3), 035001.

Suzuki, T. K., Yoshii, Y., & Kajino, T. (1999). Evolution of Beryllium and Boron in the Inhomogeneous Early Galaxy. *ApJ*, 522, L125–L128.

Swenson, F. J. & Faulkner, J. (1992). Lithium dilution through main-sequence mass loss. *ApJ*, 395, 654–674.

Swenson, F. J., Faulkner, J., Iglesias, C. A., Rogers, F. J., & Alexander, D. R. (1994). The classical Hyades lithium problem resolved? *ApJ*, 422, L79–L82.

Swenson, F. J., Stringfellow, G. S., & Faulkner, J. (1990). Is there a classical Hyades lithium problem? *ApJ*, 348, L33–L36.

Symons, T. A. (2017). photPARTY: Python Automated Square-Aperture Photometry (Masters Thesis, University of Kansas). *ProQuest Dissertations and Theses.* Retrieved from http://hdl.handle.net/1808/25830.

Tajitsu, A., Sadakane, K., Naito, H., Arai, A., & Aoki, W. (2015). Explosive lithium production in the classical nova V339 Del (Nova Delphini 2013). *Nature*, 518, 381–384.

Takeda, Y., Honda, S., Kawanomoto, S., Ando, H., & Sakurai, T. (2010). Behavior of Li abundances in solar-analog stars. II. Evidence of the connection with rotation and stellar activity. *A&A*, 515, A93.

Talon, S. & Charbonnel, C. (2003). Angular momentum transport by internal gravity waves. I - Pop I main sequence stars. *A&A*, 405, 1025–1032.

Talon, S. & Charbonnel, C. (2005). Hydrodynamical stellar models including rotation, internal gravity waves, and atomic diffusion. I. Formalism and tests on Pop I dwarfs. *A&A*, 440, 981–994.

Taylor, B. J. (1996). Supermetallicity at the Quarter-Century Mark: A Conservative Statistician's Review of the Evidence. *ApJS*, 102, 105.

Thévenin, F., Oreshina, A. V., Baturin, V. A., Gorshkov, A. B., Morel, P., & Provost, J. (2017). Evolution of lithium abundance in the Sun and solar twins. *A&A*, 598, A64.

Thomas, D., Schramm, D. N., Olive, K. A., & Fields, B. D. (1993). Primordial nucleosynthesis and the abundances of beryllium and boron. *ApJ*, 406, 569–579.

Travaglio, C., Randich, S., Galli, D., Lattanzio, J., Elliott, L. M., Forestini, M., & Ferrini, F. (2001). Galactic Chemical Evolution of Lithium: Interplay between Stellar Sources. *ApJ*, 559, 909–924.

Trevisan, M., Barbuy, B., Eriksson, K., Gustafsson, B., Grenon, M., & Pompéia, L. (2011). Analysis of old very metal rich stars in the solar neighbourhood. *A&A*, 535, A42.

Trevisan, M., Barbuy, B., Grenon, M., Gustafsson, B., & Pompéia, L. (2010). FEROS Abundance Analysis of 21 Bulgelike SMR Stars. In K. Cunha, M. Spite, & B. Barbuy (Eds.), *Chemical Abundances in the Universe: Connecting First Stars to Planets*, volume 265 of *IAU Symposium* (pp. 382–383).

Twarog, B. A. & Anthony-Twarog, B. J. (1995). Ca II H and K Filter Photometry on the UVBY System. II. The Catalog of Observations. *AJ*, 109, 2828.

Valenti, J. A. & Piskunov, N. (1996). Spectroscopy made easy: A new tool for fitting observations with synthetic spectra. *A&AS*, 118, 595–603.

Ventura, P. & D'Antona, F. (2010). The role of lithium production in massive AGB and super-AGB stars for the understanding of multiple populations in globular clusters. *MNRAS*, 402, L72–L76.

Wagoner, R. V., Fowler, W. A., & Hoyle, F. (1967). On the Synthesis of Elements at Very High Temperatures. *ApJ*, 148, 3.

Walker, T. P., Steigman, G., Kang, H.-S., Schramm, D. M., & Olive, K. A. (1991). Primordial nucleosynthesis redux. *ApJ*, 376, 51–69.

Wallace, L., Hinkle, K., & Livingston, W. (1998). *An atlas of the spectrum of the solar photosphere from 13,500 to 28,000 cm-1 (3570 to 7405 A)*.

Wallerstein, G. & Sneden, C. (1982). A K giant with an unusually high abundance of lithium - HD 112127. *ApJ*, 255, 577–584.

Waters, C. Z. & Hollek, J. K. (2013). ROBOSPECT: Automated Equivalent Width Measurement. *PASP*, 125, 1164.

Wenger, M., Ochsenbein, F., Egret, D., Dubois, P., Bonnarel, F., Borde, S., Genova, F., Jasniewicz, G., Laloë, S., Lesteven, S., & Monier, R. (2000). The SIMBAD astronomical database. The CDS reference database for astronomical objects. *A&AS*, 143, 9–22.

Xiong, D. R. & Deng, L. (2009). Lithium depletion in late-type dwarfs. *MNRAS*, 395, 2013–2028.

Yang, S.-C., Sarajedini, A., Deliyannis, C. P., Sarrazine, A. R., Kim, S. C., & Kyeong, J. (2013). WIYN Open Cluster Study LII: Wide-field CCD Photometry of the Old Open Cluster NGC 6819. *ApJ*, 762, 3.

Yanny, B., Rockosi, C., Newberg, H. J., Knapp, G. R., Adelman-McCarthy, J. K., Alcorn, B., Allam, S., Allende Prieto, C., An, D., Anderson, K. S. J., Anderson, S., Bailer-Jones, C. A. L., Bastian, S., Beers, T. C., Bell, E., Belokurov, V., Bizyaev, D., Blythe, N., Bochanski, J. J., Boroski, W. N., Brinchmann, J., Brinkmann, J., Brewington, H., Carey, L., Cudworth, K. M.,

Evans, M., Evans, N. W., Gates, E., Gänsicke, B. T., Gillespie, B., Gilmore, G., Nebot Gomez-Moran, A., Grebel, E. K., Greenwell, J., Gunn, J. E., Jordan, C., Jordan, W., Harding, P., Harris, H., Hendry, J. S., Holder, D., Ivans, I. I., Ivezič, Ž., Jester, S., Johnson, J. A., Kent, S. M., Kleinman, S., Kniazev, A., Krzesinski, J., Kron, R., Kuropatkin, N., Lebedeva, S., Lee, Y. S., French Leger, R., Lépine, S., Levine, S., Lin, H., Long, D. C., Loomis, C., Lupton, R., Malanushenko, O., Malanushenko, V., Margon, B., Martinez-Delgado, D., McGehee, P., Monet, D., Morrison, H. L., Munn, J. A., Neilsen, Jr., E. H., Nitta, A., Norris, J. E., Oravetz, D., Owen, R., Padmanabhan, N., Pan, K., Peterson, R. S., Pier, J. R., Platson, J., Re Fiorentin, P., Richards, G. T., Rix, H.-W., Schlegel, D. J., Schneider, D. P., Schreiber, M. R., Schwope, A., Sibley, V., Simmons, A., Snedden, S. A., Allyn Smith, J., Stark, L., Stauffer, F., Steinmetz, M., Stoughton, C., SubbaRao, M., Szalay, A., Szkody, P., Thakar, A. R., Sivarani, T., Tucker, D., Uomoto, A., Vanden Berk, D., Vidrih, S., Wadadekar, Y., Watters, S., Wilhelm, R., Wyse, R. F. G., Yarger, J., & Zucker, D. (2009). SEGUE: A Spectroscopic Survey of 240,000 Stars with g = 14-20. *AJ*, 137, 4377–4399.

York, D. G., Adelman, J., Anderson, Jr., J. E., Anderson, S. F., Annis, J., Bahcall, N. A., Bakken, J. A., Barkhouser, R., Bastian, S., Berman, E., Boroski, W. N., Bracker, S., Briegel, C., Briggs, J. W., Brinkmann, J., Brunner, R., Burles, S., Carey, L., Carr, M. A., Castander, F. J., Chen, B., Colestock, P. L., Connolly, A. J., Crocker, J. H., Csabai, I., Czarapata, P. C., Davis, J. E., Doi, M., Dombeck, T., Eisenstein, D., Ellman, N., Elms, B. R., Evans, M. L., Fan, X., Federwitz, G. R., Fiscelli, L., Friedman, S., Frieman, J. A., Fukugita, M., Gillespie, B., Gunn, J. E., Gurbani, V. K., de Haas, E., Haldeman, M., Harris, F. H., Hayes, J., Heckman, T. M., Hennessy, G. S., Hindsley, R. B., Holm, S., Holmgren, D. J., Huang, C.-h., Hull, C., Husby, D., Ichikawa, S.-I., Ichikawa, T., Ivezić, Ž., Kent, S., Kim, R. S. J., Kinney, E., Klaene, M., Kleinman, A. N., Kleinman, S., Knapp, G. R., Korienek, J., Kron, R. G., Kunszt, P. Z., Lamb, D. Q., Lee, B., Leger, R. F., Limmongkol, S., Lindenmeyer, C., Long, D. C., Loomis, C., Loveday, J., Lucinio, R., Lupton, R. H., MacKinnon, B., Mannery, E. J., Mantsch, P. M., Margon, B., McGehee, P., McKay, T. A., Meiksin, A., Merelli, A., Monet, D. G., Munn, J. A., Narayanan, V. K., Nash, T., Neilsen, E., Neswold, R., Newberg, H. J., Nichol, R. C., Nicinski, T., Nonino, M., Okada, N.,

Okamura, S., Ostriker, J. P., Owen, R., Pauls, A. G., Peoples, J., Peterson, R. L., Petravick, D., Pier, J. R., Pope, A., Pordes, R., Prosapio, A., Rechenmacher, R., Quinn, T. R., Richards, G. T., Richmond, M. W., Rivetta, C. H., Rockosi, C. M., Ruthmansdorfer, K., Sandford, D., Schlegel, D. J., Schneider, D. P., Sekiguchi, M., Sergey, G., Shimasaku, K., Siegmund, W. A., Smee, S., Smith, J. A., Snedden, S., Stone, R., Stoughton, C., Strauss, M. A., Stubbs, C., SubbaRao, M., Szalay, A. S., Szapudi, I., Szokoly, G. P., Thakar, A. R., Tremonti, C., Tucker, D. L., Uomoto, A., Vanden Berk, D., Vogeley, M. S., Waddell, P., Wang, S.-i., Watanabe, M., Weinberg, D. H., Yanny, B., Yasuda, N., & SDSS Collaboration (2000). The Sloan Digital Sky Survey: Technical Summary. *AJ*, 120, 1579–1587.